SEMICONDUCTORS VOLUME 33, NUMBER 5 MAY 1999

REVIEW

Induced photopleochroism in semiconductors Review

F. P. Kesamanly and V. Yu. Rud'*

St. Petersburg State Technical University, 195257 St. Petersburg, Russia

Yu. V. Rud'

A. F. Ioffe Physicotechnical Institute, Russian Academy of Sciences, 194021 St. Petersburg, Russia

(Submitted August 24, 1998; accepted for publication September 22, 1998)
Fiz. Tekh. Poluprovodn. **33**, 513–536 (May 1999)

The results of experimental investigations of induced photopleochroism of elementary (Si, Ge), binary (III–V, II–VI), and more complicated diamond-like semiconductors (III–V—III–V solid solutions, ternary compounds I–III–VI and II–IV–V compounds) and photosensitive structures based on them are discussed and generalized. The laws of induced photopleochroism, which have been established for various types of phototransducers, and their relation with the parameters of semiconductors are analyzed. The possibilities of practical applications of induced polarization photosensitivity of isotropic semiconductors in polarimetric structures and in the diagnostics of the quality of the semiconductors are discussed.
[S1063-7826(99)00105-2]

1. INTRODUCTION

A complete description of optical radiation includes, in addition to the intensity and photon energy, the state of polarization of the light wave.[1–5] In this respect, the present growth of semiconductor optoelectronics based on source-to-detector information transfer and reception by intensity and wavelength modulation of a light flux is one-sided. It is completely obvious that the development of optoelectronic systems in which the state of polarization also plays the role of an information parameter will make it possible to increase system capacity substantially. The need to develop polarized optoelectronics is also stimulated by the rapid growth of applications of linearly polarized light (LPL) in science and technology.[6–8] In this connection, fundamental research on the anisotropy of photoelectric phenomena is evolving into a central direction in the physics and technology of semiconductors.

A qualitative breakthrough in this field involved the use of natural photopleochroism (NP) in photoconversion structures based on oriented anisotropic semiconductors from several crystal classes.[9,10] Thus the first phototransducers, whose quantum efficiency is determined by the position of the polarization plane of LPL relative to the principal crystallographic axes of the semiconductor, were developed.[9] The still inadequate, for large-scale applications of NP, technological familiarity of anisotropic semiconductor materials is stimulating assessment of the classic cubic semiconductors, whose technological base is well-developed, for use in polarimetric photodetectors.

For a long time attempts have been made throughout the world to use isotropic semiconductors (ISs) for analyzing polarized radiation, for example, by adding to IS photodetectors an external polarizing component and by producing uniaxial deformation[11] or conditions for photon drag of charge carriers[12] and for photovoltaic effects.[13–16] In the most widely used approach a polarization-insensitive photodetector is equipped with an external polarizing component and the polarization parameters of the incident radiation are determined on the basis of the intensity measured with the photodetector. In such systems there always arises the problem of spectral matching of the polarizing component and the photodetector, and, in addition, the polarizing component generally introduces additional radiation losses in the optical channel and thereby lowers the detection power of the system with respect to polarization. It should also be underscored that polarimetric systems with an external (relative to the photodetector) polarizing component are also not widely used because of structural design complications.[17] Polarization-sensitive IS photodetectors based on the approaches considered above have never been demonstrated explicitly.

A major step forward in this problem appeared only with the discovery, in the 1980s at A. F. Ioffe Physicotechnical Institute, of a new type of photopleochroism induced by oblique incidence of LPL on the receiving plane of a photodetector.[18] This type of photopleochroism is determined entirely by the optical processes occurring at the interface between a semiconductor and the medium from which the LPL is incident on the semiconductor and, in contrast to NP,[10] there are no limitations with respect to the structure and phase state of the semiconductor. Thus polarimetric photodetectors with record-high azimuthal photosensitivity $\approx 0.2\ \mathrm{A/W \cdot deg}$ and wide-band or narrowly selective regimes of photodetection of natural and linearly polarized light, as well as with continuous tuning of the induced photopleochroism (IP) have been developed. The first demonstrations of the possibilities of obtaining gigantic induced photopleochroism (GIP) and using polarization photosensitivity spectroscopy for rapid diagnostics of the quality of finished structures have been performed in the structures obtained.

Many original publications and announcements reporting the results of investigations of IP in various photosensitive structures based on a large group of semiconductor materials from the basic classes have now appeared at various levels of scientific conferences. In our review article the physical mechanisms of the new photoelectric phenomenon are examined and approaches are developed for obtaining and controlling the parameters of polarimetric semiconductor photodetectors based on this effect. The characteristic features of the observed phenomena, which could find wide application in the development of polarization photoelectronics systems and in diagnostics of finished polarimetric structures, are also discussed.

2. PHOTOPLEOCHROISM OF ISOTROPIC SEMICONDUCTORS WITH OBLIQUE INCIDENCE OF LPL

There exists a wide range of semiconductor photoelectric devices based on isotropic materials.[19–30] Photodetectors based on elementary, binary, and more complicated crystals, as well as glassy semiconductors have long been used to record the intensity of optical radiation. This is due to the fact that optical transitions in the energy spectrum of isotropic crystal and glassy semiconductors are equally probable for any polarization of the radiation. Since anisotropy was not observed in investigations of their photosensitivity spectra, the possibilities of direct detection of LPL using photodetectors consisting of ISs were not discussed at all in the scientific literature before the appearance of Ref. 18, where the then unexpected possibility of using isotropic semiconductors in a completely new (for them) function—as a photoanalyzer—was predicted and demonstrated.

2.1. Photosensitivity anisotropy of isotropic semiconductors

When the surface of an isotropic semiconductor is illuminated with LPL along the normal to the front plane (the angle of incidence of the LPL $\alpha_0 = 0°$), the photosensitivity (PS) is independent of the position of the electric field vector **E** of the light wave relative to the principal crystallographic axes in the semiconductor. For $\alpha_0 > 0°$, according to the Fresnel relations, nonequivalent reflection and refraction of rays with different polarization azimuths, which depend on the permittivities of the adjoining media, occur at the air/IS boundary. The intensity of the radiation transmitted into the semiconductor is a function of the azimuthal angle θ between **E** and the plane of incidence (PI) of the radiation. For this reason, for $\alpha_0 > 0°$ the density of photogenerated charge carriers in an isotropic semiconductor depends on θ.

We shall consider the simplest case of a flat interface on which an LPL beam is incident at angle α_0 (Fig. 1). The electric $\mathbf{E}_0$ and magnetic $\mathbf{H}_0$ vectors of the incident wave can be written in the covariant representation[31,32] as follows:

$$\mathbf{E}_0 = \mathbf{E}_0^S + \mathbf{E}_0^P = A_0 \mathbf{a}' + B_0 [\mathbf{n}_0 \cdot \mathbf{a}'],$$

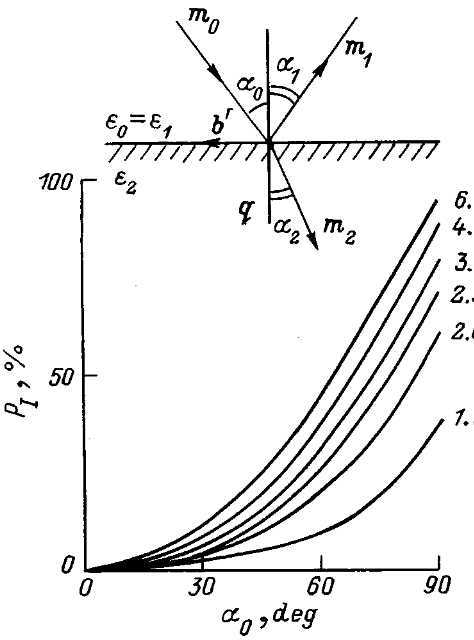

FIG. 1. Diagram of optical processes at the air/IS interface and the computed dependences $P_I(\alpha_0)$ for semiconductors with different refractive indices (indicated on the curves).

$$\mathbf{H}_0 = \mathbf{H}_0^S + \mathbf{H}_0^P = A_0 [\mathbf{m}_0 \cdot \mathbf{a}'] - B_0 n_0 \mathbf{a}', \tag{1}$$

where A_0 and B_0 are the scalar amplitudes of the incident wave with the corresponding polarizations, $\mathbf{a}'$, $\mathbf{b}'$, and $\mathbf{q}'$ are the unit basis vectors, $\mathbf{n}_0$ is the vector of the wave normal to the incident wave, n_0 and n_2 are, respectively, the refractive indices of air and the semiconductor, and $\mathbf{m}_0$ and $\mathbf{m}_2$ are the refraction vectors of the incident and refracted waves (Fig. 1). We can then represent the intensity of the radiation fluxes with oblique incidence of LPL can be represented in terms of the radiation power vector **P** and the unit vector **q** normal to the interface as:

$$\Phi = \langle \mathbf{P}_i \cdot \mathbf{q} \rangle = (C/4\pi) \langle \mathrm{Re}\, \mathbf{E}_i \rangle^2 \mathbf{m}_i \cdot \mathbf{q}$$
$$= (C/4\pi) \langle \mathrm{Re}\, \mathbf{E}_i \rangle^2 \eta_i, \tag{2}$$

where $\eta_i = n_i \cos \alpha_i$, and $i = 0, 1, 2$.

In this case the intensities of the incident wave can be written as

$$\mathbf{\Phi}_0^S = (C/4\pi) A_0^2 \eta_0 \quad \text{and} \quad \mathbf{\Phi}_0^P = (C/4\pi) B_0^2 \eta_0, \tag{3}$$

and the intensities of the refracted wave as

$$\Phi_2^S = (C/4\pi) A_2^2 \eta_2 \quad \text{and} \quad \Phi_2^P = (C/4\pi) B_2^2 \eta_2. \tag{4}$$

Using the Fresnel formulas in the covariant representation,[32] we obtain for the refracted waves

$$A_2 = \{(2\eta_0)/(\eta_0 + \eta_2)\} A_0,$$
$$B_2 = \{(2 n_0 n_2 \eta_0)/(n_2^2 \eta_0 + n_0^2 \eta_2)\} B_0. \tag{5}$$

Substituting the Fresnel formulas (5) into Eq. (4) shows that when the intensities of the incident LPL with different polarization azimuths are the same ($A_0 = B_0$), the intensities of the waves refracted into the semiconductor for orthogonal polarizations $\mathbf{\Phi}_2^S$ and $\mathbf{\Phi}_2^P$ become nonequivalent for all α_0

$\neq 0°$. Since the density of photogenerated pairs in an IS is determined by the intensity of the absorbed radiation, the photosensitivity (PS) for each polarization can be written in the form

$$i^P = C\cdot\mathbf{\Phi}_2^P, \quad i^S = C\cdot\mathbf{\Phi}_2^S, \tag{6}$$

where the constant C includes all contributions, which are independent of the polarization of the LPL, to the PS, for example, the optical absorption coefficient, the quantum yield, the electron–hole pair separation factor, and so on.

Then, using Eqs. (4) and (6), we can write the coefficient of induced photopleochroism

$$P_I = (i^P - i^S)/(i^P + i^S)\times 100\% \tag{7}$$

can be put in the form

$$P_I = (B_2^2 - A_2^2)/(B_2^2 + A_2^2). \tag{8}$$

In the simplest case where the amplitudes of the differently polarized waves incident on the air/IS boundary are equal ($A_0 = B_0$), using $\varepsilon_0 = n_0^2 = 1$, the expression for the induced photopleochroism coefficient can be put into the covariant form

$$P_I = \{(\varepsilon_2 - 1)(\eta_2^2 - \varepsilon_2\eta_0^2)\}/$$
$$\{4\varepsilon_2\eta_0\eta^2 - (\varepsilon_2 + 1)(\eta_2^2 - \varepsilon_2\eta_0^2)\}, \tag{9}$$

while in the explicit form it expresses the dependence of the IP on the angle of incidence and the refractive index of the semiconductor

$$P_I = \{(\varepsilon_2 - 1)\sin^2\alpha_0\}/\{(\varepsilon_2 + 1)[2\varepsilon_2 - (\varepsilon_2 + 1)\sin^2\alpha_0]$$
$$+ 4\varepsilon_2\cos\alpha_0(\varepsilon_2\sin^2\alpha_0)^{1/2}\}. \tag{10}$$

Investigations of the functional dependences of the IP coefficient of semiconductor phototransducers using Eq. (10) led to the establishment of a number of fundamental laws of polarization photosensitivity.[33,34]

When an IS is illuminated along the normal to the front plane ($\alpha_0 = 0°$), the identity $P_I \equiv 0$ should be satisfied and as the angle of incidence increases $\alpha_0 > 0°$, the IP starts to increase continuously for all $n > 1$ (Fig. 1) according to a parabolic law

$$P_I = \chi\cdot\alpha_0^2, \tag{11}$$

where the coefficient χ varies in a narrow range from 0.010 to 0.012 with large variations of n from 2.5 to 5, which covers the most important materials used in semiconductor electronics.[35,36] The maximum values of the IP coefficient

$$P_I^m = \{(\varepsilon_2 - 1)/(\varepsilon_2 + 1)\}^2 \tag{12}$$

are obtained near glancing geometry ($\alpha_0 \to 90°$) of illumination of the surface and for known ISs fall into the range 55–85%. Since for $\alpha_0 = 90°$ the LPL beam grazes along the surface, the photocurrents i^P and i^S drop to zero and the maximum value P_I^m is unattainable.

Induced photopleochroism can arise only if $n_2 > n_0$, and its growth with the refractive index of the IS is sublinear (Fig. 2).

Finally, in contrast to NP[9,10] the calculation of the spectral dependence of IP taking account of the optical parameters of the IS, predicts slow growth of P_I with increasing photon energy in the entire range of PS (Fig. 3). This law is determined by the relatively weak dichroism of the refractive index of semiconductors in their region of PS,[37] by the fact that the refractive index is greater than the extinction index [$n \gg k$ (Ref. 37)] and by the inequality $n^2 \gg 1$. The main contribution to the increase in P_I is due to the increase in the difference in the permittivities of the adjoining media.

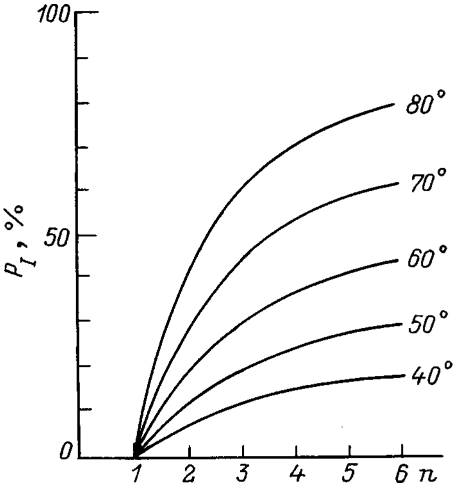

FIG. 2. Computed curves $P_I(n)$ for various angles of incidence (indicated on the curves).

2.2. Experimental procedure for investigations of induced photopleochroism

The experimental apparatus for studying polarization PS induced by oblique incidence of LPL on a flat air/IS interface is largely the same as that developed for investigating NP. However, to use the method of Ref. 10 for investigating IP, different relations must be established. First, the PS for a

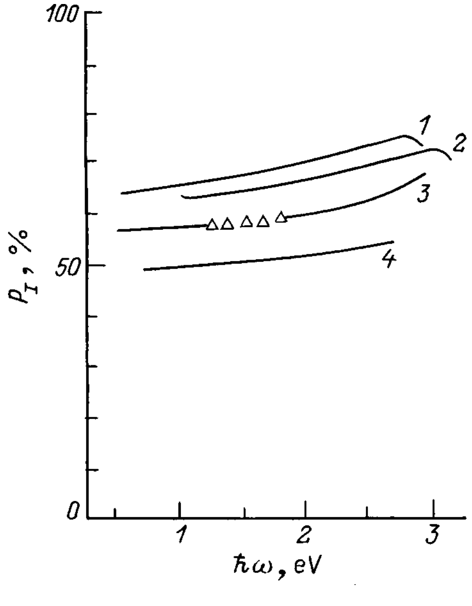

FIG. 3. Computed dependences $P_I(\hbar\omega)$ for photodetectors based on GaAs (*1*), InP (*2*), Si (*3*, the triangles indicate the experimental data), and ZnS (*4*) at $T = 300$ K (α_0, deg: *1*, *2*, *4*—80, *3*—75).

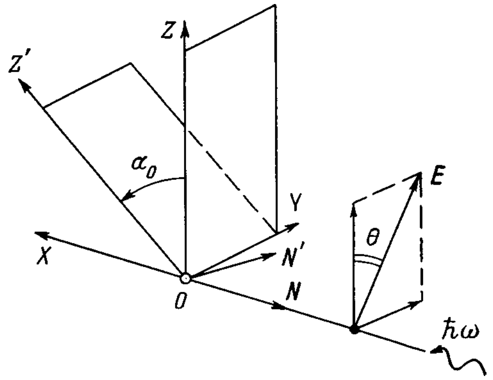

FIG. 4. Illumination scheme for investigation of induced photopleochroism in semiconductors.

fixed photon energy is measured as a function of the azimuthal angle Θ between **E** and the plane of incidence of the LPL on the receiving plane of a uniform IS or photosensitive structure fabricated using an IS. However, if the measurements of the NP are performed only for the angle of incidence $\alpha_0 = 0°$, then in the case of IP such a measurement is not enough and detailed measurements of the azimuthal dependences of the photocurrent must be performed for each fixed angle of incidence of the LPL in the range $0° \leqslant \alpha_0 < 90°$ with the step in α_0 determined in each specific measurement. The azimuthal photosensitivity dependences i_Θ obtained by scanning the angle of incidence $0° \leqslant \alpha_0 < 90°$ and wavelength of the LPL in the PS range are fed into the data acquisition and processing system. An imaging system is used to survey and process the PS dependences and to compare the experimental data with the computed dependences of the polarization parameters.[34]

The analysis of the PS dependences for the case where the polarization plane is also the plane of incidence of the LPL—$\mathbf{E} \| \mathrm{PI}$ for $i^P(\alpha_0)$ and in $\mathbf{E} \perp \mathrm{PI}$ for $i^S(\alpha_0)$—becomes especially important. Comparing the experimental curves $i^P(\alpha_0)$ and $i^S(\alpha_0)$ with the expected curves from analysis of the transmission of a light wave through the air/IS boundary using the Fresnel formulas opens up the possibility of rapid diagnostics of the quality of the front plane of the semiconductor and for monitoring antireflection. Polarization investigations of PS require that the ratio of i^P and i^S for $\alpha_0 = 0°$ be determined carefully. If $i^P \equiv i^S$, then there is a basis for concluding that there is a relative absence of NP, while $i^P \neq i^S$ for $\alpha_0 = 0°$ implies that both natural and induced photopleochroism appear together. Special test measurements are required in order to distinguish the contributions of these effects which are of a different nature.

The method for investigating IP consists in the following. Let an LPL beam be incident along X on the front plane of a photodetector consisting of an IS (Fig. 4). If $X \| \mathbf{N}$, where **N** is the vector normal to the front plane of the semiconductor, then the photosensitivity will not depend on the polarization, since in the absence of induced anisotropy (for example, uniaxial deformation) the absorption of radiation with arbitrary polarization is equally probable. If the front plane rotates around the Z (or Y) axis, the normal $\mathbf{N}'$ becomes noncollinear with the direction of propagation of the LPL and the angle of incidence $\alpha_0 > 0°$. As a result, the transmission coefficient of the air/IS interface for LPL and therefore the photosensitivity of the isotropic medium become dependent on the position of **E** relative to Z. The intensity of the LPL flux transmitted through the detecting plane will be determined by the relation

$$\Phi_2 = \Phi_0[\tau_P^2(\alpha_0)\cos^2\Theta + \tau_S^2(\alpha_0)\sin^2\Theta], \tag{13}$$

where Φ_0 is the intensity of the incident LPL flux, Θ is the azimuthal angle between **E** and the rotation axis Z, and τ_P and τ_S are the amplitude transmission coefficients of the air/IS interface for s and p polarizations. Assuming the photoflux to be proportional to Φ_0, we find that for a fixed angle of incidence $0° \leqslant \alpha_0 < 90°$ of the LPL beam the sensitivity will obey the periodic law

$$i_\Theta = i^P\cos^2\Theta + i^S\sin^2\Theta. \tag{14}$$

Therefore, under oblique incidence of LPL on the surface of an IS, because of the anisotropy of the transmission of the radiation through the detecting surface, the PS shows the same azimuthal dependence as for a uniaxial semiconductor for $\alpha_0 = 0°$.[10] This matching is not random and is determined by the fact that the symmetry of the absorption oscillator in a uniaxial crystal and the energy losses at the air/IS boundary are the same when $\alpha_0 \neq 0°$. The coefficient of IP, defined as the ratio of the difference in the photosensitivities to their sum for orthogonal s and p polarizations of the LPL, is conventionally used as a numerical characteristic of induced polarization PS.[38,39]

The predicted new mechanism of polarization PS[18] was immediately demonstrated for the basic materials and phototransducers used in semiconductor electronics devices fabricated from crystal and glassy semiconductors.[39]

An example of the typical polarization curves of the short-circuit photocurrent of a serially produced Si photodiode is shown in Fig. 5. When the front plane is illuminated, the photocurrent with $\alpha_0 = 0°$ does not depend on the azimuthal angle Θ (curve *1*), while for oblique incidence of LPL (curve *2*) the experimental values of the photocurrent start to vary in accordance with Eq. (14).

The experimental angular dependences $P_I(\alpha_0)$ for a Si photodiode (Fig. 5) also demonstrate the correctness of the laws predicted from the analysis of the optical processes occurring at the air/IS interface. In fact, $P_I = 0$ for illumination along the normal, and as α_0 increases, $\alpha_0 > 0°$, induced photopleochroism arises and increases in accordance with Eq. (11). Induced photopleochroism was also found to have the remarkable property that the spectral dependence of P_I is relatively weak in the entire range of PS of a structure based on an isotropic semiconductor.

We note that even these first experimental observations of IP have confirmed the high potential of the new photoelectric phenomenon for producing a component base for polarization photoelectronics using existing technologies and devices.

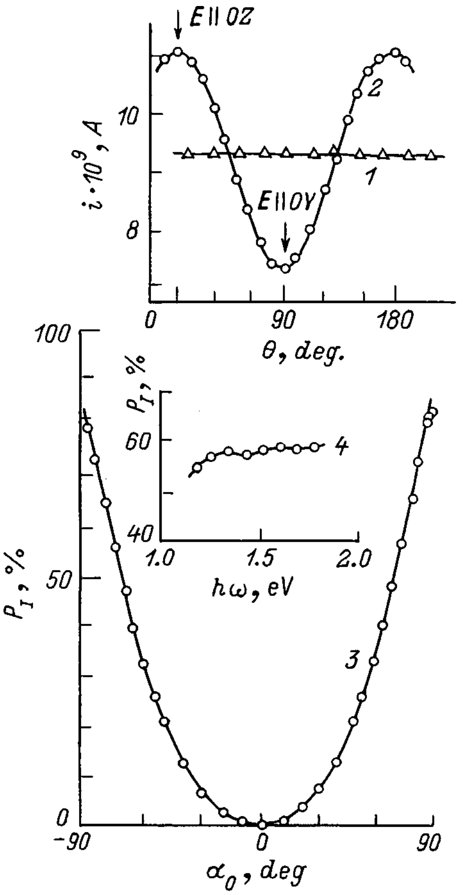

FIG. 5. Polarization curves of the photocurrent (α_0, deg: *1*—0, *2*—75; $\lambda = 0.95\,\mu$m), the curves $P_I(\alpha_0)$ [*3*—experiment—dots, solid curve—calculation using Eq. (11)] and $P_I(\hbar\omega)$ (*4*, $\alpha_0 = 75°$) for a n–p-Si structure.

3. INDUCED PHOTOPLEOCHROISM OF SCHOTTKY BARRIERS BASED ON III–V SEMICONDUCTORS AND THEIR SOLID SOLUTIONS

It has been known for a long time that Schottky barriers based on III–V semiconductors and their solid solutions are sensitive to radiation intensity.[40–42] This is due to the fact that absorption in crystals with a sphalerite lattice is isotropic because of the degeneracy of the states of the upper valence band, and for this reason such materials have not been considered at all for application in polarization photoelectronics. After the discovery of IP[18] such structures actually became the first object used for thorough investigation of the basic laws of the new photoelectric phenomenon.[43–51]

The barriers for polarization investigations were produced on wafers with (100) or (111) orientations of homogeneous crystals or epitaxial layers of the binary compounds GaAs and GaP, as well as the solid solutions $\mathrm{GaP}_x\mathrm{As}_{1-x}$, $\mathrm{Ga}_{1-x}\mathrm{Al}_x\mathrm{As}$, and $\mathrm{Ga}_{1-x}\mathrm{Al}_x\mathrm{P}$. Unilayer Au and Ni or bilayer Ni–Au coatings were deposited by vacuum sputtering or chemical deposition. The film thicknesses were ordinarily in the range 100–200 Å. The films were deposited on mechanically and then chemically polished surfaces of the indicated semiconductors and on the growth surface of epitaxial layers without any additional treatment. It is important that during polarization measurements the surface of the barrier contact is illuminated with a parallel LPL beam as close as possible to $\alpha_0 \to 90°$, where the photocurrent can still be measured. Accordingly, special attention is devoted to eliminating vignetting of the detecting plane of the barriers and eliminating any possibility of illumination of the end planes.

3.1. Wide-band induced photopleochroism

The wide-band photosensitivity of Schottky barriers with respect to natural radiation is well known.[42,52] The structures obtained by the method described above showed a high, for phototransducers of this type, photosensitivity S_I. Their wide-band character is illustrated by the large total widths $\delta_{1/2}$ of the spectra at half-height with illumination from the barrier contact side (Table I).

Investigations of the obtained structures in LPL showed that polarization PS in Schottky barriers on bulk crystals and epitaxial layers, in the presence of positional disordering in the solid solutions and irrespective of the nature of the metals employed and the method for depositing the metals on the surface of isotropic III–V semiconductors (Table I), first appears only when the direction of the LPL beam deviates from the normal to the barrier surface. The azimuthal dependences of the photocurrent of all barriers with $\alpha_0 \neq 0°$ follow the periodic law (14), and the inequality $i^P > i^S$, which follows from a Fresnel analysis of the transmission through an air/IS interface, holds in the entire region of PS.[2,7,8]

For Schottky barriers with a mirror receiving plane, the typical angular dependences of the photocurrents, their polarization difference $\Delta i = i^P - i^S$, and the coefficient P_I are

TABLE I. Photoelectric properties of Schottky barriers based on III–V semiconductors at $T = 300$ K (illumination from the barrier-contact side).

Semiconductor	Barrier	S_I, A/W	$\delta_{1/2}$, eV	P_I^m,*%	$\Delta\hbar\omega_P$, eV	Φ_I, A/W·deg
n-GaAs	Ni	0.12	0.6	62(80)	1.4–1.8	0.15
	Au	0.11	0.3	68–74(80)	1.5–2.6	0.14
	Ni+Au	0.16	0.5	70(80)	1.4–1.8	0.22
n-GaP	Au	0.14	0.75	64(80)	2.4–3.6	0.18
	Al	0.14	0.80	68(80)	2.5–3.5	0.19
	Au	0.15	0.70	74(80)	2.3–3.6	0.21
n-$\mathrm{Ga}_{1-x}\mathrm{Al}_x\mathrm{As}$	Au	0.07	1.1	45(75)	1.8–3.6	0.065
n-$\mathrm{Ga}_{1-x}\mathrm{Al}_x\mathrm{P}$	Au	0.07	1.0	39(75)	2.0–3.6	0.055
n-$\mathrm{GaP}_x\mathrm{As}_{1-x}$	Au	0.14	1.0	74(80)	2.2–3.4	0.2

Note: *The angle of incidence is shown in parentheses.

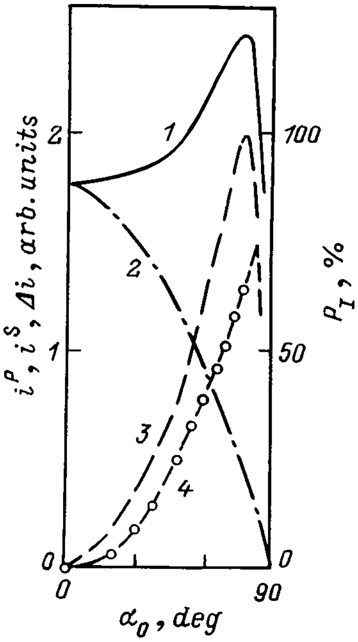

FIG. 6. i^P (*1*), i^S (*2*), Δi (*3*), and P_I (*4*) for a Ni/n-GaAs structure versus the angle of incidence of LPL from the Ni side ($\lambda = 0.87\ \mu$m, $T = 300$ K).

shown in Fig. 6. The main laws are as follows. When the polarization plane is also the plane of incidence, the photocurrent i^P increases, reaches a maximum near the Brewster angle α_0^B, and then decreases. At the same time, as soon as $\alpha_0 > 0°$ the photocurrent i^S decreases monotonically. The fact that $i^P(\alpha_0)$ and $i^S(\alpha_0)$ are different demonstrates the validity of the classical Fresnel analysis of the processes leading to transmission through an interface between two media.[2,7] An important parameter for estimating the perfection of the outer surface of the barrier is the photocurrent ratio $A = i_m^P / i_0^P$, where i_m^P and i_0^P are, respectively, the values of the photocurrent at the maximum and for $\alpha_0 = 0°$. Experimental investigations of Schottky barriers show that in high-quality structures $A > 1$ corresponds to a decrease of reflection losses. As the quality of the receiving plane of the structures decreases, the ratio decreases to such an extent that $A < 1$ could happen just as for the s wave in the case of even an ideal surface. For $A < 1$ the dependence $i^P(\alpha_0)$ becomes qualitatively similar to $i^S(\alpha_0)$, though the inequality $i^P > i^S$ with $\alpha_0 = \text{const}$ remains. This character of $i^P(\alpha_0)$ does not agree with the results of the conventional analysis, using the Fresnel formulas,[2,7] of the optical processes during transmission through the interface between two media.

The important conclusion that the polarized difference of the photocurrents in Schottky barriers reaches a maximum near α_0^B also follows from Fig. 6. This quantity also depends on the optical quality of the barrier contact and the quantum photoconversion efficiency.

As follows from Fig. 6, the IP coefficient is 0 for $\alpha_0 = 0°$, and for $\alpha_0 > 0°$ it increases according to the quadratic law (11). For fixed angles α_0 the value of P_I is determined by the semiconductor used in the barrier structure and is essentially independent of the method of deposition and the nature of the metal. Estimates of the refractive index from the experimental values of P_I, using Eq. (10), are ordinarily close to the known values for ISs. This can serve as a basis for concluding that the anisotropy of the optical processes is determined mostly by the properties of the semiconductor, while the semitransparent thin layer of metal is neutral in this respect.

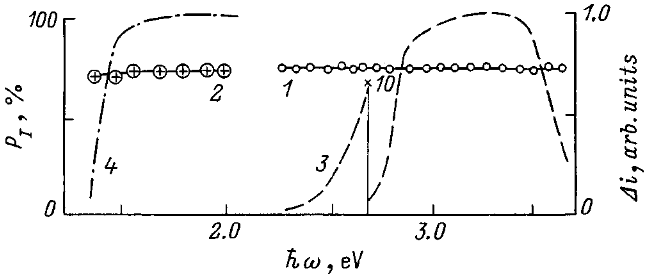

FIG. 7. $P_I(\hbar\omega)$ (*1, 2*) and $\Delta i(\hbar\omega)$ (*3, 4*) for the Schottky barriers Au/n-GaP (*1, 3*) and Ni/n-GaAs (*3, 4*) at $T = 300$ K.

Finally, we shall analyze the dichroism of the parameters of the IP of Schottky barriers with wide-band photosensitivity with respect to the radiation intensity. As one can see from Fig. 7, for Schottky barriers on GaAs and GaP the IP coefficient remains virtually constant for $\alpha_0 = \text{const}$ in the entire range of PS. Therefore, whereas the NP in anisotropic semiconductors is sharply selective[9,10] the IP is constant and covers the entire range of photosensitivity of the IS, in agreement with the analysis in Ref. 34.

The maximum azimuthal PS of Schottky barriers, determined from the relation[53]

$$\Phi_I = 2 S_I P_I, \tag{15}$$

reaches record-high values for structures consisting of anisotropic semiconductors (Table I). It is evident from Fig. 7 that, in contrast to P_I, the polarized difference of the photocurrents in metal/IS structures has shown a selective character. Since $\Phi_I \sim \Delta i$,[9,10] it is evident that the polarization PS of Schottky barriers is of practical interest in their range of maximum photosensitivity. For Schottky barriers the long-wavelength edge of Δi is controlled by the conventional parameters for structures of this type. The position of the long-wavelength edge in them is determined by the band gap E_G, while the short-wavelength dropoff of the PS is suppressed by an effective barrier. For this reason, controlling the band gap during the formation of III–V solid solutions makes it possible to control the long-wavelength edge of the IP, and Φ_I and its extent in the short-wavelength region can be controlled by the nature and method of deposition of the barrier material.

3.2. Selective induced photopleochroism

The transition from wide-band to selective detection of LPL, often required in practice, was discovered on surface-barrier structures immediately after wide-band structures.[54,55]

Structures in which a flat surface of the semiconductor could be illuminated with LPL in oblique geometry and the opposite surface of the semiconductor contained a barrier were produced for these investigations. In sun light the photosensitivity spectra of such structures are narrow-band spectra (Table II). This is due to the influence of radiation ab-

TABLE II. Photoelectric properties of Schottky barriers based on III–V semiconductors at $T = 300$ K (illumination from the III–V side).

Structure	S_I, A/W	$\delta_{1/2}$, meV	P_I^m,* %	$\Delta\hbar\omega_P$, eV	Φ_I, A/W·deg
Au/n-GaAs	0.13	20–24	45(75)	1.38	0.003
Au/n-GaP$_{0.7}$As$_{0.3}$	0.14	120–130	65(80)	2.18	0.020

Note: *The angle of incidence is shown in parentheses.

sorption in the interior volume of the IS. The energy position of the short-wavelength edge of the PS is determined by the thickness of the semiconductor wafer and by the character of the interband transitions. For example, the width of the spectral band of PS in GaAs barriers is much narrower than in an indirect-gap solid solution with a flat absorption edge.

As one can see from Fig. 8, the angular dependences of the polarization characteristics with the Schottky barrier illuminated from the semiconductor side are the same as for illumination from the metal-layer side. This corresponds to the conclusion that the semiconductor plays a determining role even when the structure is illuminated through a half-transmitting contact. It should be noted that when the same structure is illuminated from the IS side, the ratio A is ordinarily higher than for illumination of a metal-coated wafer by LPL. It follows from this fact that the optical quality of the free surface is higher than that of the metal-coated surface. On the whole, the tunable curve $P_I(\alpha_0)$ shows that when barrier structures are illuminated from the IS side, a transition from a polarization-insensitive regime ($P_I \equiv 0$) to the polarimetric regime is possible, just as in the geometry where these structures are illuminated from the barrier-contact side.

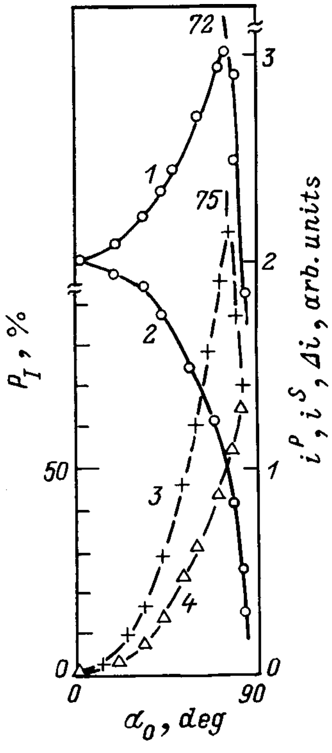

FIG. 8. i^P (*1*), i^S (*2*), Δi (*3*), and P_I (*4*) for a Au/n-GaP$_{0.7}$As$_{0.3}$ structure versus the angle of incidence of LPL from the GaP$_{0.7}$As$_{0.3}$ side ($\lambda = 0.57$ μm, $T = 300$ K).

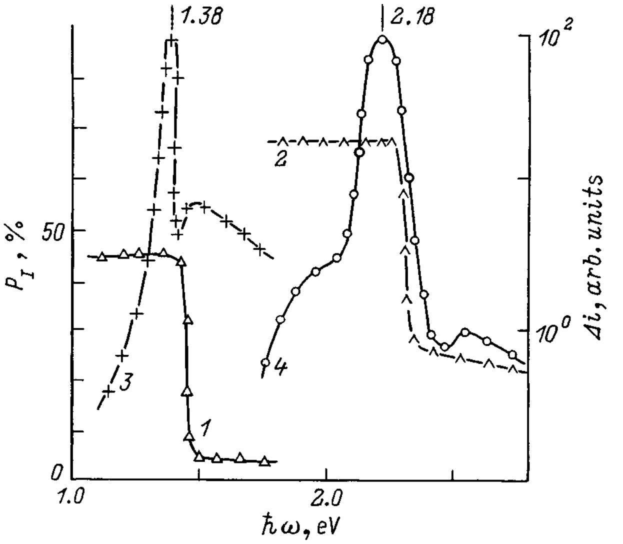

FIG. 9. P_I (*1, 2*) and Δi (*3, 4*) spectra of Au/n-GaAs (*1, 3*) and Au/n-GaP$_{0.7}$As$_{0.3}$ (*2, 4*) structures with illumination from the semiconductor side at $T = 300$ K.

A sharp short-wavelength dropoff near E_G appears in the spectral dependence of the IP coefficient on switching to a geometry where the barriers are illuminated through the interior volume of the semiconductor, while in the region of a weak optical absorption the IP remains nonselective, while the values of P_I (Table II) give a value of n close to the known value for the semiconductor. The nonselective character of P_I, as follows from Fig. 9, is observed for different PS mechanisms, such as interband absorption and photoemission of electrons from the metal into the semiconductor.

It follows from Eq. (15), taking into account the spectral contour of the polarized difference in the photocurrents with a maximum near E_G of the semiconductor (Fig. 9, curves *3* and *4*), that the maximum azimuthal photosensitivity Φ_I of Schottky barriers illuminated from the IS side has the form of a narrow band with a maximum near E_G. It is evident that the spectral position of the maximum of the azimuthal PS can be controlled in a wide spectral range from infrared (IR) to ultraviolet (UV) by varying the band gap by adjusting the wafer thickness and the atomic composition of the compounds and their solid solutions.

The values of Φ_I and the spectral band widths presented in Table II demonstrate the suitability of Schottky barriers on III–V crystals for use in selective photoanalyzers of LPL.

4. INDUCED PHOTOPLEOCHROISM OF ITO/SI(III–V) STRUCTURES

Wide-gap high-conductivity oxides, including mixtures of indium and tin oxides (ITO), are used to increase the quantum efficiency of phototransducers for sunlight.[56,57] Investigations of the polarized PS of such structures have been

TABLE III. Photoelectric properties of ITO/Si(III–V) heterojunctions at $T=300$ K.

Structure	S_I, A/W	$\delta_{1/2}$, eV	$P_I^{\min}$,* %	Φ_I, A/W·deg
ITO/n-Si	0.09	2.0	2(70)	0.08
ITO/n-GaP	0.1	1.0	15(80)	0.04
ITO/n-GaP$_{0.42}$As$_{0.58}$	0.1	0.9	2(75)	0.045
ITO/p^+-p-InP	0.1	2.0	2(70)	0.08

Note: *The angle of incidence is shown in parentheses.

undertaken in the last few years and have led to the observation of a number of interesting features of induced photopleochroism.[58–60]

4.1. Polarized photosensitivity of ITO/GaP(GaP$_x$As$_{1-x}$) heterojunctions

The structures were produced by magnetron sputtering of an indium and tin target in an oxidizing oxygen–argon medium. The films were deposited on the (100) plane of GaP and GaP$_x$As$_{1-x}$ single crystals. All structures possessed wide-band PS spectra (Table III). The angular dependences $P_I(\alpha_0)$ in the heterojunctions (HJs) based on the GaP and n-GaP$_x$As$_{1-x}$ wafers illuminated from the ITO side (Fig. 10) follow the quadratic law (11). The difference observed in the values of P_I for various HJs and for $\alpha_0>30°$ with the same n-ITO entrance plane could be due to oscillations of the refractive index as a function of the technological conditions. On the basis of an analysis using Eq. (10) the values $n=1.4-1.8$ can be correlated to the experimental curves $P_I(\alpha_0)$, which agrees satisfactorily with the known values for ITO.[56]

The typical spectra $P_I(\hbar\omega)$ for HJs of this type (Fig. 10, curves *3* and *4*) also show a much weaker IP with respect to a Schottky barrier based on these materials. It can be concluded on this basis that the induced photopleochroism of ITO/GaP(GaP$_x$As$_{1-x}$) HJs is determined by the anisotropy of the optical processes at the air/ITO interface, while in Schottky barriers the determining processes were those at the air/IS interface. A large difference between HJs based on ITO and Schottky barriers is dichroism of P_I, which conflicts with the analysis in Ref. 18. In Ref. 58 this new feature was attributed to a possible superposition of additional selective photopleochroism of unknown nature on the IP.

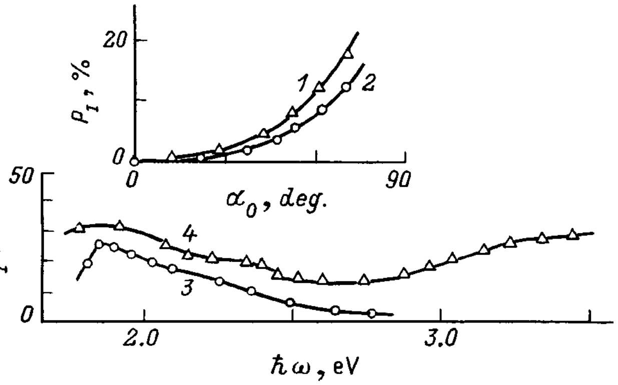

FIG. 10. $P_I(\alpha_0)$ ($\hbar\omega$, eV: *1*—1.91, *2*—2.82) and $P_I(\hbar\omega)$ (α_0, deg: *3*—75, *4*—80) of ITO/GaP$_{0.42}$As$_{0.58}$ (*1, 2*) and ITP/GaP (*3, 4*) HJs at $T=300$ K.

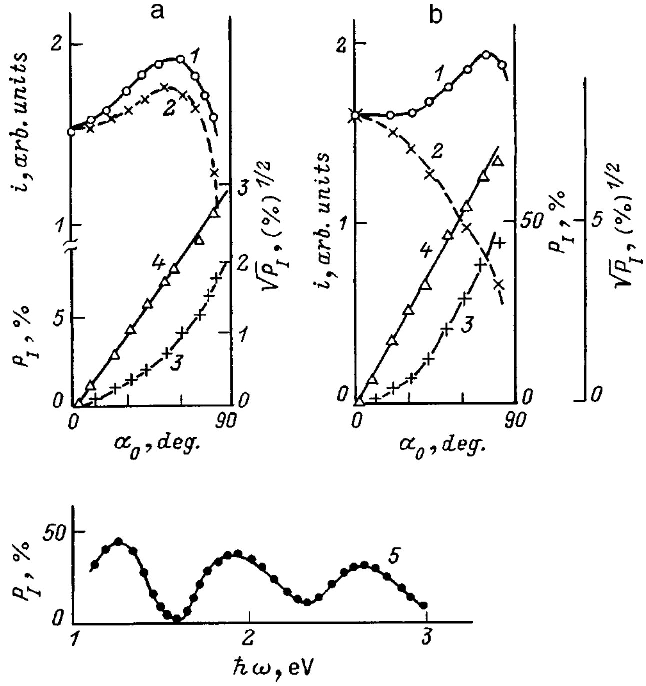

FIG. 11. $i^P(\alpha_0)$ (*1*), $i^S(\alpha_0)$ (*2*), $P_I(\alpha_0)$ (*3*—P_I, *4*—$P_I^{1/2}$, $\hbar\omega$, eV: a—1.0, b—1.27), and $P_I(\hbar\omega)$ ($\alpha_0=70°$) (*5*) for an ITO/n-Si solar cell at $T=300$ K.

4.2. Polarized photosensitivity of ITO/p-Si(p-InP) solar cells

The structures were obtained by pulverizing alcohol solutions of mixtures of indium and tin chlorides on the surface of heated (111) Si and (100) InP wafers. When illuminated with sunlight ITO/p-Si and ITO/p-InP HJs exhibit wide-band PS (Table III), and maxima and minima, indicating interference of the radiation, can be clearly resolved in the photocurrent spectra.

The angular dependences of the photocurrents for the p and s waves acquire sensitivity to the incident-photon energy precisely for such HJs. Figure 11 shows two types of dependences observed for the photocurrents $i^P(\alpha_0)$ and $i^S(\alpha_0)$. In one dependence (Fig. 11a, curves *1* and *2*) the angular dependences $i^P(\alpha_0)$ and $i^S(\alpha_0)$ are similar, indicating that the reflection losses decrease for both p and s waves simultaneously. The distance between $i^P(\alpha_0)$ and $i^S(\alpha_0)$ for the same values of α_0 depends on the photon energy and is different for different HJs. It should be underscored that the observed increase in i^S with α_0 and the attainment of a maximum photocurrent near the Brewster angle do not correspond to the Fresnel analysis of the transmission of radiation through the air/ITO interface.[2,7] One can also see from Fig. 11b (curves *1* and *2*) that in the same structure there are spectral ranges where $i^P(\alpha_0)$ and $i^S(\alpha_0)$ are in complete agreement with the Fresnel analysis of the transmission of a light wave through the interface between two media.[2,7]

It is important to underscore that the angular dependence of P_I in ITO-based solar cells is described by a quadratic law (Figs. 11, a and b, curves *3* and *4*). However, in contrast to

TABLE IV. Photoelectric properties of III–V/IV heterojunctions at $T=300$ K.

Structure	S_I, A/W	$\hbar\omega^m$, eV	$\delta_{1/2}$, eV	P_I^m,*%	$\Delta\hbar\omega_P$, eV	Φ_I, A/W·deg
p-GaAs/n-Ge	0.02	1.38	0.025	60(78)	0.7–1.6	0.02
p-GaP/n-Si	0.16	1.4–1.6	0.6	58(75)	1–2.3	0.18
$p-n$-GaP/n-Si	0.04	2.6	0.26	46(75)	2.3–2.7	0.06
n-GaP/p-Si	0.15	1.8–2.0	0.8–1.9	58–68(75)	1.2–3.1	0.17
n-GaAs/p-Si	0.015	1.33	0.17	57(75)	1.35–1.45	0.026
n-GaAs$_{0.3}$P$_{0.7}$/p-Si	0.1	1.8–1.9	0.69	60(75)	1.3–2.3	0.11
p-n-GaAs/n-Si	0.02	1.39	0.06	58–60(75)	1.3–1.45	0.0024

Note: *The angle of incidence of LPL is indicated in parentheses.

Schottky barriers, for ITO/p-Si and ITO/p-InP HJs the IP coefficient fluctuates for different structures and changes in the PS range. A typical example of the spectral dependence $P_I(\hbar\omega)$ for such HJs is presented in Fig. 11 (curve *5*). The oscillatory character of the IP, which in Refs. 59 and 60 is attributed to the interference of LPL in the entrance window of solar cells, is clearly seen. Turning to the spectral dependences of the quantum efficiency of p- and s-wave phototransducers, it is evident that the oscillations of the photocurrents i^P and i^S oscillate in antiphase. Therefore a minimum of i^S corresponds to a maximum of i^P and vice versa. For this reason, since $i^P>i^S$, as is characteristic for IP, the maximum value of P_I occurs in the region of the maximum of i^P and the minimum of i^S and the minimum of P_I occurs near the minimum of i^P and the maximum of i^S, where the polarized difference of the photocurrents is minimum. The new hypothesis that the maximum antireflection effect corresponds to the condition

$$P_I=0, \tag{16}$$

so that $i^P=i^S$, was advanced on the basis of these investigations. In this respect, the spectral dependences of IP make it possible to determine directly the photon energy range corresponding to maximum antireflection. Taking into account this condition near the maxima of P_I the important conclusion can be drawn that the maximum polarized difference of the photocurrents reflects maximum weakening of s-wave antireflection. For this reason, an estimate of n from the maximum of P_I gives for ITO/p-Si and ITO/p-InP solar cells virtually the same value $n=1.4-1.8$, which is close to the value known for ITO.[56]

On the whole, the above-considered studies of ITO-based HJs, together with the experimental values of the azimuthal PS (Table III), show that these phototransducers can be used as wide-band photoanalyzers for LPL, and polarization measurements themselves can be used to monitor the antireflection properties and to adjust the conditions for obtaining solar cells of this type.

5. INDUCED PHOTOPLEOCHROISM OF III–V/Si(Ge) HETEROJUNCTIONS

Interest in epitaxial films of III–V semiconductors on silicon and germanium substrates arose relatively long ago and investigations in this direction have been continuously expanding,[61–67] since they give hope of combining the functional possibilities of the principal materials of semiconductor electronics for a new-generation of optoelectronic devices. Until very recently, photoelectric phenomena in such structures were studied only in sunlight. Investigations of photosensitivity using polarized photoelectric spectroscopy have been carried out only recently.[50,68–73] We shall review the main results of these works.

The objects of polarized investigations of PS were structures obtained by gas-phase epitaxy in an open chloride system.[73–76] The substrates consisted of 0.3–0.4-mm-thick (100) Si and Ge wafers with approximately 4–6° disorientation from the [110] direction. The thickness of the epitaxial films and structures based on them was controlled in the range 1–25 μm by the growth conditions. The basic types of experimental structures and their photoelectric parameters are given in Table IV. For illumination from the wide-gap component side, a wide-band effect appears for all HJs. The long-wavelength edge of the PS with respect to the radiation intensity is determined by E_G of the substrates, while the short-wavelength edge is determined by absorption in the wide-gap film. The region $\hbar\omega^m$ of maximum PS and the total width $\delta_{1/2}$ of the spectra at half-height depend on the doping conditions and the III–V film thicknesses.

Under illumination with LPL polarization photosensitivity $i^P>i^S$ arises only for $\alpha_0>0°$. For perfect epitaxial layers in all HJs the dependences of i^P and i^S on the angle of incidence agree with the Fresnel analysis[2,7] of the transmission of LPL through an air/IS interface and indicate a decrease of the reflection losses only for the p-wave (Fig. 12, curves *1* and *2*). The relation $i^P>i^S$ remains valid in HJs with a relief surface (Fig. 12, curves *3* and *4*), but oblique incidence no longer gives rise to an increase in the photocurrent with increasing α_0 for either p or s polarization. Therefore, just as for Schottky barriers the polarization measurements of the photocurrent are obviously related to the quality of the films forming a HJ.

The coefficient of IP in structures of the type under consideration varies as a continuous function of the angle of incidence of the LPL $P_I\sim\alpha_0^2$. An estimate of the refractive index taking account of the experimental data on P_I and α_0 (Table IV) gives close to the known values of n for the semiconductors through which the LPL enters the active region of the structures. For the same HJ of this type, in principle, there exist two different tunable curves $P_I(\alpha_0)$, and they are different only because the difference in the refractive indices of the materials used for the upper epitaxial layer and substrate are different.[71] It should be underscored also

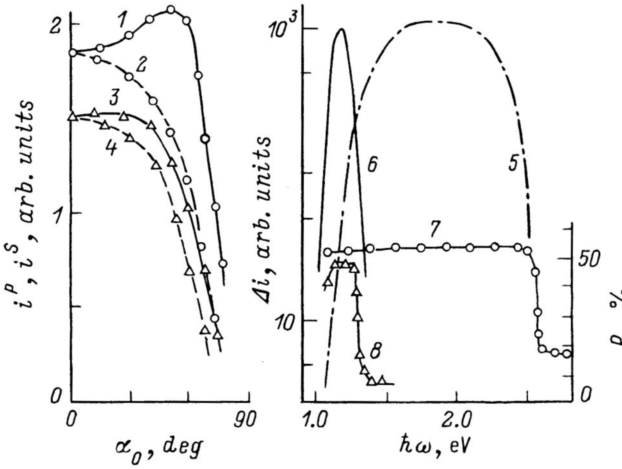

FIG. 12. Photocurrents (*1, 3*—i^P, *2, 4*—i^S, $\lambda = 0.49\,\mu$m) versus the angle of incidence on the surface of a $p-n$-GaP/n-Si structure (*1, 2*—mirror surface of GaP, *3, 4*—relief surface) and the $\Delta i(\hbar\omega)$ (*5, 6*) and $P_I(\hbar\omega)$ (*7, 8*) spectra of a n-GaP/p-Si (*1–5, 7*—illumination from the GaP side; *6, 8*—from the Si side, *5–8*—$\alpha_0 = 70°$) at $T = 300$ K.

that in all HJs $P_I(\alpha_0)$ vanishes at $\alpha_0 = 0$. This shows that photopleochroism, which can arise, for example, because of directed deformation of a thin epitaxial film grown on a thick substrate, in the HJs obtained is negligible compared with the photopleochroism induced by the oblique incidence of LPL.

The spectral dependences of the polarized difference of the photocurrents of III–V/Si(Ge) HJs in Fig. 12 (curves *5* and *6*) are illustrated for an n-GaP/Si structure in two possible photodetection geometries. The spectral contour of Δi is identical to the spectral dependence of the photocurrent in unpolarized light, since the angle α_0 determines only the magnitudes of the photocurrents i^P and i^S. It is evident from Fig. 12 (curves *5* and *6*) that when the HJ is illuminated from the GaP side the spectrum of Δi is wide-band and it is different from zero between E_G of the adjoining semiconductors. Therefore the polarized PS induced by oblique incidence of LPL exhibits a polarized "window effect." When the HJ is illuminated from the Si side, the window becomes substantially narrower, and the spectrum Δi becomes selective and is bounded on the short-wavelength side by absorption in the narrow-gap component of structures of this type.

The photodetection geometry strongly influences the spectral contour of IP (Fig. 12, curves *7* and *8*). Thus, when the HJ is illuminated from the GaP side the IP coefficient remains constant in a wide spectral region, while for illumination from the side of the thicker Si substrate the spectrum of P_I becomes selective, remaining constant only within $\delta_{1/2}$. The short-wavelength edge of P_I seemingly "follows" the dropoff in Δi. This behavior was manifested for HJs with epitaxial GaP$_x$As$_{1-x}$ films, where as x increases, the short-wavelength edge of P_I starts to shift in a regular manner in the direction of lower photon energies because of the decrease in E_G.[70] For n-GaP/Si structures it was also established that the spectral position of the short-wavelength edge of P_I also shifts into the long-wavelength region as the thickness of the GaP films increases.[50,68] Therefore the appearance of a short-wavelength edge in the P_I spectra is determined by the effect of absorption of LPL in the wide-gap component of the HJ. This is confirmed by the polarized investigations of the PS of Schottky barriers, for which the short-wavelength edge of P_I did not appear at all.[49,50] The position of the long-wavelength edge of P_I corresponds to the onset of interband transitions in the substrate material.[70]

It is important to note that IP in both geometries of photodetection of LPL has the same positive sign because $i^P > i^S$, and in this respect it differs fundamentally from NP, whose sign changes as soon as absorption appears in the interior volume of an anisotropic semiconductor.[9,10] For HJs based on anisotropic semiconductors, for example, GaP/Si, the increase in optical absorption in Si with illumination from the substrate side and for $\hbar\omega > 1.2$ eV decreases P_I, because the layer of photogenerated charge carriers moves away from the active region of the HJ. A similar result obtains for $\hbar\omega > 2.4$ eV under illumination from the GaP side. The short-wavelength dropoffs of P_I are due to this. However, since the absorption of LPL in Si and GaP is isotropic, the absorption depth of p- and s-polarized radiation is found to be the same. For this reason, since for transmission of LPL through air/Si and air/GaP interfaces in oblique geometry the absorption coefficients satisfy $\alpha^P > \alpha^S$, the relation $i^P > i^S$ holds. This is why a sign change of Δi and P_I is not observed in the entire range of photosensitivity of HJs consisting of the isotropic semiconductors Si, Ge, and III–V compounds, while changing the atomic composition and the thicknesses of the epitaxial films makes it possible to control the width $\Delta\hbar\omega_P$ of the bands of constant IP.

The high azimuthal PS (Table IV) and the possibilities of controlling its spectral range by adjusting the atomic composition of the films and substrates show that there is promise in using the HJs obtained as wide-band and selective photoanalyzers for LPL.

6. INDUCED PHOTOPLEOCHROISM OF CdS/InP HETEROJUNCTIONS

Photosensitivity based on direct-gap II–VI and III–V compounds (especially CdS and InP) has long been of interest as a means for obtaining high-efficiency conversion of sunlight into electricity. Even though the conditions for joining substances with different types of lattices and different lattice parameters were unfavorable, this difficult problem was solved and solar cells with high radiation resistance and efficiency up to 18% were obtained.[77–80] Switching from the conventional investigations of PS to polarized investigations revealed the relationship between the polarization parameters of such HJs and the conditions for matching their components. This could find applications in the diagnostics of the quality of structures of this type.[81,82]

The n-CdS films were deposited on single-crystal p-InP wafers with (100), (111)A, and (111)B orientations by the gas-phase method in a continuous-flow system using hydrogen. Deposition was conducted at temperatures in the range 700–750 °C. The most photosensitive HJs were obtained when 2–4-μm thick p-InP epitaxial films were additionally grown on (100) InP wafers with 4–5° disorientation in the

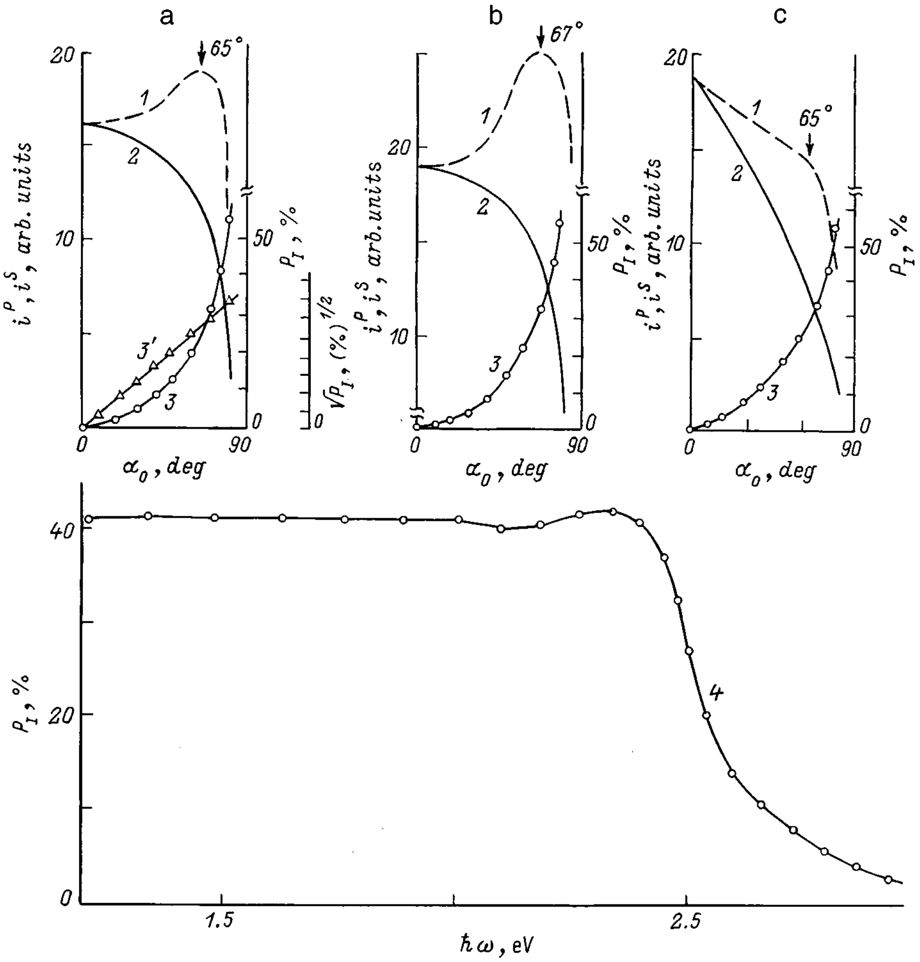

FIG. 13. $i^P(\alpha_0)$ (*1*), $i^S(\alpha_0)$ (*2*), $P_I(\alpha_0)$ (*3, 3′*), and $P_I(\hbar\omega)$ (*4*) for a CdS/InP HJ at $T=300$ K. The structures are illuminated from the CdS side; InP orientation: a—(111)B, b—(111)A, c—(100); *1, 2, 3, 3′*—$\hbar\omega=1.33$ eV; *4*—$\alpha_0=75°$.

[110] direction in the continuous-flow system In–PCl_3–H_2, after which the n-CdS films were grown on them. The maximum PS of such structures reaches 0.13 A/W, and the effect of the window with respect to the radiation intensity is observed between the band gaps of these semiconductors. The maximum widths of the PS bands are obtained by growing CdS on the $(111)B$ plane of InP.[82]

For illumination with LPL along the normal to the CdS plane, the photocurrent of the HJ was found to be independent of the position of the polarization plane. This makes it possible to draw the important conclusion that photoactive absorption in the HJ CdS/InP remains isotropic in the presence of the changes made in the crystallographic orientation of the InP substrates. For oblique incidence of LPL, IP appears in these structures and grows in accordance with the law (11) without showing sensitivity to changes in the orientation of the substrates (Fig. 13, curves *3* and *3′*). Using Eq. (10) we obtain, on the basis of the experimental curves $P_I(\alpha_0)$, $n\approx 2.5$ for CdS/InP structures, in agreement with the data for CdS.[36] This gives a basis for assuming that the photoelectric anisotropy induced in a HJ by oblique incidence of LPL does not depend on the orientation of the substrates but rather it is entirely determined by the nature of the CdS films.

At the same time, as one can see from Figs. 13, a and b, the HJs are clearly sensitive to the orientation of the InP substrates. For CdS films with a mirror outer surface, which can be grown reproducibly on InP substrates with $(111)A$ and $(111)B$ orientations, the experimental curves $i^P(\alpha_0)$ and $i^S(\alpha_0)$ agree with the analysis based on the Fresnel relations for the amplitude transmission coefficient of an air/CdS interface for LPL.[2,7] The photocurrent i^S decreases monotonically with increasing α_0, while for i^P a sharp maximum appears near the pseudo-Brewster reflection angle, while the ratio A reaches values of 1.2–1.3, indicating substantial suppression of the reflection losses in $\mathbf{E}\|$PI polarization. This decrease is maximum in a HJ with $(111)B$ crystallographic orientation of the substrates, once again indicating that the CdS films grown on the $(111)B$ InP plane are of higher quality.

For HJs on (100) InP wafers (Fig. 13, curves *1* and *2*) the photocurrents i^P and i^S, retaining their polarization dependence $i^P > i^S$, showed a monotonic decrease with increasing $\alpha_0 > 0°$. This phenomenon was already observed in polarized measurements on Schottky barriers and HJs with a receiving plane of lowered quality. On this basis the character of the dependences $i^P(\alpha_0)$ in HJs on (100) InP substrates can also be attributed to the degradation of the optical quality of CdS films with such InP orientation. Therefore the polarized changes of the photocurrent make it possible to determine the refractive index and the quality of the entrance material in finished structures.

The polarized difference in the photocurrents of CdS/InP HJs appeared at energies between E_G of the adjacent media.

By changing the InP orientation it is possible to control the spectral contour of the azimuthal PS, since P_I in the region of the maximum polarized difference in the photocurrents remains essentially constant (Fig. 13, curve *4*) in accordance with Ref. 18, while its value is chosen from the dependence on the angle of incidence of the LPL. It is important to note that the magnitude of the IP in CdS/InP HJs ''does not feel'' the changes in the orientation of the InP substrates. The drop off of the IP coefficient in the short-wavelength region, just as in the HJs III–IV/Si(Ge), corresponds to the onset of interband absorption in the wide-gap component CdS of the heterojunction. The maximum azimuthal photosensitivity of the HJ CdS/InP is $\Phi = 0.13\,\mathrm{A/W\cdot deg}$ at $T = 300\,\mathrm{K}$, which is comparable to the possibilities of photoanalyzers based on Schottky barriers. The wide-band character of the quantum efficiency of photoconversion and the IP coefficient show that CdS/InP solar cells (SCs) can also be used as wide-range (1.2–2.4 eV) highly sensitive photoanalyzers for LPL. It is also important to keep in mind that improving the optical quality of the outer surface of CdS films, which is monitored by polarization measurements of the photocurrent, can additionally increase the quantum efficiency of photoconversion near the pseudo-Brewster angle and therefore raise by another $\simeq 30\%$ the azimuthal photosensitivity obtained in Ref. 82.

7. INDUCED PHOTOPLEOCHROISM OF GaAlAs/GaAs HETEROJUNCTIONS

The discovery and fabrication of the first ideal GaAlAs/GaAs HJs under the leadership of Academician Zh. I. Alfërov at the A. F. Ioffe Physicotechnical Institute was in its time marked by the development of a new generation of devices: semiconductor lasers, high-efficiency solar cells, and so on.[83–86] Efficiencies of 24.6% (AMO, 100 suns) and 27.5% (AM 1.5, 100 suns) have already been attained in solar cells based on such structures.[87] The method of polarized photosensitivity spectroscopy, which can be used to observe the relationship between the polarized PS and the antireflection effect, has been used only recently for studying HJs of this type.[88,89]

The photoconverting structures for polarized measurements were obtained by liquid-phase epitaxy from a limited volume of a Ga–Al–As fluxed solution on a (100) n-GaAs wafer. Epitaxial $Ga_{0.3}Al_{0.7}As$ films up to 2 μm thick were coated with a $\simeq 1.5\,\mu$m thick anodic oxide film. A wide-band spectral characteristic of PS ($\delta_{1/2} = 1.7-1.8\,\mathrm{eV}$) appears in all HJs, and the efficiency reaches 20%.

Polarized PS is not observed when the LPL is incident along the normal to the plane of the anodic oxide. This behavior is attributable to the isotropic properties of the absorbing medium and the absence of directed deformations in $Ga_{0.3}Al_{0.7}As$ films because the parameters of the crystal lattice match. For this reason, NP in such structures turned out to be negligible in the entire range of photosensitivity.

The inequality $i^P > i^S$ and induced polarized PS, which follows the law $P_I \sim \alpha_0^2$, arises for oblique incidence of LPL $\alpha_0 > 0°$. This law holds in the entire spectral range of PS, whereas P_I was found to depend on the photon energy (Fig. 14). This is due to the changes occurring in the character of the angular dependences of the photocurrent within the entire photosensitivity range of the HJ. For $\hbar\omega < 1.5\,\mathrm{eV}$ the dependences $i^P(\alpha_0)$ and $i^S(\alpha_0)$ are standard and are described by the Fresnel formulas,[7,8] whereas for $\hbar\omega > 1.5\,\mathrm{eV}$ they become similar to $i^P(\alpha_0)$, making it possible to interpret them as a decrease of reflection losses for p- and s-polarized light as a result of interference effects. The presence of a maximum in the angular dependences of i^P shows that the front plane of the phototransducers oxide/GaAlAs/GaAs is of high optical quality.

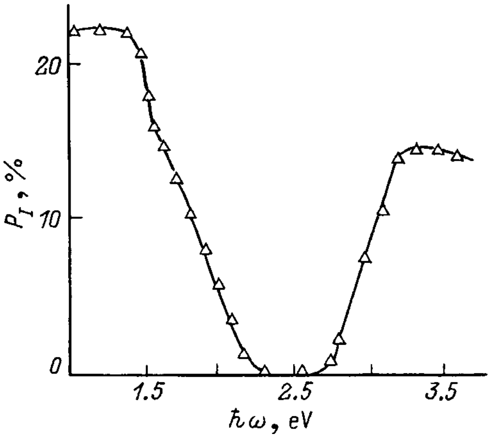

FIG. 14. P_I spectra for the structure oxide/$GaAl_{0.7}As_{0.3}$/GaAs ($T = 300$ K, $\alpha_0 = 75°$, illumination from the oxide side).

A distinguishing feature of the IP of the structure studied in Refs. 88 and 89 is the strong dichroism of P_I (Fig. 14). The IP coefficient is constant only in the long-wavelength spectral region ($\hbar\omega < 1.4\,\mathrm{eV}$), just as in Schottky barriers in the entire range of PS.[50,51] An estimate, using Eq. (10), from the experimental values $P_I \simeq 20-22\%$ (Fig. 14) gives $n \simeq 1.8$, which matches the data for the anodic oxide GaAlAs.[90] On this basis the IP of the experimental HJs in the long-wavelength range can be attributed to optical processes at the air/oxide interface. The ''dip'' observed in the spectrum of P_I at energies from 1.5 to 3 eV corresponds to the region of maximum antireflection of the structures, in agreement with the measurements of the optical reflection R on the same HJs. When reflection losses for p and s polarizations start to decrease with increasing angle of incidence of the LPL, the angular dependences of the photocurrents are observed to converge $i^P(\alpha_0) \rightarrow i^S(\alpha_0)$, and P_I decreases at the same time. According to this ideology, the antireflection effect is maximum when $i^P = i^S$. As one can see from Fig. 14, the maximum antireflection in the experimental HJs occurs from 2.2–2.8 eV, where $P_I \simeq 0$. It is obvious that such polarization monitoring of the antireflection region in HJs can be used to adjust the technological conditions.

In the absence of antireflection coatings in GaAlAs/GaAs HJs, the maximum azimuthal PS $\Phi \simeq 0.1\,\mathrm{A/W\cdot deg}$ ($T = 300\,\mathrm{K}$, $\alpha_0 = 75°$) occurs in a wide spectral range from 1 to 3 eV because of vanishing of the interference antireflection. This motivates the use of such HJs in a new field for these devices—polarization photoelectronics.

8. INDUCED PHOTOPLEOCHROISM OF CuInSe$_2$-BASED THIN-FILM STRUCTURES

Ternary semiconductor compounds and their solid solutions are being increasingly used in research as materials for high-efficiency radiation-resistant photovoltaic systems.[91–95] The most efficient thin-film solar cells (TSCs) have been produced from Cu(In, Ga) Se$_2$ polycrystalline films (CIGS).[92] We shall examine the results of investigations of thin film structures based on CuInSe$_2$ (CIS) and CIGS by polarized photoelectric spectroscopy.[95–98]

8.1. Polarized photosensitivity of *n*-CdS/*p*-CuInSe$_2$ thin-film structures

CuInSe$_2$ films with thicknesses 2–5 μm were deposited on a glass surface by magnetron sputtering of a CIS target.[99] CdS⟨In⟩ films with thicknesses 2–5 μm were deposited on the post-growth CIS surface by vacuum sublimation. The photosensitivity of the best HJs reached 0.5 mA/W, and for illumination from the CdS side it was observed in the region between the band gaps of the components of the HJ.

The angular dependences of the photocurrent are described by the Fresnel formulas. These dependences show that in the HJs photopleochroism arises only when $\alpha_0 > 0°$ and follows the law (11). According to Eq. (10), the experimental value $P_I \simeq 64\%$ at $\alpha_0 = 80°$ corresponds to $n \simeq 3.1$, which is higher than the known refractive index $n = 2.5$ for CdS[100] and closer to the value $n = 3.0$ for CIS.[36] This gives us a basis for inferring that the anisotropy of the PS of thin-film HJs illuminated from the CdS side is determined mainly by transmission of light through the heterojunction and subsequent absorption in the narrow-gap component. The observed increase in i^P with α_0 indicates a decrease of reflection losses without deposition of an antireflection coating and simultaneously attests to a high quality of the cadmium sulfide films.

The coefficient IP of CdS/CIS structures for $\alpha_0 =$ const remains high in the entire range of photosensitivity and is virtually independent of the photon energy, in agreement with the analysis in Ref. 34.

The maximum azimuthal PS in HJs of this type is $\Phi = 5$ mA/W·deg ($T = 300$ K, $\alpha_0 = 80°$) and characterizes them as wide-range (0.8–2.5 eV) analyzers for LPL, which at $\alpha_0 = 0°$ lose this capability and become sensitive only to the radiation intensity.[96,97]

8.2. Polarized photosensitivity of ZnO/CdS/CuIn,GaSe$_2$ thin-film solar cells

The CIGS films were deposited on molybdenum-coated glass plates by vacuum thermal evaporation from individual sources. The composition corresponded to the ratio In/(In+Ga) = 0.25. A CdS film was deposited on the CIGS surface, after which a ZnO film was deposited by magnetron sputtering of a ZnO target. The total thickness of the structures is 3–5 μm. Under AM-1.5 illumination conditions the efficiency of the best structures is 15%.

The long-wavelength photosensitivity edge of TSCs is determined by direct transitions in CIGS and two thresholds appear on the short-wavelength side in the PS spectrum because of the absorption in CdS and then also in ZnO. The width of the spectral photosensitivity bands of TSCs, $\delta_{1/2} \simeq 1.3$–1.6 eV, at $T = 300$ K depends on the thicknesses of the wide-gap films. Equidistant peaks in the PS spectra of the best TCSs were first observed in Refs. 95 and 98. These peaks could be due to interference in the ZnO film.

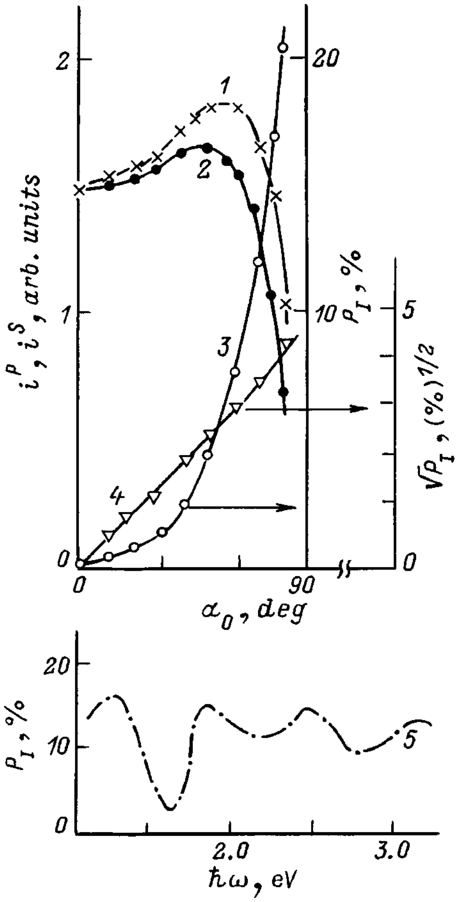

FIG. 15. $i^P(\alpha_0)$ (*1*), $i^S(\alpha_0)$ (*2*), $P_I(\alpha_0)$ (*3*—P_I, *4*—$P_I^{1/2}$, $\hbar\omega = 2.0$ eV) and $P_I(\hbar\omega)$ ($\alpha_0 = 70°$) (*5*) for a ZnO/CdS/Cu(In, Ga)Se$_2$ thin film solar cell at $T = 300$ K.

Only IP is characteristic for TSCs in polarized light. As follows from Fig. 15 (curves *1* and *2*), the inequality between the photocurrents $i^P > i^S$ arises for $\alpha_0 > 0°$, and the angular dependences of i^P and i^S show a similar behavior. These dependences attest to a high perfection of the front surface on the one hand and to a simultaneous decrease of the p- and s-wave reflection losses on the other. Therefore antireflection is attained in these TSCs for both polarizations. The IP coefficient of the TSCs increases continuously as $P_I \sim \alpha_0^2$ (Fig. 15, curves *3* and *4*). Characteristically, the values of P_I with $\alpha_0 =$ const for different TSCs differed somewhat from one another and fell into the range 10–20%. An estimate of n from the experimental values of P_I, using Eq. (10), gives a refractive index $n \simeq 1.2$–1.7, which is less than the known value for ZnO.[36] The observed decrease of the experimental values of P_I relative to the values estimated from Eq. (10) using the refractive index for ZnO could be due to interference of LPL in the ZnO films.

Sharp oscillations arise in the spectrum of P_I for HJs with the maximum efficiency (Fig. 15, curve *5*). These oscil-

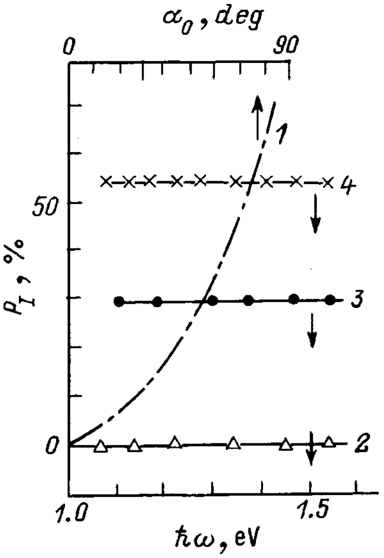

FIG. 16. $P_I(\alpha_0)$ (*1*, $\hbar\omega = 1.15$ eV) and $P_I(\hbar\omega)$ (α_0, deg: *2*—0, *3*—50, *4*—75) for a n-$MnIn_2Te_4$/p-Si HJ at $T = 300$ K. Illumination from the $MnIn_2Te_4$ side).

lations correspond to interference features in the photosensitivity spectrum. As the efficiency decreases, the oscillations decrease to such an extent that the spectrum P_I loses dichroism in a wide spectral range, although the value of P_I remains less than that estimated on the basis of the refractive index. The oscillations in the experimental values of P_I and their weak spectral dependence can be explained by the antireflection effects in the ZnO film. Taking as a measure of antireflection $P_I \approx 0$, the authors of Ref. 101 concluded that the strongest antireflection in TSCs was obtained with approximately 1000 nm thick ZnO films.

Therefore CIGS-based TSCs can be used as wide-band photoanalyzers, and polarized spectroscopy of their photosensitivity can be used for making adjustment in the TSC technology.

9. INDUCED PHOTOPLEOCHROISM OF $MnIn_2Te_4$/Si HETEROJUNCTIONS

Photosensitive structures produced using semimagnetic semiconductors are of great interest because of the possibilities of extending the functional range of optoelectronic devices.[102,103] After the complicated problem of obtaining thin films of one of such semiconductors, $MnIn_2Te_4$ was solved, the induced photopleochroism of structures based on them was investigated.[104,105]

Vacuum thermal sputtering was used to deposit 0.1–0.3 μm thick p-$MnIn_2Te_4$ films on a (111) Si wafer. The PS spectra of these HJs illuminated from the $MnIn_2Te_4$ side are, as a rule, wide-band ($\delta_{1/2} \simeq 2.2$ eV) with maximum photosensitivity 0.1 mA/W at $T = 300$ K.

The photopleochroism observed in such structures is, by its very nature, induced and follows a law $P_I \sim \alpha_0^2$ (Fig. 16). At $\alpha_0 = 75°$ the coefficient $P_I \simeq 55\%$, which makes it possible to use the method to estimate $n \simeq 3.0$ for the ternary compound used in films. The authors of Ref. 105 believe that the simply obtainable HJs can be used as photoanalyzers for LPL with azimuthal photosensitivity $\Phi \simeq 0.2$ mA/W·deg at $T = 300$ K, which can be continuously controlled by the angle of incidence of the LPL (Fig. 16).

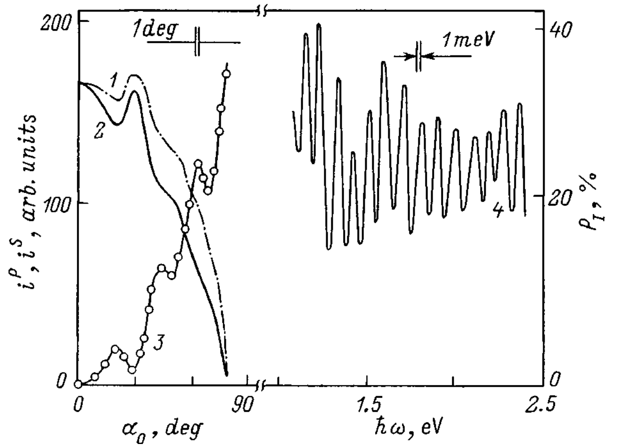

FIG. 17. $i^P(\alpha_0)$ (*1*), $i^S(\alpha_0)$ (*2*), $P_I(\alpha_0)$ (*3*) at $\hbar\omega = 1.4$ eV, and $P_I(\hbar\omega)$ (*4*, $\alpha_0 = 75°$) for a PSi/Si structure $T = 300$ K.

10. INDUCED PHOTOPLEOCHROISM OF A HETEROCONTACT OF POROUS AND SINGLE-CRYSTAL SILICON

A new approach to controlling the fundamental properties of semiconductors that is based on the formation of nanosize clusters in a semiconductor matrix has been under active development in the last few years.[86,106,107] Increasingly, the dimension in semiconductors is lowered.[108,109] We shall consider the manifestation of polarized PS in structures based on porous silicon.[110–113]

Anodic etching of wafers has been used to obtain HJs.[108,110] This made it possible to form films of porous silicon (PSi) with thicknesses ranging from several to tens of microns. Under illumination from the PSi side, as a rule, wide-band PS obtains in these HJs. The energy position of the long-wavelength PS edge is determined by interband absorption in Si, and the total band width is $\delta_{1/2} \simeq 1.3$ eV for approximately 10 μm thick PSi films and increases with decreasing thickness. For example, in HJs with a $\simeq 1$ μm thick PSi film the photocurrent was not found to decrease to 3 eV at all. The photosensitivity spectra of the HJs usually contains up to 20 equidistant peaks, which, taking into account the refractive index of PSi,[114] make it possible to estimate film thicknesses in agreement with the directly determined values. The fact that a rich interference pattern is observed itself indicates very high perfection of the PSi films.[110–112]

It follows from polarized investigations of the photosensitivity of PSi/Si HJs that only IP appeared in such structures, since the photoconductivity is isotropic in both components. The dependences of the photocurrents i^P and i^S even in HJs with a mirror outer PSi plane showed a nonmonotonic dropoff for $\alpha_0 > 0°$ (Fig. 17, curves *1* and *2*) and differ from the dependences expected from the Fresnel analysis of the transmission of LPL through the air/PSi interface.[2,7] The authors of Ref. 111 were the first to observe oscillations in the angular dependences of P_I of such HJs. In their opinion these oscillations are due to the interference of LPL in the PSi films (Fig. 17, curve *3*). The growth of the IP with increasing α_0 approximately follows the quadratic law (11), and estimates using Eq. (10) and the experimental values $P_I = 20-25\%$ ($\alpha_0 = 70°$) give $n \approx 1.7$, which differs from the known values of n for crystalline Si and makes it possible to attribute the polarization photosensitivity of HJs to phenomena at the air/PSi interface. The spectral dependences of P_I of the HJ PSi/Si show oscillatory behavior (Fig. 17, curve *4*), which is due to the interference of LPL in the PSi film.

The observed oscillations of IP in the HJ PSi/Si[111] are of fundamental importance and could find application in selective photoanalyzers of LPL. In addition, they demonstrate new possibilities of polarized photoelectric anisotropy for fast diagnostics of the quality of nanostructural films.

11. INDUCED PHOTOPLEOCHROISM OF GALLIUM-NITRIDE-BASED HETEROJUNCTIONS

Gallium nitride is one of the semiconductor materials which are now being intensively studied. The substantial progress made in the technology of this wide-gap semiconductor has made this material promising for use in short-wavelength and high-temperature optoelectronics, phototransducers, and so on.[115–118] It is of special interest to solve the problems of integrating GaN with Si and III–V semiconductors. This could open up applications of the current electronics materials not only as substrates for large-area GaN wafers but also for real integration of the unique functional characteristics of such semiconductors. We note that the overwhelming majority of investigations of photoelectric phenomena in GaN and GaN-based structures have been performed with unpolarized radiation. We shall examine some results of these investigations of GaN performed using polarized photoelectric spectroscopy.[119,120]

The GaN layers were grown on the (111) and (100) planes of n- and p-type Si and GaP wafers by chemical deposition from the gas phase in an open gas-transport system. For the GaN/Si structures it was established that the PS reaches $\simeq 0.15$ A/W with (111) Si substrates, and the photosensitivity of the HJ is two to four orders of magnitude lower for the (100) Si orientation. The GaN layers on Si substrates were 10–20 μm thick, while the GaN layers on GaP were only 0.5 μm thick. In both types of structures the PS spectra were wide-band ($\delta_{1/2} \simeq 1.8$ eV in GaN/Si and $\delta_{1/2} \simeq 0.7$ eV in GaN/GaP).

When such HJs are illuminated along the normal to the GaN films, photoactive absorption is isotropic, while under oblique incidence of LPL the inequality $i^P > i^S$ holds in the entire PS range. For GaN-based HJs the character of the angular dependences of the photocurrents i^P and i^S depended on film quality. In the HJ GaN/Si with a rough outer surface of the GaN films, the photocurrents for p- and s-polarization decreased with increasing angle of incidence, while in the HJs GaN/Si and GaN/GaP with mirror surfaces of the GaN films the photocurrents i^P and i^S increased with α_0. This behavior is determined by the decrease of the reflection losses and is due to interference of LPL in the wide-gap film. In both types of HJs, as the angle of incidence of the LPL on the GaN surface increases, P_I increases according to the quadratic law (11), i.e., just as in the absence of interference phenomena.

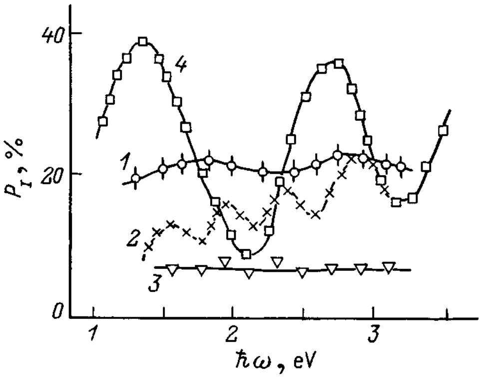

FIG. 18. P_I spectra of n-GaN/p-Si HJ (*1*—sample 59.1.1, *2*—60.1.2.1, *3*—60.1.2) and a n-GaN/p-GaP HJ (*4*—sample 106-1r) at $T = 300$ K and $\alpha_0 = 75°$.

Investigations of Ip spectra in the HJs GaN/Si and GaN/GaP (Fig. 18) show that the magnitude of the IP varies from sample to sample and in most cases undergoes oscillations, varying within the range of PS. Estimates based on Eq. (10), taking into account the known refractive index of GaN,[36] give $P_I \simeq 35-40\%$. This value of P_I is reached at the maxima of the spectral dependence of IP for only one of the structures and for a definite photon energy (Fig. 18, curve *4*). In this sample, the IP decreases relative to the computed value $P_I \simeq 35-40\%$ away from this energy and also on switching to other structures. This decrease of the photopleochroism can be attributed to changes in the parameters of the GaN films, which changes the antireflection effect.

The induced photopleochroism observed[119,120] in HJs based on gallium nitride films demonstrates that such films can be used as selective (Fig. 18, curve *4*) photoanalyzers of LPL with maximum azimuthal photosensitivity $\Phi = 10$ mA/W·deg ($T = 300$ K, $\alpha_0 = 75°$), while the dependences established for the values and spectral contours of P_I can be used for diagnostics of GaN film quality.

12. GIGANTIC INDUCED PHOTOPLEOCHROISM

A central problem in the fabrication of photodetectors for LPL is ensuring high photopleochroism.[9] It follows from the expression (12) that the maximum IP coefficient for a uniform IS is determined by the value of n and for known semiconductors falls in the range 55–85%. The experimental data examined above for P_I of the most diverse diode structures in isotropic semiconductors and multilayer systems based on them also demonstrate that $P_I^m < 100\%$. In 1993, at A. F. Ioffe Physicotechnical Institute, a qualitative breakthrough was made in this problem and a new photoelectric effect was observed experimentally—gigantic induced photopleochroism, where P_I increases sharply $P_I \to \pm\infty$.[50,121–123]

The fundamental idea is to get the sign of the photocurrent to change on switching from p to s polarization. Then it is easy to see from Eq. (7) that P_I overcomes the 100% limit.

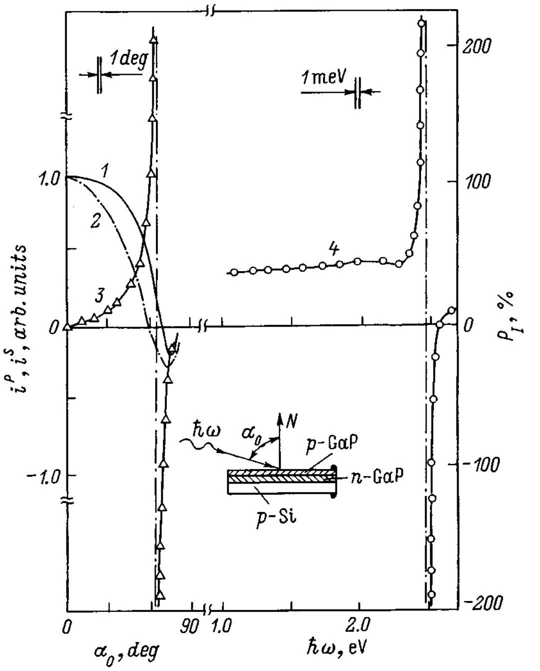

FIG. 19. $i^P(\alpha_0)$ (*1*), $i^S(\alpha_0)$ (*2*), $P_I(\alpha_0)$ (*3*), and $P_I(\hbar\omega)$ (*4*, $\alpha_0 = 75°$) for a $p-n$-GaP/p-Si structure at $T = 300$ K. Illumination from the GaP side, *1–3*—$\lambda = 0.500$ μm. Inset: Illumination scheme.

As follows from the analysis presented above, none of the structural types allowed this to occur. To obtain GIP in Refs. 121–123 structures with two active regions, which differ with respect to the direction of the electric fields, were developed on the basis of isotropic semiconductors.

We shall examine the behavior of the GIP for structures with two $n-p$ junctions on a Si substrate. To obtain such a structure, first a 3–4 μm thick n-GaP epitaxial film was grown on a Si substrate. As a result, the structure containing a n-GaP/p-Si HJ and a $p-n$-GaP homojunction accounted for the inversion of the sign of the photocurrent upon illumination with sunlight. The inversion stems from the fact that in the long-wavelength (relative to the inversion point $\hbar\omega_I$) region the PS is determined by the HJ p-Si/n-GaP, while in the short-wavelength region the sign of the total photocurrent is determined by the upper, relative to the LPL beam, homojunction $p-n$-GaP.

For structures illuminated from the GaP side by LPL which inverts the sign of the photocurrent, photopleochroism arises as soon as $\alpha_0 > 0°$, just as in noninverting structures. Irrespective of the polarity of the photocurrent, the sign of the IP remained positive and the angular dependence of the IP followed the periodic law (11).

New behavior arises near the wavelength at which the sign inversion of the photocurrent and IP as a result of the change in α_0 (Fig. 19). For each photocurrent i^P and i^S there appears an angle of incidence at which the sign changes, and the angular dependences themselves can no longer be described by the Fresnel formulas.[2,7] This occurs because the competition between the photocurrents from each $n-p$ junction is also superimposed on the anisotropy of light transmission through the air/IS boundary. In accordance with Eq. (7), because of the sign inversion of i^P and i^S a point of discontinuity appears in the angular dependence $P_I(a_0)$ and photopleochroism approaches infinity, $P_I \rightarrow \pm\infty$, while the experimental values are at the level $\pm(400-700)\%$.

Therefore polarity inversion of the photocurrents at a definite angle of incidence of the LPL gives rise to GIP, where $P_I \rightarrow \pm\infty$ (Fig. 19, curve *3*).

Interesting behavior is also observed in the azimuthal dependences of the photocurrents, where the ratio of i^P and i^S, as well as the inversion of their polarity at definite values of α_0 and $\hbar\omega$, are controlled by the azimuthal angle Θ.

Inversion of the photocurrent polarity occurs in the spectral dependences i^P and i^S of such structures for p and s polarizations at different photon energies, and in the region between these points there exists an energy at which the photocurrents are equal to one another in amplitude but differ in polarity. According to Eq. (7), the GIP $P_I \rightarrow \pm\infty$ arises precisely under these conditions. An example of the spectral dependence of P_I for one of the $p-n$-GaP/p-Si structures is displayed in Fig. 19 (curve *4*). The spectral dependence of P_I has the form of a hyperbola; the energy position of the asymptote of this hyperbola is determined from the condition that the amplitudes of differently directed photocurrents i^P and i^S are equal. The GIP $P_I \rightarrow \pm\infty$ arises precisely near the asymptote, and the energy position of the asymptote can be displaced continuously by applying an external voltage, thereby accomplishing rapid tuning of the spectral position of the narrowly selective GIP.

Gigantic IP has also been obtained in double-barrier structures of a different type, Au/n-GaAs/Au and Au/n-GaP$_x$As$_{1-x}$/Au. The possibility of controlling the composition of the solid solution serves as an additional channel for monitoring the spectral range of the GIP.[50,122,123]

In summary, a new photoelectric effect—GIP, which was first predicted and then observed, thus opens up the possibility of applications of double-barrier structures based on isotropic semiconductors as highly sensitive, tunable, narrowly selective photoanalyzers for LPL.

13. SIMULTANEOUS APPEARANCE OF NATURAL AND INDUCED PHOTOPLEOCHROISM

In connection with the fact that the physical factors for the appearance of NP are absent in isotropic semiconductors,[9,10] in all variants of detection of LPL examined above the polarization PS was determined primarily by light transmission through an interface. It is obvious that for photodetectors based on anisotropic semiconductors as soon as the incidence of LPL becomes oblique photopleochroism is caused by the superposition of the photopleochroism induced by oblique incidence and the natural photopleochroism. The problem of the summation of the contributions of these different photoelectric phenomena in an anisotropic medium has been examined in Refs. 9 and 124–126. The main results of this analysis reduce to the following.

Let a light wave whose polarization plane **E** is parallel or perpendicular to the plane of incidence *XZ* be incident in the direction *OX* on the illuminated surface *ZY* of the structure (Fig. 4). For oblique incidence of LPL on the *ZY* plane the amplitude of the refracted wave is determined by the Fresnel

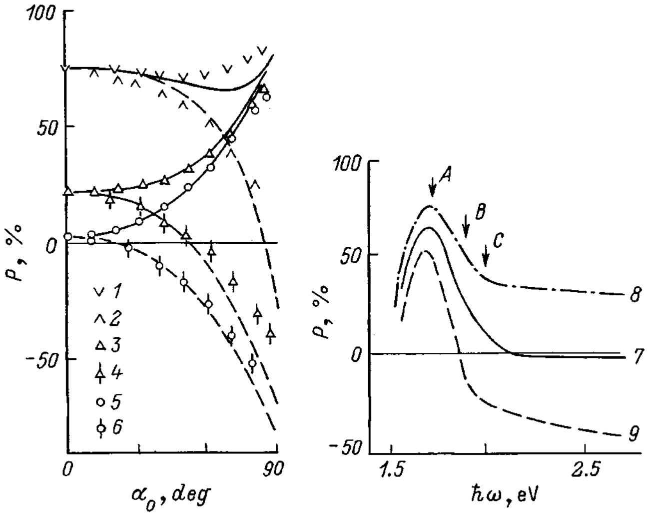

FIG. 20. Experimental curves $P_I(\alpha_0)$ ($\hbar\omega$, eV: *1, 2*—1.60; *3, 4*—1.91; *5, 6*—2.00; *1, 3, 5*—**c**$\|XZ$, *2, 4, 6*—**c**$\|YZ$, solid curves—calculation using Eq. (17), dashed curves—calculation using Eq. (18)) and $P_I(\hbar\omega)$ [α_0, deg: *7*—0, *8, 9*—70; *8*—**c**$\|XZ$, *9*—**c**$\|YZ$, the arrows *A*, *B*, and *C* mark the interband transition energies for CdGeP$_2$ (Ref. 127)].

formulas.[2] Assuming that the change in the state of polarization of the incident radiation as a result of being refracted can be disregarded, the photopleochroism for uniaxial anisotropy of the medium with **c**$\|XZ$ orientation of the tetragonal axis will have the form

$$P^{\|}=[i_{\psi}-i^{O}\cos^2(\alpha_0-\psi)]/[i_{\psi}+i^{O}\cos^2(\alpha_0-\psi)], \quad (17)$$

and in **c**$\|YZ$ orientation

$$P^{\perp}=[i_{\psi}\cos^2(\alpha_0-\psi)-i^{O}]/[i_{\psi}\cos^2(\alpha_0-\psi)+i^{O}], \quad (18)$$

where $i_{\psi}=i^{E}\cos^2\psi+i^{O}\sin^2\psi$, $\psi=\sin^{-1}(\sin\alpha_0/n)$, and i^{O} and i^{E} are the photocurrents observed with illumination of the semiconductor by the ordinary (**E**$\perp$**c**) and extraordinary (**E**$\|$**c**) light wave. From Eqs. (17) and (18) follows the well-known relation for NP for illumination of an isotropic medium along the normal to the receiving plane ($\alpha_0=0°$) by an LPL beam:[9,10]

$$P_N=(i^{O}-i^{E})/(i^{O}+i^{E}), \quad (19)$$

which for an isotropic medium ($i^{O}\equiv i^{E}$) gives $P_N\equiv 0$.

The typical experimental angular dependences obtained for photopleochroism by illuminating $n-p$-CdGeP$_2$ structures with LPL with several photon energies from the photosensitivity range are compared in Fig. 20 (curves *1–6*) with the dependences computed using Eqs. (17) and (18). The values of the photopleochroism at $\alpha_0=0°$ are determined only by the NP, which depends on the fundamental properties of this semiconductor. It is important to note that for $\alpha_0>0°$ the experimental values of the photopleochroism start to differ from P_N, and the experimental angular dependences of $P^{\|}$ and $P^{\perp}$ correlate satisfactorily with the computed curves obtained using Eqs. (17) and (18).

The next important law of the superposition of induced photopleochroism on natural photopleochroism is that when the PI coincides with the tetragonal axis **c** of CdGeP$_2$ the photopleochroism increases continuously relative to the positive NP as α_0 increases. For example, the characteristic value $P_N=21\%$ for structures with $\hbar\omega=1.91$ eV can be continuously increased to 63% ($\alpha_0=80°$), i.e., by a factor of 3. Characteristically, the maximum value of $P^{\|}$ as $\alpha_0\rightarrow 90°$ does not depend on the natural anisotropy of CdGeP$_2$ and is entirely determined only by the refractive index of the semiconductor.

Conversely, increasing α_0 in **c**$\|YZ$ orientation decreases $P^{\perp}$ relative to P_N with $P^{\perp}$ becoming negative. It is also evident from Fig. 20 that as P_N increases, the value of α_0 at which the photosensitivity of the structure loses the natural anisotropy and becomes photoisotropic ($P=0$) shifts in the direction of large angles of incidence of LPL. This occurs because in such an illumination geometry the sign of the IP is opposite to that of P_N, and at the point of inversion of $P^{\perp}$ the natural and induced components of photopleochroism are equal in amplitude ($P_N=P_I$). The different influence, observed in the course of these measurements, of the relative orientation of the plane of incidence of LPL relative to the tetragonal axis in an anisotropic crystal on photopleochroism is due to the fact that for **c**$\|XZ$ a light wave with **E**$\perp$**c** which is weakly absorbed in CdGeP$_2$ is reflected more strongly, while for **c**$\|YZ$ orientation reflection of the wave with **E**$\|$**c** which is strongly absorbed in CdGeP$_2$ dominates.

The spectral contours of photopleochroism for structures based on anisotropic semiconductors at $\alpha_0=0°$ is entirely determined by NP.[9,50] The maximum of the positive photopleochroism of these structures is reached in the region of direct *A* transitions, and as the *B* and *C* transitions, which dominate in **E**$\perp$**c** polarization, of electrons from valence-band subbands split off by the crystal field and spin-orbit interaction into the conduction band, the positive photopleochroism P_N decreases virtually to zero in the region $\hbar\omega>2.1$ eV (Fig. 20, curve *7*).[9,127] Under conditions of oblique incidence of LPL (Fig. 20, curves *8* and *9*) photopleochroism in the entire region of photosensitivity with **c**$\|XZ$ increases and at $\alpha_0=70°$ it reaches 30–40% in the short-wavelength region.

The shape of the *P* spectra remains unchanged under oblique illumination, because the spectral contour of photopleochroism is determined by the energy spectrum and the selection rules for interband optical transitions in the anisotropic semiconductor, while the observed changes in the magnitude of photopleochroism are determined, right up to sign inversion, by the processes involved in the transmission of LPL through the air/semiconductor interface. Since these processes do not change the spectral contour of P_N, there are grounds for assuming that they are nonselective. This conclusion agrees with the analysis in Ref. 34.

The laws of formation of photopleochroism which were examined for $n-p$-CdGeP$_2$ structures have also been confirmed by investigations of the photoconductivity of uniaxial CdSe crystals with a type of positional ordering of the atoms different from that in chalcopyrite.[125]

Therefore combining NP with IP opens up new possibilities for rapid control of the magnitude and spectral contour of the polarization photosensitivity of phototransducers based on anisotropic semiconductors.

14. PRACTICAL CONSEQUENCES OF THE OBSERVATION OF INDUCED PHOTOPLEOCHROISM

The main practical consequence of the new photoelectric phenomenon—induced photopleochroism—and the subsequent detailed experimental study of its laws on diverse types of phototransducers, which were produced under laboratory conditions for a specific problem, undoubtedly must be treated as a polarization sensitization of isotropic semiconductors and structures based on them. This qualitative breakthrough solved the problem, which arose after the discovery of NP,[9] of the shortage of anisotropic semiconductors meeting the technological requirements of semiconductor electronics. In other words, the wide practical applications of anisotropic semiconductors as materials for polarized photoelectronics were held back because the technological base for these materials had not yet expanded beyond the research laboratories. This made it very tempting to use isotropic semiconductors for which the technological base is commercially well-developed for the needs of polarized photoelectronics. The realization of these hopes is completely analyzed for the first time in the present review. Induced photopleochroism is a universal photoelectric phenomenon, which is observed in virtually any semiconductor. For this reason, record-high values of azimuthal photosensitivity, for example, 0.22 A/W·deg in Ni/n-GaAs structures, for semiconductor photoanalyzers have already been obtained in phototransducers based on the main materials used in semiconductor electronics—silicon and III–V compounds.

Now that after the discovery of IP polarized photoelectronics has been supplied with the well-known semiconductors the problem of a materials shortage in this field can be regarded as solved. For this reason the prospects for taking semiconductor optoelectronics to the polarized level are now quite real.

The development of the physical principles of tuning of the magnitude and spectral range of IP is one of the most important practical consequences of research on IP. Soon after the discovery of GIP in IS-based structures the value $P_I < 100\%$, the limit determined by the refractive index of the semiconductor and previously thought to be an unsurpassable maximum value, was surpassed, making it possible for a photoanalyzer with gigantic induced photopleochroism to operate in the selective regime.

The development of the method of polarized photoelectric spectroscopy also opened up new possibilities for diagnostics of the optical quality of photoconversion structures and thereby for optimizing their fabrication technology.

Finally, it should be noted that the polarization diagnostics of antireflection is conducted in the region of high PS, which makes it possible to determine to a high degree of reliability whether or not i^P and i^S are equal. Considering that the conventional method for finding the region of antireflection by means of optical reflection measurements is conducted for low values of the reflection coefficient ($R \to 0$), the advantages of the polarized photoelectric method (PPM) become more than obvious. For finished structures, where the front plane of the phototransducer is equipped with a contact grid, the reflection method becomes unusable and, as a rule, diagnostics are performed before the contacts are deposited, while PPM[9,50] is also applicable even if a contact grid is present. It is also necessary to take account of the fact that reflection measurements under conditions $R \to 0$ require quite large areas, while PPM can also be used for areas on the order of 0.1×0.1 mm. For this reason PPM enables diagnostics with a light probe diameter of about 0.2 mm and thereby yields information about the local uniformity of the antireflection regions, which reflection measurements cannot do. Finally, for relief surfaces the standard method of R measurements is unsuitable because of diffuse scattering, and it must be made more complicated. For PPM the surface structure does not limit diagnostics in any way.

Polarization investigations of the photosensitivity have also led to the development of a new approach to increasing the efficiency of photodetectors for LPL, making it possible to eliminate the complicated and expensive technology for producing antireflection coatings.[128] This approach is based on the fact that when the polarization plane of LPL coincides with the plane of incidence, the short-circuit photocurrent with a receiving surface of good optical quality exhibits a maximum as α_0 increases, just as in the case of a Si photodiode (Fig. 21, curve *1*). The photocurrent i^P reaches a maximum near the Brewster angle, where $R \to 0$.[2] As p polarization continuously transforms into s polarization the increase on the photocurrent with increasing α_0 decreases and vanishes. For this reason, the observed increase of i^P with increasing angle of incidence on a mirror front surface of a Si photodiode is explained by the elimination of reflection losses. The increase of the photocurrent i^P at the Brewster angle is achieved in the entire range of photosensitivity (Fig. 21, curves *2* and *3*), and the efficiency at $\alpha_0 = 75°$ is 47% higher than that at $\alpha_0 = 0°$. This increase corresponds to complete elimination of reflection losses in the entire range of photosensitivity. As one can see from the analysis presented above, this phenomenon is observed in all phototransducers with a perfect front plane, and the efficiency increase vanished as the quality of the front plane decreased.

Therefore, oblique incidence of LPL makes it possible to eliminate reflection losses in the entire range of photosensitivity of a phototransducer. An important point is that this phenomenon makes it possible to do away with the search for and the complicated technology for producing, as a rule, multilayer antireflection coatings and thereby to decrease the cost and simplify the process of producing phototransducers. It should be underscored that the phenomenon is suitable for all semiconductors. This is especially valuable for new materials, for which antireflecting coatings have not been developed at all.

15. CONCLUSIONS

This review shows that in the years after the first observation of induced photopleochroism[18] impressive progress has been made in physicotechnical investigations of the phenomenon and in its diverse applications, in the control of the parameters of photosensitive structures based on isotropic semiconductor materials, and in finding actual practical applications. The level that has been achieved for the polariza-

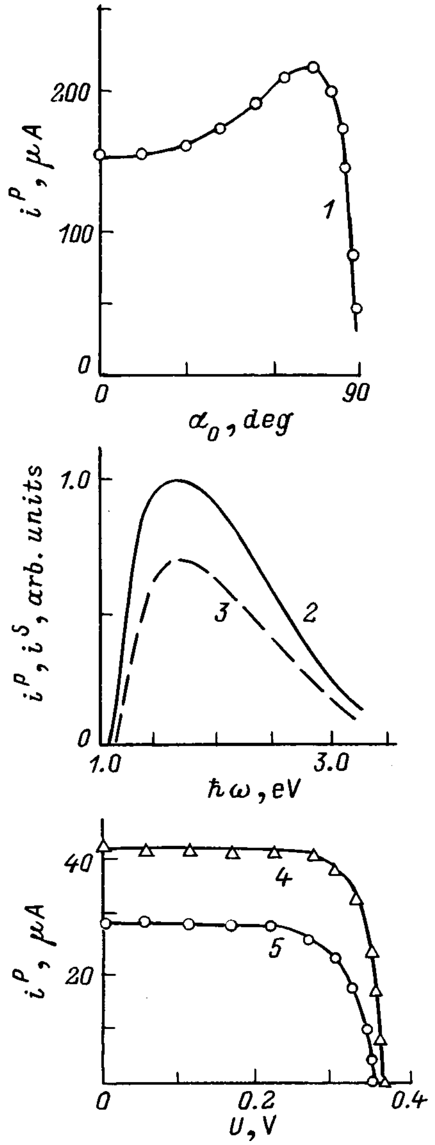

FIG. 21. $i^P(\alpha_0)$ (*1*) and the spectra $i^P(\hbar\omega)$ (*2*) and $i^S(\hbar\omega)$ (*3*) and the load characteristics (*4, 5*) of a Si photodiode at $T=300\,\text{K}$ (*1, 4, 5*—$\lambda=0.63\,\mu\text{m}$; P, mW/cm^2: *1*—0.9; *4, 5*—0.2; α_0, deg: *3, 5*—0; *2, 4*—75).

tion parameters on Schottky barriers and heterojunctions, consisting of III–V semiconductors and their solid solutions, in photodetectors with a narrowly selective GIP now makes it possible to use these structures in the development of semiconductor optoelectronic systems, where together with radiation intensity the orientation of the polarization plane of LPL is also use as an information carrier. Fundamental successes have been achieved in the use of isotropic III–V semiconductors and their solid solutions in photodetectors with narrowly selective GIP. Further progress in the field of LPL photodetectors with induced photopleochroism requires the development of theoretical models of the phenomenon. This will increase our understanding of the physics of the phenomenon and enable computer simulation of a new generation of polarimetric structures.

Investigations of induced photopleochroism and its realization in various phototransducers are from our standpoint, on the whole, one of the most productive directions of the modern physics and technology of semiconductor structures.

The original works cited in this review were supported by the Russian Fund for Fundamental Research, the Ministry of Science of the Russian Federation, and INTAS.

We thank Academician of the Russian Academy of Sciences B. P. Zakharchenya and Professor V. F. Masterov for their support of this direction and for helpful discussions and also Professor H. W. Schock (Stuttgart University, Germany), A. A. Lebedev, V. M. Andreev, and Yu. V. Zhilyaev for fruitful collaboration.

---

[*] E-mail: rudvas@uniys.hop.stu.neva.ru

[1] M. Born and E. Wolf, *Principels of Optics*, 4th edition [Pergamon Press, Oxford, 1969; Nauka, Moscow, 1970].
[2] G. S. Landsberg, *Optics* (Nauka, Moscow, 1976).
[3] F. S. Crawford, Jr., *Waves* [McGraw-Hill, New York, 1968; Nauka, Moscow, 1976].
[4] R. W. Ditchburn, *Light*, 2nd edition [Blackie, London, 1963; Nauka, Moscow, 1965].
[5] W. A. Shurcliff, *Polarized Light: Production and Use* [Harvard University Press, Cambridge, MA, 1962; Nauka, Moscow, 1970].
[6] N. D. Zhevandrov, *Applications of Linearly Polarized Light* (Nauka, Moscow, 1978).
[7] R. Azzam and N. Bashara, *Ellipsometry and Polarized Light* [North-Holland, New York, 1977; Mir, Moscow, 1981].
[8] Yu. I. Ukhanov, *Optical Properties of Semiconductors* (Nauka, Moscow, 1977).
[9] Yu. V. Rud', Izv. Vyssh. Uchebn. Zaved. Fiz. **8**, 68 (1986).
[10] F. P. Kesamanly, V. Yu. Rud', and Yu. V. Rud', Fiz. Tekh. Poluprovodn. **30**, 1921 (1996) [Semiconductors **30**, 1001 (1996)].
[11] É. É. Godik, V. I. Dosov, O. V. Lamykin, and V. P. Sinis, Prib. Tekh. Éksp. **5**, 199 (1977).
[12] P. M. Valov, *Doctoral Dissertation* (A. F. Ioffe Physicotechnical Institute, Soviet Academy of Sciences, Leningrad, Russia, 1980).
[13] V. M. Asnin, A. A. Bakun, A. M. Danishevskiĭ, E. L. Ivchenko, and G. E. Pikus, JETP Lett. **28**, 74 (1978).
[14] M. P. Petrov and A. I. Grachev, JETP Lett. **30**, 15 (1979).
[15] V. M. Belinicher, V. K. Malinovskiĭ, and B. I. Sturman, Zh. Éksp. Teor. Fiz. **73**, 692 (1977) [Sov. Phys. JETP **46**, 362 (1977)].
[16] A. M. Glass, D. von Linde, and N. T. Negran, Appl. Phys. Lett. **25**, 233 (1974).
[17] É. D. Pankov and V. V. Korotaev, *Polarized Angle Meters* (Nedra, Moscow, 1991).
[18] Yu. V. Rud' and G. A. Medvedkin, Inventor's Certificate, SSSR, No. 671634. [Byul. izobret., No. 41 (1980)].
[19] R. Bube, *Photoconductivity of Solids* [John Wiley, New York, 1960; Inostr. Lit., Moscow, 1962].
[20] S. M. Ryvkin, *Photoelectric Effects in Semiconductors* [Consultants Bureau, New York, 1964; GIFML, Moscow, 1963].
[21] J. Schaiffe, *Physical Properties and Construction of Semiconductor Devices* (GÉI, Moscow, 1963).
[22] V. I. Fistul', *Introduction to Semiconductors* (Vyssh. shkola, Moscow, 1975).
[23] *Narrow-Gap Semiconductors and Their Applications* (Mir, Moscow, 1969).
[24] T. Moss, G. Burrel, and B. Ellis, *Semiconductor Opto-Electronics* [Wiley, New York, 1973; Mir, 1976].
[25] L. V. Tarasov, *Physical Principles of Quantum Electronics* (Sov. radio, Moscow, 1976).
[26] Yu. P. Safonov and Yu. G. Andrianov, *Infrared Technology and Space* (Sov. radio, Moscow, 1978).
[27] G. Chol, Y. Marfaing, M. Munsch, P. Thorel, and P. Combette, *Les Détecteurs de Rayonnement Infra-Rouge* [Dunod, Paris, 1966; Mir, Moscow, 1969].
[28] B. L. Sharma and R. K. Purohit, *Semiconductor Heterojunctions* [Pergamon Press, Oxford, 1974; Sov. radio, Moscow, 1978].
[29] *Semiconductor Photodetectors: Ultraviolet, Visible, and Near-Infrared Ranges*, edited by V. I. Stafeeva (Radio i svyaz', Moscow, 1984).

[30] V. A. Zuev and V. G. Popov, *Photoelectric MIS Devices* (Radio i svyaz', Moscow, 1983).

[31] V. I. Fedorov, *Optics of Anisotropic Media* (Izd. Akad. Nauk BSSR, Minsk, 1958).

[32] V. I. Fedorov and V. V. Filippov, *Reflection and Refraction of Light by Transparent Crystals* (Nauka i tekhnika, Minsk, 1976).

[33] G. A. Medvedkin, Author's Abstract of Candidate's Dissertation (A. F. Ioffe Physicotechnical Institute, USSR Academy of Sciences, 1980).

[34] G. A. Medvedkin and Yu. V. Rud', Phys. Status Solidi A **67**, 333 (1981).

[35] P. I. Baranskiĭ, V. P. Klochkov, and I. V. Potykevich, *Handbook of Semiconductor Electronics* (Naukova dumka, Kiev, 1975).

[36] *Handbook of the Physical and Chemical Properties of Semiconductors* (Nauka, Moscow, 1979).

[37] V. V. Sobolev, *Optical Fundamental Spectra of III–V Compounds* (Shtiintsa, Kishinev, 1979).

[38] Yu. V. Rud' and K. Ovezov, Fiz. Tekh. Poluprovodn. **10**, 951 (1976) [Sov. Phys. Semicond. **10**, 561 (1976)].

[39] G. A. Medvedkin and Yu. V. Rud', Pis'ma Zh. Tekh. Fiz. **6**(16), 986 (1980) [Sov. Tech. Phys. Lett. **6**, 760 (1980)].

[40] A. Milnes and D. L. Feucht, *Heterojunctions and Metal-Semiconductor Junctions* [Academic Press, New York, 1972; Mir, Moscow, 1975].

[41] J. I. Pankove, *Optical Processes in Semiconductors* [Prentice-Hall, Englewood Cliffs, NJ, 1971; Mir, Moscow, 1973].

[42] E. V. Buzaneva, *Microstructures of Intergrated Electronics* (Sov. radio, Moscow, 1990).

[43] S. G. Konnikov, D. Melebaev, V. Yu. Rud', and M. Serginov, Pis'ma Zh. Tekh. Fiz. **18**(18), 39 (1992) [Sov. Tech. Phys. Lett. **18**, 382 (1992)].

[44] S. G. Konnikov, G. D. Melebaeva, V. Yu. Rud', and M. Serginov, Pis'ma Zh. Tekh. Fiz. **18**(24), 32 (1992) [Sov. Tech. Phys. Lett. **18**, 806 (1992)].

[45] S. G. Konnikov, D. Melebaev, and V. Yu. Rud', Pis'ma Zh. Tekh. Fiz. **18**(12), 11 (1992) [Sov. Tech. Phys. Lett. **18**, 371 (1992)].

[46] A. Berkeliev, L. M. Kapitonova, D. Melebaev, V. Yu. Rud', M. Serginov, and S. Tilevov, Pis'ma Zh. Tekh. Fiz. **18**(15), 50 (1992) [Sov. Tech. Phys. Lett. **18**, 492 (1992)].

[47] S. G. Konnikov, D. Melebaev, V. Yu. Rud', A. Berkeliev, O. V. Kornyakova, and M. Kh. Rozyeva, Pis'ma Zh. Tekh. Fiz. **19**(2), 8 (1993) [Tech. Phys. Lett. **19**, 39 (1993)].

[48] S. G. Konnikov, D. Melebaev, V. Yu. Rud', A. Berkeliev, M. G. Durdymuradova, and O. V. Kornyakova, Pis'ma Zh. Tekh. Fiz. **19**(4), 57 (1993) [Tech. Phys. Lett. **19**, 124 (1993)].

[49] S. G. Konnikov, D. Melebaev, and Yu. V. Rud', Fiz. Tekh. Poluprovodn. **27**, 761 (1993) [Semiconductors **27**, 416 (1993)].

[50] V. Yu. Rud', Author's Abstract of Condidate's Dissertation (A. F. Ioffe Physicotechnical Institute, Russian Academy of Sciences, St. Petersburg, 1995).

[51] S. G. Konnikov, V. Yu. Rud', Yu. V. Rud', D. Melebaev, A. Berkeliev, M. Serginov, and S. Tilevov, Jpn. J. Appl. Phys. **32**, 515 (1993).

[52] A. Berkeliev, Yu. A. Gol'dberg, D. Melebaev, and B. V. Tsarenkov, Fiz. Tekh. Poluprovodn. **10**, 1532 (1976) [Sov. Phys. Semicond. **10**, 908 (1976)].

[53] G. A. Medvedkin, Yu. V. Rud', and M. A. Tairov, Phys. Status Solidi A **115**, 11 (1989).

[54] S. G. Konnikov, G. D. Melebaeva, D. Melebaev, V. Yu. Rud', Yu. V. Rud', and M. Serginov, Pis'ma Zh. Tekh. Fiz. **19**(2), 1 (1993) [Tech. Phys. Lett. **19**, 37 (1993)].

[55] S. G. Konnikov, D. Melebaev, V. Yu. Rud', Yu. V. Rud', A. Berkeliev, S. Tilevov, and N. N. Faleev, Pis'ma Zh. Tekh. Fiz. **19**(3), 63 (1993) [Tech. Phys. Lett. **19**, 94 (1993)].

[56] M. M. Koltun, *Optics amd Metrology of Sunlight* (Nauka, Moscow, 1985).

[57] O. P. Agnihatri and B. K. Gupta, *Selective Surfaces in Solar Cells* (Mir, Moscow, 1984).

[58] S. G. Konnikov, D. Melebaev, V. Yu. Rud', M. Serginov, S. Tilevov, and Zh. Khanov, Pis'ma Zh. Tekh. Fiz. **18**(24), 11 (1992) [Sov. Tech. Phys. Lett. **18**, 371 (1992)].

[59] V. M. Botnaryuk, A. V. Koval', A. I. Simashkevich, D. A. Shcherban', V. Yu. Rud', and Yu. V. Rud', Fiz. Tekh. Poluprovodn. **31**, 800 (1997) [Semiconductors **31**, 677 (1997)].

[60] V. M. Botnaryuk, L. V. Gorchak, S. D. Raevskiĭ, D. A. Shcherban', V. Yu. Rud', and Yu. V. Rud', Zh. Tekh. Fiz. **68**, 72 (1998) [Tech. Phys. **43**, 546 (1998)].

[61] V. M. Tuchkevich, Fiz. Tekh. Poluprovodn. **11**, 2065 (1977) [Sov. Phys. Semicond. **11**, 1213 (1977)].

[62] J. S. Kasperis, R. S. Yatsko, and P. A. Newman, Technical Report Ecom-2471, VS Army Electronics Command (New Jersey, Fort Monmonth, 1964).

[63] Y. Huber and G. H. Wintstel, Siemens Forsch.-Entwick. Bericht. **2**, 171 (1973).

[64] S. Gonda, Y. Matsushima, S. Mukai, Y. Makita, and O. Igarashi, Jpn. J. Appl. Phys. **17**, 1043 (1978).

[65] H. Mori, M. Ogasawara, M. Yamamoto, and S. Tachigawa, Appl. Phys. Lett. **51**, 1245 (1987).

[66] N. N. Gerasimenko, L. V. Lezheĭko, E. V. Lyubopitnova, L. V. Sharonova, A. G. Sharshunov, A. Ya. Shik, and Yu. V. Shmartsev, Fiz. Tekh. Poluprovodn. **15**, 1088 (1981) [Sov. Phys. Semicond. **15**, 626 (1981)].

[67] L. V. Karlina, E. I. Leonov, L. V. Sharonova, and Yu. V. Shmartsev, Fiz. Tekh. Poluprovodn. **15**, 1202 (1981) [Sov. Phys. Semicond. **15**, 692 (1981)].

[68] Yu. V. Zhilyaev, N. Nazarov, and Yu. V. Rud', Pis'ma Zh. Tekh. Fiz. **19**(8), 44 (1993) [Tech. Phys. Lett. **19**, 491 (1993)].

[69] Yu. V. Zhilyaev, N. Nazarov, V. Yu. Rud', Yu. V. Rud', and L. M. Fedorov, Fiz. Tekh. Poluprovodn. **27**, 1610 (1993) [Semiconductors **27**, 890 (1993)].

[70] Yu. V. Zhilyaev, A. Berkeliev, N. Nazarov, V. Yu. Rud', Yu. V. Rud', and L. M. Fedorov, Pis'ma Zh. Tekh. Fiz. **19**(8), 53 (1993) [Tech. Phys. Lett. **19**, 494 (1993)].

[71] A. Berkeliev, Yu. V. Zhilyaev, N. Nazarov, V. Yu. Rud', and Yu. V. Rud', Fiz. Tekh. Poluprovodn. **28**, 14 (1994) [Semiconductors **28**, 8 (1994)].

[72] Yu. V. Zhilyaev, N. Nazarov, V. Yu. Rud', Yu. V. Rud', and L. M. Fedorov, Fiz. Tekh. Poluprovodn. **28**, 1820 (1994) [Semiconductors **28**, 1006 (1994)].

[73] N. Nazarov, Author's Abstract of Doctoral Dissertation (FTI ANT, Ashgabat, 1994).

[74] Yu. V. Zhilyaev, V. V. Krivolapchuk, N. Nazarov, I. P. Nikitina, N. K. Poletaev, D. V. Sergeev, V. V. Travnikov, and L. M. Fedorov, Fiz. Tekh. Poluprovodn. **24**, 1303 (1990) [Sov. Phys. Semicond. **24**, 819 (1990)].

[75] V. V. Evstropov, Yu. V. Zhilyaev, N. Nazarov, D. V. Sergeev, and L. M. Fedorov, Fiz. Tekh. Poluprovodn. **27**, 668 (1993) [Semiconductors **27**, 369 (1993)].

[76] *Current Topics in Materials Science*, edited by E. Kaldis (Elsevier, North-Holland, 1982).

[77] S. Wagner, J. L. Shay, K. J. Bachmann, and E. Buehler, Appl. Phys. Lett. **20**, 220 (1976).

[78] A. Yoshikawa and Y. Sakai, Solid-State Electron. **20**, 133 (1977).

[79] K. Ito and T. Ohsawa, Jpn. J. Appl. Phys. **14**, 1259 (1975).

[80] V. M. Botnaryuk, L. V. Gorchak, G. N. Grigoreva, M. B. Kagan, T. A. Kozireva, T. L. Lybasherskaya, E. V. Russu, and A. V. Simashkevich, Sol. Energy Mater. **20**, 359 (1990).

[81] V. M. Botnaryuk, L. V. Gorchak, V. N. Pleshka, V. Yu. Rud', and Yu. V. Rud', Fiz. Tekh. Poluprovodn. **31**, 243 (1997) [Semiconductors **31**, 139 (1997)].

[82] V. M. Botnaryuk, L. V. Gorchak, I. I. Diakonu, V. Yu. Rud', and Yu. V. Rud', Fiz. Tekh. Poluprovodn. **32**, 72 (1998) [Semiconductors **32**, 61 (1998)].

[83] Zh. I. Alferov, Fiz. Tekh. Poluprovodn. **11**, 2072 (1977) [Sov. Phys. Semicond. **11**, 1216 (1977)].

[84] Zh. I. Alferov, V. N. Andreev, E. L. Portnoĭ, and N. I. Protasov, Fiz. Tekh. Poluprovodn. **3**, 1324 (1969) [Sov. Phys. Semicond. **3**, 1103 (1969)].

[85] Zh. I. Alferov, V. N. Andreev, N. S. Zimogorova, and D. N. Tret'yakov, Fiz. Tekh. Poluprovodn. **3**, 1373 (1969) [Sov. Phys. Semicond. **3**, 1633 (1969)].

[86] Zh. I. Alferov, Fiz. Tekh. Poluprovodn. **32**, 1 (1998) [Semiconductors **32**, 1 (1998)].

[87] V. M. Andreev, A. B. Kazantsev, V. P. Chvostikov, E. V. Paleeva, V. D. Rumyantsev, and M. Z. Shvarts, in *Proceedings of the 1st WCPEC*, Hawaii, December 5–9, 1994, 2096 (1994).

[88] A. Berdinobatov, N. Nazarov, V. Yu. Rud', Yu. V. Rud', and V. M. Sarkisova, Fiz. Tekh. Poluprovodn. **32**, 714 (1998) [Semiconductors **32**, 642 (1998)].

[89] V. Yu. Rud', *International Opto-Electronics Seminar* (St. Petersburg, 1998), p. 36.

[90] I. N. Sorokin, V. Z. Petrova, Yu. D. Chistyakov, N. R. Angina, and L. E. Gat'ko, Zarubezh. élektron. tekhn., **14**(209), 64 (1979).

[91] A. M. Gabor, J. R. Tuttle, D. S. Albin, M. A. Contreras, R. Noufi, and A. M. Hermann, J. Appl. Phys. **65**, 198 (1994).

[92] L. Stolt, J. Hodstrom, J. Kessler, M. Ruch, K.-O. Velthaus, and H. W. Schock, Appl. Phys. Lett. **62**, 597 (1993).

[93] J. Hodstrom, H. Olsen, M. Bodegard, A. Kylner, L. Stolt, D. Hariskos, M. Ruch, and H. W. Schock, in *Proceedings of the 23rd Photovoltaic Specialists Conference*, Lonisville (1993).

[94] M. Hornung, K. W. Benz, L. Morgulis, D. Schmid, and H. W. Schock, J. Cryst. Growth **154**, 315 (1995).

[95] T. Walter, V. Yu. Rud', Yu. V. Rud', and H. W. Schock, Fiz. Tekh. Poluprovodn. **31**, 806 (1997) [Semiconductors **31**, 681 (1997)].

[96] N. N. Konstantinova, M. A. Magomedov, V. Yu. Rud', and Yu. V. Rud', Fiz. Tekh. Poluprovodn. **26**, 1861 (1992) [Semiconductors **26**, 1043 (1992)].

[97] N. N. Konstantinova, M. A. Magomedov, V. Yu. Rud', and Yu. V. Rud', Jpn. J. Appl. Phys. **32**, 106 (1993).

[98] V. Yu. Rud', Yu. V. Rud', T. Walter, and H. W. Schock, Inst. Phys. Conf. Ser. No 152, Paper presented at the ICTMC-11, Salford, Sept. 8–12, 1997, 1998 IOP Publish. Ltd. (1998), p. 971.

[99] J. A. Thornton and T. C. Lomasson, Sol. Cells **16**, 165 (1986).

[100] L. L. Kazmerskii, M. Hallerst, P. J. Ireland, R. A. Mickelsen, and W. S. Chen, J. Vac. Sci. Technol. **1**, 395 (1983).

[101] V. Yu. Rud', Yu. V. Rud', and H. W. Schock, Int. Conf. Polycryst. Semicond. (Schwäbische Gmünd, Germany, 1998), p. 37.

[102] É. L. Nagaev, *The Physics of Magnetic Semiconductors* (Nauka, Moscow, 1979).

[103] *Magnetic Semiconductors* [Tr. FI AN SSSR (Moscow) **139**, 172 (1982)].

[104] R. N. Bekimbetov, V. D. Prochukhan, Yu. V. Rud', and M. A. Tairov, Fiz. Tekh. Poluprovodn. **21**, 1916 (1987) [Sov. Phys. Semicond. **21**, 1162 (1987)].

[105] R. N. Bekimbetov, V. D. Prochukhan, Yu. V. Rud', and M. A. Tairov, Zh. Tekh. Fiz. **57**, 2403 (1987) [Sov. Phys. Tech. Phys. **32**, 1458 (1987)].

[106] N. N. Ledentsov, V. M. Ustinov, V. A. Shchukin, P. S. Kop'ev, Zh. I. Alferov, and D. Bimberg, Fiz. Tekh. Poluprovodn. **32**, 385 (1998) [Semiconductors **32**, 343 (1998)].

[107] M. G. Mil'vidskiĭ and V. V. Chaldyshev, Fiz. Tekh. Poluprovodn. **32**, 513 (1998) [Semiconductors **32**, 457 (1998)].

[108] L. T. Canham, Appl. Phys. Lett. **57**, 1046 (1990).

[109] M. S. Brandt, H. D. Fachs, and M. Stutzmann, Solid State Commun. **81**, 307 (1992).

[110] E. V. Astrova, A. A. Lebedev, A. D. Remenyuk, V. Yu. Rud', and Yu. V. Rud', Fiz. Tekh. Poluprovodn. **31**, 223 (1997) [Semiconductors **31**, 121 (1997)].

[111] V. Yu. Rud' and Yu. V. Rud', Fiz. Tekh. Poluprovodn. **31**, 247 (1997) [Semiconductors **31**, 143 (1997)].

[112] E. V. Astrova, A. A. Lebedev, A. D. Remenyuk, V. Yu. Rud', and Yu. V. Rud', Thin Solid Films **297**, 129 (1997).

[113] A. A. Lebedev, V. Yu. Rud', Yu. V. Rud', and S. Iida, Inst. Phys. Conf. Ser. **152**, 425 (1998).

[114] S. M. Prokes, Appl. Phys. Lett. **62**, 3224 (1993).

[115] X. H. Yang, T. J. Schmidt, W. Shan, J. J. Song, and B. Goldendery, Appl. Phys. Lett. **66**, 1 (1995).

[116] S. J. Pearton and C. Kuo, MRS Bull. (Feb., 1997), p. 17.

[117] S. Nakamura, MRS Bull. (Feb., 1997), p. 29.

[118] M. S. Shur and M. A. Khun, MRS Bull. (Feb., 1997), p. 44.

[119] V. M. Botnaryuk, V. V. Bel'kov, Yu. V. Zhilyaev, S. D. Raevskiĭ, V. Yu. Rud', Yu. V. Rud', and L. M. Fedorov, Fiz. Tekh. Poluprovodn. **32**, 1206 (1998) [Semiconductors **32**, 1077 (1998)].

[120] V. F. Agekyan, V. I. Ivanov-Omskiĭ, V. N. Knyazevskiĭ, V. Yu. Rud', and Yu. V. Rud', Fiz. Tekh. Poluprovodn. **32**, 1203 (1998) [Semiconductors **32**, 1075 (1998)].

[121] A. Berkeliev, Yu. V. Zhilyaev, N. Nazarov, V. Yu. Rud', Yu. V. Rud', and L. M. Fedorov, Fiz. Tekh. Poluprovodn. **27**, 1623 (1993) [Semiconductors **27**, 897 (1993)].

[122] S. G. Konnikov, G. D. Melebaeva, D. Melebaev, V. Yu. Rud', and Yu. V. Rud', Pis'ma Zh. Tekh. Fiz. **19**(8), 18 (1993) [Tech. Phys. Lett. **19**, 233 (1993)].

[123] D. Melebaev, V. Yu. Rud', and Yu. V. Rud', Cryst. Res. Technol. **31S**, 269 (1996).

[124] A. A. Abdurakhimov and Yu. V. Rud', Pis'ma Zh. Tekh. Fiz. **8**(4), 227 (1982) [Sov. Tech. Phys. Lett. **8**, 99 (1982)].

[125] A. A. Abdurakhimov, Yu. V. Rud', V. E. Skoryukin, and Yu. K. Undalov, Zh. Prikl. Spektrosk. **37**, 463 (1982).

[126] Yu. V. Rud', Jpn. J. Appl. Phys. **32**, 512 (1993).

[127] J. L. Shay and J. H. Wernick, *Ternary Chalcopyrite Semiconductors: Growth, Electronic Properties, and Applications* (Oxford, Pergamon Press, 1975).

[128] G. A. Medvedkin, Yu. V. Rud', and V. E. Skoryukin, Zh. Tekh. Fiz. **52**, 2418 (1982) [Sov. Phys. Tech. Phys. **27**, 1491 (1982)].

Translated by M. E. Alferieff

ATOMIC STRUCTURE AND NON-ELECTRONIC PROPERTIES OF SEMICONDUCTORS

Effect of *in situ* photoexcitation of *n*-type Si as a result of ion implantation at low doses on the formation of radiation defects

M. Yu. Barabanenkov, A. V. Leonov, V. N. Mordkovich, and N. M. Omel'yanovskaya

Institute of Microelectronics Technology and Ultrapure Materials, Russian Academy of Sciences,
142432 Chernogolovka, Russia

(Submitted February 13, 1998; accepted for publication October 8, 1998)
Fiz. Tekh. Poluprovodn. **33**, 537–541 (May 1999)

The effect of *in situ* photoexcitation of the electronic subsystem of a semiconductor as a result of implantation of low ion doses on the formation of complexes of radiation defects in *n*-type Si is investigated by the DLTS method. The *n*-type Si samples were irradiated with 150-keV O_2^+ and N_2^+ ions at the same dose 10^{11} cm^{-2} and Ar$^+$ ions at doses 7×10^{10} and 2×10^{11} cm^{-2}. With the exception of the latter case, the ion energy and dose were chosen so as to produce approximately the same number of initially displaced Si atoms and the same depth distribution of such atoms from the target surface. The temperature of the *n*-type Si samples during irradiation was 300 or 600 K. Photoexcitation of the semiconductor was performed using UV radiation with various power densities. It is shown that radiative heating of the samples during ion implantation suppresses the formation of radiation-defect complexes, while photoexcitation of *n*-type Si, in contrast, intensifies their formation. It is found that the effect of illumination increases with decreasing ion mass and with increasing target temperature. The effect of UV illumination on defect formation in *n*-type Si as a function of sample temperature during ion implantation is established. It is found that the density of divacancies in *n*-type Si saturates with increasing illumination intensity. *© 1999 American Institute of Physics.* [S1063-7826(99)00205-7]

1. INTRODUCTION

It has been shown in a number of studies[1–6] that exposure to UV light of the surface of Si samples irradiated with accelerated ions or electrons changes the character of the accumulation of radiation defects produced in the semiconductor by the particles. Specifically, *in situ* photoexcitation of the electronic subsystem of Si under certain conditions decreases the degree of radiation damage near the surface of the crystal,[2,3] and the effect of the light flux does not reduce simply to additional heating of the target, which gives rise to partial annealing of the simple defects. In Ref. 7 it was established, by comparing the experimental results on ion implantation in doses $10^{13}-10^{14}$ cm^{-2} in *p*-type Si samples at liquid-nitrogen temperature and *n*-type Si samples at room temperature, that the UV produces a nonthermal effect. Rutherford backscattering (RBS) spectra[7] of the accelerated ions show that *in situ* photoexcitation affects most strongly the degree of radiation damage of Si at low temperature (77 K) and that the effect of illumination is substantially weaker for a silicon target at room temperature. This dependence cannot be extended directly to substantially lower doses of implanted ions for at least the following two reasons. In the first place, the character of the radiation damage in Si changes greatly. It is known that an individual ion with moderate mass and kinetic energy in the range 20–160 keV produces in Si either very simple defects[8,9] or microscopic nonamorphous regions of disorder (RD).[10,11] The overlapping of individual RDs, which causes the regions to grow in size and become amorphous, occurs starting at doses $10^{13}-10^{14}$ cm^{-2} (Ref. 10). For this reason, substantially lower implantation doses make it possible to avoid effective accumulation of radiation defects as a result of overlapping of RDs and therefore prevent the formation of anomalously intense sources for nonequilibrium — photogenerated, in the context of our study — charge carriers.[12,13] Secondly, the spectrum of radiation defects in Si irradiated with low ion doses depends on the type of conductivity of Si and the type of ion[14] (of course, a comparison can be made provided that different ions produce the same number of initially displaced target atoms). On this basis it is obvious that for low implantation doses, where there are fewer electrically active defects than dopant atoms, the effect of illumination and of the temperature of *n*- and *p*-Si samples must be studied separately. In this article we report the results of an experimental study of the effectiveness of *in situ* UV illumination during implantation on the formation of complexes of radiation defects in *n*-Si samples held at two different temperatures during implantation of low doses of three different types of ions.

2. EXPERIMENTAL CONDITIONS

The *n*-type Si wafers (KÉF-20, ⟨100⟩) were irradiated with O_2^+ and N_2^+ molecular beams with the same dose

10^{11} cm^{-2} and ion current density 2.5 nA/cm^2 and by Ar$^+$ ions with doses 7×10^{10} and 2×10^{11} cm^{-2} and current density 1 nA/cm^2 with the ions accelerated to 150 keV. Ion implantation was conducted in samples held at room temperature, $T_i=300$ K, or heated to $T_i=600$ K resistively, i.e. using a furnace. Photoexcitation of *n*-Si was performed using a high-pressure mercury lamp. The power density of the light flux on the target surface was 4 mW/cm^2, and for implantation of Ar$^+$ ions high illumination power densities 10, 17, and 25 mW/cm^2 were also used. According to Ref. 1, illumination increases the Si temperature during ion implantation by no more than 15 °C with light power density $W=60$ mW/cm^2. It is assumed, therefore, that illumination with $W\leq25$ mW/cm^2 heats the target hardly at all.

According to calculations[14] using the TRIM code, O_2^+ or N_2^+ and Ar$^+$ ion doses of 10^{11} and 7×10^{10} cm^{-2}, respectively, gave approximately the same number of initially displaced Si atoms ($\sim6\times10^{18}$ cm^{-3}) with essentially the same spatial distributions of the primary defects. Since the ion doses used in our experiments are low, the molecular effect[15] was disregarded in the calculation of the densities of radiation defects produced by accelerated molecular ions. Moreover, low ion current densities allowed us to ignore the dependence of the production rate of radiation defects in Si on the dose accumulation rate (see, for example, Ref. 16).

The degree of compensation of the irradiated Si layer by radiation defects was determined by the method of capacitance–voltage measurements. No shift was observed, to within the 10–15% accuracy of this method, in the lower plateau of the capacitance–voltage characteristics of the test samples. This shows that the change in the density of the majority charge carriers is small. Correspondingly, the density of electrically active defects in the irradiated samples did not exceed 15% of the dopant density (2×10^{14} cm^{-3} for KÉF-20); i.e., it did not exceed 3×10^{13} cm^{-3}.

The parameters of the deep levels produced by radiation defects were determined by deep-level transient spectroscopy (DLTS). For the measurements, Schottky barriers were produced on the front side of the irradiated samples by vacuum thermal sputtering of Au and ohmic contacts were produced on the backside. The DLTS spectra were measured with a -2 V constant reverse bias and a $+2$ V carrier pulse amplitude. In the text below and in the DLTS spectra the peaks E_1 ($E_c-0.18$ eV), E_2 ($E_c-0.46$ eV), and E_3 ($E_c-0.5$ eV) are due to the formation of *A* centers (E_1), divacancies (E_2), and multivacancy complexes (E_3).

3. EXPERIMENTAL RESULTS AND DISCUSSION

The DLTS spectra of *n*-type Si samples irradiated with Ar$^+$ ions at room temperature (curve *1*) and at 600 K (curve *2*) are shown in Fig. 1. The normalized values of the divacancy density (the peak E_2) in *n*-Si irradiated with O_2^+ and N_2^+ ions are presented in Table I. We recall that in the latter case a single peak E_2 is observed in the DLTS spectra.[14] It follows from these data that the increase in the temperature of the samples during ion implantation (T_i) results in a decrease in the amplitude of the peak E_2 in the DLTS spectra obtained for these samples, signifying a decrease in the density of divacancy complexes.

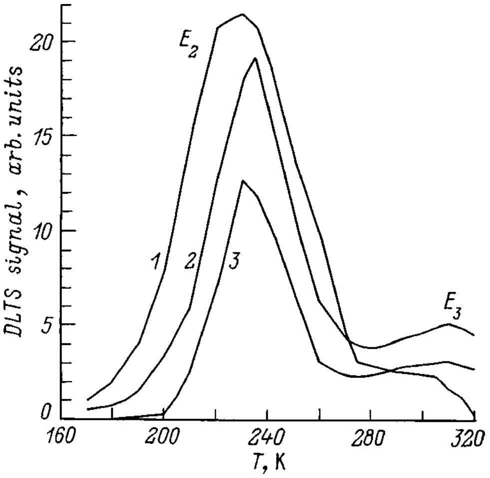

FIG. 1. DLTS spectra of *n*-type Si samples implanted with 150-keV Ar$^+$ ions with dose 7×10^{10} cm^{-2} at temperatures $T_i=300$ (*1*), 600 K (*2*), and 600 K with *in situ* illumination (*3*).

Photoexcitation of *n*-Si was found to have an effect opposite to that of heating. Comparison of curves *2* and *3* in Fig. 1 (Ar$^+$ ion implantation) and the data in Table I (N_2^+ and O_2^+ ions) shows that illumination of the samples during implantation of different ions increases the peaks in the corresponding spectra.

We note that for implantation of O_2^+ ions the amplitudes of the E_1 and E_3 peaks, just like the amplitude of the E_2 peak, in the DLTS spectra depend on the experimental conditions (heating or illumination of the target). However, as one can see from Fig. 1 (compare curves *1* and *2*), the increase in the temperature of Si during the implantation of Ar$^+$ results in an increase in the amplitude of the peak E_3 (though by a small amount) against the background of a decrease in the E_2 peak.

The effectiveness of the influence of temperature and *in situ* photoexcitation of *n*-Si samples on the accumulation of radiation defects in their interior volume during ion implantation can be judged from Figs. 2 and 3. These figures show that amplitude ratio of the E_2 peaks, which have changed the most under the action of temperature and light, as a function of the mass *M* of the ion bombarding the silicon. Curve *1* in Fig. 2 shows that for ''dark'' implantation the difference arising in the density of secondary defects as a result of the different sample temperatures during irradiation decreases

TABLE I. Ratio of the divacancy density (E_2 peak) to the electron density in *n*-type Si irradiated with 150-keV N_2^+ and O_2^+ ions with dose 10^{11} cm^{-2}.

		E_2	
T_i, K	W, mW/cm^2	N_2^+	O_2^+
300	0	0.102	0.062
	4	0.174	0.091
600	0	0.032	0.025
	4	0.32	0.060

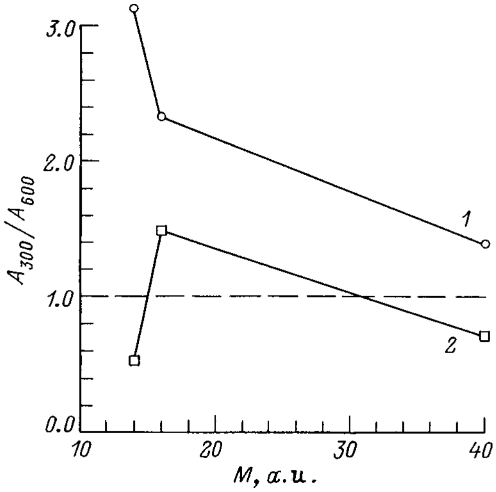

FIG. 2. Amplitude ratio of the E_2 peaks in the spectra of *n*-Si samples corresponding to temperatures 300 (A_{300}) and 600 K (A_{600}) versus the ion mass *M*. *1* — Dark implantation, *2* — implantation with photoexcitation of silicon.

monotonically with increasing ion mass, i.e. $A_{300}/A_{600}\rightarrow 1$. Here A_{T_i} is the amplitude of the E_2 peak in the DLTS spectrum of the sample irradiated at the corresponding absolute temperature T_i. Under photoexcitation conditions with increasing target temperature (see curve *2* in Fig. 2) the amplitude of the E_2 peak increases with the implantation of N_2^+ and Ar^+ and decreases with the implantation of O_2^+.

In Fig. 3 the amplitude ratio of the E_2 peaks during photoexcitation (A_{light}) and in the absence of photoexcitation (A_{dark}) is plotted along the ordinate. Comparison of curves *1* and *2* in this figure shows that photoexcitation acts most effectively on the formation of secondary defects at a high target temperature (in Fig. 3 curve *2* lies above curve *1*). Moreover, as the ion mass increases, i.e. as the linear density of generation of point defects increases (N^+ or O^+ ions produce ~0.2 displacements/ion ·Å, while Ar^+ ions produce four times more displacements[14]) with the same total number of ions, the effectiveness of UV irradiation decreases irrespective of the temperature of the *n*-Si samples.

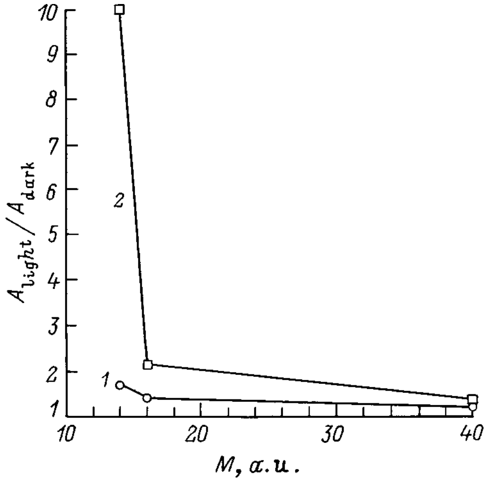

FIG. 3. Amplitude ratio of the E_2 peaks in the spectra of *n*-type Si samples with implantation and photoexcitation of the silicon (A_{light}) and with dark implantation (A_{dark}). Implantation temperature T_i, K: *1* — 300, *2* — 600.

The following should be noted with regard to Figs. 2 and 3. First, in these figures the masses of the O^+ and N^+ ions, rather than the masses of the molecular ions, are plotted along the abscissa, following the conventional assumption that molecular ions decompose over a path on the order of several lattice constants of the irradiated crystal. Secondly, the left-most points (curves *2*), which correspond in both figures to the implantation of N_2^+ ions, are separated well from the other two points which represent the implantation of O_2^+ and Ar^+ ions. Clearly, this difference stems from the fact that upon implantation of N_2^+ ions in small doses, divacancies are basically the only type of radiation-defect complexes encountered here.[14] The amplitude of the E_2 peak in the DLTS spectrum, which corresponds to them, is much larger than the amplitude of the same peak in the analogous spectra of *n*-Si samples implanted with O_2^+ and Ar^+ ions. For this reason, even the change produced in the amplitude of the peak by UV illumination of silicon (Fig. 2) or by heating of the silicon (Fig. 3) as a result of bombardment by nitrogen ions is greater than the change in the same peak in the spectra of *n*-Si samples implanted with either of the other two ions.

As shown above, photoexcitation of *n*-Si becomes ineffective for higher-density cascades of atomic collisions produced by the ion stopping in the crystal with a fixed total number of primary radiation defects introduced by these ions. For example, illumination of *n*-Si has virtually no effect on the amplitude of the divacancy peak even for Ar^+ ions (see Fig. 3). However, as the argon ion dose increases to 2×10^{11} cm^{-2}, the effect of photoexcitation of the semiconductor again becomes appreciable. Specifically, the E_2 peak in the DLTS spectrum of silicon irradiated at room temperature in the presence of illumination is 1.8 times greater than the same peak in the spectrum of Si implanted with ions with no illumination.

The density of radiation-defect complexes depends on the UV illumination intensity. This dependence is shown in Fig. 4 for implantation of Ar^+ ions with dose 7×10^{10} cm^{-2}: the increase in the divacancy density starts to decrease substantially at $W\sim 10$ mW/cm^2 and approaches zero as the light power density increases further. At the same time, the change in the density of *A* centers (Fig. 4, curve *2*) and multivacancy complexes (Fig. 4, curve *3*) is of a different character: this pair of curves is virtually symmetric with respect to a line which is parallel to the abscissa and which intersects the ordinate at the point corresponding to the half-sum of the amplitudes of the E_1 and E_3 peaks. If the vacancy nature of both types of defects is taken into account, it is obvious that the change in the illumination intensity determines the change in the number of elementary vacancies minus the vacancies which are used in the formation of divacancies which are needed to form the *A* centers and multivacancy clusters.

The results in Fig. 4 thus show that the process leading to the formation of defect complexes can be controlled directly at the stage of relaxation of cascades of atomic dis-

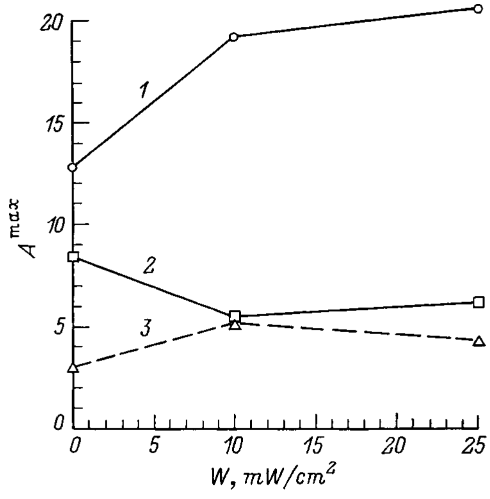

FIG. 4. Amplitudes ($A^{\max}$) of the divacancy E_2 (*1*), *A*-center E_1 (*2*), and multivacancy-complex E_3 (*3*) peaks in the DLTS spectra of *n*-type Si samples implanted with 150-keV Ar^+ ions with dose $7\times10^{10}\ \mathrm{cm}^{-2}$ at $T_i=600$ K versus the UV illumination power density.

placements by adjusting the intensity of photoexcitation of *n*-Si irradiated with ions.

Finally, we wish to make two points. First, returning to the results of Ref. 7, which are described in the introduction, and comparing them with the results of our study, we can draw the following conclusion. The action of UV illumination is nonmonotonic with respect to the dose of implanted ions: at low doses ($\sim10^{11}\ \mathrm{cm}^{-2}$) illumination of *n*-Si increases the yield of the reaction leading to the formation of divacancies, whereas at higher doses ($\sim10^{13}-10^{14}\ \mathrm{cm}^{-2}$), in contrast, it suppresses the yield. Secondly, the results presented here show that the action of resistive heating and photoexcitation of *n*-Si on the formation of divacancy complexes during ion implantation is additive to some extent. When the sample temperature is raised to 600 K, the amplitude of the E_2 peak in the DLTS spectrum of this sample decreases (see, for example, curves *1* and *2* in Fig. 1). At the same time, photoexcitation of the heated sample during ion implantation increases the amplitude of the E_2 peak almost to the value characteristic of *n*-type Si implanted at room temperature (see curves *2* and *3* in Fig. 1).

4. CONCLUSIONS

In our study we established that for implantation of low doses ($\sim10^{11}\ \mathrm{cm}^{-2}$) of nitrogen, oxygen, or argon ions in *n*-Si (1) the effect of *in situ* photoexcitation and resistive heating of a semiconductor on the formation of radiation-defect complexes does not depend on the type of implanted ions, (2) resistive heating of *n*-Si to 600 K during ion implantation decreases the density of secondary defects, while photoexcitation of the electronic subsystem of the semiconductor with UV radiation, in contrast, stimulates their production, (3) the action of UV illumination on the formation of secondary radiation defects is stronger at higher sample temperature, (4) irrespective of the temperature of *n*-Si ($T_i=300$ or 600 K), the effect of UV illumination decreases with increasing mass of the implanted ions, (5) the curve of the divacancy density versus the UV illumination intensity saturates with increasing light intensity, and (6) for irradiation of *n*-Si with Ar^+ ions the densities of *A* centers, divacancies, and multivacancy complexes can be changed by changing the intensity of the UV illumination of the semiconductor during ion implantation.

This work was supported in part by the program ''Physics of Solid-State Nanostructures'' (Project N97-1063).

[1] Yu. N. Erokhin, A. G. Ital'yantsev, and V. N. Mordkovich, Pis'ma Zh. Tekh. Fiz. **14**, 835 (1988) [Sov. Tech. Phys. Lett. **14**, 372 (1988)].

[2] A. B. Danilin, Yu. N. Erokhin, and V. N. Mordkovich, Pis'ma Zh. Tekh. Fiz. **15**, 1 (1989) [Sov. Tech. Phys. Lett. **15**, 829 (1989)].

[3] A. B. Danilin, Yu. N. Erokhin, and V. N. Mordkovich, Nucl. Instrum. Methods Phys. Res. B **59/60**, 985 (1991).

[4] S. N. Boldyrev, V. N. Mordkovich, N. M. Omel'yanovskaya, O. V. Feklisova, and N. Ya. Yarykin, Fiz. Tekh. Poluprovodn. **28**, 1826 (1994) [Semiconductors **28**, 1008 (1994)].

[5] S. N. Boldyrev, V. N. Mordkovich, and N. M. Omelyanovskaya, Phys. Status Solidi A **143**, K71 (1994).

[6] Yu. N. Erokhin, A. G. Ital'yantsev, A. A. Malinin, and V. N. Mordkovich, Radiat. Eff. Defects Solids **128**, 187 (1994).

[7] A. B. Danilin, Yu. N. Erokhin, V. N. Mordkovich, N. Hatzopoulos, and P. L. F. Hemment, Nucl. Instrum. Methods Phys. Res. B **69**, 268 (1992).

[8] K. L. Brower and W. Beezhold, J. Appl. Phys. **43**, 3499 (1972).

[9] N. N. Gerasimenko, A. V. Dvurechenskiĭ, and G. P. Lebedev, Fiz. Tekh. Poluprovodn. **7**, 2297 (1973) [Sov. Phys. Semicond. **7**, 1530 (1973)].

[10] J. A. Davis, J. Denhartog, L. Ericsson, and J. Meier, in *Ion Implantation Doping of Semiconductors* (Mir, Moscow, 1971, p. 273).

[11] I. H. Wilson, H. J. Zheng, U. Knipping, and I. S. T. Tsong, Phys. Rev. B **38**, 8444 (1988).

[12] I. V. Antonova and S. S. Shaĭmeev, Fiz. Tekh. Poluprovodn. **29**, 605 (1995) [Semiconductors **29**, 315 (1995)].

[13] A. I. Baranov and L. S. Smirnov, Fiz. Tekh. Poluprovodn. **7**, 2227 (1973) [Sov. Phys. Semicond. **7**, 1752 (1973)].

[14] M. Yu. Barabanenko, A. V. Leonov, V. N. Mordkovich, and N. M. Omel'yanovskaya, Fiz. Tekh. Poluprovodn. **32**, 523 (1998) [Semiconductors **32**, 466 (1998)].

[15] I. A. Abroyan and L. M. Nikulina, Fiz. Tekh. Poluprovodn. **30**, 1893 (1996) [Semiconductors **30**, 990 (1996)].

[16] I. N. Gerasimenko, B. A. Zaĭtsev, V. I. Panov, L. S. Smirnov, and E. G. Tishkovskiĭ, Fiz. Tekh. Poluprovodn. **7**, 1433 (1973) [Sov. Phys. Semicond. **7**, 960 (1973)].

Translated by M. E. Alferieff

Effect of the irradiation intensity on the efficiency of the production radiation defects in *n*- and *p*-type Si crystals

T. A. Pagava and Z. V. Basheleishvili

Georgian Technical University, 380075, Tbilisi, Georgia

(Submitted September 14, 1998; accepted for publication October 8, 1998)
Fiz. Tekh. Poluprovodn. **33**, 542–543 (May 1999)

The effect of the electron flux density φ on the efficiency η of the production of radiation defects in *n*- and *p*-type Si samples is investigated. It is shown that the application of an electric field to the sample during irradiation affects $\varphi(\eta)$ only in *n*-type Si crystals. This is explained by the charge state of Frenkel pairs at the moment of formation at low irradiation energies. [S1063-7826(99)00305-1]

The reason why the irradiation flux density φ affects the production efficiency η of radiation defects has still not been determined. Experimental studies of silicon and germanium single crystals irradiated with fast electrons or γ rays either have been able to observe the existence of such an effect or it was not observed. The quantities η_A, η_E, and η_{V_2} in *n*-type silicon were found to vary nonmonotonically.[1] In Ref. 2 it was assumed that the observed dependences are due to the effect of φ on the rate of annihilation of primary defects and not on secondary processes.

In Ref. 3 it was assumed that the dependence of η_A on φ is due to secondary processes — a change in the rate of capture of vacancies by oxygen as a result of a change in the charge density of the vacancies.

In Ref. 4 it was concluded that the existence of a dependence $\eta_A(\varphi)$ is due to a change in the probability of annihilation of interstitial atoms by intrinsic vacancies as φ changes.

In Ref. 5 it was found that there exists a critical value φ_c which separates the region where such a dependence exists from the region where η_A is independent of φ ($\varphi_c = 5 \times 10^{12}$ cm$^{-2}\cdot$s^{-1}).

In the present work we investigated *n*- and *p*-type silicon samples obtained by zone melting and doped with phosphorus and boron, respectively, to the same density $\sim 6 \times 10^{13}$ cm^{-3}. The oxygen content in the samples was $\sim 2 \times 10^{16}$ cm^{-3}. and the density of growth dislocations did not exceed $\sim 10^3 - 10^4$ cm^{-2}. The samples were irradiated with 2-MeV electrons.

The investigations were performed by the method of local irradiation followed by measurement of the bulk photovoltage (U_{ph}) along the irradiated region of the sample. This method is described in detail in Ref. 6.

It is known that $U_{\text{ph}} \sim \partial\rho/\partial x$, and the gradient $\partial\rho$ of the

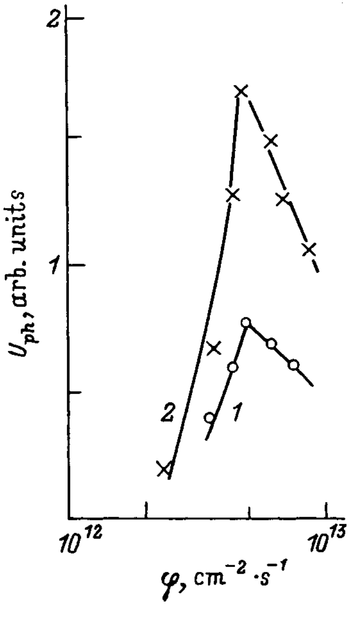

FIG. 1. Volume photovoltage versus the electron flux density in *n*-type silicon crystals; *1* — $E=0$, *2* — $E=110$ V/cm.

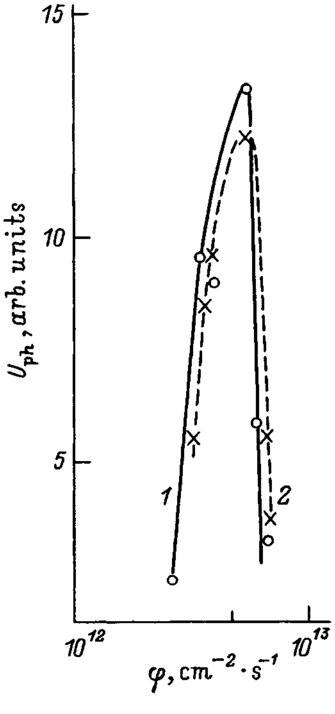

FIG. 2. Volume photovoltage versus the electron flux density in *p*-type silicon crystals; *1* — $E=0$, *2* — $E=110$ V/cm.

resistivity depends not only on the density of *A* centers but also on the total concentration of a wide spectrum of defects.

In *n*-type Si samples U_{ph} increases in a definite range of φ $((2-5)\times 10^{12}\ \mathrm{cm}^{-2}\cdot \mathrm{s}^{-1})$ (Fig. 1, curve *1*). This shows that in contrast to *A* centers[5] η for other radiation defects sharply increases in this interval, passes through a maximum at $\varphi_c = 5\times 10^{12}\ \mathrm{cm}^{-2}\cdot \mathrm{s}^{-1}$, and then sharply decreases.

The application of an electric field ($E=110$ V/cm) to the samples during irradiation does not change the value of φ_c, and the curve $U_{\mathrm{ph}}(\varphi)$ shifts in the direction of large values of U_{ph} (Fig. 1, curve *2*).

In *p*-type Si samples, the dependence $U_{\mathrm{ph}}(\varphi)$ and the value of φ_c remain the same (Fig. 2). The curves $U_{\mathrm{ph}}(\varphi)$ for samples irradiated with and without an external electric field are virtually identical.

As known from Ref. 6, in *n*-Si crystals vacancies are negatively charged at the moment of formation and interstitial atoms are positively charged. In *p*-Si crystals Frenkel pairs are positively charged.[7]

As one can see from the experimental data, the application of an electric field to the sample during irradiation influences $U_{\mathrm{ph}}(\varphi)$ not only in *n*-type Si samples. This shows that at low irradiation energies the charge state of the primary radiation defects must be taken into account in order to explain the observed behavior.

[1] P. F. Lugakov and V. V. Luk'yanitsa, Fiz. Tekh. Poluprovodn. **18**, 345 (1984) [Sov. Phys. Semicond. **18**, 215 (1984)].

[2] V. I. Kozhevnikov and V. V. Mikhnevich, Fiz. Tekh. Poluprovodn. **15**, 1598 (1981) [Sov. Phys. Semicond. **15**, 924 (1981)].

[3] J. S. Blakemore, *Semiconductor Statistics* (Pergamon Press, New York, 1962).

[4] J. W. Corbett and G. D. Watkins, Phys. Rev. **138**, 555 (1965).

[5] A. A. Zolotukhin, A. K. Kovalenko, T. M. Meshcheryakova, L. S. Milevskiĭ, and T. A. Pagava, Fiz. Tekh. Poluprovodn. **9**, 1201 (1975) [Sov. Phys. Semicond. **9**, 800 (1975)].

[6] L. S. Milevskiĭ and V. S. Garnyk, Fiz. Tekh. Poluprovodn. **13**, 1369 (1979) [Sov. Phys. Semicond. **13**, 801 (1979)].

[7] Z. V. Basheleishvili, T. L. Bzhalava, T. A. Pagava, and V. V. Sanadze, Soorshch. Akad. Nauk GSSR, Fiz. **116**, 297 (1984).

Translated by M. E. Alferieff

Spontaneously forming periodic composition-modulated InGaAsP structures

N. A. Bert, L. S. Vavilova, I. P. Ipatova, V. A. Kapitonov, A. V. Murashova, N. A. Pikhtin,
A. A. Sitnikova, I. S. Tarasov,*) and V. A. Shchukin

A. F. Ioffe Physicotechnical Institute, Russian Academy of Sciences, 194021 St. Petersburg, Russia

(Submitted October 23, 1998; accepted for publication November 2, 1998)
Fiz. Tekh. Poluprovodn. **33**, 544–548 (May 1999)

InGaAsP epitaxial layers, which are obtained in the instability region on InP (001) and GaAs (001) substrates, are investigated by photoluminescence and transmission-electron-microscopy methods. The results are discussed on the basis of the theory of spinodal decomposition of solid solutions. It is established experimentally that in certain temperature and composition ranges the solid solutions InGaAsP are a system of charged, alternating (in mutually perpendicular directions [100] and [010]) domains of a solid solution with two different compositions and different lattice constants. The domain structure is very clearly defined at the surface of the epitaxial film and becomes blurred in the film near the substrate. The data obtained very likely show spinodal decomposition of the solid solutions InGaAsP in the test samples. © *1999 American Institute of Physics.* [S1063-7826(99)00405-6]

1. INTRODUCTION

Experimental studies (see, for example, Ref. 1) have shown that in certain temperature and composition ranges homogeneous solid solutions of semiconductors based on III–V compounds are unstable and decompose into periodic structures with alternating composition. The first experimental studies of this subject were of an accidental character, since their main goal was to obtain a stable homogeneous solid solution. The latest investigations of the instability of solid solutions suggest that this phenomenon can be used to obtain spontaneously forming nanoheterostructures.

To describe this instability of multicomponent solid solutions Stringfellow[2] employed the theory of spinodal decomposition[3,4] developed for metal alloys. A similar analysis of the instability of quaternary solid solutions[5] has been performed using the model of regular solid solutions.[6] This made it possible to obtain more realistic values of the critical decomposition temperatures.

Our work[7–10] on the photoluminescence and x-ray microstructural properties of the solid solutions InGaAsP in the instability region made it possible to demonstrate agreement between the experimental results and the proposed theory.

In the present paper we make a detailed comparison of the results of theoretical and experimental studies of the quaternary solid solutions InGaAsP in the instability region. The experimental samples were obtained by liquid epitaxy on InP (001) and GaAs (001) substrates under technological conditions that stimulate spinodal decomposition.

2. THEORY

Solid solutions of semiconductors are disordered systems in which the composition fluctuates from point to point. For a quaternary solid solution of the type $A_{1-x}B_xC_{1-y}D_y$ such fluctuations are $\delta x(\mathbf{r})$ and $\delta y(\mathbf{r})$, determined by the relations $x(\mathbf{r})=\bar{x}+\delta x(\mathbf{r})$ and $y(\mathbf{r})=\bar{y}+\delta y(\mathbf{r})$, where $\bar{x}$ and $\bar{y}$ correspond to the average composition. A homogeneous solid solution decomposes into a composition-modulated periodic structure as a result of instability with respect to composition fluctuations. Instability means that the free energy of the modulated solid solution with such a composition is less than the free energy of a homogeneous solid solution with a composition corresponding to $\bar{x}+\bar{y}$.

The change produced in the chemical free energy as a result of fluctuations of the composition of the solid solution can be written as

$$\delta F_{\text{chem}}=\int \{[H(x(\mathbf{r}),y(\mathbf{r}))-TS_{\text{mix}}(x(\mathbf{r}),y(\mathbf{r}))] - [H(\bar{x},\bar{y})-TS_{\text{mix}}(\bar{x},\bar{y})]\}dV. \tag{1}$$

Here $H(x(\mathbf{r}),y(\mathbf{r}))$ is the enthalpy of the system, $S_{\text{mix}}(x(\mathbf{r}),y(\mathbf{r}))$ is the mixing entropy, and T is the temperature. A homogeneous solid solution is unstable when the formation enthalpy of the solid solution $A_{1-x}B_xC_{1-y}D_y$ from the binary components AC, AD, BC, and BD is positive, i.e. when the difference

$$\Delta H=(1-x)(1-y)H_{\text{AC}}+(1-x)yH_{\text{AD}}+x(1-y)H_{BC} +xyH_{\text{BD}}-H_{\text{multi}} \tag{2}$$

is positive. Here the sum of the first four terms is the enthalpy of a homogeneous solid solution, and H_{multi} is the enthalpy of a multiphase system. This means that a certain amount of energy must be expended to produce a homogeneous solid solution. At $T=0$ the free energy of a composition-modulated mixture of the pure materials AC, AD, BC, and BD is less than that of the uniform solid solution $A_{1-x}B_xC_{1-y}D_y$. At $T\neq 0$ the contribution of the mixing entropy S_{mix} to the free energy gives rise to mixing of the components and stabilizes the homogeneous solid solution, despite the composition fluctuations $\delta x(\mathbf{r})$ and $\delta y(\mathbf{r})$. In addition, according to Vegard's rule, the lattice constant of the solid solution depends on its composition

$$a(\mathbf{r})=a[x(\mathbf{r}),y(\mathbf{r})]. \tag{3}$$

As a result of the composition fluctuations $\delta x(\mathbf{r})$ and $\delta y(\mathbf{r})$, the lattice constant is different in different regions of the solid solution. Joining of the regions requires elastic deformation of the medium, which possesses a corresponding elastic free energy $\delta F_{\rm el}$. In a homogeneous solid solution the elastic free energy due to the composition fluctuations is zero — $\delta F_{\rm el}=0$, while in an inhomogeneous solution $\delta F_{\rm el}>0$. This elastic energy also stabilizes a solid solution with composition $\overline{x}$ and $\overline{y}$. Since the chemical energies of the mixed components AC, AD, BC, and BD are close, the change $\delta F_{\rm chem}$ in the chemical energy on mixing is small, comparable in magnitude to the elastic energy $\delta F_{\rm el}$. This is why the ratio of the chemical energy, which contains the mixing entropy, and the elastic energy plays a determining role in the formation of a modulated structure. The change in the total free energy of a system whose stability is to be analyzed consists of the chemical contribution (1) and the elastic free energy

$$\delta F=\delta F_{\rm chem}+\delta F_{\rm el}. \tag{4}$$

An investigation[2,5] of the stability of a quaternary solid solution of the type $A_{1-x}B_xC_{1-y}D_y$ showed that at temperatures above a critical temperature, $T>T_c$, quaternary solid solutions are stable for any values of x and y; i.e., the contribution of the mixing entropy $S_{\rm mix}$ is so large that the composition fluctuations cannot decrease the total free energy. At temperatures $T<T_c$ there exists a region of compositions where a homogeneous solid solution is absolutely unstable, i.e., it is unstable even with respect to infinitesimal composition fluctuations $\delta x(\mathbf{r})$ and $\delta y(\mathbf{r})$, which decrease the chemical free energy. The composition fluctuations $\delta x(\mathbf{r})$ and $\delta y(\mathbf{r})$ in a solid solution are the order parameter of spinodal decomposition.

Figure 1 shows a composition diagram for InGaAsP. The diagram shows regions of absolutely unstable (*1*), metastable (*2*), and stable (*3*) solid solutions, calculated at $T=900$ K (Ref. 12). Solid solutions belonging to the region of metastable states are unstable with respect to composition fluctuations with finite amplitude.

In Refs. 2, 5, 11, and 12 it is shown that the final state of a thermodynamic phase transition is a system of stressed, i.e. compressed and stretched, layers with alternating composition, which are called elastic concentration domains. This system of layers is formed by an inelastic ''soft mode'' (composition fluctuation) with wave vector parallel to the direction of the weakest compression. In III–V semiconductors, as a result of the elastic anisotropy of the crystal, these directions are [001], [010], and [100]. Such an orientation of the elastic domains, which is observed in the experimental samples, very likely indicates the possibility of spinodal decomposition of the solid solution.

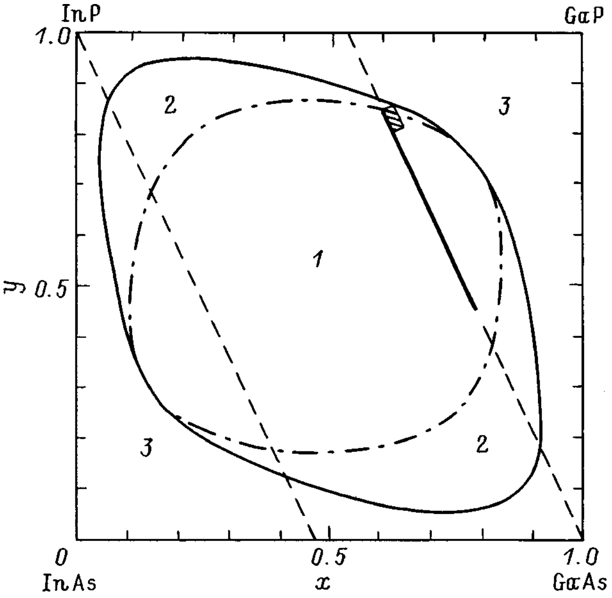

FIG. 1. Composition diagram for the solid solution $In_{1-x}Ga_xAs_{1-y}P_y$. The dashed straight lines show the solid solutions InGaAsP, isoperiodic to the substrates InP (001) and GaAs (001). Calculation at $T=900$ K (Ref. 12): *1* — region of absolutely unstable solid solutions; *2* — region of metastable solid solutions; *3* — region of absolutely stable solid solutions. Two regions of spinodal decomposition, which were experimentally determined for InGaAsP samples grown at temperatures $T_g=1023$ K (Ref. 10) (solid segment) and $T_g=1063$ K (Ref. 16)(hatched segment) are shown on the straight line of the solid solutions isoperiodic with GaAs (001).

To bring the analysis closer to a real object, in Refs. 13–15 the stability of epitaxial films of the solid solution $A_{1-x}B_xC$, coherently joined with the (001) substrate consisting of a cubic crystal, was investigated. In this case the soft mode is a surface soft mode, whose amplitude is maximum near the growing surface and decreases exponentially into the volume of the film (z direction). The theoretically computed equilibrium composition profile of an epitaxial film for the solid solution $A_{1-x}B_xC$ is shown in Fig. 2. Since there are no elastic stresses on the freely growing surface, the elastic energy of the soft mode ($F_{\rm el}^{\rm film}$) is ~1/3 of the volume elastic energy ($F_{\rm el}^{\rm vol}$):

$$F_{\rm el}^{\rm film}=\frac{C_{11}}{2(C_{11}+C_{12})}F_{\rm el}^{\rm vol}\approx\frac{1}{3}F_{\rm el}^{\rm vol}. \tag{5}$$

The critical temperatures of the spinodal decomposition of the films of quaternary solid solutions are therefore less than the critical decomposition temperatures of bulk crystals and lie in the range 400–1200 K. This corresponds to real growth

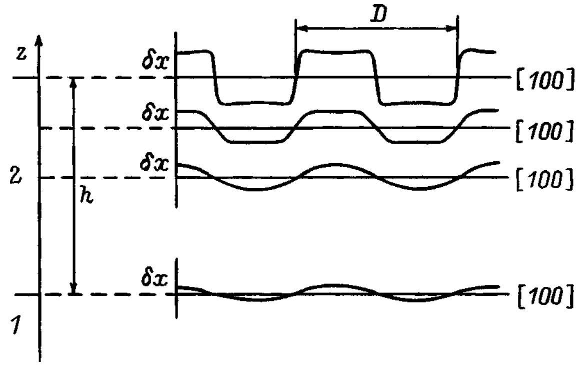

FIG. 2. Theoretically computed equilibrium composition profile of the solid solution $A_{1-x}B_xC$ in an epitaxial film (*2*) on the substrate (*1*). D — composition modulation period; h — epitaxial film thickness.

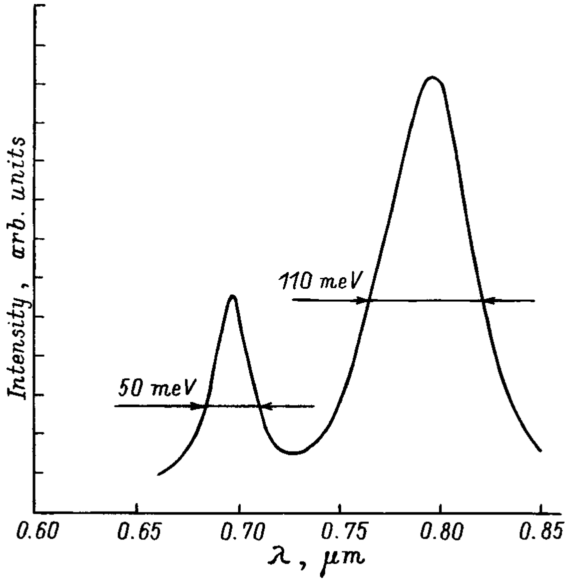

FIG. 3. Photoluminescence spectrum at 300 K of an epitaxial InGaAsP layer grown on a GaAs substrate in the region of unstable quaternary solid solutions.

and decomposition temperatures of epitaxial films of III–V solid solutions (the computed value of T_c for the solid solutions InGaAsP is[12] 1275 K).

3. EXPERIMENTS

In Refs. 7–10, which are devoted to photoluminescence and x-ray microstructural investigations, the boundaries of existence of the region of spinodal decomposition were determined for the solid solutions InGaAsP which are isoperiodic with the substrates InP (001) and GaAs (001). The epitaxial InGaAsP layers, prepared by liquid epitaxy at growth temperatures below the critical temperature ($T_g < T_c$), have in the region of spinodal decomposition a characteristic photoluminescence (PL) spectrum consisting of two bands. As an example, such a spectrum is presented in Fig. 3 for an InGaAsP sample grown on a GaAs (001) substrate at temperature $T_g = 1023$ K. The existence of the two bands in the PL spectra of such samples suggests that the epitaxial layer is inhomogeneous and consists of two solid solutions with different compositions. Those samples were investigated using transmission electron microscopy (TEM). Figure 4a shows a typical image of such a sample in diffraction contrast in a TEM investigation in a planar geometry. Here the intensity modulation is observed in the mutually perpendicular directions [100] and [010], which correspond to the directions of the weakest compression of the cubic crystal, which is an indication of the possibility of spinodal decomposition of the solid solution. The epitaxial InGaAsP layers grown in the region of absolutely stable solid solutions have one peak in the PL spectra. Periodic modulation of the intensity is not observed in the corresponding TEM images of these samples. These two facts show that such epitaxial InGaAsP layers are homogeneous solid solutions.

Figure 1 shows two experimentally determined regions of spinodal decomposition of the solid solutions InGaAsP, which are isoperiodic with GaAs (001) and were grown at temperatures $T_g = 1023$ K (Ref. 10) and 1063 K (Ref. 16). Increasing the growth temperature substantially decreases the region of compositions of the solid solutions InGaAsP which have (first) two bands in the PL spectra (Fig. 3) and (second) a periodic TEM pattern of intensity modulation (Fig. 4a). This shows that the growth temperature is close to the critical temperature of spinodal decomposition.

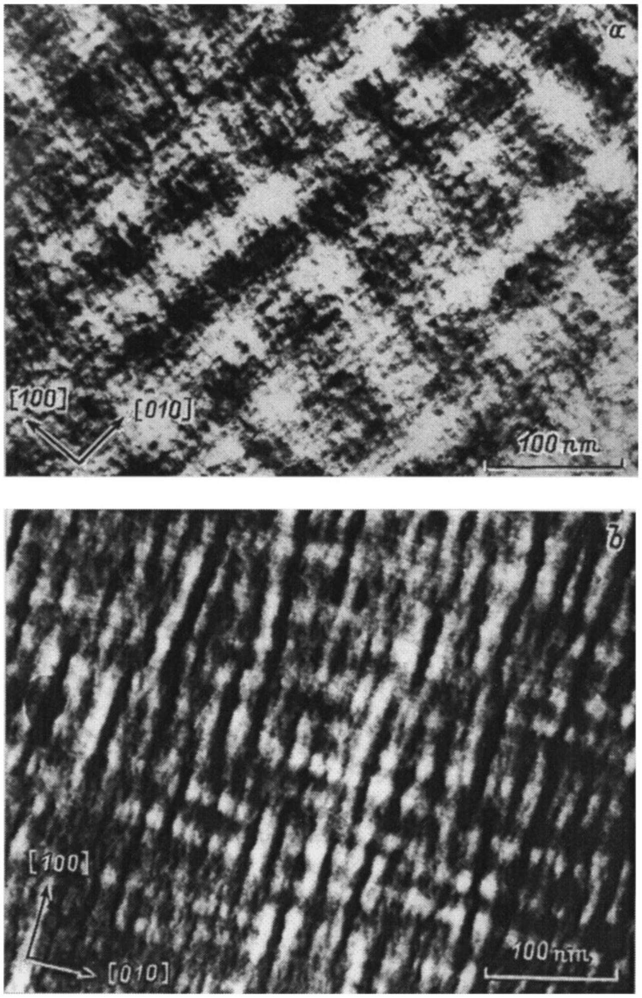

FIG. 4. TEM images of an InGaAsP sample. The images were obtained in planar geometry in the reflections: a — 200 (sensitive to the composition of the solid solution); b — 220 (sensitive to the stresses in the sample). The InGaAsP epitaxial layer was grown on an InP (001) substrate in the region of instability of the solid solutions with $T_g = 867$ K.

TEM investigations in a planar geometry of InGaAsP/InP (001) epitaxial layers grown in the instability region established the presence of elastic stresses at the boundaries of regions with different compositions. The samples were investigated in two reflections — 220 and 200. The image in Fig. 4b was obtained in the 220 reflection, where the contrast reflects local deviations from Bragg conditions in regions where the structure is enriched with and depleted of the atoms of the heavier element, as well as at the boundaries between them. This leads to the appearance of periodically alternating black–white stripes in the image. The observed period is ~35±5 nm. The image of the same region of the experimental sample in Fig. 4a was obtained in the reflection

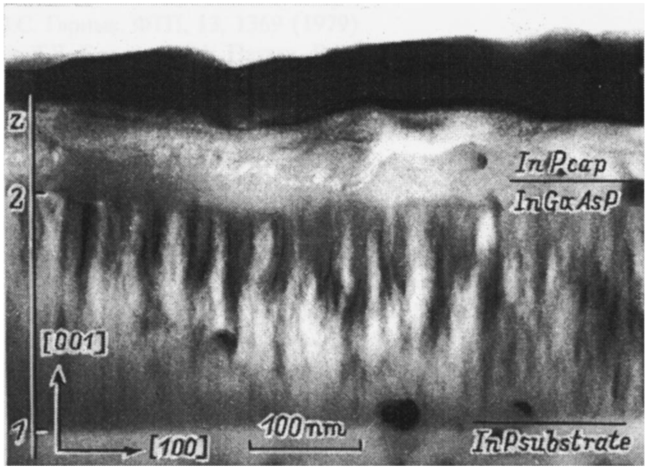

FIG. 5. TEM image of an InGaAsP sample in the transverse section. The InGaAsP epitaxial layer was grown on an InP (001) substrate in the region of instability of solid solutions with $T_g = 870$ K.

200, which is sensitive to the chemical composition, and intensity modulation is also seen. The period observed in Fig. 4a is ~62±6 nm. Therefore, the repetition period of the alternating regions in the reflection 220 is almost two times smaller than in the reflection 200. Hence it follows that the sign of the deformation changes at the boundary of regions with different compositions. The quantum efficiency of the PL of the stressed periodic structure is close to 100%, which rules out residual deformation (dislocations produced by the mismatch of the lattice parameters of the two solid solutions). This result is completely consistent with the idea of a soft mode which forms alternating elastic domains with different compositions.

The TEM investigations of the transverse section of InGaAsP/InP (001) epitaxial layers showed the presence of a periodic structure predominantly at the surface of the film. The periodic structure washes out in a direction into the layer and it is completely absent at the interface with the substrate (Fig. 5), in qualitative agreement with the computed dependence shown in Fig. 2 (Ref. 15).

4. CONCLUSIONS

Our investigations have shown that quaternary solid solutions with positive formation enthalpy become unstable at a certain critical temperature. Such an instability gives rise to a system of stressed alternating domains with two different compositions in the solid solution and different lattice constants. The domains alternate in two mutually perpendicular directions [100] and [010], which correspond to the directions of weakest compression of cubic crystals of III–V semiconductors. The elastic concentration domains are particularly well defined at the film surface and wash out in a direction toward the substrate. The quantum efficiency of the PL of the stressed periodic structure is close to 100%.

In summary, comparing the results of theoretical investigations of the spinodal decomposition of the solid solutions of III–V semiconductors with the experimental data for InGaAsP samples grown by liquid epitaxy in the instability region enabled us to conclude that in our experimental samples we have very likley observed spinodal decomposition of InGaAsP solid solutions.

This work was supported by the Russian Fund for Fundamental Research (Grants 97-02-18105, 98-02-18304), the Russian State Program of the Ministry of Science and Technology ''Surface Atomic Structures'' (Grant 95-2.23), the Russian State Program of the Ministry of Science and Technology ''Nanostructures'' (Grant 97-0214), and the Russian State Program ''Leading Science Schools'' (Grant 96.15-96.348).

*)E-Mail: tarasov@hpld.ioffe.rssi.ru; Fax: (812) 247-80-38

---

[1] A. Zunger and S. Mahajan, in *Handbook of Semiconductors*, edited by T. S. Moss, Vol. 3, edited by S. Mahajan, (Elsevier, 1994) p. 1399.
[2] G. B. Stringfellow, J. Cryst. Growth **58**, 194 (1982); G. B. Stringfellow, J. Cryst. Growth **65**, 454 (1983).
[3] J. W. Cahn, Trans. Met. Soc. **242**, 166 (1967).
[4] A. G. Khachaturyan, *Theory of Structural Transformations in Solids* (John Wiley and Sons, New York, 1983).
[5] I. P. Ipatova, V. A. Shchukin, V. G. Malyshkin, A. Yu. Maslov, and E. Anastassakis, Solid State Commun. **78**, 19 (1991).
[6] M. Ilegems and M. B. Panish, J. Phys. Chem. Solids **35**, 409 (1974).
[7] I. S. Tarasov, N. A. Pikhtin, A. V. Murashova, A. V. Lyutetskiĭ, A. Yu. Leshko, M. A. Ivanov, N. A. Bert, and Zh. I. Alfërov, in *2nd Russian Conference on Semiconductor Physics, RKFP'96*, Zvenigorod, 1996, Vol. 1, p. 40.
[8] I. S. Tarasov, L. S. Vavilova, N. I. Katsavets, A. V. Lyutetskiy, A. V. Murashova, N. A. Pikhtin, N. A. Bert, and Zh. I. Alferov, in *Abstracts International Symposium on Nanostructures: Physics and Technology*, St. Petersburg, 1996, p. 362.
[9] I. S. Tarasov, L. S. Vavilova, I. P. Ipatova, A. V. Lyutetskiy, A. V. Murashova, N. A. Pikhtin, V. A. Shchukin, and Zh. I. Alferov, in *Proceedings of the 23rd International Symposium on Compound Semiconductors ISCS-23* (St. Petersburg, 1996), 1997, p. 117.
[10] L. S. Vavilova, A. V. Ivanova, V. A. Kapitonov, A. V. Murashova, I. S. Tarasov, I. N. Arsent'ev, N. A. Bert, Yu. G. Musikhin, N. A. Pikhtin, and N. N. Faleev, Fiz. Tekh. Poluprovodn. **32**, 658 (1998) [Semiconductors **32**, 590 (1998)].
[11] B. de Cremoux, J. Physique **43**, C5–19 (1982).
[12] I. P. Ipatova, V. G. Malyshkin, A. Yu. Maslov, and V. A. Shchukin, Fiz. Tekh. Poluprovodn. **26**, 285 (1993) [Semiconductors **26**, 158 (1993)].
[13] I. P. Ipatova, V. G. Malyshkin, and V. A. Shchukin, J. Appl. Phys. **74**, 7198 (1993).
[14] I. P. Ipatova, V. G. Malyshkin, and V. A. Shchukin, Philos. Mag. **70**, 557 (1994).
[15] D. Bimbert, I. P. Ipatova, P. S. Kop'ev, N. N. Ledentsov, V. G. Malyshkin, and V. A. Shchukin, Usp. Fiz. Nauk **167**(3), 552 (1997).
[16] Seiji Mukai, J. Appl. Phys. **54**, 2635 (1983).

Translated by M. E. Alferieff

SEMICONDUCTORS VOLUME 33, NUMBER 5 MAY 1999

ELECTRONIC AND OPTICAL PROPERTIES OF SEMICONDUCTORS

Absorption of infrared radiation by free charge carriers in *n*-type $Cd_{1-x}Zn_xTe$

A. I. Belogorokhov,* A. G. Belov, V. M. Lakeenkov, and N. A. Smirnova

Institute of Rare Metals ''Giredmed,'' 109017 Moscow, Russia

L. I. Belogorokhova

M. V. Lomonosov Moscow State University, 119899 Moscow, Russia

(Submitted June 24, 1998; accepted for publication July 28, 1998)
Fiz. Tekh. Poluprovodn. **33**, 549–552 (May 1999)

The infrared transmission spectra of single-crystal samples of *n*-type CdTe and *n*-type $Cd_{1-x}Zn_xTe$ at 295 and 77 K were investigated. The experimental data are analyzed under the assumption that the observed spectral dependences of the transmission coefficient are due to absorption of infrared radiation by free charge carriers. It is shown that the computational results agree satisfactorily with the experimental data. The electron densities and mobilities calculated from the transmission spectra are close to their values obtained from electric measurements. © *1999 American Institute of Physics.* [S1063-7826(99)00505-0]

1. INTRODUCTION

Interest in cadmium telluride and the solid solutions $Cd_{1-x}Zn_xTe$ has recently increased appreciably because of two basic reasons. First, the solid solution $Cd_{1-x}Zn_xTe$ is the most promising substrate material for $Cd_xHg_{1-x}Te$/CdTe epitaxial heterostructures. Secondly, it has a number of advantages over other semiconductors for use as a material for nuclear-radiation detectors. However, it is obvious that this compound has not been adequately studied. Only its optical properties have been partially investigated. Ivestigation of the electric properties encounter great difficulties, especially in performing measurements at liquid-nitrogen and liquid-helium temperatures, i.e., in the cases where the most valuable information can be obtained about the density of free charge carriers, the ionization energies of impurity levels, the ratio of the donor and acceptor densities, and so on.

Analysis of existing published data shows that the authors generally report very little about the results of electric measurements and only rarely discuss the difficulties which they encounter in performing low-temperature measurements. Obtaining contacts to cadmium–zinc telluride, which are ohmic in a wide temperature range, is a difficult technical problem which is yet to be solved.

The lack of ohmic contacts is an obstacle for Hall measurements. However, optic measurements are completely free of this problem. In the cases where optic and electric measurements can be performed on the same samples the information obtained is much more valuable. In our study we attempted to determine the density of free charge carriers in *n*-type $Cd_{1-x}Zn_xTe$ crystals by two methods — from the IR transmission spectra and from electric measurements — and to compare the results of two fundamentally different experiments.

2. EXPERIMENTAL PROCEDURE. SAMPLE PREPARATION

Single-crystal *n*-type $Cd_{1-x}Zn_xTe$ $(0\leqslant x\leqslant 0.06)$ samples were investigated (the parameters of some samples are presented in Table I). The crystals, which were obtained by the Bridgman method, consisted of two or three single-crystal blocks which were oriented in the (111) direction and cut into 1.4 to 1.6-mm-thick wafers.

For optical measurements the wafers were ground on both sides and then chemicomechanically polished using the polishing etchant Br_2 : HBr:ethylene glycol. These operations made it possible to remove the damaged layer completely and to obtain a close-to-mirror surface.

The structural perfection of the samples was investigated by the metallography method. To reveal the dislocation structure on the A(111) surface, the samples were treated with a selective etchant consisting of a 50% water solution of CrO_3 and HF (3:2 parts by volume). In our experimental samples the dislocation density was $(4-6)\times 10^4\ \mathrm{cm}^{-2}$, and there were no small-angle boundaries or inclusions of a second phase.

The measurements of the electric parameters were performed at room temperature ($T=295$ K) and liquid-nitrogen temperature ($T=77.3$ K) by the van der Pauw method; the Hall coefficient was measured with magnetic induction $B=0.5$ T. The measurements were performed on close-to-rectangular samples with dimensions not exceeding $4\times 10\ \mathrm{mm}^2$. A sample was chipped out from a plate, and contacts were soldered to fresh cleavage surfaces using indium. No more than 5 min elapsed between the cleaving and the soldering of the contacts, so that there was not enough time for the cleavage surfaces to become contaminated. The current–voltage characteristics were used to check ohmicity of the contacts. It was established that our method for preparing the contacts gives satisfactory results. As the sample

TABLE I. Parameters of the experimental *n*-type samples.

Sample No.	Material	Sample thickness *d*, mm	Temperature *T*, K	Electron density		Electron mobility	
				N_{opt}, cm^{-3}	N_{el}, cm^{-3}	μ_{opt}, cm^2/(V·s)	μ_{el}, cm^2/(V·s)
1	$Cd_{0.96}Zn_{0.04}Te$	1.07	295	6.6×10^{16}	6.3×10^{16}	770	740
			77.3	4.0×10^{16}	3.9×10^{16}	1300	1200
2	$Cd_{0.96}Zn_{0.04}Te$	1.01	295	1.9×10^{16}	2.7×10^{16}	870	810
			77.3	1.6×10^{16}	1.3×10^{16}	900	1200
3	$Cd_{0.97}Zn_{0.03}Te$	0.67	295	8.2×10^{15}	8.9×10^{15}	670	630
			77.3	4.3×10^{15}	4.5×10^{15}	960	970
4	$Cd_{0.94}Zn_{0.06}Te$	0.92	295	1.1×10^{15}	1.1×10^{15}	970	890
			77.3	8.2×10^{14}	8.0×10^{14}	8800	8900
5	CdTe	1.20	295	1.9×10^{14}	2.3×10^{14}	960	760
			77.3	1.3×10^{14}	1.2×10^{14}	5200	5100

temperature decreased, deviations of the current–voltage characteristics from linearity were observed, especially for samples with $n\leqslant 10^{15}$ cm^{-3}, but these deviations were negligible and had virtually no effect on the electric measurements. For samples with $n>10^{15}$ cm^{-3} the contacts were ohmic at all temperatures.

The optical spectra in the wave number range 3000–300 cm^{-1} were obtained on an IFS-113v Fourier spectrometer (Brüker Company, Germany). The spectral resolution was 0.5 cm^{-1} in the entire range. A continuous-flow helium cryostat, manufactured by the Oxford Instruments Company (Great Britain), was used for the low-temperature measurements. The light spot was no more than 2 mm in size.

The mathematical analysis of the transmission spectra consisted of making a least-squares fit of the computed curve to the experimental spectrum by varying two independent variables: the density N and the mobility μ of the free charge carriers. The fitting method which we used can be described as follows.

Cadmium telluride is a wide-gap semiconductor with a ~1.5-eV gap, so that for an electronic sample the holes have no influence because of their small number. In this case (monopolar *n*-type semiconductor) the dependence of the absorption α on the frequency ω can be expressed as[1]

$$\alpha=\frac{4\pi e N_{\mathrm{opt}}\mu_{\mathrm{opt}}}{cn[1+\omega^2(m_{\mathrm{opt}}\mu_{\mathrm{opt}}/e)^2]}. \tag{1}$$

Here N_{opt}, m_{opt}, and μ_{opt} are, respectively, the density, effective mass, and mobility of the free charge carriers (the subscript ''opt'' means that these parameters are all determined from the transmission spectra), n is the refractive index of the material, e is the electron charge, and c is the velocity of light in vacuum.

Using the minimum wave number in the experimental spectral range ($\nu=300$ cm^{-1}) and the typical mobilities for our samples [$\mu_{\mathrm{opt}}\approx 10^3$ cm^2/(V·s)], we find the second term in the denominator in Eq. (1) to be 40 (minimum estimate). Therefore the number 1 in the denominator can be ignored, and since $\omega=2\pi\nu c$, we can write Eq. (1) in the form

$$\alpha=\frac{N_{\mathrm{opt}}e^3}{\pi c^3 n\mu_{\mathrm{opt}}m_{\mathrm{opt}}^2\nu^2}. \tag{2}$$

The electron effective mass was determined from the relation[2]

$$m_{\mathrm{opt}}=\frac{3h^2E_g}{16\pi^2P_{c\nu}^2}. \tag{3}$$

Here $h=6.62\times10^{-34}$ J·s is Planck's constant, and $P_{c\nu}$ is the matrix element of the interaction of the valence and conduction bands [assumed to be independent of temperature and zinc concentration and equal to 9.0×10^{-8} eV·cm (Ref. 3)]. For the solid solution $Cd_{1-x}Zn_xTe$ the band gap E_g was calculated from the relation given in Ref. 4 for $T=5$ K; the thermal coefficient of variation of the band gap was assumed to be temperature-independent in the interval 5–300 K and equal to $dE_g/dT=-4.5\times10^{-4}$ eV/deg (Ref. 5). Using Eq. (3) for pure cadmium telluride ($x=0$) we obtain $E_g=1.468$ eV, $m_{\mathrm{opt}}=0.103m_0$ at $T=295$ K and $E_g=1.566$ eV, $m_{\mathrm{opt}}=0.110m_0$ at $T=77.3$ K (m_0 is the free electron mass).

If the value of α is known, then the transmission coefficient can be easily determined from the relation[1]

$$\tilde{T}=\frac{(1-R)^2e^{-\alpha d}}{1-R^2e^{-2\alpha d}}, \tag{4}$$

where R is the single-reflection coefficient,

$$R=\frac{(n-1)^2+k^2}{(n+1)^2+k^2}, \tag{5}$$

and $k=\alpha/4\pi\nu$ is the extinction coefficient.

The computed curves $\overline{T}(\nu)$ were obtained using the relations (2)–(5) by varying the parameters N_{opt} and μ_{opt} in Eq. (2). The refractive index n was assumed to be independent of the wave number and taken to be 2.70 at $T=295$ K and 2.65 at $T=77.3$ K (Ref. 6). The values obtained for N_{opt} and μ_{opt} are presented in Table I, which also gives the values of the density N_{el} and mobility μ_{el} calculated from the electric measurements.

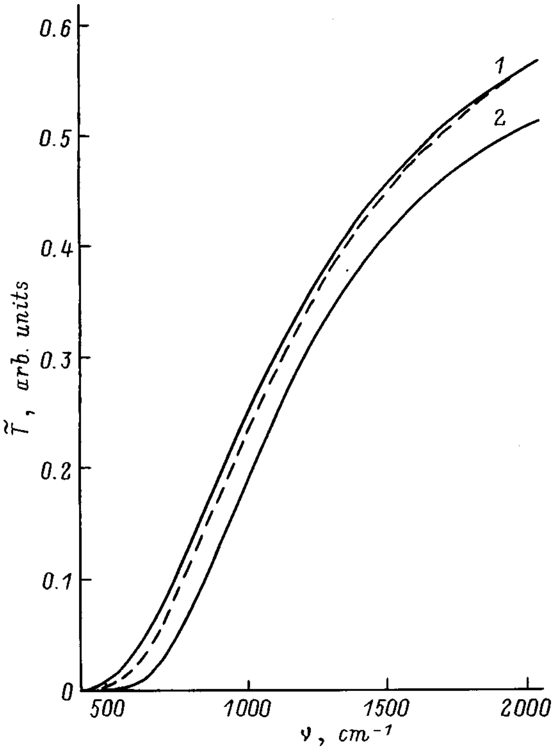

FIG. 1. Typical experimental transmission spectra of the solid solution $Cd_{1-x}Zn_xTe$ (sample *1*) at $T=77.3$ (*1*) and 295 K (*2*). Dashed line — computed transmission spectrum of sample *1* at $T=77.3$ K.

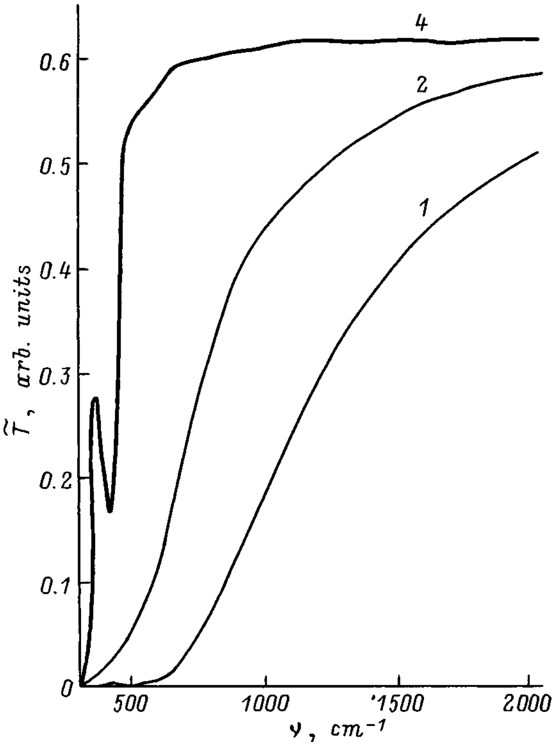

FIG. 2. Transmission spectra of $Cd_{1-x}Zn_xTe$ samples with different electron densities at $T=295$ K. The numbers on the curves correspond to the numbers of the samples in Table I.

3. EXPERIMENTAL RESULTS AND DISCUSSION

Typical transmission spectra of *n*-type CdTe and *n*-type $Cd_{1-x}Zn_xTe$ samples at $T=295$ and 77.3 K are shown in Fig. 1. As one can see from the figure, the transmission coefficient increases in the entire spectral interval as the temperature of the sample is lowered. Since the experimental IR range lies far from the region of intrinsic transitions (E_g corresponds to $\nu \approx 12500$ cm^{-1}), and since there are no distinct absorption bands in the transmission spectra, we assumed that the monotonically increasing function $\tilde{T}(\nu)$ (Fig. 1) is attributable to IR absorption by free charge carriers. Using the fitting procedure described above, we obtained the values of N_{opt} and μ_{opt} which are presented in Table I. How close the theoretical curve is to the experimental curve can be judged from Fig. 1, which shows the computed and experimental transmission spectra of sample 1 at $T=77.3$ K. As one can see from Fig. 1, the agreement between the computed and experimental data is completely satisfactory.

Figure 2 shows the spectral dependence of the transmission coefficient as a function of the density of free charge carriers at $T=295$ K. We see that as the electron density decreases, the spectrum shifts leftward into the region of smaller wave numbers and the transmission coefficient increases. Curve 4 corresponds to a sample with $N_{\mathrm{opt}}=1.1 \times 10^{15}$ cm^{-3}. For such electron densities the IR absorption by free charge carriers has an effect only in the long-wavelength part of the spectrum ($\nu \leqslant 1000$ cm^{-1}). In the region $\nu > 1000$ cm^{-1} the transmission coefficient is essentially independent of the wave number. The features observed on the curve 4 in the interval $\nu < 500$ cm^{-1} are due to multiphonon processes and are not related to IR absorption by free charge carriers.

Comparison of the optic and electric measurements (see Table I) shows that N_{opt} and N_{el} differ by no more than a factor of 1.5 and μ_{opt} and μ_{el} differ by even less; the observed difference is in either direction (i.e., there is no systematic error).

The results obtained by us show unambiguously that the observed spectral dependences of the transmission coefficient of n-$Cd_{1-x}Zn_xTe$ samples can be described completely satisfactorily by IR absorption by free charge carriers. There were no tellurium-based inclusions in our samples, so that the hypothesis of the existence of tellurium precipitates,[7,8] which lead to dependences $\tilde{T}(\nu)$ of the form 1 and 2 (Fig. 1), seems to us to be incorrect, since it is incomprehensible why the dependences $\tilde{T}(\nu)$ incease as a result of scattering of radiation by certain inhomogeneities in the material. It follows from general considerations that the opposite situation should occur.

For *p*-type cadmium telluride–zinc samples, absorption due to hole transitions between valence subbands is added to the IR absorption by free charge carriers, making it difficult to interpret the transmission spectra. Both absorption mechanisms lead to an increasing function $\tilde{T}(\nu)$. The study of the optic and electrical properties of *p*-type material is a subject for a separate investigation.

This work was performed as part of a Russian Fund for Fundamental Research Project No. 96-02-18853.

*E-Mail: abelog@glas.apc.org; Fax: (095) 4387664

---

[1] T. Moss, H. Barrel, and B. Ellis, *Semiconductor Optoelectronics* [Mir, Moscow, 1976, pp. 27, 45, and 51].
[2] B. M. Askerov, *Kinetic Effects in Semiconductors* (Nauka, Leningrad, 1970), p. 39.
[3] M. Cardona, J. Phys. Chem. Solids **24**(4), 1543 (1963).
[4] M. J. S. H. Brasil, M. C. Tamargo, R. E. Nahory, H. L. Gilchrist, and R. J. Martin, Appl. Phys. Lett. **59**(10), 1206 (1991).
[5] N. N. Berchenko, V. E. Krevs, and V. G. Sredin, *Semiconductor Solid Solutions and Their Applications* (Voenizdat, Moscow, 1982), p. 73.
[6] J. Baars and F. Sorger, Solid State Commun. **10**(9), 875 (1972).
[7] W. J. Kim, M. J. Park, S. U. Kim, T. S. Lee, J. M. Kim, W. J. Song, and S. H. Suh, J. Cryst. Growth **104**(3), 677 (1990).
[8] B. Li, J. Zhu, X. Zhang, and J. Chu, J. Cryst. Growth **181**, 204 (1997).

Translated by M. E. Alferieff

SEMICONDUCTORS VOLUME 33, NUMBER 5 MAY 1999

Optoelectronic effects in semi-insulating CdTe single crystals and structures based on them

G. A. Il'chuk and N. A. Ukrainets

L'vov State Polytechnical University, 290646 L'vov, Ukraine

V. I. Ivanov-Omskiĭ and Yu. V. Rud'

A. F. Ioffe Physicotechnical Institute, Russian Academy of Sciences, 194021 St.Petersburg, Russia

V. Yu. Rud'

State Technical University, 195251 St.Petersburg, Russia

(Submitted August 19, 1998; accepted for publication July 7, 1998)
Fiz. Tekh. Poluprovodn. **33**, 553–558 (May 1999)

The authors describe a gas-transport reaction method they recently developed using the compounds $NH_4Cl\,(Br, I)$ as transport agents. Using this method, they were able to grow semi-insulating cadmium telluride single crystals with carrier concentrations $p=10^8-10^{10}$ cm^{-3} at $T=300$ K. These crystals were used to fabricate In–CdTe surface-barrier structures with peak voltaic photosensitivities of $\sim 10^5$ V/W. Their investigations of the emission properties of homogeneous crystals at $T=77$ K and distinctive features of their photosensitivity spectra revealed that these material characteristics derive from the use of Cl, Br, and I as dopants. By illuminating their In–CdTe structures with linearly polarized light at oblique incidence, they generated induced photopleochroism, which was measured and used to determine the refraction index of the material, which is found to be $n=2.8$. The paper concludes with a discussion of how these structures can be used as photodetectors of natural and linearly polarized light. © *1999 American Institute of Physics.* [S1063-7826(99)00605-5]

Cadmium telluride is one of several promising semiconductor materials derived from the solid solution $Cd_xHg_{1-x}Te$ that can be used for solid-state detectors of nuclear radiation,[1,2] solar energy converters, and optoelectronic modulators of laser light. For these materials, the growth conditions, impurities introduced, and lattice defects generated during fabrication have a decisive influence on the parameters of the crystals and devices based on them.[2,3] Although group-VII elements of the periodic table can be used as dopants to make semi-insulating single crystals of CdTe, recent papers[3–9] have only discussed one of these elements to data - chlorine. In this paper we investigate the physical properties of uniform single crystals of CdTe grown by a new chemical transport reactions technique we have developed[10–14] that uses $NH_4Cl\,(Br,I)$ as transport agents. We also investigate how illumination by laser light[15] during the growth process stimulates doping by the halogens: chlorine, bromine, and iodine.

SAMPLES AND MEASUREMENT METHODS

The single-crystal semi-insulating CdTe sample crystals which we investigated were grown by the method of chemical transport reactions. In these experiments an argon laser was used to stimulate the growth process (radiation wavelength $\lambda=0.44\,\mu$m, power $P=1$ W) in the cw regime. The electrical properties of these crystal samples, which after growth were naturally faceted in the form of parallelepipeds with average dimensions $0.5\times0.5\times5.0$ mm, were investigated using weak electric and magnetic fields. Hall-effect measurements made at $T=300$ K revealed that carrier concentrations in these crystals were $10^8-10^{10}\,cm^{-3}$ and their mobilities were $\sim 50\,cm^2/(V\cdot s)$. Analysis of the signs of the Hall effect and thermoelectric power implies that in the overwhelming majority of our samples conductivity takes place via holes. The electrical properties of these crystals were the same for all three transport agents used. In our photoluminescence (PL) studies we used focused light from a helium-neon laser ($\lambda=0.4\,\mu$m, $P=15$ mW), which is strongly absorbed in CdTe, as an optical excitation source with a probe diameter of ~ 0.1 mm. The photoluminescence emission was analyzed using an MDR-3 monochromator based on a diffraction grating with 600 lines/mm, and a PEU-62 photomultiplier. The PL was recorded from the side of the sample on which the excitation light was incident. The PL intensities and line shapes were quite reproducible as the surface of the single crystal under study was scanned, indicating considerable uniformity. The crystal surfaces were not subjected to any processing prior to the PL measurements. In–CdTe surface-barrier structures were prepared by thermally depositing indium layers with thickness $d\simeq 1\,\mu$m on mirror-smooth surfaces of CdTe single crystals in vacuum (residual pressure $p=10^{-5}$ Torr). Chemically deposited Au layers were used as ohmic contacts. No thermal processing was used either in making the contacts to the structure or subsequently. A SPM-2 monochromator with a SiO_2 prism was used to measure the spectral dependence of the photosensi-

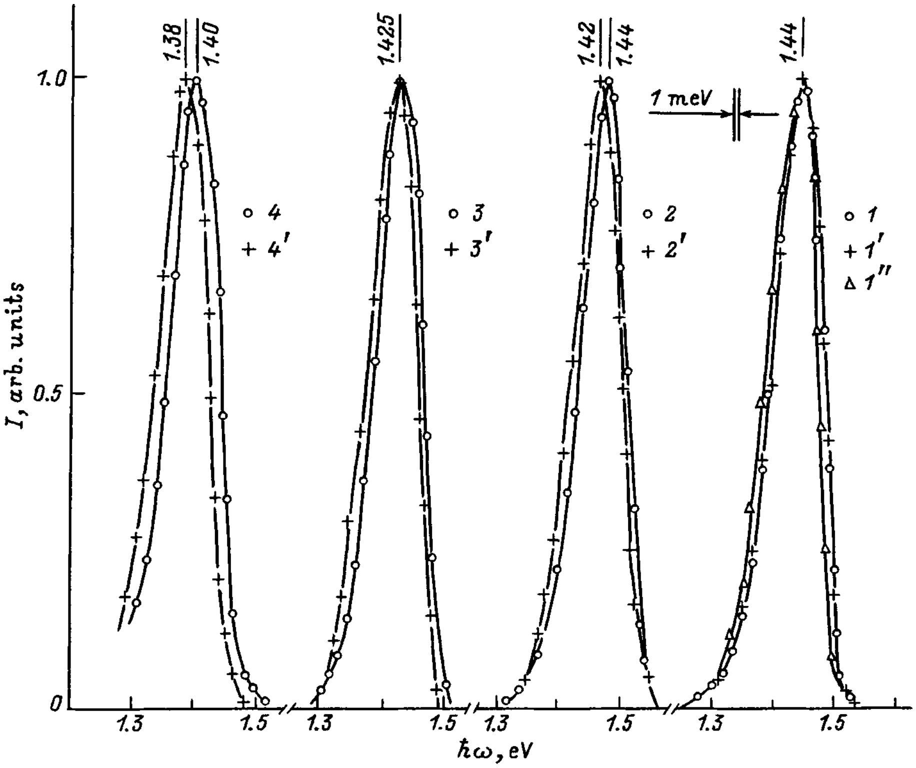

FIG. 1. Spectral dependence of the steady-state photoluminescence (I) at $T = 77$ K for CdTe crystals grown by the method of chemical transport reaction using various transport agents: *1, 1′, 1″* — NH_4Cl; *2, 2′, 3, 3′* — NH_4Br; *4, 4′* — NH_4I without activation (*1, 1′, 1″, 2, 2′, 4, 4′*) and with activation of the growth medium by a laser (*3, 3′*). The spectra are normalized to maximum intensity. The excitation intensity L/L_0: (*1–4*) — 1.0, (*1′–4′*) — 0.15, *1″* — 0.05. Energy maxima are shown in eV. The spectral width of the slit was 1 meV.

tivity of these CdTe structures. Under the experimental conditions, the photoresponse was proportional to the intensity of the incident light.

RESULTS OF EXPERIMENT AND DISCUSSION

Measurements of the kinetic coefficients of CdTe single crystals obtained by our new chemical transport reactions technique led us to conclude that our fabrication conditions resulted in semi-insulating material independent of the particular halogen used (chlorine, bromine, or iodine). We therefore feel justified in asserting that all the group-VII impurities provide a high degree of compensation in CdTe. Our conclusion agrees with well-known results of doping cadmium telluride with chlorine.[6,8] By analogy with those studies[6,8] these results are attributable to compensation of shallow hydrogenic donors (with ionization energy $E_D \approx 0.014$ eV) by intrinsic acceptors that form in cadmium telluride as a result of halogen incorporation. These acceptors are associated with singly charged vacancies in the cadmium sublattice V'_{Cd} (ionization energy $E_A = 0.06$ eV). Hence, as in the case of CdTe⟨Cl⟩ crystals,[6,8] our gas-phase process allows us to obtain strongly compensated single crystals because the majority of isolated impurities and defects are in electrically inert states, ensuring ''self-purification'' of the material.[16]

Typical spectral dependences of the steady-state PL for our CdTe single crystals are shown in Fig. 1. This figure shows that the spectral dependences of CdTe crystals grown using various transport agents, both without and with use of laser light to activate the growth processes, turn out to be similar. All consist only of a single rather broad band. The parameters of the PL spectra are listed in Table I. From this table we see that the total half-width of the bands at half-height $\delta_{1/2}$ is practically insensitive to the chemical composition of the transport agent, and also is independent of whether laser light was used or not in the chemical transport reaction process. The large value $\delta_{1/2} \approx 90$ meV indicates that the emission process is nonelementary in character. The PL bands were asymmetric for all the CdTe crystals we obtained; as a rule, the short-wavelength half-width δ_{sw} was smaller than the long-wavelength δ_{lw}. Figure 1 shows that decreasing the power density of the PL excitation light L leaves the spectral line shape of the recombination light virtually unchanged for all our single crystals. However, the line shape can shift as a whole towards the long-wavelength region of the spectrum (curves *2* and *3*), or exhibit changes only in the wings of the band while keeping the ''centers'' of the PL band maxima unchanged (curves *1* and *3*). The fact that in all the samples the energy $\hbar\omega_m$ at which the spectral dependence of the PL is a maximum is found to be smaller than the value of the bandgap width E_g for cadmium

TABLE I. PL parameters of CdTe⟨VII⟩ single crystals at 77 K.

Transport agent	$\hbar\omega$, eV	$\delta_{1/2}$, meV	δ_{lw}, meV	δ_{sw}, meV	$\Delta\hbar\omega_m$, meV	I
NH_4Cl	1.440	92	50	42	0	0.08
NH_4Br	1.432	90	55	35	12	1.00
NH_4Br*	1.425	92	50	42	0	0.85
NH_4I	1.400	90	50	40	16	0.30

Note: $\Delta\hbar\omega_m$ is the shift in the maximum of the PL bands as the excitation power decreases by an order of magnitude. I is the PL intensity normalized by the intensity of PL in single crystals obtained using NH_4Br without activating laser light; the conditions for excitation of PL are standard. *Activating laser illumination was used during the growth process.

TABLE II. Photosensitivity parameters for CdTe⟨VII⟩ surface-barrier structures at 300 K.

Transport agent	$\hbar\omega_m$, eV	S, eV^{-1}	S_v^m, V/W	$w_{1/2}$, meV	Φ_u^m, V/W·deg
NH_4Cl	1.475	35	9×10^4	120	1×10^5
NH_4Br	1.450	33	10^5	75	1.2×10^5
NH_4I	1.360	35	6×10^3	60	7×10^3

Note: Φ_u^m is the maximum value of Φ_u. $w_{1/2}$ is the width of the band at half-height.

telluride,[17] and also the experimental influence of the power density on the PL parameters (Fig. 1 and Table I), allows us to assert that radiative transitions in these CdTe crystals are caused by donor-acceptor recombination.[18] In this case, observed differences in the rates of shift $\Delta\hbar\omega_m$ of the bands towards longer wavelengths (Table I) from one crystal to another as the PL pump power density decreases must be associated with differences in the concentrations of donor-acceptor pairs and the way in which the group-VII atom enters into a pair. The fact that CdTe samples grown using NH_4I as a transport agent exhibit the most rapid shifts of the PL spectral band probably indicates that the concentration of donor-acceptor pairs that form during the growth process is highest in this material.

The overall similarity of the PL spectral dependences of our CdTe crystals could be a reflection of similar microstructures of the radiating centers, which consist of donor-acceptor pairs made up of a group-VII substitutional atom at a tellurium atomic site and the cadmium vacancy closest to it in the Cd sublattice. From Table I it also follows that the most intense PL is observed in CdTe crystals grown without laser activation in the presence of the transport agent NH_4Br.

Our PL investigations were supplemented by experimental studies of the photovoltaic effect in In–CdTe⟨VII⟩ structures. Upon illumination, all these structures exhibited a photovoltaic effect, whose sign was independent of the incident photon energy or where the structure was illuminated by the excitation light. This suggests that the photovoltaic effect is caused by separation of photogenerated charge by the electric field of a single energy barrier. For all the structures we made, the photovoltaic effect was largest when the illumination was from the side of the indium contact, which in all cases was charged negative with respect to the CdTe. We found that the structures with maximum voltage photosensitivity ($S_v^m = 10^5$ V/W at $T = 300$ K) were typically those based on single crystals grown using NH_4Br as a transport agent and without activation of the growth process by laser light. The lowest values of S_v^m (see Table II) were observed for structures made from CdTe crystals grown using iodine-containing transport agents. On comparing the voltage photosensitivity with the PL (Tables I and II), we note that that these effects are largest in CdTe crystals grown using the bromine-containing transport agent NH_4Br and without activation of the growth process by laser light. This fact probably implies that compensation of the group-VII donors by intrinsic acceptors V_{Cd}, i.e., the self-purification effect, is maximized in cadmium telluride when the gas-transport process is implemented using NH_4Br. Figure 2 shows typical spectral dependences of the relative photoconversion quantum efficiency (η) for several In–CdTe⟨VII⟩ structures, and some of their photosensitivity parameters are listed in Table II.

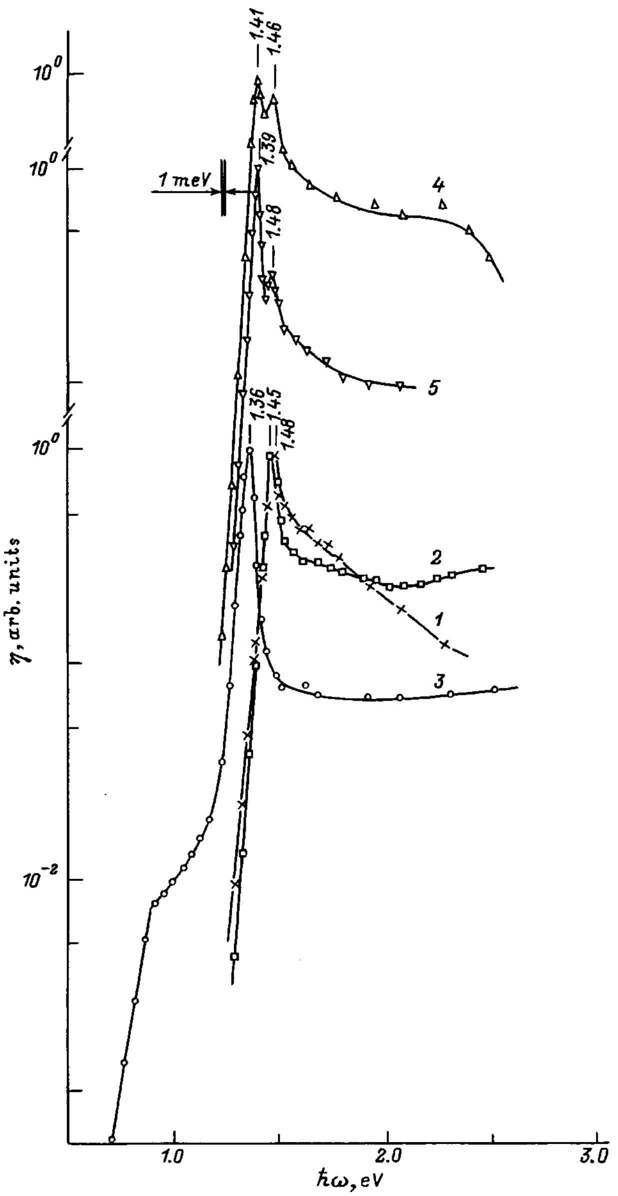

FIG. 2. Spectral dependences of the quantum efficiency of In–CdTe⟨VII⟩ photoconversion structures based on single-crystal CdTe obtained using various transport agents: NH_4Cl (*1*), NH_4Br (*2, 4, 5*), NH_4I (*3*) at $T = 300$ K. The curves are normalized to their absolute maxima. No activation of the growth medium was used. Curves *5* and *4* are shifted along the ordinate axis. The energy maxima are shown in eV. The spectral width of the gap was 1 meV.

The photosensitivities of these surface-barrier structures exhibit the following regularities. The photosensitivity spectra of the structures (Fig. 2, curves *1–3*) are found to be similar to the PL spectra of the original CdTe single crystals (Fig. 1). In all the structures, the long-wavelength edge of the photosensitivity is exponential in form with a very large slope, i.e., $S = d(\ln\eta)/d(\hbar\omega) \approx 32-35\ \mathrm{eV}^{-1}$. This is characteristic of direct interband optical transitions, which are the expected transitions in CdTe.[18] In all these surface-barrier structures, the exponential increase in photosensitivity terminates in a rapid decrease at short wavelengths, which could be due to the influence of surface recombination.

A second characteristic feature of the photosensitivity spectra of these structures is the shift in the absolute maximum (energy $\hbar\omega_m$) towards longer wavelengths of the spectrum as bromine replaces chlorine as the transporting agent, and is then replaced by iodine (Fig. 2, curves *1–3*). The same kind of sensitivity to transport agent is observed in the PL spectra (Fig. 1). This circumstance probably indicates a relation between the energy position of the absolute maximum and the nature of the doping impurity. In this case we should point out that the spectral positions of the absolute maximum of the photosensitivity $\hbar\omega_m$ of structures based on single crystals of CdTe grown using chlorine- and bromine-containing agents are close to the width of the CdTe band gap.[19–21] This fact serves as an additional argument in favor of highly effective self-purification of CdTe (Ref. 4) when the specific agents NH_4Br and NH_4Cl are used in the fabrication process. When we go to NH_4I, the photosensitivity maximum is located at energies considerably lower than E_g, and the spectrum exhibits a broad band in the long-wavelength region of the spectrum starting with a sharp increase in η at $\hbar\omega \approx 0.7$ eV. We assign this band to transitions of acceptors from the valence band to a level V''_{Cd} localized in the middle of the band gap.[8] Based on the data of Fig. 2 (curves *1–3*) we can conclude that the concentration of such centers is highest when the CdTe crystal is grown in the presence of NH_4I.

Several surface-barrier structures based on CdTe single crystals grown using NH_4Br exhibited an additional feature in the spectra of η (Fig. 2, curves *4* and *5*): an additional photosensitivity peak in addition to the short-wavelength peak. We measured the ratio of these peak heights from one structure to another. This feature could be due to weakening of the self-purification effect, resulting in a new long-wavelength peak in the photosensitivity, in addition to the short-wavelength peak. The new peak indicates photoactive absorption with the participation of levels from a new set of lattice defects. Consequently, the spectral dependence of the photovoltaic effect can be used to monitor the quality of semi-insulating single crystals of CdTe before they are used to make nuclear radiation detectors.

Studies of the photosensitivity of these structures in linearly polarized light showed that when the barriers were illuminated along the normal to the surface, changing the orientation of the electric field **E** of the light wave relative to the principal crystallographic planes of the CdTe substrates had virtually no effect on the magnitude of the photocurrent over the entire photosensitivity range, regardless of the way the substrates were grown. On the one hand, this is a consequence of the fact that the probability for interband optical transitions in cubic CdTe crystals does not depend on the polarization of the light; on the other hand, it also allows us to conclude that our fabrication conditions do not lead to the appearance of directed strain in these samples.

Figure 3 shows angular dependences of the short-circuit photocurrent that are typical of all of our structures, when the light wave is polarized in the plane of incidence **E**∥PI (photocurrent i^p) and perpendicular to it (**E**⊥PI) (photocurrent i^s), and the coefficient of induced photopleochroism

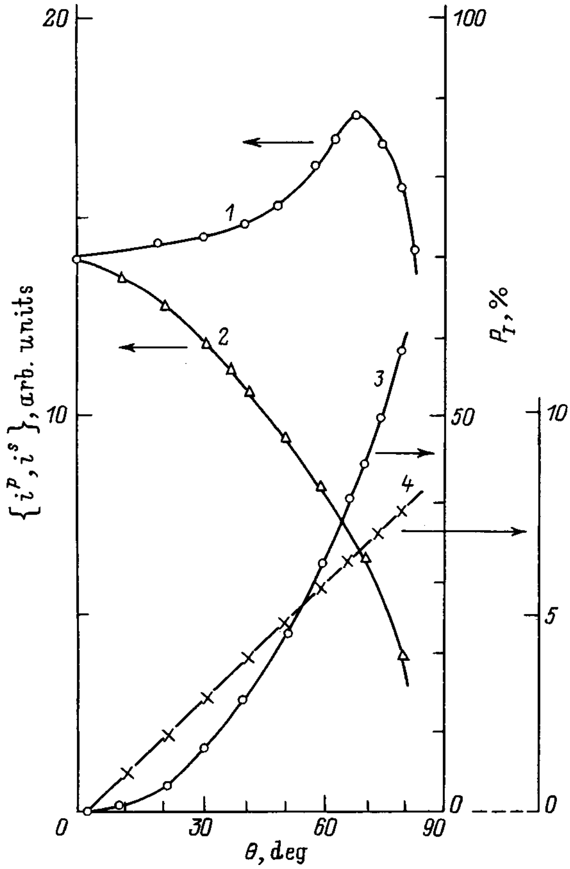

FIG. 3. Dependence of the short-circuit photocurrents i^p (*1*), i^s (*2*) and the coefficient of induced photopleochroism P_I (*3, 4*) on the angle of incidence θ of linearly polarized light on the surface of In–CdTe structures at $T = 300$ K for photon energies $\hbar\omega = 1.48$ eV. The CdTe crystal was obtained using NH_4Cl without laser illumination of the growth medium. The angular resolution was 1°.

$$P_I = \frac{i^p - i^s}{i^p + i^s}.$$

These quantities are plotted versus the angle θ at which the linearly polarized light is incident on the structure surface. The method of polarization studied was well described in Ref. 22. From Fig. 3 it is clear that the photocurrent i^p first increases with increasing angle of incidence, passes through a maximum near $\theta \approx 60°$, and then decreases for $\theta > 60°$. At the same time, the photocurrent i^s decreases as soon as $\theta > 0°$. These regularities are in agreement with analysis of the optical processes based on the Fresnel formulas[23,24] for oblique incidence of linearly polarized light on an air–CdTe boundary. In this model, the increase in photocurrent i^p attests to effective elimination of scattering losses upon reflection of light with polarization **E**∥PI, which has a maximum in the vicinity of the pseudo-Brewster angle $\theta_B \approx 60°$ (Fig. 3, curve *1*). In the structures we studied, the ratio $i^p(\theta_B)/i^p(\theta = 0°)$ usually lies in the range 1.2–1.3, which is consistent with the elimination of scattering losses during reflection.

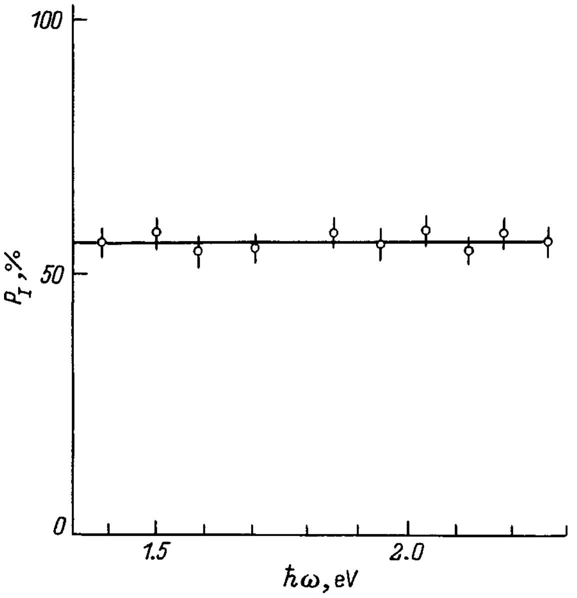

FIG. 4. Spectral dependence of the coefficient of induced photopleochroism for In–CdTe structures at $T=300$ K. The CdTe crystal was grown using NH_4Cl without activation of the growing medium. $\theta=80°$.

Another characteristic detail worth noting (Fig. 3, curves *3* and *4*) is the way the induced photopleochroism curves ''leave'' the origin. Because of the isotropic character of photoactive absorption in CdTe at $\theta=0°$, as soon as the angle of incidence of the linearly polarized light becomes nonzero, we see the appearance of an induced photopleochroism, which increases according to a quadratic law $P_I \propto \theta^2$, consistent with the analysis of Ref. 25. In all cases where we grew a crystal and made a barrier structure, the quantity $P_I=55-58\%$ at angles of incidence $\theta=80°$. An estimate of the index of refraction based on these values gives a value of 2.8, in good agreement with known values of this parameter.[21]

A typical spectral dependence of the induced photopleochroism from one of these surface-barrier In–CdTe⟨VII⟩ structures is shown in Fig. 4. For $\theta=$const, the induced photopleochroism is found to be nearly constant over the entire range of photosensitivity, which confirms the conclusions of Ref. 25.

The most important figure of merit of a polarimetric detector is its azimuthal photosensitivity $\Phi_u=2S_uP_I$.[22,26] In light of the nonselective character of P_I (Fig. 4) and the spectral dependence of η (Fig. 2), we can assert that when $\theta=$const, the maximum value of Φ_u (Table II) is determined by the spectral position of the maximum of η (Fig. 2). The values of Φ_u exhibited by surface-barrier structures based on the CdTe⟨VII⟩ single crystals we have grown indicate that they could be used as high-sensitivity wide-band photoanalyzers of linearly polarized light, whose photogeneration regime can be expressly changed from polarization insensitive ($\theta=0°$) to polarimetric ($\theta\neq 0°$).

[1] S. M. Ryvkin, O. A. Matveev, and N. B. Strokan, *Semiconductor Counters for Nuclear particles* [in Russian] [Semiconductors, Vol. 10 (''Science'' Association, Leningrad division, 1963)].

[2] E. N. Arkad'eva, O. A. Matveev, Yu. V. Rud', and S. M. Ryvkin, Zh. Tekh. Fiz. **36**, 1146 (1966) [Sov. Phys. Tech. Phys. **11**, 846 (1966)].

[3] R. Triboulet, Y. Marfainy, A. Corriet, and P. Siffert, J. Appl. Phys. **45**, 2759 (1974).

[4] P. Höschl, Rev. Phys. Appl. **12**, 229 (1977).

[5] N. V. Agrinskaya and T. V. Mashovets, Fiz. Tekh. Poluprovodn. **28**, 1505 (1994) [Semiconductors **28**, 843 (1994)].

[6] N. V. Agrinskaya and O. A. Matveev, Fiz. Tekh. Poluprovodn. **17**, 394 (1983) [Sov. Phys. Semicond. **17**, 245 (1983)].

[7] N. V. Agrinskaya, N. N. Zinov'ev, O. A. Matveev, and I. D. Yaroshetskiĭ, Fiz. Tekh. Poluprovodn. **14**, 172 (1980) [Sov. Phys. Semicond. **14**, 100 (1980)].

[8] N. V. Agrinskaya and O. A. Matveev, Fiz. Tekh. Poluprovodn. **21**, 542 (1987) [Sov. Phys. Semicond. **21**, 333 (1987)].

[9] N. V. Agrinskaya, O. A. Matveev, A. V. Nikitin, and V. A. Sokolova, Fiz. Tekh. Poluprovodn. **21**, 676 (1987) [Sov. Phys. Semicond. **21**, 414 (1987)].

[10] I. D. Nabitovich, Yu. G. Arkhomenko, G. A. Il'chuk, and S. P. Pavlishin, Izv. Akad. Nauk SSSR, Neorg. Mater. **18** (2), 211 (1982).

[11] I. D. Nabitovich, Yu. G. Arkhomenko, G. A. Il'chuk, and S. P. Pavlishin, Zh. Fiz. Khim. **57** (6), 1356 (1983).

[12] Yu. G. Arkhomenko, G. A. Il'chuk, I. E. Lopatinskiĭ, and S. P. Pavlishin, Izv. Akad. Nauk SSSR, Neorg. Mater. **17** (8), 1357 (1981).

[13] Yu. G. Arkhomenko, G. A. Il'chuk, S. P. Pavlishin, and S. I. Petrenko, Izv. Akad. Nauk SSSR, Neorg. Mater. **18** (7), 1117 (1982).

[14] Yu. G. Arkhomenko, G. A. Il'chuk, I. V. Kurilo, and S. P. Pavlishin, Izv. Akad. Nauk SSSR, Neorg. Mater. **20** (9), 1494 (1984).

[15] G. A. Ilchuk, I. F. Viblyi, V. O. Dol'nikov, and N. A. Ukrainets, *E-MRS'96 Spring Meeting* (Strasbourg, 1998).

[16] O. A. Matveev, E. D. Arkad'ev, and L. A. Goncharov, Dok. Akad. Nauk (SSSR) **221**, 325 (1975) [Dokl. Akad. Nauk **20**, 220 (1975)].

[17] Yu. V. Rud', K. V. Sanin, and Yu. G. Shreter, Fiz. Tekh. Poluprovodn. **5**, 654 (1971) [Sov. Phys. Semicond. **5**, 712 (1971)].

[18] J. I. Pankove, *Optical Processes in Semiconductors* [Prentice-Hall, Englewood Cliffs, N. J., 1971; Mir, Moscow, 1973].

[19] A. G. Milnes and D. L. Feucht, *Heterojunctions and Metal-Semiconductor Junctions* [Academic Press, New York, 1972; Mir, Moscow, 1975].

[20] *Physics and Chemistry of II-VI Compounds*, edited by M. Aven and J. S. Prener [North-Holland, Amsterdam, 1967; S. A. Medvedeva (Ed.) Mir, Moscow, 1970].

[21] *Physical and Chemical Properties of Semiconducting Materials: Handbook* [in Russian], Nauka, Moscow (1978), p. 340.

[22] V. Yu. Rud', Doctoral Diss. (Ioffe Physicotech. Inst., Russ. Acad. Sci., St. Petersburg, 1995).

[23] R. M. Azzam and N. M. Bashara, *Ellipsometry and Polarized Light* [North-Holland, Amsterdam, 1977; Mir, Moscow, 1981].

[24] G. S. Landsberg, *Optics* [in Russian] (Higher School, Moscow, 1976).

[25] G. A. Medvedkin and Yu. V. Rud', Phys. Status Solidi A **67**, 333 (1981).

[26] G. A. Medvedkin, Yu. V. Rud', and M. A. Tairov, Phys. Status Solidi A **115**, 11 (1989).

Translated by Frank J. Crowne

SEMICONDUCTORS VOLUME 33, NUMBER 5 MAY 1999

Photoluminescence of Si_3N_4 films implanted with Ge^+ and Ar^+ ions

I. E. Tyschenko*) and V. A. Volodin

Institute of Semiconductor Physics Siberian Branch of the Russian Academy of Sciences,
630090 Novosibirsk, Russia

L. Rebohle, M. Voelskov, and V. Skorupa

Institute of Ion-Beam Physics and Materials Science Rossendorf Research Center, Dresden, Germany

(Submitted August 25, 1998; accepted for publication September 9, 1998)
Fiz. Tekh. Poluprovodn. **33**, 559–566 (May 1999)

The room-temperature photoluminescence emission and excitation spectra of Si_3N_4 films implanted with Ge^+ and Ar^+ ions were investigated as a function of the ion dose and temperature of subsequent annealing. It was established that the implantation of bond-forming Ge atoms during annealing right up to temperature $T_a = 1000\,^\circ C$ stimulates the formation of centers emitting in the green and violet regions of the spectrum. Implantation of inert Ar^+ ions introduces predominantly nonradiative defect centers. Comparative analysis of the photoluminescence spectra, Rutherford backscattering data, and Raman scattering spectra shows that the radiative recombination is due not to quantum-well effects in Ge nanocrystals but rather recombination at the defects ≡Si–Si≡, ≡Si–Ge≡, and ≡Ge–Ge≡. *© 1999 American Institute of Physics.* [S1063-7826(99)00705-X]

1. INTRODUCTION

The investigation of thermally grown silicon dioxide films on silicon crystals implanted with Si^+ or Ge^+ ions,[1–4] as a material which emits at room temperature in the visible region of the spectrum and which is most compatible with silicon integrated technology, has been attracting increasing interest in the last few years. Si_3N_4 layers are also widely used for fabricating silicon devices. This insulator possesses a variety of remarkable properties that enable its use, for example, for masking films, in LOCOS technology (local oxidation of silicon), and for other applications where the penetration of various impurities into the active region of the silicon wafer must be decreased.[5] The study of the optical properties of silicon nitride films grown by various methods has revealed several photoluminescence (PL) bands in the visible region of the spectrum. The intensity and energy position of these bands differed somewhat, depending on the film-deposition method employed. In Refs. 6–8 a wide PL band was observed in the wavelength range $\lambda = 450 - 600$ nm (photon energy $\hbar\omega = 2.75 - 2$ eV). This band is excited in silicon nitride films, grown by various methods, at room temperature. When the energy of the exciting photon is increased from $\hbar\omega_{ex} = 4$ eV (wavelength 310 nm) to $\hbar\omega_{ex} = 5.3$ eV(~ 230 nm), the relative intensity of the green line increases compared with the violet line.[9] The excitation maximum of the violet band is observed at energies $4.8 - 4.6$ eV ($260 - 270$ nm) and that of the green band is shifted to higher energies — near 5.2 eV (240 nm). A red PL line is also excited at energies ~ 4.6 eV (~ 270 nm). The nature of these PL bands has still not been determined. The short relaxation times of these PL bands ($10^{-7} - 10^{-8}$ s) indicate that the transitions are of a intracenter character. In the literature it is assumed that these PL bands are all due to Si–Si defects in silicon nitride.[7,10] However, further experimental studies are needed to confirm this hypothesis.

The opinion that Si_3N_4 films have advantages over SiO_2 films for producing silicon-based light-emitting materials is sometimes stated in the literature.[11] However, there are virtually no data on the production of such materials and virtually no information about their properties. In our previous study, we observed an intense band of violet photo- and electroluminescence of SiO_2 films implanted with Ge^+ ions,[12] and we attributed this band to ≡Si–Si≡ and ≡Ge–Si≡ centers in the silicon dioxide framework. There is virtually no published information on the modification of the optical properties of silicon nitride by ion bombardment. Such investigations would make it possible, on the one hand, to obtain information about possible practical applications of such films as radiation sources and, on the other, to clarify the nature of the observed photoluminescence bands. To determine the contribution of intrinsic defects generated by ion implantation and the contribution of bond-forming atoms to the process leading to the production of light-emitting centers in silicon nitride, we investigated the room-temperature PL of Si_3N_4 films grown on single-crystal Ar^+- and Ge^+-implanted silicon wafers.

2. EXPERIMENTAL PROCEDURE

The starting substrates consised of single-crystal *n*-type silicon wafers with resistivity $3 - 10\ \Omega \cdot$cm and {100} orientation. Si_3N_4 layers, 300 nm thick, were deposited in a low-pressure reactor from a $NH_3 + SiH_2Cl_2$ mixture at temperature 775 °C. Prior to the deposition of the silicon nitride, a 25-nm-thick transitional oxide layer was grown on the silicon wafers. Implantation of the silicon nitride films was conducted with 150-keV Si^+ ions or 100-keV Ar^+ ions. In each

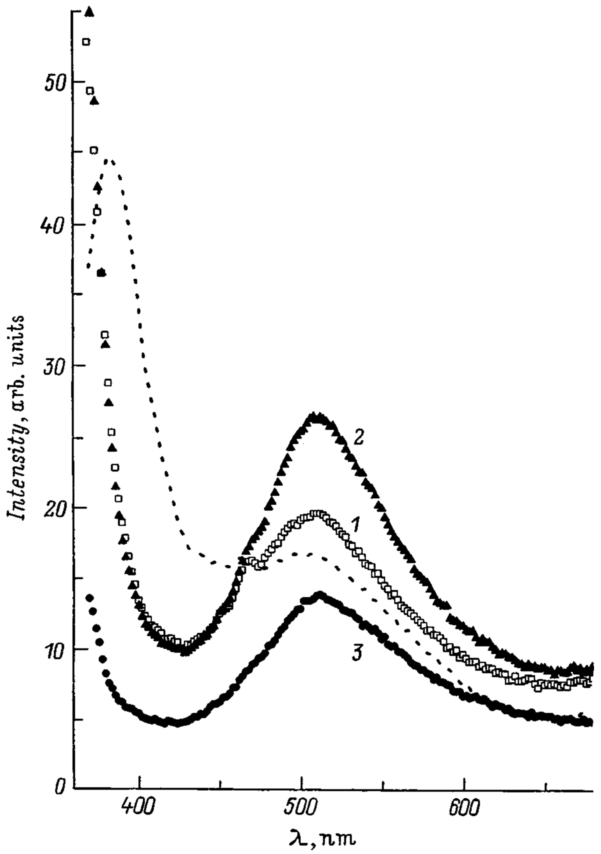

FIG. 1. PL spectra of Si_3N_4 films before (dashed line) and after implantation with 150-keV Si^+ ions with dose 0.5×10^{16} cm^{-2} (LD) and 30-min anneals at $T_a=600$ (*1*), 1000 (*2*), and 1200 °C (*3*) in an N_2 atmosphere. The wavelength of the excitation radiation is $\lambda_{ex}=350$ nm.

case the ion dose was 0.5×10^{16} cm^{-2} (low dose — LD), 1.4×10^{16} cm^{-2} (medium dose — MD), and 4.2×10^{16} cm^{-2} (high dose — HD). The parameters of the ions were chosen so that the maximum of the ion distribution would be located inside the silicon nitride film, and the maximum densities of the implanted atoms with the corresponding doses would be equal. Cooling with liquid nitirgen maintained the substrate temperature during irradiation at $-(145-155)$°C in all cases. The ion current density was 0.5–1.0 μA/cm^2. Subsequent anneals were performed at temperatures T_a=400–1300 °C for 30 min in an N_2 atmosphere. The PL spectra and the PL excitation spectra were measured at room temperature on the Spex Fluoromax setup. An ultraviolet lamp served as the source of excitation radiation; the required wavelength was separated with a monochromator. The distribution of the implanted atoms was investigated by Rutherford backscattering (RBS) of 1.7-MeV He^+ ions. The structural changes in the ion-implanted layers were monitored by Raman scattering.

3. RESULTS

Figure 1 shows the PL spectra of Si_3N_4 films implanted with LD Ge^+ ions and annealed at temperatures 600–1200 °C. The figure also shows the PL spectrum from the initial, unimplanted silicon nitride. The spectra were excited by radiation with wavelength $\lambda_{ex}=350$ nm ($\hbar\omega_{ex}\simeq3.5$ eV). It is evident that visible-range PL is excited at room temperature even in the unimplanted silicon nitride. The main PL peak lies in the violet region of the spectrum with a maximum near $\lambda=380$ nm ($\hbar\omega_{ex}\simeq3.2$ eV). A wide peak is also observed in the green region of the spectrum near $\lambda=520$ nm ($\hbar\omega\simeq2.4$ eV). The intensity of this peak is only two times lower than that of the violet PL band. Ion implantation of Ge^+ suppresses these PL bands. Subsequent anneals restored the intensity of the violet and green PL. Thus, the effect of annealing Ge^+-implanted layers was that even after $T_a=600$ °C the intensity of both the green and violet peaks was higher than their initial values and continued to increase with T_a to 1000 °C. The energy position of the green PL peak remained virtually unchanged, while the violet peak exhibited a small short-wavelength shift. A further increase of T_a to 1200 °C again caused the PL intensity to drop below its initial value and to further shift the violet peak in the direction of short wavelengths. The PL spectra of Ar^+-implanted silicon nitride films show a somewhat different behavior as a function of T_a (Fig. 2). In this case annealing restored only the intensity of the green PL band to its initial value; the effect reached its peak at $T_a=600$ °C. The violet PL remained suppressed in this case. The PL spectra of Ar^+-implanted silicon nitride exhibited such behavior as a function of T_a, irrespective of the ion dose (see the inset in Fig. 2). At the same time, for Si^+ implantation increasing the ion dose suppressed the PL intensity in the entire experimental wavelength range. Figure 3 shows the PL spectra for three Si^+ doses after annealing at 1000 °C. Similar dependences were observed before and after anneals at various temperatures.

Figure 4 shows the excitation spectra of the violet and green PL peaks of the initial silicon nitride, as well as the nitride implanted with LD Si^+ ions and annealed at 1000 °C. It is interesting to note that the excitation spectra of both the violet and green PL bands have the same form for both unimplanted and implanted Si_3N_4. In all cases indicated, maxima are recorded in the PL excitation spectra near $\lambda_{ex}=270$ nm ($\hbar\omega_{ex}\simeq4.6$ eV), 310 nm ($\sim$4.0 eV), and 390 nm ($\sim$3.2 eV).

To determine the mechanisms leading to the formation of light-emitting centers, we investigated by the RBS method the distribution profiles of implanted germanium over the depth d before and after anneals at T_a=400–1300 °C. These profiles are shown in Fig. 5 for the case of HD Ge^+ ions. It is obvious that up to $T_a=1200$ °C there is no diffusion displacement of implanted atoms in silicon nitride, and only annealing at $T_a=1300$ °C induces redistribution of germanium over the entire thickness of the film. The main maximum of the distribution shifts to a depth corresponding to the projected range R_p, to depth $\sim$170 nm, which corresponds approximately to the boundary between the initially implanted and unimplanted regions of the Si_3N_4 film. Germanium accumulates partially at the SiO_2/Si interface.

We used Raman scattering to study the structural properties of the layers. Figure 6 shows the spectra from Ge^+-implanted films after 30-min anneals at temperatures 600, 1000, 1300 °C. These spectra were measured in the geometry Z(XY)Z, where X, Y, and Z are axes corresponding

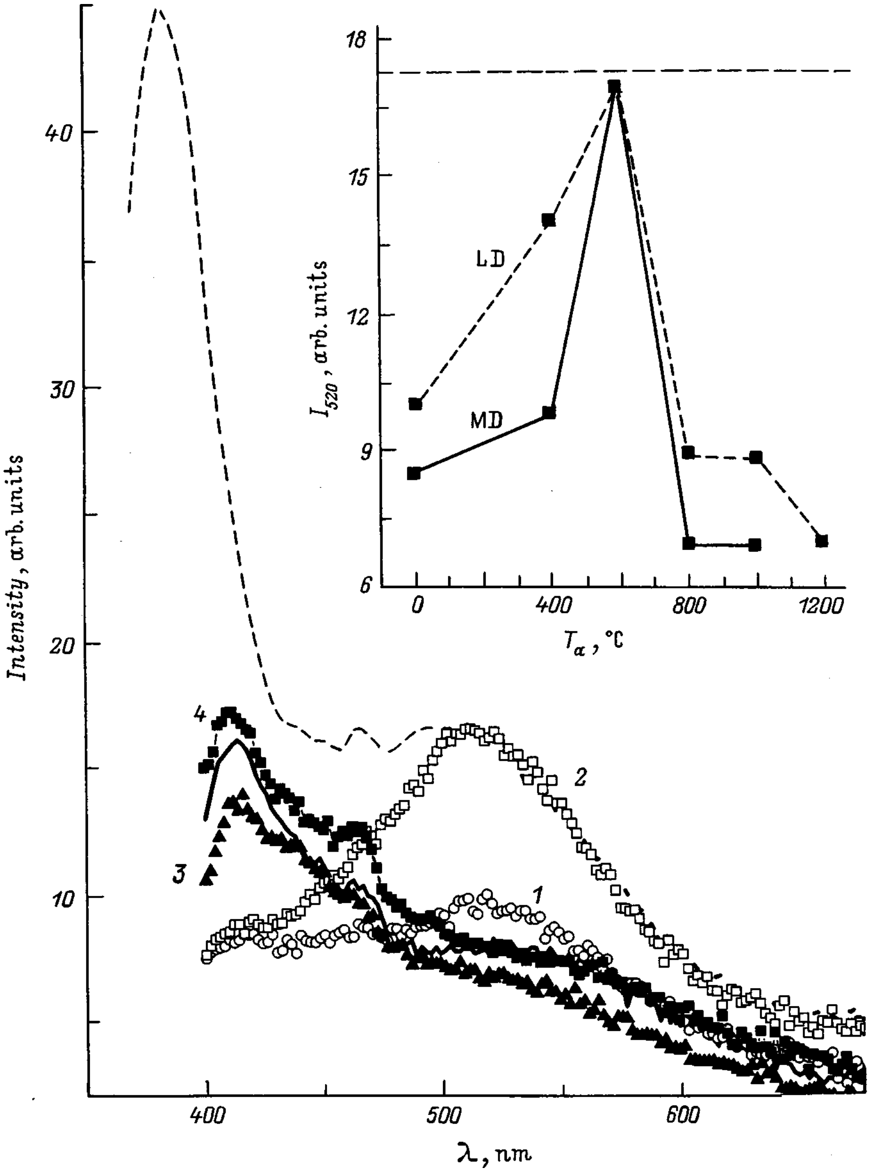

FIG. 2. PL spectra of Si_3N_4 films before (dashed line) and after implantation with 100-keV Ar^+ ions with dose 1.4×10^{16} cm^{-2} (MD) before (solid line) and after 30 min anneals at $T_a = 400$ (*1*), 600 (*2*), 1000 (*3*), and 1200 °C in an N_2 atmosphere. The wavelength of the excitation radiation is $\lambda_{ex} = 350$ nm. Inset: PL intensity at the maximum with $\lambda = 520$ nm (I_{520}) versus annealing temperature for doses 0.5×10^{16} cm^{-2} (LD) and 1.4×10^{16} cm^{-2}; horizontal dashed line — intensity of the PL of unimplanted Si_3N_4.

to the directions (100), (010), and (001). The Raman scattering spectra were featureless, compared with the spectra of the initial unimplanted Si_3N_4, up to $T_a = 1000$ °C. Only annealing at 1300 °C gives an asymmetric peak with a principal maximum near 300 cm^{-1}, which corresponds to crystalline germanium, and a shoulder, whose nature is not completely understood, in the wavelength interval $-(295-280)$ cm^{-1}. There are three possible reasons for the shoulder: 1) the presence of a phase of amorphous Ge inclusions; 2) formation of smaller germanium nanocrystals; and 3) a nanocrystalline germanium–silicon nitride interface.

4. DISCUSSION

The violet and green PL bands which we observed were previously observed in unimplanted Si_3N_4 synthesized by various methods. However, as mentioned in the introduction, the nature of these bands remains undetermined. In our experiments ion bombardment with Ar^+ and Ge^+ ions suppressed these PL bands, and subsequent annealing restored or even increased their intensity. This means that ion implantation of silicon nitride in combination with subsequent annealing introduces radiative and nonradiative recombination centers. These centers could be associated with defects generated by ion bombardment and with the presence of high concentrations of excess Ge atoms in the Si_3N_4 host. An important experimental result is that the excitation spectra of the violet and green PL bands are the same and that the behavior of the bands after Si^+ implantation followed by annealing is the same. The observed similarity of the excitation spectra cannot be attributed to, for example, interference in the silicon nitride films. Similar peaks have also been observed previously[6,13] in the excitation spectra of violet, green, and red PL bands of unimplanted Si_3N_4 films which were grown by other methods with various thicknesses. In our experiments the intensity of the green and violet PL peaks increases at the same time as T_a increases right up to 1000 °C. Their excitation spectra also remained essentially unchanged in the process. This indicates that the bands are linked with the same recombination center. On the other hand, there is no doubt that Ge atoms play a role in the

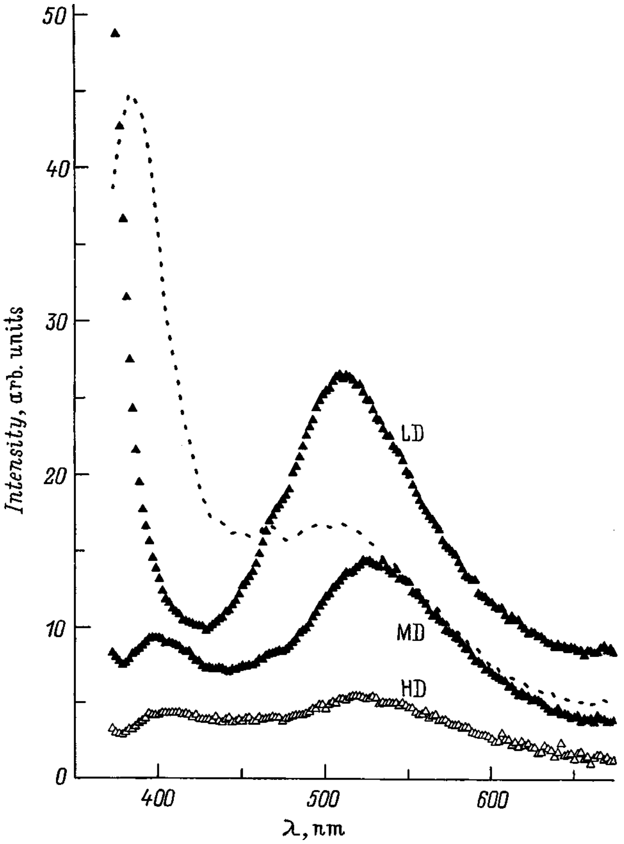

FIG. 3. PL spectra of Si_3N_4 films before (dashed line) and after implantation with 150-keV Ge^+ ions with doses 0.5×10^{16} cm^{-2} (LD), 1.4×10^{16} cm^{-2} (MD), and 4.2×10^{16} cm^{-2} (HD) and 30-min anneal at $T_a=1000$ °C in an N_2 atmosphere. The wavelength of the excitation radiation is $\lambda_{ex}=350$ nm.

formation of these centers. Comparing the data on the Si^+ dose dependence of the PL intensity (Fig. 2) and the Raman-scattering results (Fig. 4) shows that the centers emitting in the violet and green regions of the spectrum are not associated with Ge nanocrystals and that they may contain only a minimum number of germanium atoms. Moreover, the RBS data show that these light-emitting centers are formed not as a result of diffusive contraction of Ge atoms, but rather by restructuring of the short-range order in the Si_3N_4 host, for example, via restructuring of the bonds between the nearest atoms. It is unlikely that hydrogen atoms play a role, as indicated in Ref. 10, in the structure of this center. This is supported by the fact that the intensity of the violet and green PL peaks continues to increase right up to $T_a=1000$ °C. It is also unlikely that hydrogen is present in Si_3N_4 films at such high temperatures. The most likely source of the PL bands that we observed could be, for example, a center which, by analogy with an oxgyen vacancy in SiO_2, can be associated with the center $\equiv$Si–Si$\equiv$ in the silicon nitride structure. The existence of such centers was articulated in Ref. 14 in an investigation of nonstoichiometric silicon nitide with excess Si, as well as in Ref. 15 in a study of the optical absorption edge of silicon nitride implanted with boron ions. These centers are formed as a result of recombination of triply coordinated atoms $\equiv$Si• at subsequent anneal temperatures $T_a\approx600$ °C. At these temperatures the most efficient process should be the formation of $\equiv$Si–Si$\equiv$ bonds[16] and a corresponding increase in the intensity of green and violet PL. However, in our experiments, after implantation of Ar^+ ions, when there are no excess bond-forming atoms in the nitride matrix, we observed restoration of only the green PL in the process of annealing of the defects; the violet PL was not restored. This fact could be interpreted in favor of green and violet PL having different natures, but a different explanation of the observed effect is also possible. The atoms or complexes of atoms which are present in the silicon nitride and which are not associated with the host atoms, such as the Ar atoms and bubbles, could introduce additional nonradiative recombination levels, which decreases primarily the probability of radiative transitions leading to violet PL. At the same time, the presence of bond-forming Ge atoms in the Si_3N_4 host gives rise with annealing to the formation of largely radiative recombination centers. It is interesting to note that in unimplanted silicon nitride films annealing even at $T_a=900$ °C for 30 min results in a factor of 2 decrease of the intensity of the green PL peak ($\lambda\simeq520$ nm).[17] The process leading to the formation of light-emitting centers with

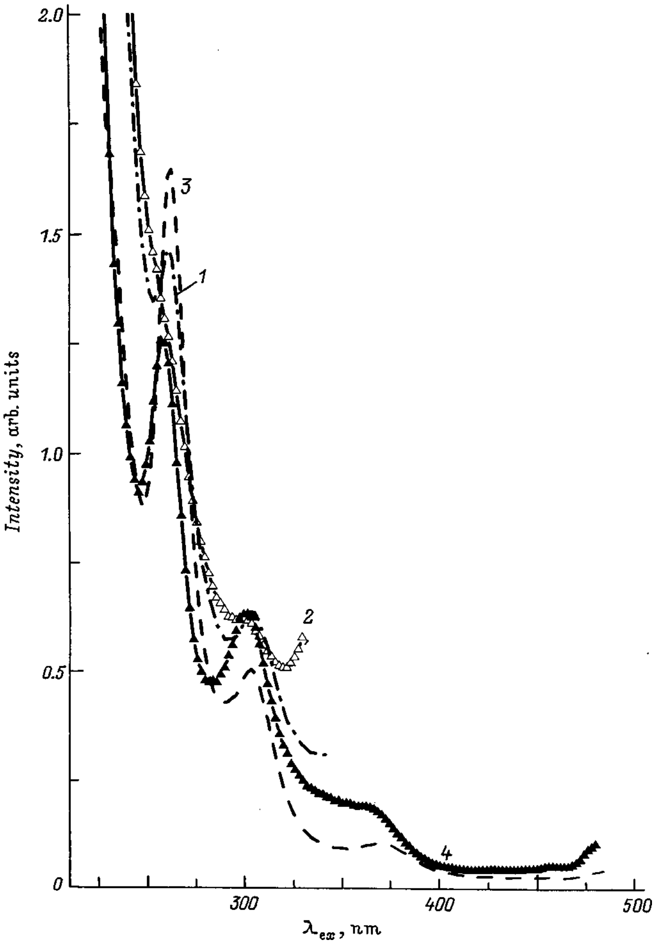

FIG. 4. Excitation spectra of the violet (*1, 2*) and green (*3, 4*) PL peaks of Si_3N_4 films before (*1, 3*) and after (*2, 4*) implantation of 150-keV Ge^+ ions with dose 0.5×10^{16} cm^{-2} (LD) $T_a=1000$ °C and 30-min anneal in an N_2 atmosphere. PL wavelength λ, nm: *1* — 380, *2* — 368, *3* — 520, *4* — 510.

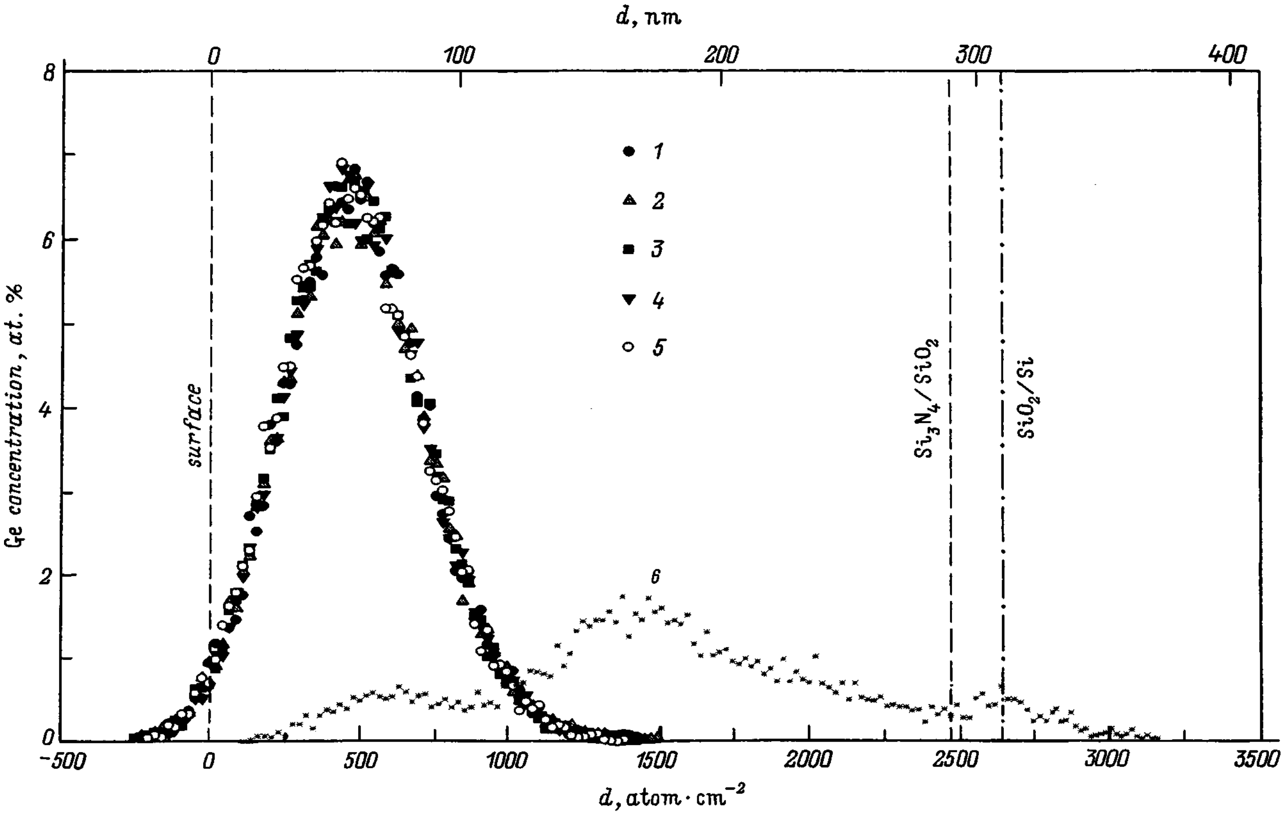

FIG. 5. Profiles of the germanium distribution in Si_3N_4 films implanted with 150-keV Ge^+ ions with dose 4.2×10^{16} cm^{-2} (HD) before (*1*) and after 30-min anneals at $T_a=600$ (*2*), 800 (*3*), 1000 (*4*), 1200 (*5*), and 1300 °C (*6*) in an N_2 atmosphere. The profiles were obtained by Rutherford backscattering of 1.7-MeV He^+ ions.

the participation of excess Ge atoms is found to be shifted in the direction of higher annealing temperatures and can proceed according to the scheme

$$\equiv\text{Si}-\text{N}= \rightarrow \equiv\text{Si}\bullet + \bullet\text{N}=, \tag{1}$$

$$\equiv\text{Si}\bullet + \bullet\text{Ge}\equiv \rightarrow \equiv\text{Si}-\text{Ge}\equiv. \tag{2}$$

The formation of ≡Ge–Ge≡ centers can also occur in a similar manner. However, it is still surprising that upon implantation of Ge atoms in the silicon nitride framework the green PL peak is not shifted along the energy scale as compared with the PL peak from unimplanted silicon nitride and from silicon nitride implanted with argon ions. This suggests that there is a possible relation between the localized states of the centers ≡Si–Si≡, ≡Si–Ge≡, and ≡Ge–Ge≡ and the levels due to, for example, the nitrogen complexes. This hypothesis was previously advanced in Ref. 7. In our case this hypothesis could also explain not only the fact that the energy of the green PL peak is constant but also the fact that the intensity of this peak increases in the presence of excess Ge atoms in the Si_3N_4 framework, which in the process of formation of ≡Si–Ge≡ and ≡Ge–Ge≡ centers also results in an increase of the purely nitrogen complexes. It has been assumed[15] on the basis of ESR data, which show that there are no paramagnetic centers during annealing of irradiated amorphous silicon nitride, that the defects =N• also pair with one another according to the reaction

$$=\text{N}\bullet + \bullet\text{N}= \rightarrow =\text{N}-\text{N}=. \tag{3}$$

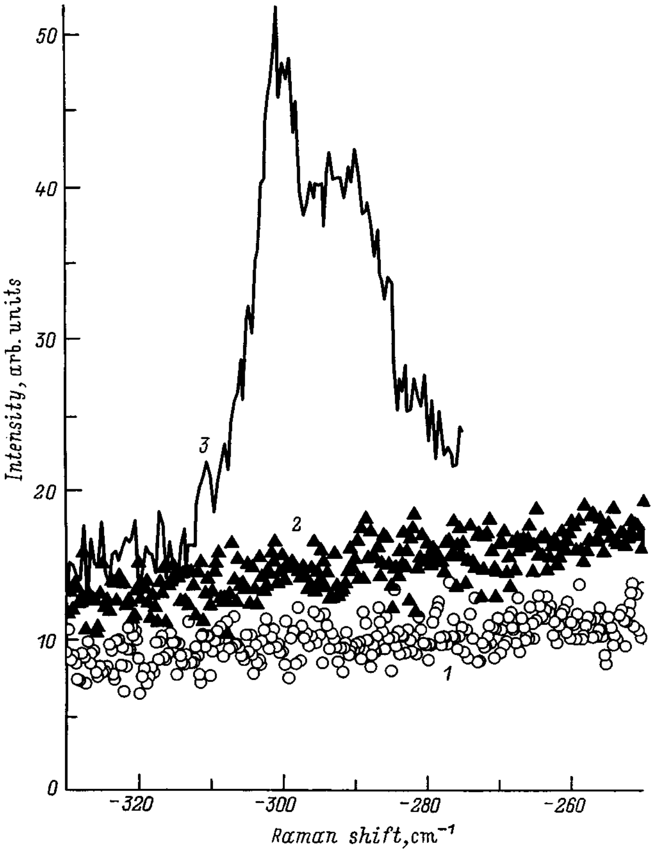

FIG. 6. Raman-scattering spectra of Si_3N_4 films implanted with 150-keV Ge^+ at doses 4.2×10^{16} cm^{-2} (HD) after 30-min anneals at $T_a=600$ (*1*), 1000 (*2*), and 1300 °C (*3*) in an N_2 atmosphere.

However, the N–N bond in silicon nitride is unstable even at temperatures 700–800 °C (Ref. 10), while in our experiments the PL peak was observed above $T_a = 1000$ °C. The most likely explanation of the fact that the energy position of the green PL peak remains constant when bond-forming Ge atoms are introduced into the Si_3N_4 host could be that the germanium atoms, which upon annealing replace the silicon atoms in the silicon nitride framework according to the scheme (1) and (2), give rise to an increase in the number of unbound silicon atoms which then form the bonds $\equiv$Si –Si$\equiv$, which are responsible for the PL bands that we observed. However, this assumption requires additional experimental confirmations.

5. CONCLUSIONS

The room-temperature PL and PL excitation spectra of Si_3N_4 films implanted with Ge^+ and Ar^+ atoms were investigated as a function of ion dose and temperature of the subsequent anneal. Together with the optical properties, the processes leading to the redistribution of the implanted atoms and the associated structural changes in the implanted silicon nitride films were studied by RBS and Raman-scattering methods. It was established that ion implantation in combination with subsequent annealing leads to the formation of both radiative and nonradiative recombination centers. The implantation of Ar^+ ions results in the formation of only nonradiative defect centers, which are annealed at $T_a \simeq 600$ °C. The presence of bond-forming Ge atoms in the Si_3N_4 host stimulates the formation of centers emitting in the green ($\lambda \simeq 520$ nm) and violet ($\lambda \simeq 380$ nm) regions of the spectrum. The PL intensity decreases with increasing Si^+ dose and increases with annealing temperature up to 1000 °C. The character of the dose dependence and the absence of redistribution of Ge atoms and changes in the Raman-scattering spectrum for annealing temperatures $T_a \leqslant 1000$ °C shows that the centers of green and violet PL are not associated with Ge nanocrystals and are formed as a result of restructuring of the bonds between nearest-neighbor atoms. Their most likely source are $\equiv$Si–Si$\equiv$, $\equiv$Si–Ge$\equiv$, and $\equiv$Ge–Ge$\equiv$ centers. The possible recombination mechanisms leading to the observed growth in the intensity of the green PL band with the energy position of its maximum remaining unchanged compared with Si_3N_4 films which have not been implanted with Ge^+ are discussed.

We wish to thank V. A. Gritsenko for a helpful discussion of this work and H. Fröb for assisting in the measurements of the photoluminescence spectra. I. E. Tyschenko thanks the Ministry of Arts and Sciences of Saxony (Germany) for financial support in the course of these investigations.

*)E-mail: tys@isp.nsc.ru; Fax: (382-2)332771

---

[1] T. Shimizu-Iwayama, K. Fujita, S. Nakao, K. Saitoh, T. Fujita, and N. Itoh, J. Appl. Phys. **75**, 7779 (1994).

[2] H. A. Atwater, K. V. Shcheglow, S. S. Wong, K. J. Vahala, R. C. Flagan, M. L. Brongersma, and A. Polman, Mater. Res. Soc. Proc. **321**, 363 (1994).

[3] W. Skorupa, R. A. Yankov, I. E. Tyschenko, H. Fröb, T. Böhme, and K. Leo, Appl. Phys. Lett. **68**, 2410 (1996).

[4] L.-S. Liao, X.-M. Bao, N.-Sh. Li, X.-Q. Zheng, and N.-B. Min, J. Lumin. **68**, 199 (1996).

[5] *Silicon Nitride in Electronics*, edited by A. V. Rzhanov (Novosibirsk, Nauka, 1982), p. 198.

[6] V. V. Vasil'ev, D. G. Esaev, and S. P. Sinittsa, Zh. Tekh. Fiz. **52**, 795 (1982) [Sov. Phys. Tech. Phys. **27**, 508 (1982)].

[7] P. A. Pundur and Yu. G. Shevalin, Izv. Akad. Nauk Latv. SSR **5**, 74 (1985).

[8] V. G. Baru, S. Bayliss, A. P. Chernushich, M. I. Elinson, P. Harris, V. A. Jitov, V. I. Pokalyakin, G. V. Stepanov, and L. Yu. Zaharov, Microelectron. Eng. **36**, 111 (1997).

[9] V. V. Vasilev, I. P. Mikhailovskii, and K. K. Svitashev, Phys. Status Solidi A **95**, K37 (1986).

[10] V. A. Gritsenko, *Structure and Electronic Structure of Amorphous Insulators in Silicon MIS Structures* (Novosibirsk, Nauka 1993), p. 280.

[11] V. A. Volodin, M. D. Efremov, and V. A. Gritsenko, Solid State Phenom. **57-58**, 501 (1997).

[12] L. Rebohle, J. von Borany, R. Grotzschel, A. Markwitz, B. Schmidt, I. E. Tyschenko, W. Skorupa, H. Fröb, and K. Leo, Appl. Phys. Lett. **71**, 19 (1997).

[13] P. A. Pundur and Yu. G. Shevalin, Zh. Prikl. Spektrosk. **5**, 843 (1986).

[14] H. J. Stein, J. Appl. Phys. **47**, 3421 (1976).

[15] V. A. Gritsenko, A. V. Rzhanov, S. P. Sinitsa, V. I. Fedchenko, and G. N. Feofanov, Dokl. Akad. Nauk SSSR **287**, 1381 (1986) [Sov. Phys. Dokl. **31**, 341 (1986)].

[16] V. A. Gritsenko and P. A. Pundur, Fiz. Tverd. Tela (Leningrad) **28**, 3239 (1986) [Sov. Phys. Solid State **28**, 1829 (1986)].

[17] V. V. Vasilev and I. P. Mikhailovskii, Phys. Status Solidi A **90**, 355 (1985).

Translated by M. E. Alferieff

SEMICONDUCTORS VOLUME 33, NUMBER 5 MAY 1999

Slow photoconductivity relaxation due to radiation defects in *p*-type Si

S. E. Mal'khanov

St. Petersburg State Technical University, 195251 St. Petersburg, Russia

(Submitted July 2, 1998; accepted for publication October 14, 1998)
Fiz. Tekh. Poluprovodn. **33**, 567–568 (May 1999)

Data on photoconductivity relaxation due to one of the radiation defects in *p*-type silicon employed in radiation technology are analyzed on the basis attachment levels. Defects formed by divacancies in a positive charge state (W^+), $\lambda = 4\ \mu$m, are investigated. It is shown that this defect is an attachment level with respect to deeper levels of radiation defects, for example, a K center (which appears clearly after preliminary short-wavelength irradiation). As a result, processes with short relaxation times appear in the photoconductivity. It is also shown that fast photoconductivity relaxation can be obtained in this material either by increasing to 15 MeV the energy of the electrons used to introduce a given radiation defect or by increasing the intensity of the irradiation with 1-MeV electrons. © *1999 American Institute of Physics.* [S1063-7826(99)00805-4]

Investigations of photoconductivity (PC) relaxation are necessary, for example, for the development of photodetectors as well as devices where fast recombination of charge carriers is critical.[1–3] In the present paper we report the results of an experimental study of slow relaxation of PC in KDB-10 silicon irradiated with 1- and 15-MeV electrons and ^{60}Co γ rays.

The experimental samples consisted of $5\times2\times0.2$ mm parallelepipeds. Ohmic contacts were produced by gradual deposition and thermal compression of aluminum along the edges of the flat face. Irradiation with 15-MeV electrons was performed in a linear electron accelerator at doses up to $10^{16}\ \mathrm{cm}^{-2}$ and irradiation with 1-MeV electrons was performed in a RTÉ-1V accelerator. The irradiation intensity was varied in the range $10^{13}-10^{14}\ \mathrm{cm}^{-2}\cdot\mathrm{s}^{-1}$. The compensation of silicon by radiation defects (RDs) to observe PC was close to 1 (the concentration of K centers — the main impurity compensating RDs — is estimated to be $10^{15}\ \mathrm{cm}^{-3}$, while the concentration of RDs that determine the slow relaxation is an order of magnitude smaller). The photoconductivity investigations were performed with an IKS-21 infrared spectrometer with an NaCl prism. A light beam was focused on the flat face of the sample in a cryostat at liquid-nitrogen temperature. The experimentally measured power of the infrared (IR) radiation was of the order of $10^{-4}\ \mathrm{W/cm}^2$ at a wavelength of 4 μm. The slit-covering time was 0.2 ms with 20-Hz modulation of square light pulses.

Figure 1a shows the relaxation of photoconductivity after the 3.9 μm IR radiation was switched off once in a sample irradiated with 1-MeV electrons. Figure 1b shows the same relaxation with periodic action of light with the covering time of the entrance slit equal to 0.2 ms. Analysis of the figure shows that the decay of the photoconductivity is described very accurately by an exponential dependence with time constant 1.9 s. Such behavior could mean that this relaxation is due to charge transfer on one level. This level (referred to below as the ''working'' level) is known to belong to a divacancy in a positive singly-charged state with a resonance-type characteristic photoionization cross section and has been observed previously.[4] (For this level the maximum photoionization cross section at 3.9 μm is $4\times10^{16}\ \mathrm{cm}^2$.) If carriers can fill this level by complicated schemes, then it can be emptied via an optimal path with the carriers being transferred to the valance-band edge.

Figure 2 shows the photoconductivity relaxation curves measured for the same sample at time intervals after the sample was first irradiated with IR radiation with wavelength corresponding to half the band gap in silicon. As follows

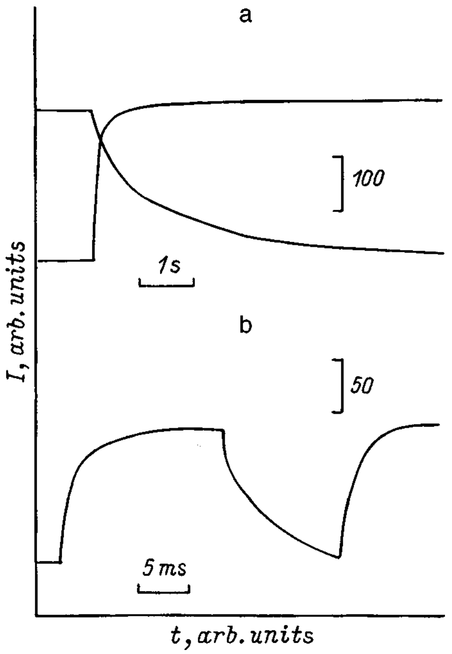

FIG. 1. Kinetics of growth and decay of stationary photoluminescence in irradiated silicon ($\lambda = 3.9\ \mu$m): a — single switching on and switching off of the light, the covering time of the entrance slit of the spectrometer is 10 ms; b — periodic action by square light pulses, the covering time of the entance slit of the spectrometer is 0.2 ms.

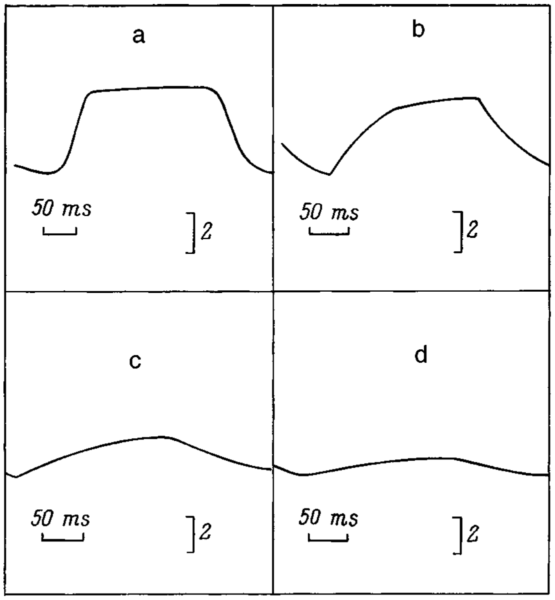

FIG. 2. Kinetics of growth and decay of stationary PC in irradiated silicon ($\lambda = 3.9\ \mu$m) after preliminary irradiation at $\lambda = 2\ \mu$m with the time elapsed after irradiation, s: a — 5, b — 30, c — 100, d — 500.

from the figure, such preliminary illumination sharply shortens the trailing edge of the relaxation curve. If it is assumed, following Ref. 2, that the working level in this situation is essentially entirely filled with holes and the relaxation process for such a stimulated filling of the working level is described well by an exponential function,[1)] then the working level is an attachment level with respect to deeper levels (for example, a level belonging to a *K* center — a RD with the highest concentration). The time constant of this process is estimated to be 390 s. In estimating the time constant of the process of stimulated filling of the working level (see Fig. 2), a very short (noninfluential) and long (strongly influential) relaxation, which we calculate to be 390 s, were observed. Disregarding the short component can result in underestimation of the relaxation time constant. In other words, stimulated filling of the working level remains for a substantial time.

The energy level spectra and, in part, defect formation in silicon bombarded by high-energy electrons have been investigated in detail in a previous work.[5] The energy level spectra in silicon irradiated with 1, 4–8, and 15-MeV electrons are largely similar to one another. However, the fraction of deeper levels increases with decreasing electron energy. The effect of this behavior is that the kinetics of PC at $\lambda = 3.9\ \mu$m in *p*-type Si exhibits long relaxation of photoconductivity, such that the operation of devices based on these RDs becomes unacceptable. A working level with the essential concentration cannot be obtained with γ irradiation.

In conclusion, I call attention to the fact that quite short photoconductivity relaxation times can be obtained by increasing the electron irradiation intensity. Note also that the present analysis is based on model ideas about the mechanisms of the attachment levels, described, for example, in Refs. 1–3.

In summary, the existence of slow relaxations of PC at $\lambda = 3.9\ \mu$m is essentially determined by the electron energies and by the intensities of electron irradiation of *p*-type silicon with the introduction of the essential spectrum of energy levels of RDs into it.

[1)] Our analysis, which was performed by comparing the experimental and theoretical dependences (except for the initial section), shows that this is indeed so.

---

[1] S. M. Ryvkin, *Photoelectric Phenomena in Semiconductors* (Fizmatgiz, Moscow, 1963).

[2] A. Milnes, *Deep Impurities in Semiconductors* [Wiley, New York, 1973; Mir, Moscow, 1977].

[3] M. S. Yunusov, M. Karimov, and B. L. Oksengendler, Fiz. Tekh. Poluprovodn. **32**, 264 (1998) [Semiconductors **32**, 238 (1998)].

[4] N. V. Kolesnikov, A. A. Lebedev, and S. E. Mal'khanov, Fiz. Tekh. Poluprovodn. **13**, 812 (1979) [Sov. Phys. Semicond. **13**, 479 (1979)].

[5] S. E. Mal'khanov, Peterburgskiĭ zhurnal élektroniki, No. 3, 16 (1997).

Translated by M. E. Alferieff

Dependence of the properties of $Cd_{1-x}Zn_xTe$ crystals on the type of intrinsic point defect formed by oxygen

N. K. Morozova, I. A. Karetnikov, V. V. Blinov, V. K. Komar, V. G. Galstan, and V. S. Zimogorskiĭ

Moscow Energy Institute (Technical University), 111250 Moscow, Russia

(Submitted September 25, 1998; accepted for publication October 14, 1998)
Fiz. Tekh. Poluprovodn. **33**, 569–573 (May 1999)

Coordinated investigations of cathodoluminescence spectra, microstructure, specific resistance and presence of oxygen in $Cd_{1-x}Zn_xTe$ crystals are used to identify how the electrical properties and degree of perfection of the crystal lattice of these materials are affected by the form in which oxygen is present as an intrinsic point defect. It is found that oxygen, which is the main background impurity in $Cd_{1-x}Zn_xTe$, forms different types of point defects at different positions in the lattice, depending on the ratio [Cd]/[Zn]. The optimum composition for making detectors of ionizing radiation, for which the crystal resistance is highest, is $Cd_{0.77}Zn_{0.23}Te$. *© 1999 American Institute of Physics.* [S1063-7826(99)00905-9]

Detectors of ionizing radiation can now be made from high-resistivity ($10^9\ \Omega\times\mathrm{cm}$) CdTe that operate at room temperature; however, their resolution does not exceed 2%.[1,2] Improving their resolution requires crystals with resistivities higher than CdTe. It has been reported[1,3] that detectors of ionizing radiation have been made with energy resolutions down to 1% at 300K using high-resistivity (up to $10^{11}\ \Omega\cdot\mathrm{cm}$) $Cd_{1-x}Zn_xTe$ crystals with a certain composition. Komar *et al.*[3] grew these crystals by the Bridgman method, using a considerable excess of metal in the starting chemical mix. The crystals as grown had *n*-type conductivity and resistivities up to $10^{10}-10^{11}\ \Omega\cdot\mathrm{cm}$. Since excesses of metal above the stoichiometric composition cause intrinsic donors, this should have produced a rather low intrinsic resistivity for the crystals, and the reason for their high resistivity is unclear.

Our goal in this study was to obtain new information regarding the nature of the defects responsible for the properties of solid-solution $Cd_{1-x}Zn_xTe$ crystals, based on combined investigation of the cathodoluminescence spectra, the resistivity, the content of ordinarily unmonitored background oxygen impurities, the microstructure, etc. Identifying the type of defect formation in these crystals would allow us to intentionally control the process of crystal growth.

Cathodoluminescence (CL) spectra were investigated at excitation levels of $10^{22}\ \mathrm{cm}^{-3}\times\mathrm{s}^{-1}$ in the 500 to 2700-nm range. The method of CL investigation was described in Ref. 4. The concentrations [Cd], [Zn], [Te] were determined by quantitative *x*-ray microanalysis.[5] The microstructure and micro-uniformity were monitored by a scanning electron microscope (SEM). Gas-chromatographic analysis was used to study the content of oxygen in the crystals.[6]

The resistivity was measured by a contact method. Point contacts were used in the form of needles (0.1 mm) made of fused-on indium.

The crystal properties were studied on fresh cleaves of $Cd_{0.8}Zn_{0.2}Te$ crystals grown from a melt using the Bridgman technique.[3] This regime ensures single-crystal growth over two-thirds of the length of the bar, after which a transition to polycrystalline material is observed with an abrupt change in the properties and a sharp boundary (see what follows). Figure 1 shows a sketch of the bar with a curved single-crystal–polycrystal boundary (see the inset). In this figure we also show where the cleaves were made. Microanalysis at all of the cleaves with respect to length *l* and radius *r* of the bar indicates an excess of metal over tellurium—the quantity [Cd + Zn]–[Te] , which correlates1) with departures from stoichiometry. This quantity, which does not change much along the bar, is $\sim(5-8)\times10^{20}\ \mathrm{cm}^{-3}$ in the ''nose'' region, $6\times10^{20}\ \mathrm{cm}^{-3}$ over the entire central region, and $7.5\times10^{20}\ \mathrm{cm}^{-3}$ at the end of the single-crystal portion of the bar. As we enter the polycrystalline region, it decreases slightly (to $4\times10^{20}\ \mathrm{cm}^{-3}$). In addition to measurements at the cleaves, we used the same microanalysis method on longitudinal slices of the bar in the directions of *l* and *r* (see the inset in Fig. 1), mapping the concentrations of [Cd] and [Zn] in steps of 1 mm. The results are in agreement with each other.

Changes in the composition along the bar correlate directly with changes in the width of the band gap of $Cd_{1-x}Zn_xTe$; therefore, we investigated the exciton spectra, whose bands shift considerably with small changes in composition (Fig. 1). Figure 1 shows the exciton spectra for various sections of the bar: the front (*1, 1'*), the main single-crystal middle section (*2, 2'*), and the polycrystalline end (*3, 3'*). The distribution of intensity of the exciton bands over the crystal is shown in Fig. 2 (curve *1*). The spectra were taken at fresh (110) cleaves at 80 and 300 K. Empirical dependences $E_g(x)$ for $Cd_{1-x}Zn_xTe$ can be found in the literature.[7–9] The calculated values of *x* based on the data of Refs. 8 and 9 agree closely with one another. For estimating *x* we use the function[9]

$$E^{\mathrm{ex}}(Cd_{1-x}Zn_xTe)=E^{\mathrm{ex}}(\mathrm{CdTe})+0.525x+0.26x^2, \qquad (1)$$

where the energy E^{ex} is in eV, $E^{\mathrm{ex}}(\mathrm{CdTe})=$ 1.579 eV is the energy of the maximum of the observed exciton band for

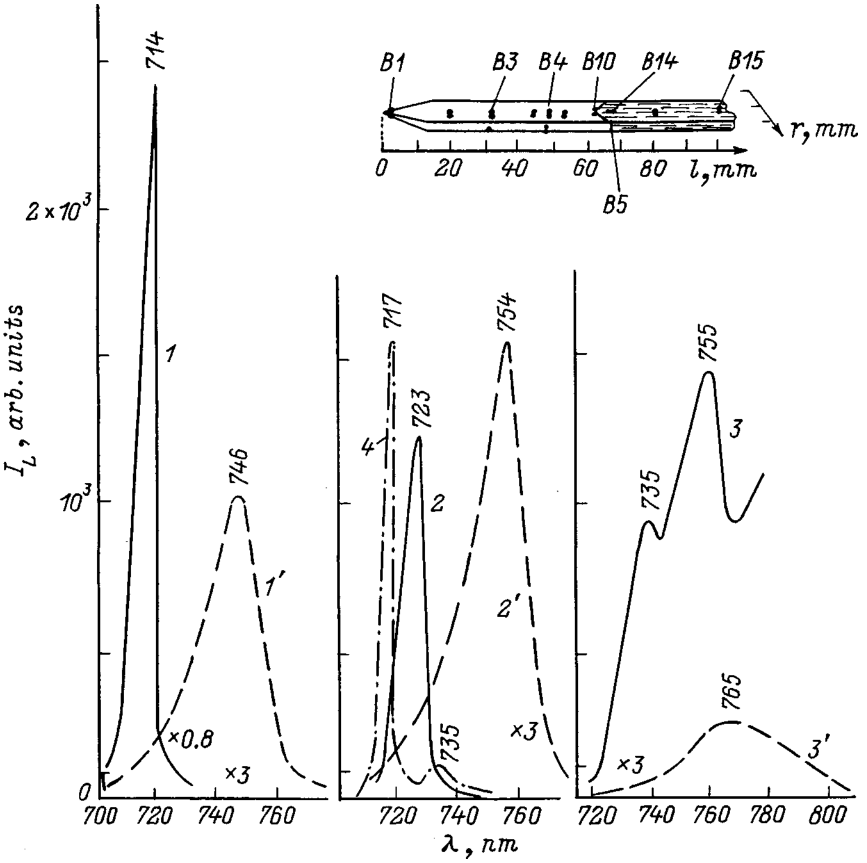

FIG. 1. Excitonic spectra of cathodoluminescence along the length of a bar of $Cd_{1-x}Zn_xTe$ at the beginning of the single-crystal portion (*1, 1′*), in the middle (*2, 2′*), and in the polycrystalline zone (*3, 3′*). *1–3* and *1′–3′* are for the central portion of the crystal, *4* is for near the crucible. Wavelengths of the maxima are expressed in nm. In the inset we sketch the bar, defining its dimensions and the position of the cleaves.

cathodoluminescence of CdTe at a temperature of 80 K, $E^{ex}(CdTe) = 1.510$ eV is the same for $T = 300$ K, and x is the mole fraction of zinc. It turns out that the computed value of x obtained from the exciton spectra is in satisfactory agreement with the results of microanalysis.

Investigations of the exciton spectra showed that in the regions of the crystal that were the first to solidify from the preset composition of the melt the exciton band was shifted towards short wavelengths, indicating an increase in the concentration [Zn]. These are the regions close to the conical bottom and wall of the crucible. The maximum content of ZnTe in the solid solution reached 27 mole % for these regions, for which the exciton band position is 713–714 nm (80 K). In the central portion of the bar the position of the exciton bands is 720–723 nm, which corresponds to ~ 24 mole % ZnTe. Thus, the composition of the bar changes in the *r* direction and in the *l* direction in the range 2–3%. These results agree with the microanalysis data. The reason for these changes in composition could be the different melting temperatures of ZnTe (1300 °C) and CdTe (1100 °C). Initially, as the crucible cools, the temperature is lower in its outer regions than it is at its center. In these regions the more refractory material crystallizes out, and the resulting solid solution is enriched with ZnTe, while the liquid phase is enriched with CdTe. The center portion of the bar solidifies later, which leads to formation of a curved crystallization front. Due to the increased conversion of ZnTe to the solid phase, the amount of zinc gradually decreases along the length of the bar, i.e., the ratio [Cd]/[Zn] increases. However,

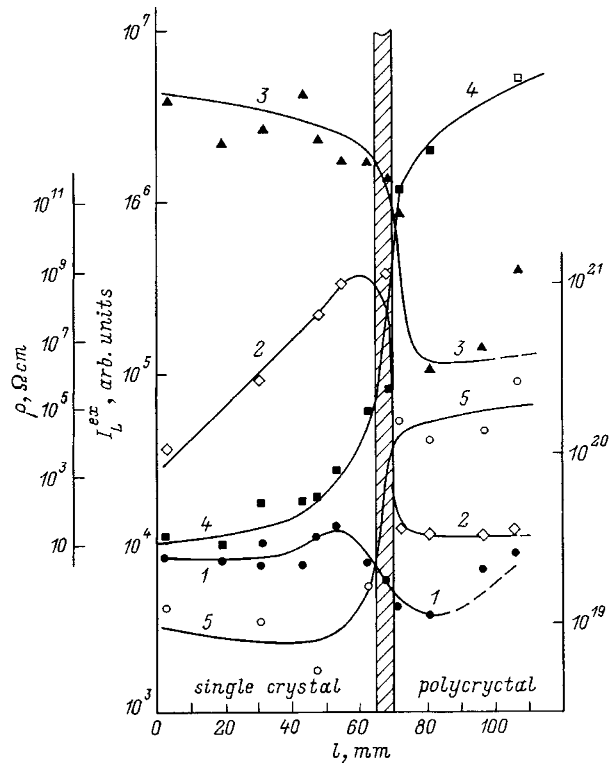

FIG. 2. Comparison of the distribution of primary characteristics of $Cd_{1-x}Zn_xTe$ down the length of the bar: *1*—intensity of the exciton band I^{ex} at 300 K, *2*—resistivity ρ, *3*—intensity of the band at $\lambda = 1200$ (1500) nm at $T = 80$ K, *4*—intensity of self-activated luminescence ($\lambda = 800$ nm) at $T = 80$ K, *5*—total concentration [O] of oxygen. The intensities of the bands are calculated from the area under the curve.

the central portion of the bar ($l \simeq$ 30–50 mm) has a composition close to 23 mole % ZnTe.

At the point where the initially preset growth regime is disrupted and the transition to polycrystalline growth begins, we observed an enhancement of the edge emission ($\lambda =$ 755 nm in Fig. 1, curve *3*). It is well known[10] that this emission is associated with the presence of shallow acceptors caused by group-I elements.

Enhancement of the edge emission line is also observed in the single-crystal portion of the bar at the wall of the crucible ($\lambda =$ 735 nm in Fig. 1, curve *4*). In this case the intensity increases and the half-width of the exciton band decreases, probably due to the appearance of a bound exciton at the same impurity centers.

The half-width and intensity of the exciton bands can be used to characterize the degree of crystal perfection of the structure.[11] Let us compare these quantities for our bulk solid-solution single crystals with those of CdTe,[12] for which the half-width of the exciton bands is 23 meV (at $T =$ 80 K) and ~ 50 meV (at $T =$ 300 K). A rapid increase in the half-width of the exciton bands ΔE^{ex} is observed in the polycrystalline portion of the bar. In this case the high emission intensity I^{ex} for the polycrystalline region attests to the perfection of its structure. Studies in the SEM showed that the crystallites are quite large (the average grain size is $\sim 150-200\,\mu$m), and their composition is uniform; therefore, the broadening of the bands is not associated with overlap of lines from fine grains of differing composition. However, in this portion of the bar the oxygen concentration [O] increases sharply (Fig. 2, curve *5*). We may assume that the increase in the half-width of the exciton bands is determined by enhancement of the exciton-phonon interaction and the contribution of LO-satellites, as was observed in Ref. 13 at large concentrations of isoelectronic centers (background impurities of oxygen at lattice sites). In fact, the content of this impurity in the semicrystalline part reaches $(2-3) \times 10^{20}\,\mathrm{cm}^{-3}$.

The half-width of the exciton bands for cleaves from the single-crystal portion of the $\mathrm{Cd}_{1-x}\mathrm{Zn}_x\mathrm{Te}$ bar was smaller or comparable to that of CdTe.[12] Along the axis of the bar, the smallest half-width of the exciton bands corresponds to cleaves at a distance l of about 50 mm. For cleaves of this region, the intensity of the exciton bands also passes through a maximum (Fig. 2, curve *1*). As is clear from Fig. 2, the resistivity along the length of the bar increases monotonically from the start of the bar ($10^4\,\Omega\cdot$ cm), and passing through a maximum at $l \approx 50$ mm ($10^{10}\,\Omega\cdot$ cm), rapidly falls off as the single-crystal–polycrystal boundary is approached, and in the polycrystalline portion of the bar comes to $10-10^2\,\Omega\cdot$ cm.

Our previous investigations of the behavior of oxygen in II–VI crystals[11–16] lead us to suspect that the reason for the high resistivity of $\mathrm{Cd}_{1-x}\mathrm{Zn}_x\mathrm{Te}$ crystals grown in the presence of excess metal in the starting chemical mix is the presence of background oxygen impurities. The concentration of oxygen was of order $10^{19}\,\mathrm{cm}^{-3}$ over the entire single-crystal portion of the bar. The oxygen interstitial O_i is an acceptor. However, we cannot associate the increase in resistivity along the length of the single-crystal portion of the bar with accumulation of oxygen impurities, because the concentration $[\mathrm{O}_i]$ is roughly constant over the entire length of the single-crystal portion of the bar. We even observed a decrease in the total oxygen content in the region of highest resistivity as the number of $\mathrm{Zn}_{\mathrm{Cd}}$ defects decreases in the composition of the solid solution. This corresponds to an increased value of the ratio of concentrations [Cd]/[Zn], which in the high-resistance region is on the order of 3.

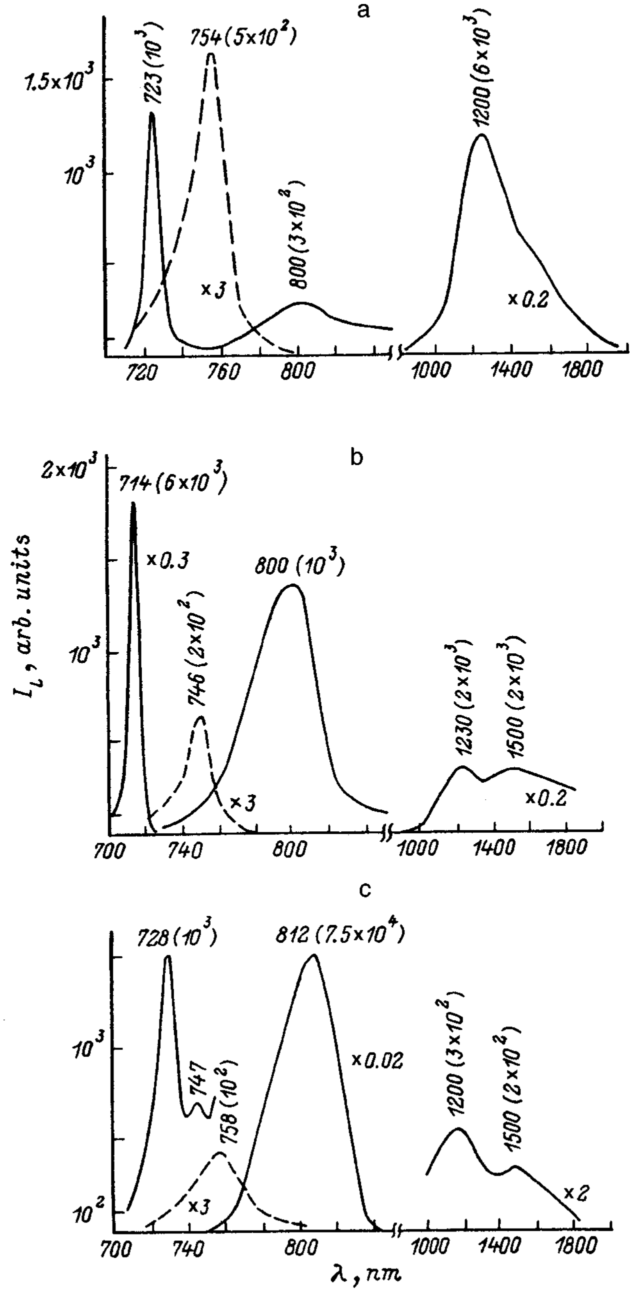

FIG. 3. Change in the cathodoluminescence spectra down the length of the $\mathrm{Cd}_{1-x}\mathrm{Zn}_x\mathrm{Te}$ bar: a—middle of the high- resistance portion, b—end of the single-crystal portion, c—polycrystalline region. Wavelengths of the maxima are expressed in nm along with intensities of the corresponding bands (in brackets). Measurement temperature: solid curves—$T = 80$ K, dashed—$T = 300$ K.

Figure 3 shows the change in the CL spectrum over a wider spectral range for "typical" cleaves along the length of the bar. Spectra were measured for the central single-crystal portion of the bar (a), the boundary between single-crystal and polycrystalline material (b), and the end of the polycrystalline portion (c). As we showed in Ref. 12, the CL spectra of $Cd_{1-x}Zn_xTe$ characteristically exhibit not only excitonic bands but also two other groups of bands in the regions ~ 800 and 1200–1500 nm. The change in intensity of these bands along the length of the bar is plotted in Fig. 2.

Investigation of the $\lambda = 1200$ (1500)-nm band shows that it does not shift either with $Cd_{1-x}Zn_xTe$ composition or with temperature, since it is determined by intracenter transitions with the participation of vacancy defect V_{Te} levels.[12] The formation of V_{Te} defects is determined by the large excess of metal in the starting chemical mix. The high intensity of the band at 1200 (1500) nm over almost the entire initial length of the single-crystal portion of the bar attests to the presence of V_{Te} in considerable concentrations (Fig. 2, curve *3*). The large excess of metal in these crystals, which is confirmed by microstructural data, probably implies the presence of the defect V_{Te} rather than shallow intrinsic donors like Cd_i. The fact that V_{Te} coexists with oxygen in concentrations of $10^{19}\,cm^{-3}$ is evidence that the oxygen is not filling lattice sites occupied by the vacancy V_{Te}. The observed concentration $[O] \simeq 10^{19}\,cm^{-3}$ is typical of solid solutions of oxygen in II–VI compounds.[11,14,15] In this form, oxygen can enter during the growth of solid-solution crystals of $Cd_{1-x}Zn_xTe$ as an O_i defect $(+\Delta V)$, which compensates for the volume discrepancy generated by the electrically neutral Zn_{Cd} center $(-\Delta V)$. In the lattice, the oxygen O_i acceptor compensates for the intrinsic donors, probably V_{Te} (see Ref. 11); as the V_{Te} concentration in the central portion of the bar decreases slightly (Fig. 2, curve *3*), the electrical resistance rapidly increases. The disruption of single-crystal growth with decreasing V_{Te} takes place quite rapidly. As is clear from Fig. 2, the high-resistance portion of curve *2* is replaced by an abrupt decrease in the resistivity toward the end of the single-crystal region, at which point all the data indicate a change in the defect type in the crystal. Even at the single-crystal–polycrystal boundary the resistivity decreases, and as we enter the polycrystalline region it falls rapidly by 7 or 8 orders of magnitude. It is clear from Fig. 2 that in this case the intensity of the $\lambda = 1200$ (1500)-nm band also decreases rapidly (i.e., the $[V_{Te}]$ concentration decreases), while the concentration [O] increases (curve *5*) and the intensity of the band at $\lambda = 800$ nm increases (curve *4*).

According to Refs. 11–16, the 800-nm band is associated with the presence of oxygen at lattice sites, i.e., O_{Te}. This defect is isoelectronic, and hence electrically neutral. As our work in Ref. 12 showed, the observed band at $\lambda \simeq 800$ nm is by its nature analogous to self-activated emission in ZnSe:Te caused by nearest-neighbor Frenkel pairs (A-centers) stabilized by oxygen at lattice sites.[13,16] The band does not exhibit the recombination properties that are typical of donor-acceptor recombination, because it is determined not by a set of (D–A) pairs with differing values of the distance between donors and acceptors r_{D-A}, but rather by only one type of pair with a constant value of r_{D-A}.

Our investigation of the 800-nm band in the CdTe–ZnTe system, in particular, its solid solutions, showed that the spectral position of these bands depends on the composition: the band shifts towards long wavelengths with increasing CdTe, as does the width of the ban gap E_g. The intensity of this emission, which is high only when there is an excess of Cd, increases rapidly in $Cd_{1-x}Zn_xTe$ with high concentrations of O_{Te}. Under these conditions, the center is stabilized when it includes both O_{Te} $(-\Delta V)$ and Cd_i $(+\Delta V)$. As shown in Refs. 10 and 12, this band consists of a set of *LO*-satellites and does not shift spectrally with temperature, and we observe only an enhancement of the short-wavelength component with increasing temperature (from 80 to 400 K).

It is clear from Fig. 2 (curve *4*) that the self-activation luminescence band at $\lambda \simeq 800$ nm in the spectrum of $Cd_{1-x}Zn_xTe$ is very weak in the main single-crystal portion of the bar that we investigated (when the oxygen is located at interstitial sites). The luminescence intensity in the 800-nm region begins to increase with decreasing intensity of the $\lambda = 1200$ (1500)-nm band, i.e., with decreasing $[V_{Te}]$ concentration, and with the abrupt decrease in the resistivity ρ (Fig. 2, curves *2* and *4*). In this case the oxygen concentration discontinuously reaches the solubility limit for this impurity in the substitutional solid solution with a large excess of Cd_i (Fig. 2, curve *5*), while at the same time the $\lambda \simeq 800$-nm band undergoes an abrupt enhancement (Fig. 2, curve *4*).

All of these data confirm the assumption we made previously regarding a change in the type of defect at the end of the single-crystal growth zone of the bar, with oxygen transferring to lattice sites $O_i \rightarrow O_{Te}$ by filling the vacancies V_{Te}. The excess metal in the crystal now appears as Cd_i defects. The main reasons for this change in the type of defect and the conversion $O_i \rightarrow O_{Te}$ are a decrease in the number of Zn_{Cd} centers, which initially keep the oxygen in interstitial sites, and an accumulation of Cd in the melt. The resistivity of the bar falls sharply when the O_i acceptors, with their initial concentration of $10^{19}\,cm^{-3}$, disappear as the oxygen atoms enter lattice sites, and shallow intrinsic Cd_i donors replace the V_{Te}.

Analysis of these results lead us to the following conclusions.

— Single-crystal $Cd_{1-x}Zn_xTe$ with excess metal concentrations on the order of $6 \times 10^{20}\,cm^{-3}$ or greater (based on microanalysis data) and high resistivities up to 10^{10} $\Omega \cdot$ cm can be grown as long as the ratio of concentrations $[Cd]/[Zn] \lesssim 3$. In these materials, intrinsic donors are compensated by interstitial oxygen $[O_i]$ with concentrations on the order of $10^{19}\,cm^{-3}$.

— When the ratio [Cd]/[Zn] becomes greater than 3, the type of dominant point defect changes, i.e., $V_{Te} \rightarrow Cd_i$, and the concentration and nature of the primary background impurity oxygen changes as well, i.e., $O_i \rightarrow O_{Te}$; as a result, the resistivity drops by eight orders of magnitude.

The results of our studies of the cathodoluminescence spectra can be used to optically monitor the quality of $Cd_{1-x}Zn_xTe$ crystals intended for use as detectors of ionizing radiation. This monitoring presupposes the presence of the high-intensity $\lambda = 1200$ (1500-nm band in the CL at $T = 80$ K and low intensity of the self-activated luminescence near $\lambda \simeq 800$ nm. The ratio of band intensities at $\lambda = 1200$ (I^{1200}) and 800 nm (I^{800}), i.e., I^{1200}/I^{800}, should be $\gtrsim 10^2$.

For the optimal composition $Cd_{0.77}Zn_{0.23}Te$ the position of the exciton band corresponds to $\lambda = 722-723$ nm at $T=80$ K or $\lambda = 754-755$ nm at $T=300$ K.

[1)] Microanalysis studies only the primary components of $Cd_{1-x}Zn_xTe$ crystals.

---

[1] R. Sudharsanan, K. B. Parnharm, and N. H. Karam, in *Proceedings of the Conference ''Laser Focus World''* (June, 1996), p. 199.

[2] J. F. Butler, F. P. Doty, and B. Apotovsky, Mater. Sci. Eng., B **16**, 291 (1993).

[3] V. K. Komar, H. Hermon, M. S. Goorsky *et al.*, *Semiconductors for Room Temperature Radiation Detector Applications II*, edited by R. B. James (Pittsburgh, PA, 1998) [Mater. Res. Soc. **487** (1998)].

[4] N. K. Morozova, L. D. Nazarova, and I. A. Karetnikov, Fiz. Tekh. Poluprovodn. **29**, 1678 (1995) [Semiconductors **29**, 873 (1995)].

[5] *Practical Scanning Electron Microscopy*, edited by V. I. Petrov (Mir, Moscow, 1978).

[6] V. S. Zimogorskiĭ, N. A. Karavanov, N. K. Morozova *et al.*, Bull. IAI **66**, 22 (1989).

[7] K. Y. Lay, N. C. Giles-Taylor, J. F. Schetzina, and K. J. Bachmann, J. Electrochem. Soc. **133**, 1049 (1986).

[8] F. P. Doty, J. F. Butler, J. F. Schetzina, and K. A. Bowers, J. Vac. Sci. Technol. B **10**, 1418 (1992).

[9] E. Rzepka, A. Lusson, and A. Riviere, J. Cryst. Growth **161**, 286 (1996).

[10] Zh. R. Panosyan, Proceedings FIAN SSSR **68**, 147 (1973).

[11] L. D. Nazarova, Doctoral Diss. (MEI, Moscow 1995).

[12] N. K. Morozova, I. A. Karetnikov, V. V. Vlinov, and D. P. Nalivaĭko, *Abstracts of Reports from the Intl. Sci.-Engin. Seminar* (MEI, Moscow, 1998) p. 238.

[13] N. K. Morozova and I. A. Karetnikov, J. Appl. Spectrosc. **65**, 394 (1998).

[14] N. K. Morozova, I. A. Karetnikov *et al.*, *Zinc Sulfide: Synthesis and Optical Properties* [in Russian], Nauka, Moscow, 1987.

[15] N. K. Morozova, V. S. Zimogorskiĭ, and A. V. Morozov, Inorg. Mater. **29**, 1014 (1993).

[16] N. K. Morozova, I. A. Karetnikov, E. M. Gavrishchuk *et al.*, Inorg. Mater. **35**, 4 (1999).

Translated by Frank J. Crowne

Low-temperature anomalies exhibited by the photoelectromagnetic effect in *p*-type $Cd_xHg_{1-x}Te$

S. G. Gasan-zade, M. V. Strikha, and G. A. Shepelskiĭ

Institute of Semiconductor Physics, National Academy of Sciences of Ukraine, 252650 Kiev, Ukraine

(Submitted August 25, 1998; accepted for publication October 22, 1998)
Fiz. Tekh. Poluprovodn. **33**, 574–579 (May 1999)

When *p*-type crystals of $Cd_xHg_{1-x}Te$ ($x=0.20-0.30$) are placed in a magnetic field in the temperature range where holes freeze out onto acceptor states ($T<$ 30 K), the current associated with the photoelectromagnetic effect (PEME) is found to exhibit sign changes. It is shown that the reason for this anomalous behavior of the PEME is the changing ratio of concentrations of equilibrium and nonequilibrium current carriers. The theoretical model derived here, which takes into account the dependence of the effective ambipolar diffusion length on this concentration ratio, gives a good description of the PEME anomalies observed in experiment. *© 1999 American Institute of Physics.* [S1063-7826(99)01005-4]

INTRODUCTION

The semiconducting solid solution $Cd_xHg_{1-x}Te$ (MCT) has long been used as a material for making infrared photodetectors. As a rule, MCT photodetectors are operated cooled ($T=77-100$ K). Although the current view is that the physical properties of MCT are sufficiently well studied, this is mainly true of *n*-type material. When it comes to MCT with hole conductivity, it is well known that at low temperatures the electrical and galvanomagnetic properties of *p*-type material exhibit a number of anomalies (see, e.g., the review article in Ref. 1), some of which have not yet been convincingly interpreted.

The fact that nearly all the anomalies in the physical properties of *p*-MCT appear at low temperatures is obviously connected with the rapid decrease in the concentration of free holes when $T<20-30$ K as the latter freeze out onto localized acceptor states. One manifestation of this change is the appearance of competing channels for *n*-type conductivity. These channels appear because of the large ratio of electron mobility to hole mobility and the presence of various kinds of extended nonuniformities in MCT crystals. These nonuniformities are associated with distinctive features of the growth technology and thermal processing of MCT solid solutions and with the formation of inverted surface layers.[2–4] The photoelectric and photomagnetic phenomena can turn out to be quite sensitive to the presence of spatial nonuniformities in these crystals or epitaxial layers. Initial results of these investigations were reported in Ref. 5.

In this paper we report on low-temperature anomalies in the photoelectromagnetic effect (PEME) in *p*-MCT. We use field, temperature, spectral, and stress measurements of the PEME to derive a theoretical model that gives a good explanation of its primary features in this material.

EXPERIMENT

The samples of *p*-$Cd_xHg_{1-x}Te$ we investigated had compositions in the range $x=0.20-0.30$ and concentrations of uncompensated impurities $N_A-N_D=2\times10^{15}-10^{18}$ cm^{-3}. The samples were made from MCT single crystals obtained by directed crystallization and annealed in saturated mercury vapor at $T=400\,°C$. The concentration of active impurities was determined from the value of the Hall coefficient R_H at the impurity freezout temperature $T=78$ K. In this case, the concentration of free holes was determined by measuring the quantity R_H at rather strong magnetic fields $H>3-5$ kOe, in order to exclude the contribution of light holes to the Hall coefficient. Particular attention was paid to processing the sample surfaces. Samples that had been previously polished by chemical-mechanical means were first etched in a 5% solution of bromine in methanol and then washed in isobutyl alcohol just before making the measurements. In certain cases, an anodic oxide was deposited on the sample surface, causing a *p*-type inversion layer, i.e., with *n*-type conductivity, to form in the skin layer of the sample. Electrical contacts were deposited using fused-on indium. The linear dimensions of the samples were $0.4-0.6\times1.5-2\times6-8$ mm^3.

The PEME measurements were made by the standard method of modulating the excitation light. As light sources we used a glowbar in the wavelength range $\lambda=1-14\,\mu$m and an LG-126 laser (at $\lambda=3.39\,\mu$m). For the samples we studied, the weak-excitation condition $\Delta p\ll p$ (where Δp is the concentration of nonequilibrium holes) was satisfied for light from the glowbar at all the temperatures investigated $T=4.2-100$ K, while for the unattenuated light from the LG-126 (power of order 5 mW) it held for $T=20-30$ K.

Figure 1 shows typical temperature dependences of the resistivity ρ and Hall coefficient R_H for the *p*-type samples we investigated. These dependences will be useful in helping us understand the origins of the low-temperature photoelectric anomalies. The exponential growth of ρ and R_H as a function of $1/T$ in the low-temperature range of impurity conductivity ($T<30$ K) is connected with freezing-out of the free holes onto acceptor levels located in the gap at energies $E_A=5-7$ meV from the top of the valence band. In this case, for samples with a freshly etched surface (curves *1* and

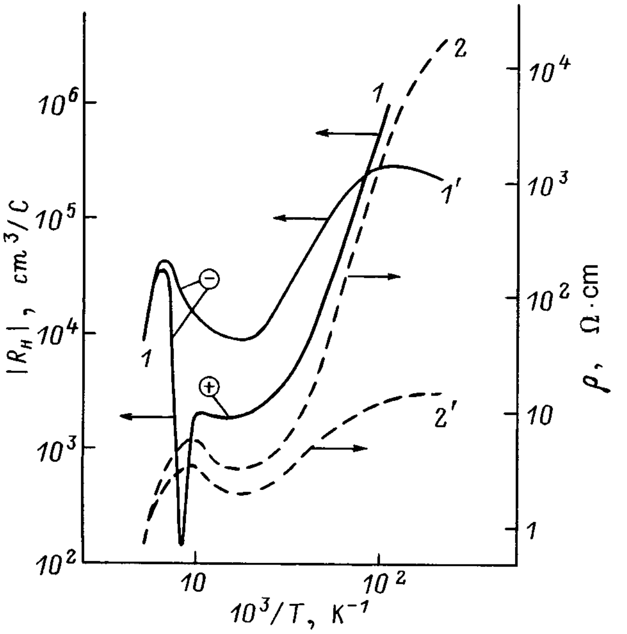

FIG. 1. Temperature dependences of the Hall coefficient R_H (*1, 1′*) and resistivity ρ (*2, 2′*) for a p-Cd$_x$Hg$_{1-x}$Te sample ($x=0.205$) and two states of the surface: *1, 2*—a freshly etched surface, *1′, 2′*—a surface with an oxide. The quantity R_H was measured at $H=5$ kOe. Sample parameters at $T=77$ K: $p=3.27\times10^{15}\,\mathrm{cm}^{-3}$, $\mu_p=3.11\times10^2\,\mathrm{cm^2/(V\cdot s)}$.

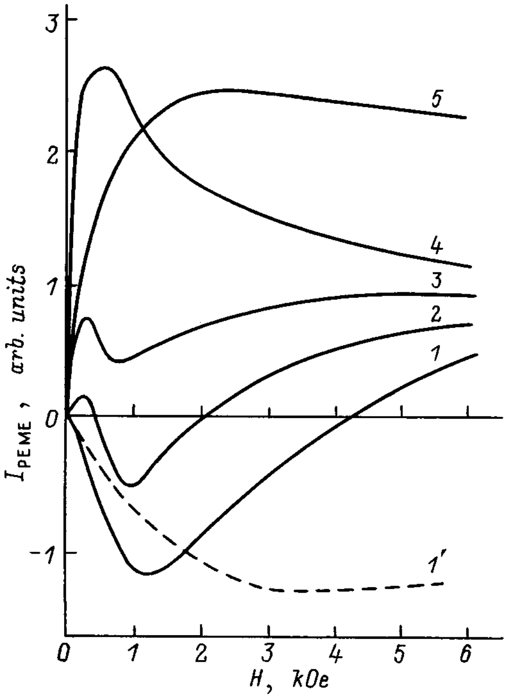

FIG. 2. Field dependence of the photomagnetic current I_{PEME} measured for the following values of temperature T, K: *1, 1′* — 4.2, *2* — 7, *3* — 10, *4* — 20, *5* — 60. The sample is the same as in Fig. 1. The intensity of excitation light was $I_0\simeq4\times10^{16}\,\mathrm{kW/(cm^2\cdot s)}$; the wavelength $\lambda=3.39$ μm. The dashed line is the function $I_{\mathrm{PEME}}(H)$ after anodic oxidation.

2) the quantity ρ has such a large value at very low temperatures that it is not possible to reliably measure the value of R_H. For certain samples we observed a second change in the sign of R_H in this temperature range. The temperature dependences of ρ and R_H were observed to be qualitatively similar for all the p-type samples with freshly etched surfaces. After a sufficiently long time in an atmosphere of air ($\sim$ 10 h), an oxide film forms on the surface of the crystal, allowing electrons to accumulate in the skin layer. As a result, the segment of rapid increase in the function $\rho(1/T)$ ends with saturation at small values of ρ. This effect is enhanced by deposition of an anodic oxide on the freshly etched surface of the sample: in this case, the hole conductivity is shunted at low temperatures by the conductivity of electrons in the inversion layer near the surface. This causes the exponential segments of the functions $\rho(1/T)$ and $R_H(1/T)$ to virtually disappear, and R_H remains negative in the entire temperature range of interest (Fig. 1, curve *1′*).

Field dependences of the photomagnetic current are shown in Fig. 2 for various values of the sample temperature. ''Normal'' behavior of the function $I_{\mathrm{PEME}}(H)$ as the magnetic field intensity H increases consists of an increasing segment that is characteristic of p-type crystals, followed by saturation of minority carriers in the strong-field range, in this case electrons (for $\mu_n H/c \gg 1$). It is clear from the figure that this pattern is observed only at $T>30$ K: when $T=4.2$ K the PEME is negative over a significant range of H (in what follows, we will refer to this sort of PEME as anomalous, by analogy with Refs. 6 and 7). At slightly higher temperatures ($T=6-8$ K), it is observed to change sign twice. Finally, in the range $T=15-30$ K it has normal sign in the entire temperature range, but the contribution of the anomalous (negative) component to the field dependence I_{PEME} is still significant, giving rise to a characteristic kink on the curve in the field range $H=1-4$ kOe.

The data in Fig. 1 indicate that in the temperature range of interest to us (4.2–30 K) the concentration of free holes decreases rapidly with decreasing temperature. Therefore, it is natural to assume that one of the main reasons for the appearance of PEME anomalies is a change in the ratio of nonequilibrium to equilibrium carrier densities. In fact, at 4.2 K the samples we investigated exhibited a decrease in the concentration of free holes by 3 or 4 orders of magnitude compared to its original value, dropping as low as $10^{11}-10^{12}\,\mathrm{cm}^{-3}$. On the other hand, the lifetime of holes increases in this same temperature range.[8] Therefore, even relatively weak light intensities $[I=10^{15}-10^{16}\,\mathrm{kW/(cm^2\cdot s)}]$ are sufficient to satisfy the strong-excitation condition $\Delta p/p \gg 1$.

In order to confirm these conclusions, we measured the field dependence of the PEME at a constant temperature of 4.2 K and at various excitation intensities I, and also at several values of uniaxial stress while keeping $T=$ const, $I=$ const. In the first case, the change in the ratio $\Delta p/p$ is due to a decrease in the quantity Δp, while in the second case it is due to an increase in p. In the latter case, p increases because uniaxial strain decreases the ionization energy of the acceptor level in MCT.[9] It is clear from Fig. 3 that in both cases the field dependences of the PEME exhibit the same features as in Fig. 2. It thus follows that PEME anomalies manifest themselves only when $\Delta p \gg p$, i.e., under strong excitation. However, we emphasize that the condition for strong excita-

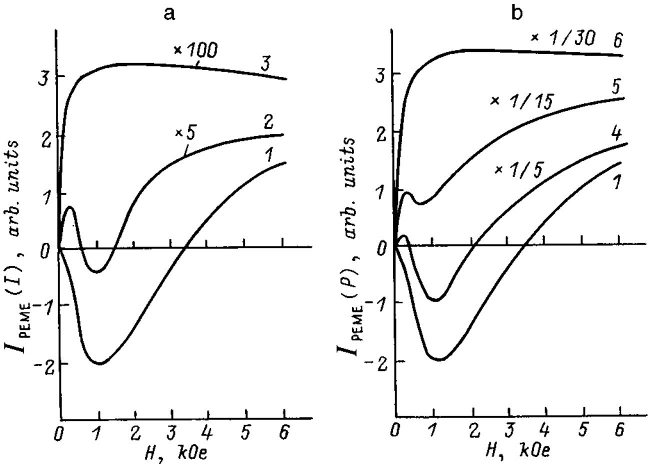

FIG. 3. Field dependence of the photomagnetic current I_{PEME} for a sample of p- $\mathrm{Cd}_x\mathrm{Hg}_{1-x}\mathrm{Te}$ ($x=0.210$): a—for values of the excitation light intensity ($\lambda=3.39\,\mu$m): *1* —$I_0\simeq 5\times 10^{16}$ kW/(cm$^2\cdot$s), *2* — $0.2\,I_0$, *3* — $0.01\,I_0$; b—for elastic strain in kilobars: *1* — 0, *4* — 1.7, *5* — 2.2, *6* —3.0. Sample parameters at $T=77$ K: $p=3.94\times 10^{15}$ cm^{-3}, $\mu_p=2.88\times 10^2$ cm^2/(V$\cdot$s).

tion for p-type MCT at low temperatures can be achieved for very moderate light intensities.

Even with other conditions fixed, the ratio of normal to anomalous PEME components can change due to the state of the sample surface. The relative magnitude of the anomalous PEME component is increased by the formation of a natural oxide film on the crystal surface after a long period in which the crystal is held in air. When an anodic oxide with thickness 150–200 Å and containing a high surface density of positive charge of $5\times 10^{11}-10^{12}$ cm^{-2} is deposited, the PEME at $T=4.2$ K has a negative sign over the entire range of H investigated (Fig. 2, curve *1′*).

THEORY

We know a number of cases[10,11] in which semiconductors exhibit anomalous PEME, where the direction of current flow and voltage polarity are opposite to their ordinary values. Based on their physical origins, we distinguish diffusion-driven and field-driven PEME anomalies.

Diffusion-driven PEME anomalies occur in thin semiconducting films, where the penetration depth of the light is large. In this case, carriers are generated almost uniformly throughout the volume of the semiconductor, and recombine primarily at the surface with a high surface recombination velocity. When the rate of recombination at the illuminated surface is appreciably larger than it is in the dark, the diffusion current of carriers will be directed primarily toward the illuminated surface, and the sign of the PEME becomes opposite to its ordinary sign. A theory of this effect was constructed in Ref. 7, and generalized in Ref. 12 to the case of crossed electric and magnetic fields.

Conversely, field-driven PEME anomalies occur in thick films ($\alpha d \gg 1$) when a layer depleted of majority carriers is present near the surface. In this case, the electric field in the space-charge region pulls minority carriers towards the illuminated surface. A review of work on PEME anomalies can be found in Ref. 13.

Since the absorption coefficient in MCT $\alpha\simeq 10^4$ cm^{-1} for the wavelengths used in our experiment, and the samples are quite thick, it is obvious that the PEME anomalies in this case cannot be diffusion-driven but rather must be field-driven, and should be associated with the presence of a near-surface space-charge electric field.[8] The results of many studies[2–4] have shown that the presence of an oxide film on the surface of p-MCT crystals leads to inversion of the surface layer, which is then depleted of majority carriers (i.e., a blocking layer).

We note that previous theoretical analysis of the PEME was based on the assumption that the effective diffusion length L is independent of the carrier concentrations n and p. This assumption is well justified for wide-gap materials like Ge and Si, where the values of the electron μ_n and hole μ_p mobilities differ by a factor of 2 or 3. However, in narrow-gap semiconductors like InSb and MCT these quantities can differ from one another by an order of magnitude, which, as we will show below, leads to important structural changes in the anomalous PEME in the temperature range where holes are ‘‘frozen out.’’

Following Ref. 6, let us write the expression for the PEME current in the presence of a space-charge layer of thickness w:

$$I_{\mathrm{PEME}}=q\eta I(\mu_n+\mu_p)\frac{H}{c}\left[-w\left(\frac{1-\exp(-\alpha w)}{\alpha w}-\frac{\exp(-\alpha w)}{1+\alpha L}\right)+\frac{L}{1+s^*L/D}\,\frac{\alpha L}{1+\alpha L}\right]. \tag{1}$$

Here q is the electron charge, η is the quantum yield, I is the intensity of the absorbed light, D is the ambipolar diffusion coefficient, and s^* is the effective surface recombination velocity, which takes into account the surface band bending. The first term in the square brackets in Eq. (1) describes the field-driven (‘‘anomalous’’) component of the PEME, while the second term describes the ordinary ‘‘diffusion-driven’’ PEME. From the form of Eq. (1) we easily see that when the first term exceeds the second in absolute value, the PEME current changes sign and becomes field-driven, i.e., anomalous.

It is important to note that Eq. (1) was obtained under certain approximations. Most importantly, it was assumed that $L \gg w$. This condition ensures quasi-equilibrium of the charge carriers in the bulk at the boundary with the space-charge layer independent of the method used to generate minority carriers. Moreover, it was assumed that the sample is thick and that the concentration of excess carriers is zero for a darkened surface.

The ratio of field-driven to diffusion-driven components in Eq. (1) was investigated in Ref. 14 for narrow-gap p-InSb. It was shown there that at liquid-nitrogen temperatures samples with a large value of s exhibited the ordinary diffusion-driven PEME over a range of comparatively small H. However, when increasing H decreases the diffusion length L to a certain critical value, the anomalous field-driven PEME begins to dominate and the PEME current changes sign. In the previous studies, in particular, in Ref. 14 use was made of the following expression to analyze the function $I_{\mathrm{PEME}}(H)$ from Eq. (1):

$$L(H)=L/[(1+(\mu_nH/c)^2)]^{1/2}. \tag{2}$$

This expression is the limiting case of a more general expression for $L(H)$ [Eqs. (16) and (18) of Ref. 10] at low levels of injection $\Delta n \ll n_0, p_0$ and for extrinsic p-type semiconductors, where $n_0 \ll p_0$. However, by virtue of the strong asymmetry of values of the electron and hole mobility, the approximation (2) for narrow-gap semiconductors requires, as we will show, a considerably stronger criterion for applicability.

Let us write the general expression for the effective diffusion length[10] in a form that is convenient for later use:

$$L^2=\tau D_n\frac{1+n/p}{n\mu_n/p\mu_p+1+(\mu_nH/c)^2(1+\mu_p n/\mu_n p)}. \tag{3}$$

Here $n=\Delta n+n_0$, $p=\Delta p+p_0$, and τ is the lifetime of carriers in the bulk (we assume that under all injection conditions the rate of recombination in an extrinsic semiconductor remains linear with respect to the concentration of excess minority carriers), where $D_n=kT\mu_n/q$ is the diffusion coefficient for electrons.

It is easy to see that Eq. (2) is a limiting case of the general expression (3) if the condition $n\mu_n/p\mu_p \ll 1$, which is considerably stronger for narrow-gap semiconductors, is satisfied (the electronic conductivity can be disregarded only when this relation holds). However, since in a narrow-gap semiconductor we have $\mu_n \gg \mu_p$, the ratio of the field-driven to diffusion-driven terms in Eq. (1) generally can be analyzed using the function $L(H,n/p)$ from Eq. (3).

We used Eq. (3) in our calculations, along with Eq. (1), for a narrow-gap material with the parameters of MCT: $D_n \approx 100\ \mathrm{cm}^2/\mathrm{s}$, $\tau \approx 10^{-8}\ \mathrm{s}$, $\mu_n/\mu_p \approx 100$, $\alpha \approx 10^4\ \mathrm{cm}^{-1}$, $s^* \approx 10^5\ \mathrm{cm/s}$, and $w \approx 10^{-4}$ cm. Figure 4 shows the results of this calculation for various ratios n/p. It is clear that at sufficiently high levels of injection $(n \approx \Delta n \approx p \approx \Delta p)$ and depletion band bending, for all H at which the approximation $L \gg w$ holds, the field-driven term dominates in Eq. (1) and the PEME is anomalous. Numerical estimates of the ratio [Eq. (3)] show that for MCT with the parameters given above this approximation is satisfied even for small H with a rather small margin. However, in the range of small H the photomagnetic effect turns out to be normal even when $n/p=0.5$, and the PEME does not change sign until L and the diffusion-driven term in Eq. (1) have decreased sufficiently, i.e., until a certain critical value of H is reached. We note that a similar dependence is found in p-InSb.[14] Finally, for $n/p \simeq 0.05$ the diffusion term in Eq. (1) dominates for all H for which the condition $L \gg w$ holds, and the PEME is normal.

Thus, at low temperatures where freeze-out of holes takes place and the relation $n=p$ is easy to implement even at rather low injection levels in the entire range of H for which Eq. (1) is applicable, the PEME is anomalous. However, as n/p decreases, we first encounter the case where the PEME is normal for small values of H but for higher values is anomalous, and then upon further decreasing n/p we encounter the case where the PEME is normal in the entire range of H. In a p-type semiconductor with initially frozen-out holes this can be achieved by three methods: lower light intensity, accompanied by lower Δn and Δp; increased temperature, accompanied by an increase in p_0; and the application of uniaxial compression, which increases p_0 by decreasing the binding energy of shallow acceptors.[9] We encountered the latter situation experimentally (Figs. 2 and 3).

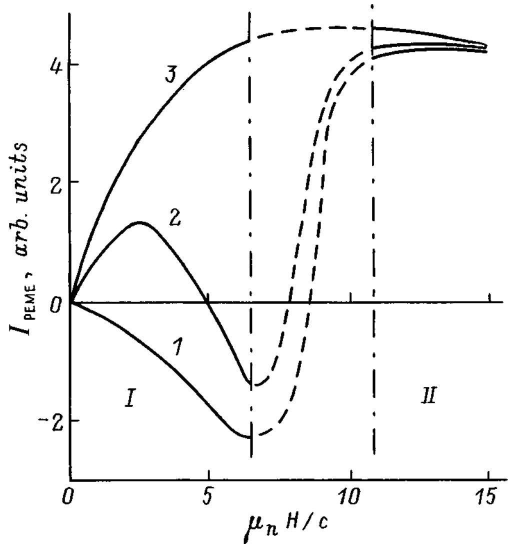

FIG. 4. Field dependence of the photomagnetic current I_{PEME} calculated for a semiconductor with the parameters of narrow-gap p-MCT based on Eq. (1) for $L(H) \ll w$ (region I) and based on the expression that takes into account only the diffusion component in expression (1) for $L(H) \gg w$ (region II). Values of the concentration ratio n/p: *1* — 1, *2* — 0.5, *3* — 0.05. The dashed curves show the assumed functions $I_{\mathrm{PEME}}(H)$ in the intermediate regime.

As we have already mentioned, the criterion for applicability of Eq. (1) is satisfaction of the relation $L(H) \gg w$. However, estimates based on Eq. (3) show that for narrow-gap semiconductors with a high ratio of electron to hole mobilities this criterion is clearly not satisfied even for comparatively small H. Conversely, when the opposite condition $L(H) \ll w$ is realized and the additional relation $\alpha w \ll 1$ holds, minority carriers are generated and recombine primarily outside the space-charge layer. In this case the PEME current is given by the standard expression for the diffusion-driven component of the PEME effect in Eq. (1). Here s^* is a modified effective surface recombination rate, which describes the rate at which electrons and holes are supplied to the boundary of the space-charge layer, and is analogous in form to the expression for s given in Ref. 14. Hence, for samples thick enough that recombination of excess carriers at the surface can be ignored in the dark, the PEME is normal for the range of magnetic fields H under study. In the range of temperatures corresponding to freeze-out of holes, and hence sufficiently high values of n/p, the PEME is anomalous at moderate values of H. However, as soon as H increases to a value determined by the relation $L(H) \approx w$, the PEME switches sign and becomes normal.

CONCLUSIONS

We have experimentally observed a number of features of the anomalous photoelectromagnetic effect in *p*-CdHgTe at low temperatures, in particular, two changes in sign with increasing field *H*. Our theoretical model allows us to unambiguously relate these features to freeze-out of free holes onto acceptor states. Because of the marked asymmetry of values of the electron and hole mobility, this allows the electronic component of the photomagnetic current to become significant. The PEME converts from anomalous to normal as the magnetic field *H* increases because the field decreases the effective ambipolar diffusion length until it is comparable to the linear dimensions of the space-charge region. The value of *H* for which this transition takes place can be used to determine the thickness of the space-charge layer. These results also lead us to conclude that estimating the recombination parameters of semiconductors like *p*-CdHgTe at low temperatures based on PEME data should be done only under conditions of weak excitation.

[1] V. I. Ivanov-Omskii, N. N. Berchenko, and A. I. Elizarov, Phys. Status Solidi A **103**, 11 (1987).

[2] R. B. Scoolar, B. K. Janousek, R. L. Alt, R. C. Carcallen, M. J. Danghtery, and A. A. Fote, J. Vac. Sci. Techn. **21**, 164 (1982).

[3] M. C. Chen, Appl. Phys. Lett. **51**, 1836 (1987).

[4] A. I. Elizarov, L. P. Zverev, V. V. Kruzhaev, G. M. Min'kov, and O. É. Rut, Fiz. Tekh. Poluprovodn. **17**, 459 (1983) [Sov. Phys. Semicond. **17**, 284 (1983)].

[5] S. G. Gasan-zade, I. P. Zhad'ko, E. A. Zinchenko, E. S. Fridrikh, and G. A. Shepel'skiĭ, Fiz. Tekh. Poluprovodn. **25**, 871 (1991) [Sov. Phys. Semicond. **25**, 527 (1991)].

[6] S. M. Gorodnitskiĭ, N. S. Zhdanovich, and Yu. I. Ravich, Fiz. Tekh. Poluprovodn. **7**, 1270 (1973) [Sov. Phys. Semicond. **7**, 853 (1973)].

[7] D. H. Lile, Phys. Rev. B **8**, 4708 (1973).

[8] S. G. Gasan-zade, V. V. Bogoboyashchiĭ, I. P. Zhad'ko, E. A. Zinchenko, and G. A. Shepel'skiĭ, Fiz. Tekh. Poluprovodn. **27**, 1508 (1993) [Semiconductors **27**, 833 (1993)].

[9] A. V. Germanenko, G. M. Min'kov, and O. É. Rut, Fiz. Tekh. Poluprovodn. **21**, 2006 (1987) [Sov. Phys. Semicond. **21**, 1216 (1987)].

[10] Yu. I. Ravich, *The Photomagnetic Effect in Semiconductors and its Applications*, [in Russian], Nauka, Moscow, 1967.

[11] A. V. Sachenko and O. V. Snitko, *Photoeffects in Semiconductor Surface Layers* [in Russian], Naukova Dumka, Kiev, 1984.

[12] S. A. Studentikin, I. A. Panaev, V. A. Kostyuchenko, and Kh.-M. Z. Torchinov, Fiz. Tekh. Poluprovodn. **27**, 744 (1993) [Semiconductors **27**, 650 (1993)].

[13] A. V. Sachenko, B. A. Novominskiĭ, and A. S. Kalshabekov, Insulators and Semiconductors **34**, 44 (1988).

[14] G. G. Babichev, N. P. Zhad'ko, and V. A. Romanov, Fiz. Tekh. Poluprovodn. **9**, 2300 (1975) [Sov. Phys. Semicond. **9**, 1488 (1975)].

Translated by Frank J. Crowne

The effect of fields due to charge centers at random locations in a semiconductor crystal on the electronic structure of neutral acceptors and on the polarization of luminescence generated by ⟨conduction band⟩-acceptor transitions

E. B. Osipov, O. V. Voronov, N. O. Sorokina, and B. V. Borisov

Cherepovets State University, Cherepovets, Russia

(Submitted December 30, 1997; accepted for publication November 4, 1998)
Fiz. Tekh. Poluprovodn. **33**, 580–582 (May 1999)

Random fields in semiconductor crystals created by charged impurities and other defects give rise to an additional splitting of acceptor levels, which by virtue of the random direction of these fields leads to a decrease in the degree of polarization of luminescence from the semiconductor when the latter is under uniaxial strain. In this paper, the usual description of depolarization of the luminescence based on the effective- temperature mechanism is generalized to include the influence of the Coulomb field of randomly located charge centers on the ground state of an acceptor in an external uniaxial strain field. It is possible to estimate the concentration of charge centers by comparing the polarization characteristics of luminescence calculated within this model from a semiconductor under pressure along the [100] axis with experimental data at low temperatures. © *1999 American Institute of Physics.* [S1063-7826(99)01105-9]

External uniaxial strain causes a splitting of fourfold-degenerate acceptor levels in semiconductors.[1] When the thermal populations of the split sublevels are unequal, the luminescence generated by conduction band-acceptor transitions is polarized. Naturally, the polarization of this luminescence decreases with increasing temperature. However, random fields in these crystals created by charged impurities in compensated semiconductors and by other defects give rise to additional splittings which by virtue of the random directions of these fields also decrease the degree of polarization of the luminescence. The effect of these random fields should be largest when the magnitudes of the splittings they create are on the average comparable to the splitting caused by uniaxial strain and the average energy of thermal motion kT.

Depolarization of light under the action of the random fields is usually described by introducing an effective temperature which exceeds the experimental temperature by several degrees.[2] The legitimacy of this procedure, however, is questionable. The fact is that when acceptor levels in a nondegenerate semiconductor are split by a fixed amount in a uniaxial strain field, the hole populations of the sublevels are related by an exponential Boltzmann factor which affects the integrated polarization of the luminescence. However, when the centers are distributed with respect to the additional random splitting, the dependence of the integrated polarization ratio on external stress cannot be a simple exponential of this kind.

In this paper we derive a model for the depolarization in which we take into account the influence of the Coulomb field of the randomly located charge centers. We find that when these fields act on an acceptor in an external uniaxial strain field, they affect the ground state most strongly. By comparing the polarization characteristics of the luminescence in the external strain field calculated within this model with the experimental data, we can estimate the concentration of charge centers.

The effect of the random field on the acceptor center (i.e., the Coulomb interaction of a charged impurity center with a hole bound to a neutral acceptor) is described by the operator

$$\hat{H}_r=-\frac{e^2}{4\pi\varepsilon\varepsilon_0|\mathbf{R}-\mathbf{r}'|}, \tag{1}$$

where $\mathbf{R}(R,\theta,\varphi)$ and $\mathbf{r}'(r',\theta',\varphi')$ are the radius vectors of the charged acceptor and hole bound to the neutral acceptor, respectively. Using an expansion of $1/|\mathbf{R}-\mathbf{r}'|$ in spherical harmonics,[3] we rewrite the matrix for the energy operator of the hole, taking into account the effect of a charged center with coordinates R,θ,ϕ on the acceptor in an external stress field p applied along the axis $z\|[001]$, in the form

$$\begin{pmatrix} A & Be^{-i\varphi} & Ce^{-2i\varphi} & 0 \\ Be^{i\varphi} & -A & 0 & Ce^{-2i\varphi} \\ Ce^{2i\varphi} & 0 & -A & -Be^{-i\varphi} \\ 0 & Ce^{2i\varphi} & -Be^{i\varphi} & A \end{pmatrix}. \tag{2}$$

This matrix, which is calculated within the approximation $R\gg r_0$, does not include the electrostatic interaction energy, which does not split the Γ_8 level. We introduce the notation

$$A=b\varepsilon_1+\frac{3}{10}D(3\cos^2\theta-1)\frac{r_0^2}{R^3},$$

$$B=D\frac{3\sqrt{3}}{5}(\sin\theta\cos\theta)\frac{r_0^2}{R^3},$$

$$C=D\frac{3\sqrt{3}}{10}(\sin^2\theta)\frac{r_0^2}{R^3},\quad D=\frac{e^2}{4\pi\varepsilon\varepsilon_0},\quad \varepsilon_1=\frac{p}{c_{11}-c_{12}},\tag{3}$$

where b is the deformation potential constant, c_{11} and c_{12} are elastic moduli of the crystal, r_0 is the radius of a bound state of a hole at a neutral acceptor, and ε is the dielectric constant of the material (for GaAs we have used $\varepsilon=3.4$ in our numerical calculations).

For the eigenvalues of the Hamiltonian we obtain the expression

$$E_{1,2}=\pm\sqrt{(b\varepsilon_1)^2+Db\varepsilon_1\frac{3}{5}(3\cos^2\theta-1)\frac{r_0^2}{R^3}+D^2\frac{9}{25}\frac{r_0^4}{R^6}}.\tag{4}$$

The effect of strain and the random field is to split the acceptor level into two sublevels whose wave functions can be written in the form of an expansion with respect to basis functions:

$$\begin{aligned}\Psi'_{E_1,E_2}&=\frac{1}{N_{1,2}}(-Be^{-i\varphi}\Psi_{3/2,\,3/2}+(A-E_{1,2})\Psi_{3/2,\,1/2}\\&\quad-Ce^{2i\varphi}\Psi_{3/2,\,-3/2}),\\ \Psi''_{E_1,E_2}&=\frac{1}{N_{1,2}}(-Ce^{-2i\varphi}\Psi_{3/2,\,3/2}+(A-E_{1,2})\Psi_{3/2,\,-1/2}\\&\quad+Be^{i\varphi}\Psi_{3/2,\,-3/2}),\\ N_{1,2}&=\sqrt{B^2+C^2+(A-E_{1,2})^2}.\end{aligned}\tag{5}$$

We chose the distribution function for the random fields with respect to magnitude and direction dW in the following way. Let N charged centers be distributed in the crystal quasicontinuously with a density

$$\rho=\frac{N}{V}=\frac{N}{(4/3)\,\pi R_0^3}.$$

Here $V=(4/3)\pi R_0^3$ is the crystal volume (a sphere whose center is at the origin of the coordinate system, which is also the point where the neutral center is located). Let us assume that the strongest splitting of the neutral acceptor is caused by the acceptor center closest to it. In this case, since the acceptors are so far apart, we can ignore the action of other charge centers.

Consider a spherical volume element (a spherical shell) $[R, R+dR]$. The probability that one of the N charged centers lies within this volume element, and that none of the other centers lie within the volume $0\leqslant r\leqslant R$, is determined by the expression

$$dW=\left(1-\int_0^R\frac{\rho}{N}4\pi r^2dr\right)^N\frac{\rho}{N}4\pi R^2dRN.$$

Assuming that the charge centers occupy any given one of the identical volume elements $R^2dR\sin\theta d\theta d\varphi$ within the spherical shell with equal probability, we obtain

$$dW=\left[1-\left(\frac{R}{R_0}\right)^3\right]^N\frac{N}{4\pi R_0^3}3R^2dR\sin\theta\,d\theta\,d\varphi.\tag{6}$$

When the number N is sufficiently large, taking into account the fact that

$$\frac{N}{R_0^3}=\frac{4}{3}\pi n,$$

where n is the concentration of charge centers, it is not difficult to obtain the relation

$$dW=e^{-(4/3)\,\pi nR^3}2\pi nR^2\sin\theta d\theta dR.\tag{7}$$

The integrated polarization ratio for luminescence is defined as follows:

$$r=\frac{I_\parallel}{I_\perp}.\tag{8}$$

Here $I_\parallel$ and $I_\perp$ are the intensities of light with electric field vectors parallel and perpendicular to the strain axis, respectively.

The intensity of the radiation is directly proportional to the square of the modulus of the matrix elements for transitions of electrons from the bottom of the conduction band to sublevels E_1 and E_2 of the split acceptor level, as well as the

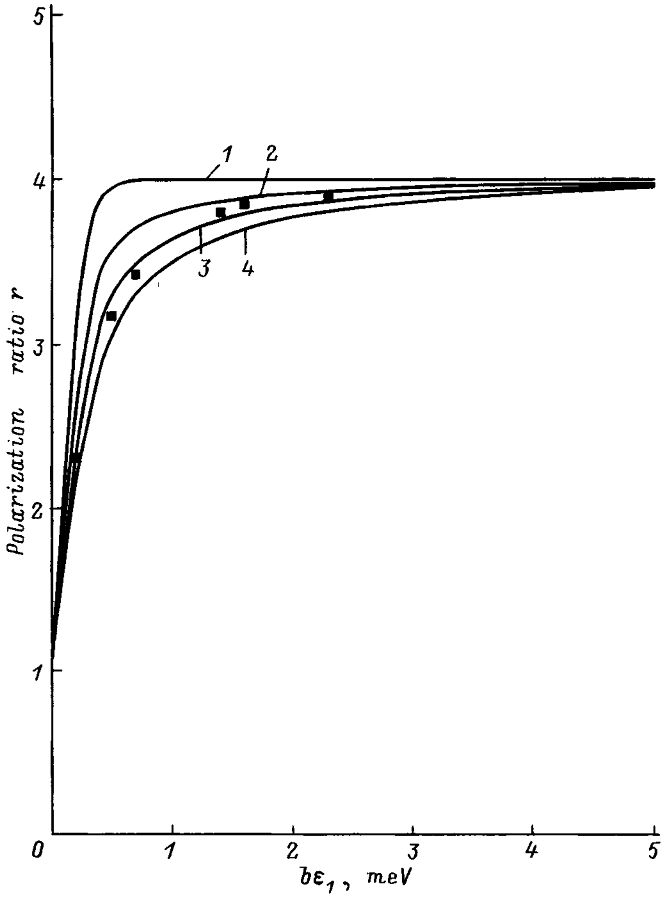

FIG. 1. Dependence of the integrated polarization ratio r on the magnitude of the splitting of the level $b\varepsilon_1$ for stress along the [100] axis: *1–4*—calculations; the points are experimental values from Ref. 2. The concentration of charge centers n, $10^{16}\,\text{cm}^{-3}$: *1* — 0, *2* — 1, *3* — 2, *4* — 3.

populations of these sublevels. Assuming that the hole populations of these split levels of the acceptor obey the Boltzmann distribution, we obtain the expressions

$$dI_{\perp}=\Omega\left(\frac{1}{N_1^2}\frac{B^2+\frac{(A-E_1)^2}{3}+C^2}{1+e^{-\frac{\delta}{kT}}}+\frac{1}{N_2^2}\frac{B^2+\frac{(A-E_2)^2}{3}+C^2}{1+e^{-\frac{\delta}{kT}}}e^{-\frac{\delta}{kT}}\right)dW, \tag{9}$$

$$dI_{\parallel}=\Omega\left(\frac{1}{N_1^2}\frac{\frac{4}{3}(A-E_1)^2}{1+e^{-\frac{\delta}{kT}}}+\frac{1}{N_2^2}\frac{\frac{4}{3}(A-E_2)^2}{1+e^{-\frac{\delta}{kT}}}e^{-\frac{\delta}{kT}}\right)dW. \tag{10}$$

Here $\delta=E_1-E_2$, k is the Boltzmann constant, and Ω is a constant that contains the square of the interband matrix element modulus. Carrying out the integrations in Eqs. (9) and (10), we find the integrated intensity of the polarization components that determine the polarization ratio (8).

Figure 1 shows the results of this calculation of the ratio r in Eq. (8) at $T=2$ K for various values of the concentration of charged impurities.

It is clear from Fig. 1 that for values of the concentration $n=2\times10^{16}\text{cm}^{-3}$ the dependence we obtain is in good agreement with the experiments from Ref. 2. The slight deviation of the experimental points from the calculated curve can be explained as a manifestation of the electron-phonon interaction which leads to a Jahn-Teller distortion of the neutral acceptor complex.

[1] G. L. Bir and G. E. Pikus, *Symmetry and Strain Effects in Semiconductors* [Wiley, New York, 1975; Nauka, Moscow, 1972].

[2] N. S. Averkiev, Z. A. Adamiya, D. I. Aladashvili, T. K. Amirov, A. A. Gutkin, E. B. Osipov, and V. E. Sedov, Fiz. Tekh. Poluprovodn. **21**, 421 (1987) [Sov. Phys. Semicond. **21**, 262 (1987)].

[3] L. D. Landau and E. M. Lifshitz, *Quantum Mechanics: Nonrelativistic Theory* [Pergamon Press, Oxford, 1980; Nauka, Moscow, 1989].

Translated by Frank J. Crowne

The effect of intense laser light on the absorption-edge region of the spectrum of a $CdCr_2Se_4$ ferromagnetic semiconductor

L. L. Golik and Z. É. Kun’kova

Institute of Radio Engineering and Electronics, Russian Academy of Sciences, 141120 Fryazino, Russia

(Submitted October 8, 1998; accepted for publication November 10, 1998)
Fiz. Tekh. Poluprovodn. **33**, 583–585 (May 1999)

The effect of intense incident laser light on the spectral dependence of the absorption of circularly polarized light is investigated in single crystals of $CdCr_2Se_4$ in the neighborhood of the absorption edge for temperatures in the range 100–130 K. The observed large changes in the shape of the edge are related to peaking of the exciton resonance, which is caused by photoexcited charge carriers that screen the internal electric fields in the crystal. © *1999 American Institute of Physics.* [S1063-7826(99)01205-3]

The ferromagnetic semiconductor $CdCr_2Se_4$ is one of the few compounds that exhibit a strong nonlinear Faraday effect.[1,2] This nonlinear effect, which occurs at temperatures below 150 K, is observed both in the ferromagnetic and paramagnetic phases. In Ref. 2 we showed that the nonlinear Faraday rotation takes place within a narrow band of energies close to the intrinsic absorption edge. We claimed there that the increase in Faraday rotation with increasing intensity of incident laser light is due to peaking of the exciton resonance, which in turn is caused by photoexcited charge carriers that screen internal electric fields associated with the fluctuation potential.[2] In order to test this assumption, we have investigated the effect of incident light intensity on the spectral dependence of the absorption of circularly polarized light in single crystals of $CdCr_2Se_4$ in the neighborhood of the intrinsic absorption edge. We note that the effect of high-power laser illumination on the absorption of light in $CdCr_2Se_4$ at $T=$ 300 K was studied in Ref. 3. However, it is believed that the levels that make up the bottom of the conduction band of $CdCr_2Se_4$ undergo a change at $T\cong$ 200 K, along with the electronic transitions responsible for the absorption edge.[4,5]

The films we investigated, with dimensions 1.5 mm×2 mm and thickness 12 μm, were obtained by cleaving and polishing single crystals. A one-beam method was used. The light source was a tunable laser based on F_2^+ color centers in LiF, excited by the second harmonic of a neodymium laser. The range of laser tunability was 830–1030 nm, the peak power generated at the maximum of the tuning curve was 25 kW, the length of the light pulse was 9 ns, and the repetition frequency was 10 s^{-1}. After being attenuated by a combination of neutral optical filters, the laser beam was focused onto the surface of the sample, which was placed in a vacuum cryostat, into a spot with a diameter on the order of 1 mm. The measurements were made using the automated apparatus described in Ref. 2. The infrared detector we used was an 18ELU-FK photomultiplier. The studies extended over the temperature range 110–130 K in a magnetic field $H=$ 4.8 kOe, which saturated the sample in the ferromagnetic phase. The $CdCr_2Se_4$ samples we used were the same as those in Ref. 2, to investigate the nonlinear Faraday rotation. The optical density at low light intensities (D_L) was computed from values of the photodetector signals with and without the sample in the path of the laser beam, taking into account its passage through the corresponding optical filters and reflection from the sample surface. The optical density at high light intensities (D_H) was calculated using the expression $D_H=D_L+\ln(I_L/I_H)$, where I_L and I_H are the magnitudes of the signals when the same combination of optical filters was placed in front of and behind the crystal under study respectively. The dependence of the reflection of the sample on the radiation intensity was disregarded.

The spectral dependences of the optical density of $CdCr_2Se_4$ for right- and left- handed circularly polarized light (D_+ and D_-, respectively, are shown in Fig. 1) for two intensity levels of the incident light measured at $T=$ 110 K. The inset shows the spectral dependence of the optical power $P(h\nu)$ from the laser we used. The low-level light intensity (curves *1*, *1′*) correspond to an optical power density at the maximum of the function $P(h\nu)$, $P_{\max}=10\text{kW/cm}^2$. The functions $D_{L+}(h\nu)$, $D_{L-}(h\nu)$, measured using a monochromator and an incandescent lamp, coincide within the limits of measurement error with the functions *1*, *1′* (Fig. 1). For the functions *2*, *2′* the optical power density incident on the sample at each wavelength was 47 times larger ($P_{\max}=$ 470 kW/cm^2). As Fig. 1 shows, a considerable distortion of the spectral dependences of the optical density is observed at high incident light power. The absorption edge of the function $D_{H+}(h\nu)$ (curve *2*) becomes sharper, and is accompanied by bleaching of the sample at low energies and darkening of the sample at high energies. The function $D_{H-}(h\nu)$ (curve *2′*) exhibits increased absorption, along with a barely discernible peak at the absorption edge. At higher temperatures the changes in the absorption of circularly polarized light with increasing laser intensity are analogous to the functions *2*, *2′* (Fig. 1); however, the magnitude of the changes decreases with increasing temperature. Because the absorption edge of $CdCr_2Se_4$ undergoes a strong shift towards lower energies at low T,[6,7] where the intensity of the light from the laser decreases sharply, the temperature range

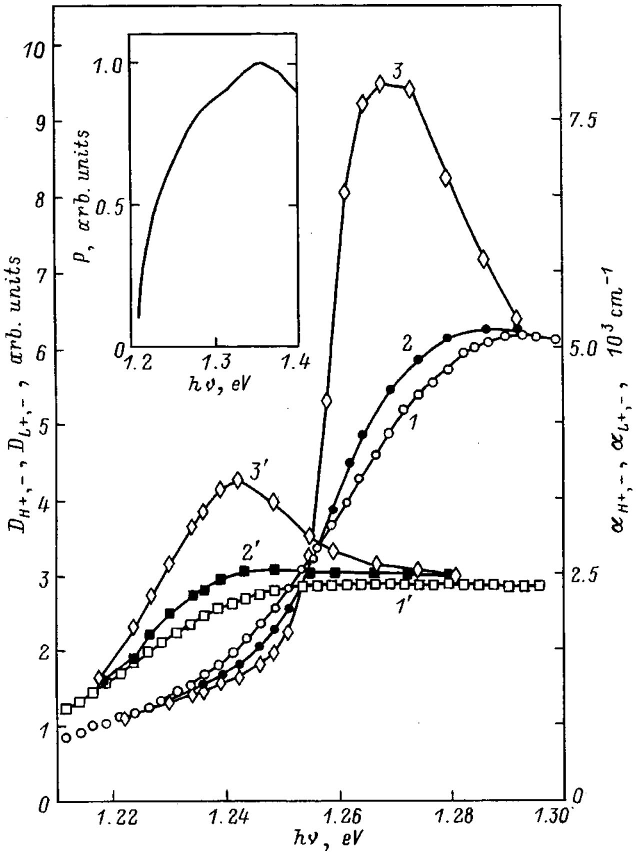

FIG. 1. Spectral dependence of the optical density (*1, 1', 2, 2'*; left-hand coordinate axis) and absorption coefficient (*1, 1', 3, 3'*; right-hand coordinate axis) for right-handed (*1–3*) and left-handed circularly polarized light (*1'–3'*) measured at various intensities of light incident on the sample $P_{\max}$, kW/cm^2: 10 (*1, 1'*) and 470 (*2, 2', 3, 3'*); the measurement temperature was $T=$ 110 K. The inset shows the spectral dependence of the optical power from the laser.

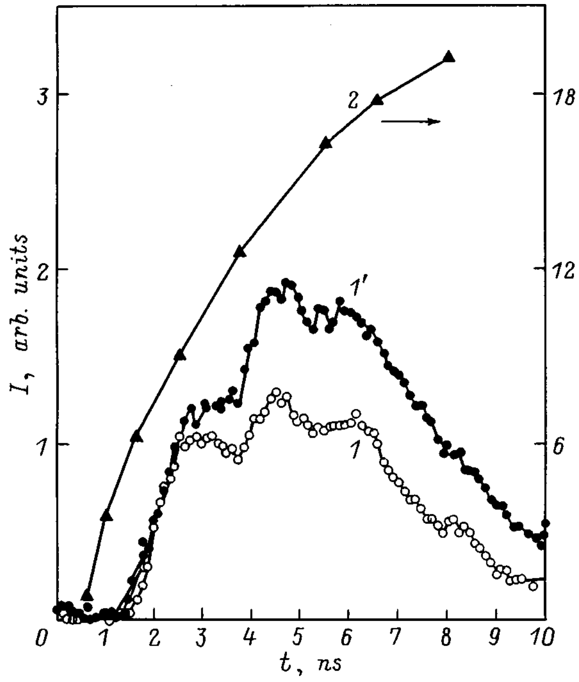

FIG. 2. Oscilloscope traces obtained for right-handed circularly polarized light with $h\nu=$ 1.246 eV at low (*1*) and high (*1'*) intensities of light incident on the sample $P_{\max}$, kW/cm^2: 10 (*1*) and 470 (*1'*); *2*—dependence of the nonlinear part of the Faraday rotation (ΔF) on the measurement time for $h\nu=$ 1.265 eV (shifted to the left by 1.5 ns relative to the oscilloscope traces *1, 1'*). Measurement temperature $T=$ 110 K.

for the measurements was limited from below by $T=100$ K. Figure 2 shows oscilloscope traces of signals that are proportional to the light intensity passing through the $CdCr_2Se_4$ crystal and the optical filter when the optical filter is located in front of (*1*) and behind (*1'*) the crystal. These oscilloscope traces extend over the range in which the sample bleaches. Here we also plot the magnitude of the nonlinear portion of the Faraday rotation versus the time at which the measurement was made within the duration of the optical pulse. It is clear that the relative values of change in transparency and nonlinear Faraday rotation increase with the length of the light pulse. The similar time dependences of the nonlinearities in the Faraday rotation and in absorption are evidence that these effects have a common cause. The functions $D_{H+,-}(h\nu)$ and $D_{L+,-}(h\nu)$ (Fig. 1) were measured at time $T=6$ ns on the oscilloscope traces.

In Ref. 7 we observed no resonance peaks at the absorption edge in the functions $D_{L+,-}(h\nu)$, which probably indicates that the crystal we investigated in that study was of lower quality. Further evidence of this conclusion is the different values of specific Faraday rotation at weak light intensities measured at the maximum of the Faraday rotation band in Refs. 2 and 7. In analyzing the functions $D_{H+,-}(h\nu)$ the following factors must be taken into account. First of all, in accordance with curve $P(h\nu)$ (Fig. 1), the different intensities of the incident light correspond to different photon energies. The lack of bleaching of the crystal when illuminated with left-circularly polarized light is probably connected with inadequate intensity of the laser light near the long-wavelength edge of the tunability range. Secondly, the quantity $D_{H+,-}>1$ over the larger part of the spectral region we studied, and the density of photoexcited charge carriers is strongly nonuniform with respect to the sample thickness. An estimate of the diffusion length (L_D) using mobility values $\mu_n \simeq \mu_p \simeq$ 10 cm^2/(V·s) taken from Refs. 8 and 9 and lifetimes of nonequilibrium charge carriers $\tau \simeq 10^{-8}-10^{-7}$ s, which are realistic for the high-resistance compensated crystal $CdCr_2Se_4$, gives $L_D \simeq 1\,\mu$m. Consequently, nonuniformity is not eliminated by diffusion. If the nonlinear Faraday rotation and nonlinear absorption in $CdCr_2Se_4$ are attributable to the appearance of nonequilibrium charge carriers,[2] then the absorption at high incident light intensities ($\alpha_{H+,-}$) is nonuniform over the sample thickness, and determining them from the ratio $D_{H+,-}/d$ (where d is the sample thickness) gives only an effective value. Assuming that the measured functions $D_{H+,-}(h\nu)$ are the sum of the optical densities of layers with varying ($\alpha_{H+,-}$) and unvarying ($\alpha_{L+,-}$) absorption coefficients, and assuming that the important change in the absorption takes place within a layer of thickness $d_{NL}=1/\alpha_H$, we can calculate $\alpha_{H+,-}(h\nu)$ from the relation $D_H=\alpha_H d_{NL}+\alpha_L(d-d_{NL})$. The functions $\alpha_{H+,-}(h\nu)$ obtained in this way are shown in Fig. 1 (curves *3* and *3'*). It is clear that a sharply expressed resonance peak appears in the neighborhood of the absorption edge. The functions $\alpha_{L+,-}(h\nu)$ coincide with the functions $D_{L+,-}(h\nu)$ (see curves *2* and *2′* in Fig. 1), and their values are plotted against the right-hand ordinate axis.

These results confirm our assertion in Ref. 2 that the nonlinear Faraday rotation in $CdCr_2Se_4$ is connected with nonlinear absorption caused by peaking of the exciton resonance, which in turn is due to the screening of internal electric fields by photoexcited charge carriers.

[1] V. G. Veselago, S. G. Rudov, and M. A. Chernikov, JETP Lett. **40**, 940 (1984).

[2] L. L. Golik and Z. E. Kun'kova, JETP Lett. **66**, 409 (1997).

[3] V. S. Viktoravichyus, R. A. Gadonas, A. P. Gal'dikas, S. I. Grebinskiĭ, S. Ya. Zakharov, V. V. Krasauskas, and A. S. Pelakauskas, Fiz. Tverd. Tela (Leningrad) **32**, 2938 (1990) [Sov. Phys. Solid State **32**, 1706 (1990)].

[4] M. I. Auslender and N. G. Bebenin, Fiz. Tverd. Tela (Leningrad) **30**, 945 (1988) [Sov. Phys. Solid State **30**, 549 (1988)].

[5] K. M. Golantr, V. V. Tugushev, and I. M. Yurin, Fiz. Tverd. Tela (Leningrad) **32**, 2100 (1990) [Sov. Phys. Solid State **32**, 1220 (1990)].

[6] G. Harbeke and H. Pinch, Phys. Rev. Lett. **17**, 1090 (1966).

[7] L. L. Golik, Z. E. Kun'kova, T. G. Aminov, and V. T. Kalinnikov, Fiz. Tverd. Tela (Leningrad) **22**, 877 (1980) [Sov. Phys. Solid State **22**, 512 (1980)].

[8] K. Kodama and T. Nimi, Jpn. J. Appl. Phys. **19**, 307 (1980).

[9] K. Kodamar, S. Doi, T. Matsumura, and T. Nimi, Jpn. J. Appl. Phys. **19**, 317 (1980).

Translated by Frank J. Crowne

SEMICONDUCTORS VOLUME 33, NUMBER 5 MAY 1999

SEMICONDUCTOR STRUCTURES, INTERFACES AND SURFACES

Saturated vertical drift velocity of electrons in silicon carbide polytypes

V. I. Sankin and A. A. Lepneva

A. F. Ioffe Physicotechnical Institute, Russian Academy of Sciences, 194021 St. Petersburg, Russia

(Submitted October 8, 1998; accepted for publication October 12, 1998)
Fiz. Tekh. Poluprovodn. **33**, 586–589 (May 1999)

Saturated drift velocities of electrons in the direction parallel to the crystal axis have been determined for the first time for a number of silicon carbide polytypes ($4H$, $6H$, $8H$, and $21R$) by investigating the current-voltage characteristics of novel three-terminal n^+-p-n^+ structures intentionally designed for the purpose. The values of these velocities are 3.3×10^6, 2×10^6, 1×10^6, and 4×10^3 cm/s respectively. These results are in qualitative agreement with a picture involving the miniband electronic structure caused by a natural superlattice in SiC. Experiments confirm the correlation between drift velocity and width of the first miniband in the various polytypes. © *1999 American Institute of Physics.* [S1063-7826(99)01305-8]

INTRODUCTION

The most important device-related characteristic of a semiconductor crystal is its saturated drift velocity, which determines the frequency limits of semiconductor devices and consequently the range of their most efficient use. This remains true for the case of silicon-carbide crystals as well. At this time, saturated drift velocities are experimentally known for two SiC polytypes ($4H$ and $6H$) in the directions perpendicular to the crystal axis.[1,2] According to these data, the velocities coincide in both polytypes, a circumstance that is also characteristic of many other parameters in these crystallographic directions. However, for the direction along the crystal axis this is usually not so, and the semiconductor parameters of various polytypes exhibit characteristic differences. It is well known that in noncubic SiC polytypes, with the exception of $2H$-SiC, the crystal axis is also the axis of a natural superlattice, which induces a miniband structure in the electronic spectrum of these polytypes. The presence of this structure should affect the values of the saturation velocities; i.e., a correlation should be observed between the velocities and the parameters of the miniband spectrum. The dependence of the drift velocity on the width of the first miniband was obtained analytically in Ref. 3 and observed in various systems with artificial superlattices, where changing the width of the miniband caused the velocity to vary from 10^6 cm/s for a relatively wide miniband[4] to less than 10^4 cm/s for a narrow miniband.[5]

In a series of prior papers[6–8] we described a number of effects in SiC polytypes $4H$, $6H$, and $8H$ that we interpreted as Bloch oscillations, electron-phonon resonances, complete localization in the first miniband, and inter-miniband tunneling. According to our interpretation, these effects are a consequence of, and, therefore confirm, the miniband character of the electronic spectrum, which in turn arises from the natural superlattice. Drift velocity data could provide yet another argument for or against this picture. Until now, such data have not been published in the literature, probably because experimental difficulties associated with fabricating microstructures in the direction of the axis of the natural superlattice have kept researchers from making the appropriate measurements. However, many devices, including high-power high-frequency transistors, are being designed to operate in exactly this geometry, so that identifying the role of the superlattice is a problem of practical interest.

EXPERIMENTAL METHOD

Our measurement method is based on the following considerations. If an experimental structure admits both a regime of space-charge-limited current flow and a drift current regime, we can obtain the saturated drift velocity by analyzing the current-voltage characteristics. For the one-dimensional problem this regime is described by the equations

$$d^2V/dX^2=\rho/\varepsilon_s, \tag{1}$$

$$J=\rho v, \tag{2}$$

where V, X, J, ρ, ε_s, and v are the voltage across the structure, the coordinate along the current direction, the current density, the space-charge density, the dielectric constant of the semiconductor, and the drift velocity, respectively. With the help of standard transformations we thus obtain the expression for the I–V characteristics of the structure

$$J=2\varepsilon_s vV/w^2, \tag{3}$$

where w is the width of the active region of the structure. We can show that the I–V characteristic obtained in this way consists of two regions. In the first region, the drift velocity depends on the field, and in the second region it is saturated and does not depend on the field. If we assume that in the first region the velocity varies as follows:

$$v=\mu V/w, \tag{4}$$

then the I–V characteristics in this region will be described by the expression

$$J=2\varepsilon_s \mu V^2/w^3. \tag{5}$$

Here μ is the mobility of the charge carriers. It should be noted that the mobility that appears in Eq. (4) can itself be a function of field; in this case the real I–V characteristics will have a dependence different from Eq. (5).

The I–V characteristics of the second region where $v = \text{const}$ are described by the expression

$$J=2\varepsilon_s v_s V/w^2, \tag{6}$$

where v_s is the saturated velocity. Accordingly, when the drift velocity is saturated, we should observe a linear region on the I–V characteristic.

EXPERIMENTAL STRUCTURE

For our investigations we used a specially designed and novel three-terminal n^+-p-n^+ structure. The structure consists of three regions which in accordance with transistor terminology we give the names emitter, base, and collector. For purposes of investigation, the material of the base is chosen to be a polytype of silicon carbide doped by a deep acceptor (scandium) in order to obtain minimum concentration of free holes (less than $10^{10}\,\text{cm}^{-3}$ at 300 K). It is obvious that this is a paradoxical way to make an effective transistor. However, as we show below, this structure provides the necessary environment for addressing the problem we pose here. Because the concentration of free holes in the base is so low, virtually any current through the base injects a concentration of electrons that exceeds the concentration of holes, which ensures that the current in the base is space-charge limited.

However, because the p-region of the $p-n$ junction is doped by deep acceptors, the operation of the n^+-p junction has certain features which we should pause to discuss. When $p \simeq 10^{10}\,\text{cm}^{-3}$, the characteristic de-ionization time for these deep acceptors in the space-charge region exceed 10^{-2} s. This implies that the forward-biased emitter n^+-p junction can be turned on only by a dc voltage or by pulses with duration $t > 10^{-2}$ s. However, once the potential barrier is lowered, injection, which is a noninertial process, can be implemented by short pulses of length $t < 10^{-6}$ s.

Let us now consider the collector $p-n^+$ junction. When it is reverse biased, the establishment of an electric field in the base is determined by the ionization of deep acceptor impurities, whose time is also rather long. Therefore, if the reverse bias is applied in sufficiently short pulses, the acceptor levels in the base remain neutral. Now, as we said above, the concentration of holes in the base does not exceed $10^{10}\,\text{cm}^{-3}$, which corresponds to no screening of electric fields over distances less than 10^{-1} cm. Then when the base width is 5–10 μm, screening in the base will be extremely weak and the field in the base may be treated as nearly uniform. Its value there will be given by $F=V/w$, where V is the magnitude of the voltage pulse, and w is the width of the base region. Thus, the motion of electrons and the current in the base will be drift-like, which will ultimately satisfy the conditions under which Eqs. (1) and (2) are valid.

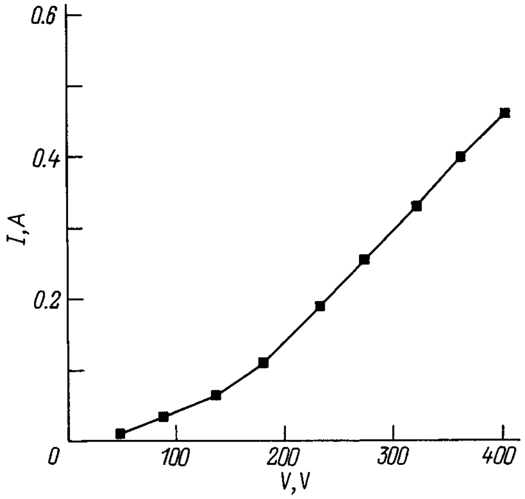

FIG. 1. The I–V characteristics of a three-electrode structure based on 4H-SiC.

This method differs significantly from traditional methods of saturating currents, in which the measurements take place in a regime of extremely high current density. The latter makes it necessary to take special measures to remove heat and fabricate high-quality contacts. For the method described here these difficulties can be avoided, since the current densities do not exceed $10^2\,A/\text{cm}^2$. The difference is in the fact that the electrons are located not in n-, but rather in p-type material, although in this case the impurity concentration (on the order of $10^{17}\,\text{cm}^{-3}$) is roughly the same as in the n-type material used in Refs. 1 and 2. The latter fact is not so important, since saturation of the velocity, which is the fundamental quantity, is determined not by impurity scattering but rather by scattering by optical phonons.

The principles of operation of this structure are as follows. A reverse-bias pulse V_p with period $t_p \simeq 10^{-7}$ s is applied between the collector and the emitter. A forward dc bias V_b is applied to the emitter-base junction. The emitter-base current associated with it has virtually no effect on the value of the injection due to the high resistance of the p-type region ($10^7 - 10^8\,\Omega$). The purpose of this bias is to decrease the height of the contact barrier. The pulse voltage applied between the collector and the emitter ensures a uniform electric field, which propagates through the base, reaches the open emitter junction, and causes injection. The injection current increases together with the value of V_p; however, it can be limited by changes in V_b. The resistance of the base region as the current pulse flows through it decreases by a factor of $10^3 - 10^4$ because electrons injected into the base are swept up by the field and once they have drifted through the base reach the collector. Thus, this experimental structure admits an injection-drift mechanism for current flow. The electric circuit that we describe corresponds to a transistor connected in common-emitter configuration.

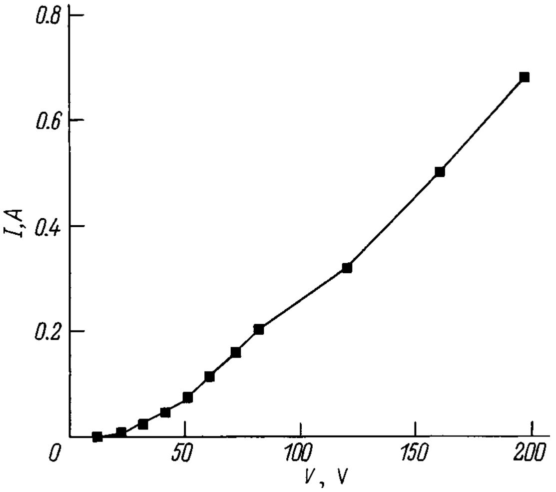

FIG. 2. The I–V characteristics of a three-electrode structure based on 6*H*-SiC.

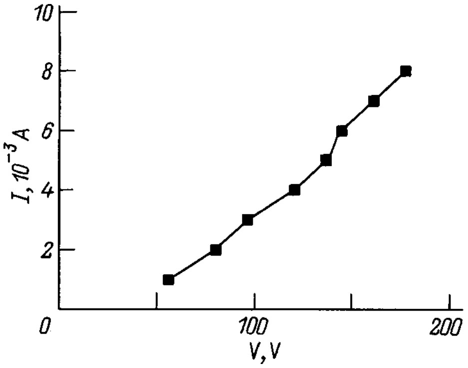

FIG. 4. The I–V characteristics of a three-electrode structure based on 21*R*-SiC.

EXPERIMENTAL RESULTS AND DISCUSSION

Figures 1–4 show the I–V characteristics of microstructures made with SiC polytypes 4*H*, 6*H*, 8*H*, and 21*R*. All the I–V characteristics except for those of 21*R*-SiC consist of a nonlinear initial region followed a linear segment. According to Eq. (5), the nonlinear region should correspond to a square-law dependence of the current on voltage $J\sim V^2$. However, in real I–V characteristics the current follows a power-law dependence $J\sim V^{1.6}$. We asserted above that square-law behavior need not be observed when the carrier mobility depends on field. In our case, its field dependence can probably be written $\mu\sim V^{-0.4}$, which cause the initial portion of the I–V characteristic to deviate from the square law.

The absence of a nonlinear initial portion on the I–V characteristics of the 21*R*-SiC sample occurs for the following reason. The very high internal resistance of these structures, a consequence of the low electron mobility of 21*R*-SiC, prevents us from recording a nonlinear initial segment of the I–V characteristics due to the low values of the current. Therefore, the I–V characteristics obtained by us have only a linear segment, which begins before the field becomes high enough to ensure a minimum current level for detection. Analysis of the I–V characteristics allows us to determine the saturation drift velocity of electrons in the superlattice of 21*R*-SiC . Its value turns out to be an extremely low, 4×10^3 cm/s, which is a consequence of the high degree of localization of carriers within the very narrow miniband. Of all the polytypes we discuss, 21*R*-SiC has the most complicated and longest-period superlattice. This latter characteristic accounts for the narrow minibands.

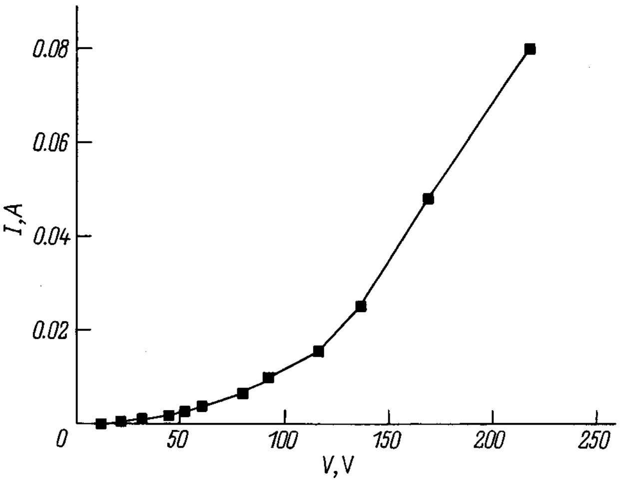

FIG. 3. The I–V characteristics of a three-electrode structure based on 8*H*-SiC.

In the series of polytypes 4*H*, 6*H*, and 8*H*, the magnitude of the superlattice period *d* increases with the polytype number from 5 to 10 Å. We estimated the width of the first miniband E_1 in polytype 6*H*-SiC based on experimental data from studies of Wannier-Stark localization in the regime where the first miniband is completely localized by an electric field.[8] Starting from the relation $E_1\sim k_d^2=\pi^2/d^2$, we can estimate the width of the first miniband in polytypes 4*H* and 8*H*, which have analogous superlattices. According to the values of the superlattice periods cited above, the value of E_1 for 4*H*-SiC is 2.25 times larger and for 8*H*-SiC roughly 1.9 times smaller than for 6*H*-SiC. The values obtained for the saturated drift velocity of electrons are: for polytype 8*H*, 10^6, for 6*H*, 2×10^6, and for 4*H*, 3.3×10^6 cm/s, which qualitatively confirm the relation $v_s\sim 1/d$.[3] Quantitative agreement of these data with the dependence given above is not expected for two reasons.

1. The simplicity of the theoretical representations, which are based on a quadratic dispersion law.

2. Experimental errors, one especially noteworthy example of which is inaccuracy in determining the width of the base *w*. Errors here can be as large as $\pm(15\text{–}20)\%$, implying an error in determining the velocity according to Eq. (5) of $\pm(30\text{–}50)\%$.

The threshold fields at which the drift velocity saturates for polytypes 4*H*, 6*H*, and 8*H* are the following: 1.55×10^5, 1.4×10^5, and 1.35×10^5 V/cm, respectively. The rather small difference among these values could be a result either of differences in objective characteristics of the polytypes or of errors of the kind mentioned above. According to Ref. 3, the drift velocity in the miniband transport regime is given by the expression

$$V_d = AFB^{-1}[1+(F/B)^2]^{-1}, \tag{7}$$

where $A = dE_1/2\hbar$, $B = \hbar/ed\tau$, d is the natural superlattice constant, E_1 is the width of the first miniband, and τ is the scattering time. The width of the first miniband is determined experimentally for $6H$-SiC and is $E_1 = 256$ meV (Ref. 8). The natural superlattice constant for $6H$-SiC is $d = 7.5$ Å. The scattering time obtained from Eq. (4) is $\tau = 5\times10^{-13}$ s; this time coincides with data from our Ref. 7, which we calculated from the threshold field criterion for Bloch oscillations.

Because of the practical impossibility of recording a region of transition from nonlinear to linear segments on the I–V curve of polytype $21R$, all we can say regarding the threshold field is that it is no larger than 1.6×10^5 V/cm. Among the polytypes investigated, $21R$-SiC is characterized by an extremely low value of the saturation drift velocity of electrons, almost three orders of magnitude below values for the remaining polytypes. This is impossible to explain within the framework of a common mechanism of electron transport. If, according to what we said above, the velocities for polytypes $4H$, $6H$, $8H$ can be reasonably explained by miniband transport, then the value of the velocity for $21R$-SiC is two orders of magnitude smaller than the value expected from miniband transport. As we noted earlier, because of the extremely narrow miniband, the electronic spectrum of polytype $21R$ becomes discrete even at rather low fields $(1-2)\times10^5$ V/cm. Note that for polytype $6H$ this field is at a minimum 6×10^5, for $8H$ it is about 4×10^5, and for $4H$ it is about 10^6 V/cm. For this reason, miniband transport at these fields is not possible in $21R$-SiC, and in all probability, the mechanism for electron transport is a hopping mechanism, which would also explain the rapid falloff of the drift velocity in this polytype.

To summarize our data, we can say that for polytypes $4H$, $6H$, and $8H$ we have observed a dependence of the drift velocity on natural superlattice parameters that is in qualitative and quantitative agreement with the simple theory of Esaki and Tsu.[3] This result is also independent confirmation of miniband transport at fields on the order of $(1-2)\times10^5$ V/cm in these polytypes, which corroborates with the picture set forth by us previously in Refs. 6–8.

The anomalously low value of drift velocity in polytype $21R$-SiC indicates that the drift mechanism is changed by the large change in parameters of the miniband spectrum. In particular, as we noted in Refs. 6 and 7, the narrowing of the miniband causes the condition for strong localization to be satisfied in weaker fields, followed by suppression of miniband transport and the likelihood of a transition to a mechanism of tunneling hopping between individual unit cells of the natural superlattice.

This work was carried out with the partial support of the Russian Fund for Fundamental Research (Project 97-02-18295) and the program MNTP ‘‘Physics of Solid-State Nanostructures’’ (Project 1-003).

[1] W. V. Muench and E. Petterpaul, J. Appl. Phys. **48**, 4823 (1977).
[2] I. A. Khan and J. A. Cooper, in *Proceedings ICSCIII-N'97* (Stockholm, 1997), p. 57.
[3] L. Esaki and R. Tsu, IBM J. Res. Dev. **14**, 61 (1970).
[4] A. Sibile, J. F. Palmier, H. Wang, and F. Mollot, Phys. Rev. Lett. **6**, 52 (1990).
[5] H. T. Grahn, K. von Klitzing, K. Ploog, and G. H. Dohler, Phys. Rev. B **43**, 12 094 (1997).
[6] V. I. Sankin and I. A. Stolichnov, Fiz. Tekh. Poluprovodn. **31**, 489 (1996) [Semiconductors **31**, 512 (1996)].
[7] V. I. Sankin and A. A. Lepneva, in *Proceedings of the International Symposium ‘‘Nanostructures: Physics and Technology’’* (St. Petersburg, Russia, 1997), p. 155.
[8] V. I. Sankin and I. A. Stolichnov, JETP Lett. **64**, 114 (1996).

Translated by Frank J. Crowne

SEMICONDUCTORS VOLUME 33, NUMBER 5 MAY 1999

Multiple Andreev reflection in hybrid AlGaAs/GaAs structures with superconducting NbN contacts

A. A. Verevkin, N. G. Ptitsina, K. V. Smirnov, B. M. Voronov, G. N. Gol'tsman,
and E. M. Gershenson

Moscow State Pedagogical University, 119435 Moscow, Russia

K. S. Yngvesson

University of Massachusetts, Amherst, MA 01003, USA

(Submitted October 12, 1998; accepted for publication October 15, 1998)
Fiz. Tekh. Poluprovodn. **33**, 590–593 (May 1999)

The conductivity of hybrid microstructures with superconducting contacts made of niobium nitride to a semiconductor with a two-dimensional electron gas in a AlGaAs/GaAs heterostructure has been investigated. Distinctive features of the behavior of the conductivity indicate the presence of multiple Andreev reflection at scattering centers in the normal region near the superconductor-semiconductor boundary. © *1999 American Institute of Physics.*
[S1063-7826(99)01405-2]

1. An interest in investigating electron transport in semiconductors with high-mobility two-dimensional electron gas (2DEG) confined between two superconducting (S) contacts (i.e., an S-2DEG-S structure) has recently increased markedly. The interest is driven by a desire to understand the many mesoscopic phenomena observed in these structures and by the possibility of applications.[1]

The main problem that arises in making these structures is the need for a transparent boundary between the superconductor (S) and the semiconductor (Smc) with a 2DEG. This problem is solved by choosing suitable superconducting and semiconducting materials such that the Schottky barrier at a junction between them is low. In the overwhelming majority of papers of this kind, the authors investigate the properties of structures in which the high-mobility 2DEG is formed in a symmetric quantum well (using InAs and InGaAs as the 2DEG channel) between Nb contacts (see, e.g., Ref. 2). In this case the superconductor is deposited on a mesa structure after removing the topmost layer (one of the three that make up the quantum well) while preserving the lower donor layer. This approach makes it possible to avoid problems with depletion of the edge regions of the semiconductor mesa structure.

However, the most attractive semiconductor material for creating such a system is the AlGaAs/GaAs heterojunction, at whose boundary a 2DEG can be obtained with the highest mobility known to date [up to $\mu \simeq 10^7$ cm^2/(V·s) at liquid-helium temperatures], which makes it possible to realize ballistic transport in these structures over distances $L > 10$ μm or, alternatively, to record the distinctive features of this type of transport more definitively over smaller distances. Marsh *et al.*[3] were the first to observe a supercurrent in these structures with contacts made of fused-on superconducting indium. In their papers, these authors discuss in detail the possibility of creating high-transparency boundaries between the superconductor and the semiconductor with a 2DEG in an AlGaAs/GaAs heterostructure by introducing artificial disorder in the form of a thin (a few nm) layer of normal metal, e.g., titanium.[4] Studies of such structures with contacts made of fused-on superconducting Sn-Pd alloy,[5] however, revealed the presence of a series resistance that greatly exceeds the computed resistance of the 2DEG channel. In papers by other authors the possibility was demonstrated of obtaining a high-transparency barrier between bulk GaAs with a δ-doped layer and aluminum,[6] bulk GaAs and tin,[7] and also niobium.[8] We note that the superconductors ordinarily used as contacts have low critical temperatures. Therefore, the majority of experimental studies were carried out in the temperature range $T \leqslant 3$ K.

2. We have made S-2DEG-S structures and studied them experimentally. The S-2DEG-S structures are based on an isolated GaAs/AlGaAs heterostructure and NbN as the superconductor, which normally is strongly disordered in films and which possesses a high superconducting transition temperature ($T_c = 15.8$ K in bulk samples). The increased transparency of the S/Smc barrier in this case makes it possible for values of the Fermi velocity in NbN ($\sim 2.5 \times 10^5$ m/s) to be close to their typical value in the 2DEG. Such a structure with high values of T_c is clearly of interest from an applications point of view; it is one of several promising types of superconducting transistor that could be used as a basis for making mixers and detectors in the teraherz region. The preliminary results of this experimental study were presented elswhere.[9]

3. The structures we fabricated had the topology shown in the inset in Fig. 1. A mesa structure with nearly vertical walls, whose height was 200 nm and width 2 μm, was fabricated by photolithography on a substrate with a heterostructure formed by a doped layer of AlGaAs with concentration $\simeq 10^{18}\,\mathrm{cm}^{-3}$, a spacer layer of AlGaAs with thickness 12 nm, and a layer of pure GaAs (the heterostructures were grown by deposition from the gas phase). The depth at which the 2DEG was located was about 110 nm from the surface. We determined the parameters of the 2DEG [concentration

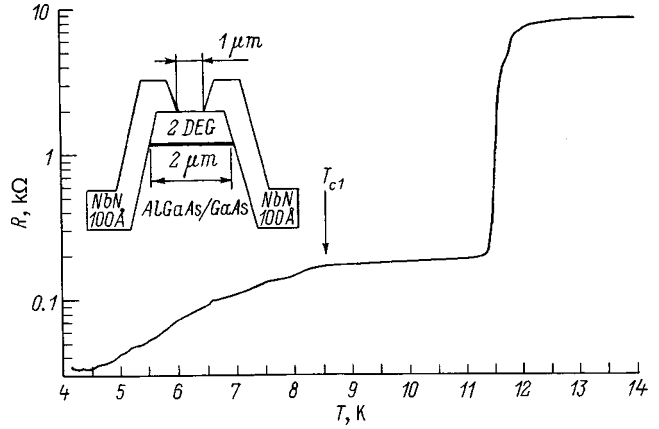

FIG. 1. Temperature dependence of the resistance of the structure at a current of 0.1 μA. The inset shows the AlGaAs/GaAs structure with superconducting contacts made of NbN.

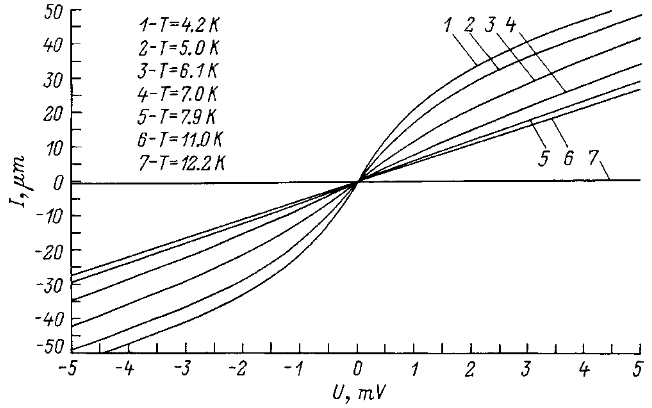

FIG. 2. The I–V characteristics of a S-2DEG-S structure at different temperatures.

$n_s = 1.5\times10^{11}$ cm^{-2}, mobility $\mu = 1.8\times10^5$cm^2/(V·s) at 4.2 K] from the period of the Shubnikov-de Haas oscillations and from Hall measurements in the dark, using samples made from the same substrate as the structures which we investigated, but with ohmic contacts. The NbN contacts were made in the form of long ''banks''—strips of width 10 μm and length 100 μm each, which overlapped the mesa structure up to a distance of about 0.5 μm from the center, leaving a gap between the strips of width 1 μm. Thus, the NbN strips form symmetric end contacts with the mesa structure of width $w = 10\mu$m, with a distance between contacts of $L = 2\mu$m.

Magnetron reactive sputtering in a mixture of nitrogen and argon was used to deposit 10-nm-thick NbN contacts on a substrate heated to 200 °C after chemical removal of the surface oxide layer. (Note that the NbN films have a high and stable critical temperature of about 9 K even at thicknesses of 3.5 nm; see Ref. 10.) The superconducting structure was fabricated by lithography and ion etching with low-energy Ar ions to a depth of 15 nm, so that only a small fraction (no more than 5 nm) of the GaAs surface capping layer was left on the upper portion of the bridge of the mesa structure, in addition to the film of superconductor. The resistance of the NbN contacts in the normal state at $T=$ 15 K is roughly 8 kΩ. They exhibit a superconducting transition at $T \approx 11$ K (with a transition width of about 0.5 K). As the temperature is further lowered, the resistance of the structure drops to a value $R_{\min} = 35\Omega$ at 4.2 K, which is close to the calculated resistance of the 2DEG channel (45 Ω). This indicates that the current through the two-dimensional layer flows in the diffusive regime, corresponding to the condition $L \geqslant l = 1.6\mu$m (where l is the mean-free path).

4. The temperature dependence of the resistance of the structure for a current of 0.1 μA in the temperature range 4.2–15 K (Fig. 1) shows that after the NbN strips become superconducting the resistance of the structure remains nearly constant in the temperature range from 9 to 11 K ($\simeq 180\Omega$), while below 8.7 K it follows a dependence of the form $R \sim \exp(-\Delta/k_BT)$, where $\Delta \approx$ 1.6 meV (here k_B is the Boltzmann constant). If we use the standard relation $2\Delta(0) = 4.1k_BT_c$ for NbN, then this value of Δ exactly corresponds to a temperature $T_{c1} =$ 8.7 K, i.e., the temperature at which the resistance starts to become temperature-dependent. In the temperature range $T <$ 8.7 K the I–V characteristics indicate the presence of an excess current (Fig. 2), whose value increases with decreasing T, while the voltage dependence of the differential resistance $R_d(U) = dU/dI(U)$ exhibits a number of characteristic features (Fig. 3). In these latter curves we observe a deep minimum at $U = 0$, whose depth decreases with increasing temperature. As U increases, plots of these same functions $R_d(U)$ clearly exhibit a knee at $U \approx 2\Delta/e \simeq$ 3.5 mV (the position of this knee, denoted in Fig. 3 by the point A, changes slightly as T varies, while the knee itself is smoothed out as T increases). At significantly higher voltages (on the order of 14 mV at $T=$ 4.2 K) a second clearly defined feature is observed: a maximum (point B in Fig. 3), whose position almost exactly follows the relation $U_{\max} \sim (T_{c1} - T)^{1/2}$. The I—V characteristics with features that exhibit similar behavior have been reported in papers in which the structures under study had fused-in superconducting contacts to bulk GaAs (Ref. 6) and to the 2DEG channel of a AlGaAs/GaAs heterostructure with contacts made of In (Ref. 4), and also in studies of other materials.

5. These features of the conductivity were viewed in Refs. 3–6 as signs of multiple Andreev reflection at the 2DEG boundary with the superconductor. At low temperatures and low voltages the energy of electrons in the semiconductor between the contacts is lower than the superconducting gap $\varepsilon < \Delta$ in NbN (the value of ε is measured from the Fermi level). An electron drifting towards the boundary from the semiconductor side with such an energy creates a hole that moves coherently in the opposite direction, which gives rise to motion of a pair in the superconductor (Andreev reflection; see Ref. 11). Reflection at scattering centers near the boundary can greatly increase the probability of a subsequent Andreev reflection compared with the case of a single reflection of a quasiparticle from the boundary, thereby increasing the transparency of the barrier at the S–2DEG boundary. At high temperatures and large biases, the current through the boundary becomes a quasiparticle current, and the resistance of the boundary is determined by normal reflection, whose probability depends on the barrier height.

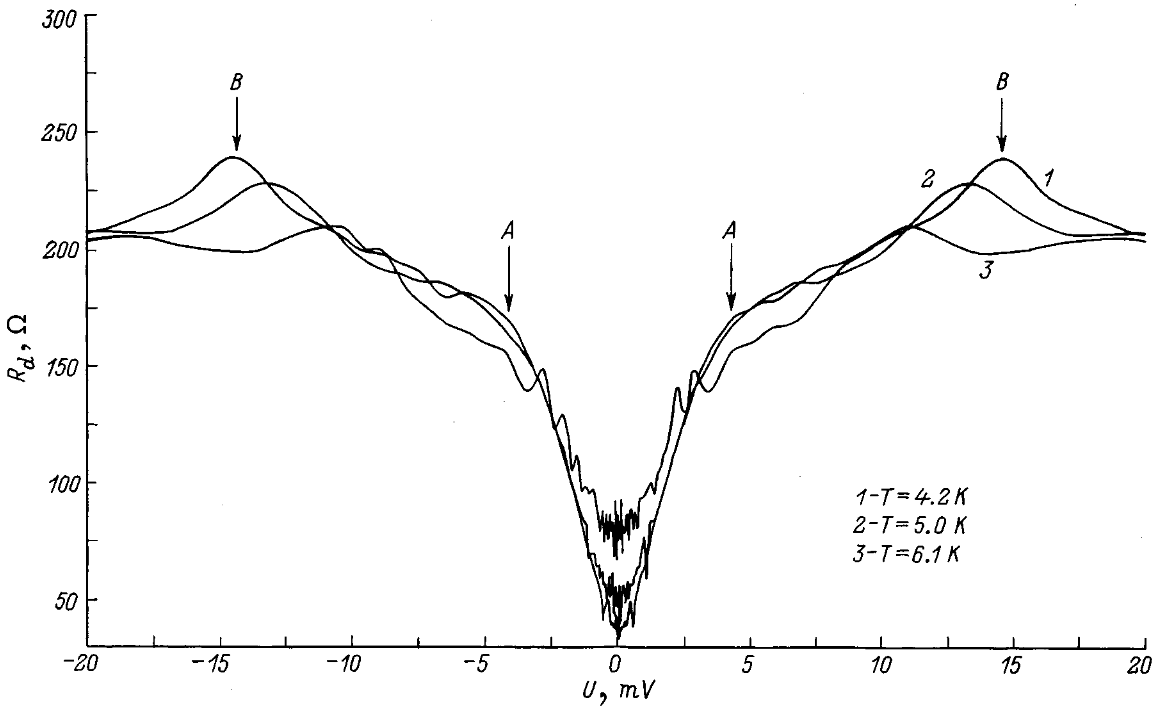

FIG. 3. Dependence of the differential resistance of the structure on voltage $R_d(U)=dU/dI(U)$.

The transition from conductivity determined by multiple Andreev reflections at scattering centers to normal conductivity should be observed at voltages of about $U\simeq\Delta/e$ at each of the contacts. For NbN with $T_c=11$ K we have $\Delta(0)\approx1.9$ meV, and the value $U_A=2\Delta/e$ coincides with the value of the voltage at which we observe a sharp change in the function $R_d(U)$ (the point A in Fig. 3). The value of the voltage U_A, which corresponds to this feature, as we have already noted, is virtually independent of temperature. At the same time, the value of Δ clearly decreases as we approach the critical temperature. An analogous situation was discussed in Ref. 4, where the mutual influence of the two effects was considered: as the temperature is raised, these effects lead to voltage changes which are opposite in sign and which correspond to the features mentioned above; specifically (a) the effect of decreasing Δ, and (b) the effect of thermal broadening of the distribution function. It should not be ruled out that the distribution function in the normal region could be a nonequilibrium function.[1]

The position of the maximum in the differential resistance denoted by the point B depends on temperature according to the law $U_B\approx(T_{c1}-T)^{1/2}$, where $T_{c1}=$ 8.7 K to an accuracy of 0.1 K corresponds to the point at which the resistance begins to decrease and becomes temperature dependent (Fig. 1) and to the value of T_{c1} obtained from the exponent of the temperature dependence of the resistance below 8.7 K (Fig. 1). This peak in the differential resistance is explained in Ref. 6 by heating of the electrons by the current in the normal region and a corresponding thermal disruption of the superconductivity near the S–Smc boundary.

As control devices we made structures analogous in their topology on substrates with bulk (in the form of epitaxial films with thickness 150 nm) surface layers of degenerate GaAs (with a concentration of about $3\times10^{18}\,\mathrm{cm}^{-3}$). The resistance of these structures below the superconducting transition temperature was considerably higher than calculated (by roughly an order of magnitude), which indicates a high resistance in the contact regions, but the primary features of the conductivity that indicate a structure with a 2DEG channel were preserved [the overall character of the function $R(T)$, the presence of a minimum in the function $R_d(U)$ at $U=0$, the characteristic temperature dependence of the position of the voltage, corresponding to a maximum in the differential resistance $U_B(T)\sim(T_{c1}-T)^{1/2}$]. Similar results were also observed in Ref. 6 in studies of the conductivity of an Al contact with an epitaxial film of GaAs and the same contact with a surface δ-doped layer in GaAs—in the second case the resistance was considerably higher than the calculated resistance of the conducting layer. It is possible that this result is connected with depletion of the edge regions of the mesa structure which arises due to the surface defects.

In summary, we have investigated a new S-2DEG-S system based on a two-dimensional electron gas in an AlGaAs/GaAs heterostructure with contacts made of superconducting NbN. The distinctive features of the conductivity we observed point to the important role of multiple Andreev reflection at the scattering centers[12] in determining the transparency of the superconductor-semiconductor barrier at temperatures below the critical temperature in the superconducting ''banks.''

This work was carried out with the support of grants No. 96-02-18614 from the Russian Fund for Fundamental Research, NATO HTECH.LG- 960606, the program ''Physics of Solid-State Nanostructures'' (No. 1-069/4), and ''Current Scientific Schools'' (No. 96-15-96426).

[1] T. M. Klapwijk, Physica B **197**, 481 (1994).

[2] A. Kastalsky, A. W. Kleinsasser, L. H. Greene, R. Bhat, F. P. Milliken, and J. P. Harbison, Phys. Rev. Lett. **67**, 3026 (1991); C. Nguyen, H. Kroemer, and E. L. Hu, Phys. Rev. Lett. **69**, 2847 (1992); H. Takayanagi, T. Akazaki, and J. Nitta, Phys. Rev. Lett. **75**, 3533 (1995); L. C. Mur, C. J. P. M. Harmans, J. E. Mooij, J. F. Carlin, A. Rudra, and M. Ilegems, Phys. Rev. B **54**, R2327 (1996).

[3] A. M. Marsh, D. A. Williams, and H. Ahmed, Phys. Rev. B **50**, 8118 (1994).

[4] A. M. Marsh, D. A. Williams, and H. Ahmed, Physica B **203**, 307 (1994).

[5] J. R. Gao, J. P. Heida, B. J. van Wees, T. M. Klapwijk, G. Borghs, and C. T. Foxon, Surf. Sci. **305**, 470 (1994).

[6] J. Kutchinsky, R. Taboryski, T. Clausen, C. B. Sorensen, A. Kristensen, P. E. Lindelof, J. Bindslev Hansen, C. Schelde Jacobsen, and J. L. Skov, Phys. Rev. Lett. **78**, 931 (1997); R. Taboryski, T. Clausen, J. Bindslev Hansen, J. L. Skov, J. Kutchinsky, C. B. Sorensen, and P. E. Lindelof, Appl. Phys. Lett. **69**, 657 (1996).

[7] K. -M. H. Lenssen, M. Matters, C. J. P. M. Harmans, J. E. Mooij, M. R. Leys, W. van Vleuten, and J. H. Wolter, Appl. Phys. Lett. **63**, 2079 (1993).

[8] Y. Sugiyama, M. Tacano, S. Sakai, and S. Kataoka, IEEE Electron. Dev. Lett. **EDL-1**, 236 (1980); V. I. Barchukova, V. N. Gubankov, E. N. Enyushkina, S. A. Kovtonyuk, I. L. Lapitskaya, M. P. Lisitskiĭ, A. D. Maksimov, V. G. Mokerov, A. V. Nikiforov, and S. S. Shmelev, Pis'ma Zh. Tekh. Fiz. **21**, 12 (1995) [Tech. Phys. Lett. **21**, 208 (1995)].

[9] A. A. Verevkin, N. G. Ptitsina, K. V. Smirnov, G. N. Gol'tsman, E. M. Gershenzon, and K. S. Yngvesson, *International Semiconductor Device Research Symposium-1997* (Charlottesville, VA, USA, 1997), p. 163.

[10] V. M. Voronov, E. M. Gershenzon, G. N. Gol'tsman, T. O. Gubkina, V. D. Semash, and L. A. Seĭdman, Superconductors **7**, 1097 (1994).

[11] A. F. Andreev, Zh. Éksp. Teor. Fiz. **19**, 1228 (1964) [Sov. Phys. JETP **19**, 833 (1964)].

[12] B. J. van Wees, P. de Vries, P. Magnee, and T. M. Klapwijk, Phys. Rev. Lett. **69**, 510 (1992).

Translated by Frank J. Crowne

SEMICONDUCTORS VOLUME 33, NUMBER 5 MAY 1999

Nanorelief of an oxidized cleaved surface of a grid of alternating $Ga_{0.7}Al_{0.3}As$ and GaAs heterolayers

A. V. Ankudinov, V. P. Evtikhiev, V. E. Tokranov, V. P. Ulin,
and A. N. Titkov

A. F. Ioffe Physicotechnical Institute, Russian Academy of Sciences, 194021 St. Petersburg, Russia

(Submitted October 29, 1998; accepted for publication November 5, 1998)
Fiz. Tekh. Poluprovodn. **33**, 594–597 (May 1999)

The morphology of an oxidized cleaved surface of a grid of alternating GaAs and $Ga_{0.7}Al_{0.3}As$ layers was investigated by atomic-force microscopy. It was found that the surface of the native oxide film on a cleaved surface possesses a quasistationary nanorelief that reflects the composition of the layers of the heterostructure. The oxide regions above the GaAlAs layers are 0.5 nm higher than the regions above the GaAs layers. Etching off the oxide film shows that a nanorelief, which is inverted with respect to the relief of the oxide surface, also forms on the bared cleaved surface. The appearance of nanoreliefs on the surface and at the bottom boundary of the native oxide film is explained by the different oxidation depths of GaAs and $Ga_{0.7}Al_{0.3}As$ and by an oxidation-induced increase in the volume. © *1999 American Institute of Physics.* [S1063-7826(99)01505-7]

In view of the advances in semiconductor nanoelectronics it is of great interest to produce various artificial nanostructures on semiconductor crystal surfaces. In the present paper we call attention to an interesting possibility of obtaining a regular quasistationary nanorelief on cleaved surfaces of semiconductor heterostructures by oxidizing the structures. It is well known that native-oxide layers on the surfaces of different semiconductors have different thicknesses.[1] A surface relief can therefore be expected to appear in an oxide film on a cleaved surface of a heterostructure, since the height of the oxide is different above different layers of the structure. Moreover, when the oxide film is removed, the bared cleaved surfaces of heterostructures also possess a surface relief, which is determined by the composition of the layers, if the oxidation depths of the materials are different. The characteristic heights of the relief on a cleaved surface of a heterostructure can be assumed to be the thickness of the native oxide on the semiconductor surface, which can be estimated to be on the order of several nanometers.[2,3]

We investigated the morphology of cleaved surfaces of a grid of alternating GaAs(250 nm)/$Ga_{0.7}Al_{0.3}As$ (250 nm) heterolayers, oxidized under room conditions, and after removal of the oxide and chemical passivation of the bared surface by nitridization in a water solution of $N_2H_4+Na_2S$ (Ref. 4). Nitridization using solutions of hydrazine made it possible to protect the cleaved surface from new oxidation by coating it with a monolayer nitride film coherently bound to the semiconductor lattice.

The surface structure was studied by atomic-force microscopy (AFM) using the R4-SZM apparatus (scanning probe microscope built by the Russian company NT-MDT, located in Zelenograd). The AFM images of the surfaces were obtained in the room atmosphere in the contact regime with 10 to 40-nN forces on the surface being studied. Triangular Si and Si_3N_4 microcantilevers with pyramidal tips, whose radius of curvature was less than 40 nm, were used. The optical system, constructed in the laboratory, for positioning the tip of the atomic-force microscope was used to position the tips of the microcantilevers in the region, located at the edge of the cleaved surface, where the heterostructure layers emerged at the cleaved surface.

The heterostructure was grown on an *n*-GaAs(001) substrate by molecular-beam epitaxy and consisted of a 50-nm-thick *n*-$Ga_{0.7}Al_{0.3}As$ layer, a 300-nm-thick *n*-GaAs buffer layer, and 10 alternating *n*-$Ga_{0.7}Al_{0.3}As$ (250 nm)/*n*-GaAs(250 nm) layers covered with a 250-nm-thick *n*-GaAs layer; i.e., the final GaAs layer was 500 nm thick. The doping level of the silicon layers was several 10^{17} cm^{-3}. The experimental cleaved surfaces were obtained in the standard, humid, room atmosphere by cleaving a sample, thinned to 100–150 μm, by pressing a Pobedit knife in the $\langle 110\rangle$ direction on the backside of the substrate. Nitridization of the cleavage surfaces was performed by the procedure described in Ref. 4.

Figure 1a shows an AFM image of an oxidized cleaved surface of a heterostructure. The image clearly shows the presence of nanorelief. Periodic alternation of light and dark stripes is clearly seen in the image. This indicates that the height of the surface relief changes at the transition from one layer to another. The disruption of periodicity at the center of the image is caused by a 2-nm-high monatomic step, formed on the surface during cleaving. The light stripes, i.e., the higher stripes, in the image are thin (50 nm) stripes above the starting GaAlAs layer and all subsequent regions above the GaAlAs layers, while the regions above the GaAs layers appear dark and are lower. The AFM-image profile presented in Fig. 1b shows that the oxidized cleaved surface above the GaAlAs layers is on average 0.5 nm higher than above the GaAs layers. The same value is also obtained with a more accurate determination from a statistical analysis of the

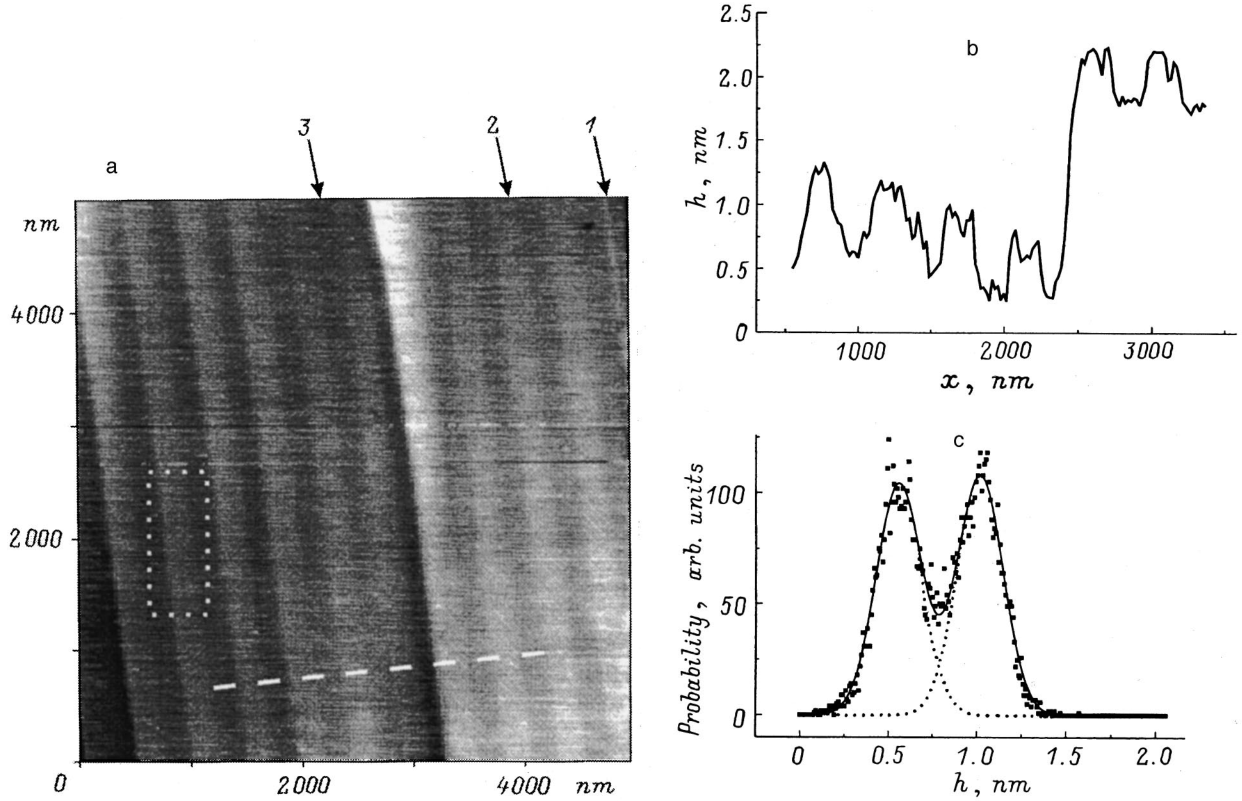

FIG. 1. a — AFM image of an oxidized cleaved surface of the heterostructure n-$Ga_{0.7}Al_{0.3}As/n$-GaAs; the arrows mark the starting GaAlAs layer (*1*) and GaAs (*2*) and GaAlAs (*3*) grid layers. b — Profile of an AFM image along the *x* coordinate along the dashed line in panel a. c — Statistical distribution of the height of the relief on the framed section of the surface in panel a; the dotted lines show the Gaussian contours and the solid line shows the total approximation; the distance between the centers of the two peaks is 0.46 nm.

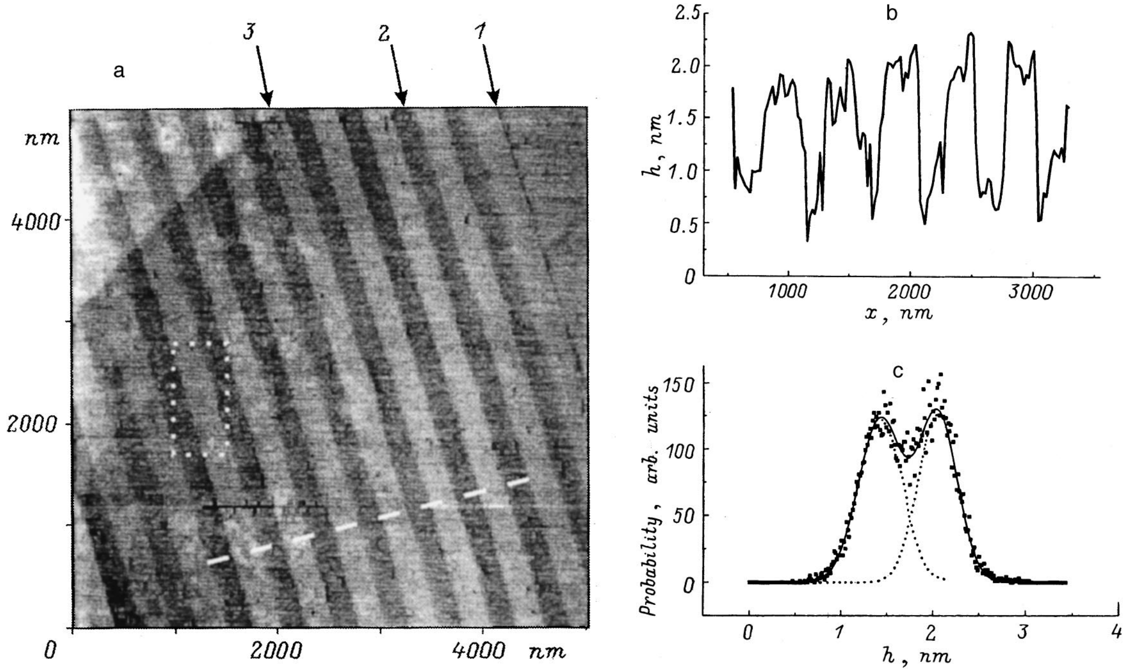

FIG. 2. a — AFM image of a cleaved surface, nitridized in a $N_2H_4+Na_2S$ solution, of the heterostructure n-$Ga_{0.7}Al_{0.3}As/n$-GaAs; the arrows mark the starting GaAlAs layer (*1*) and GaAs (*2*) and GaAlAs (*3*) grid layers. b — Profile of the AFM image along the *x* coordinate along the dashed line in panel *a*. c — Statistical distribution of the height of the relief on the framed section in panel a; the dotted line shows Gaussian contours and the solid line shows the total approximation; the distance between the centers of the two peaks is 0.62 nm.

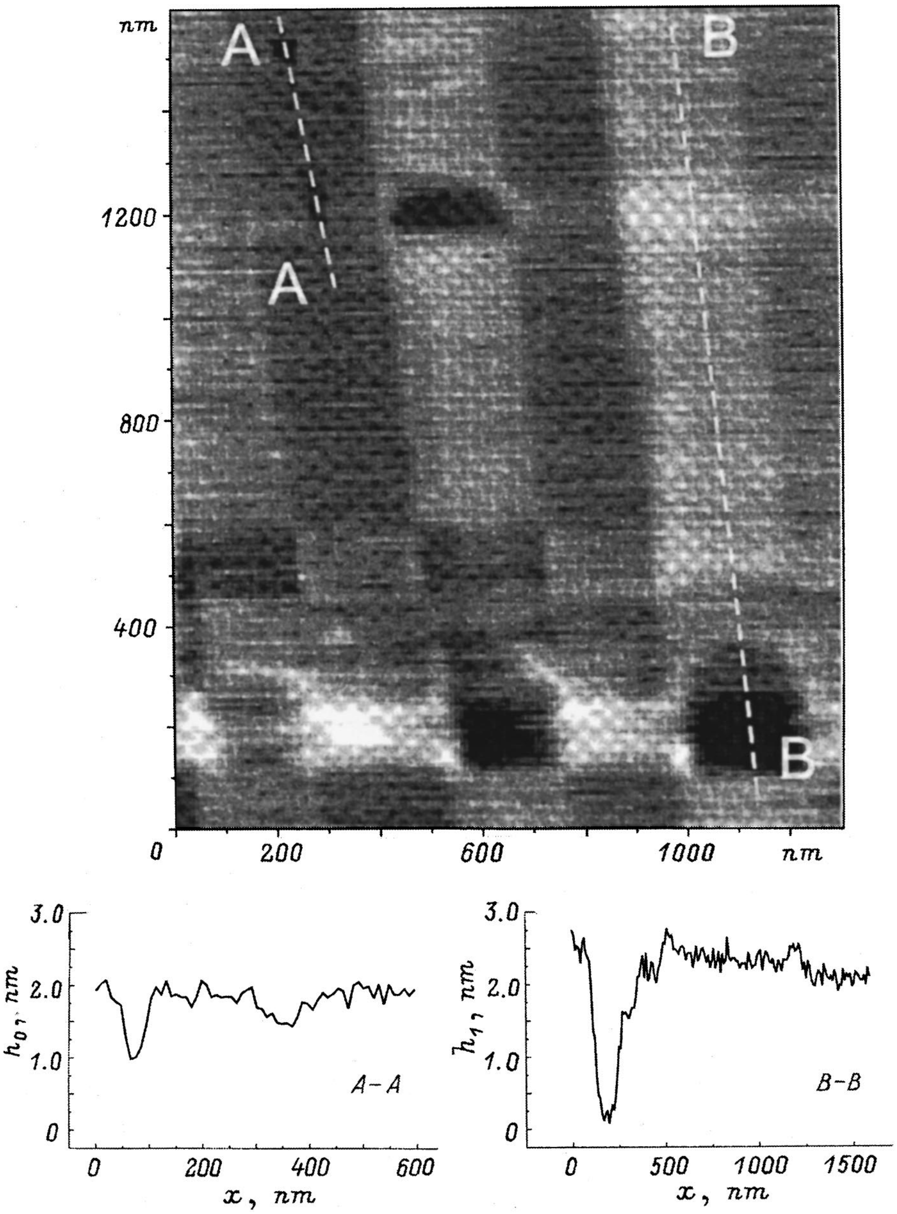

FIG. 3. AFM image of a section of an oxidized cleaved surface of a heterostructure. Local removal of the oxide film occurred in this cleaved surface as a result of repeated scanning. Bottom panels — profiles of the AFM image along the lines A–A and B–B, passing through a cavity in the oxide. The thickness of the oxide film on GaAs (h_0) and GaAlAs (h_1) can be estimated from the depth of the dips.

height (h), distribution in Fig. 1c, over the cleaved surface. This value of the difference in the heights of the oxide above the GaAlAs and GaAs layers, which was obtained in the first scan of the surface, did not change subsequently when the sample was studied several weeks and even months later. Apparently, the formation of oxide on a cleaved surface is essentially completed in less than 1 h, the time required to set the sample in the AFM and to perform the first scan of the surface. The formation time of a continuous oxide film under room conditions was estimated in Ref. 2 to be 20 min, which agrees with our data.

Figure 2a shows an AFM image of a cleaved surface which has undergone nitridization. Inversion of the surface relief of the cleaved surface after nitridization is clearly observed. Now the thin stripe of the starting GaAlAs layer and all subsequent GaAlAs layers appear darker and therefore they are lower. The profile of the AFM image and statistical analysis of the height distributions shown in Fig. 2b and 2c, respectively, yield additional information about the inverted relief. After the cleaved surface has undergone nitridization, the GaAlAs layers lie 0.6 nm below the GaAs layers. A small increase in the surface roughness is also evident; this is indicated by the larger half-width of the peaks of the height distribution in Fig. 2c as compared with Fig. 1c. We note that the sign and even the magnitude of the height differential in the AFM image of a nitridized cleaved surface remained unchanged a period of at least 1.5 months when the cleaved surface was exposed to the room atmosphere. The fact that the relief of the oxidized surface did not return evidently shows that surfaces treated in this manner are highly resistant to repeated oxidation.

Comparing the data in Figs. 1 and 2 shows that the oxide layer on the cleaved surface of the periodic GaAlAs/GaAs heterostructures is fluted, the height of the oxide layer above the GaAlAs layers is larger, and the oxide layer penetrates more deeply into these layers than into the GaAs layers. This was independently confirmed by experiments on multiple AFM scanning of an oxidized cleaved surface. Local re-

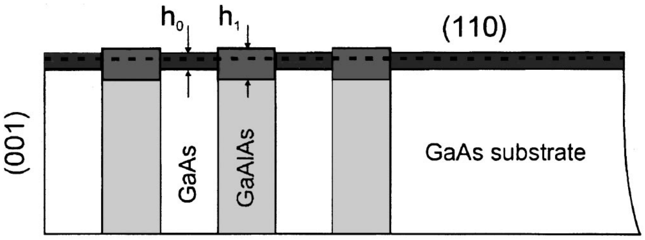

FIG. 4. Schematic representation of a native-oxide film on the cleaved surface of the experimental structure. The dashed lines show the imaginary line of the initial unoxidized cleaved surface, h_0 is the height of the oxide on GaAs, and h_1 is the height of the oxide on GaAlAs.

moval of the oxide film by the mechanical action of the probe of the atomic-force microscope was observed. Figure 3 shows the AFM image of an oxidized cleaved surface of a heterostructure with individual oxide sections which had been chipped off. The image profiles for the chipped off sections of the oxide above the GaAs and GaAlAs layers are presented beneath the figure. They give an idea of the characteristic depths of such sections, $h_0 \approx 1.0$ nm and $h_1 \approx 2.2$ nm, respectively. Comparing h_0 and h_1 suggests that the oxidation of GaAlAs layers is indeed deeper than that of GaAs layers and comes close to the depth of the relief arising on the cleaved surface of the heterostructure after nitridization.

Figure 4 shows schematically the fluting of the native-oxide film on the cleaved surface of the heterostructure. The relief observed in Fig. 2a is shown in Fig. 4 as the bottom boundary of the oxide. This is explained by the higher rate of oxidation and greater thickness of the oxide for GaAlAs than for GaAs.[1] The formation of a reverse relief on the top surface of the oxide is due to the relative increase in the volume of the oxdized layers, which leads to stretching of the layers in the direction of the free surface. The deeper oxidation of the GaAlAs layers will obviously also cause the cleaved surface to arch more above these layers.

In summary, the atomic-force microscopy method with a vertical resolution of 1 Å allowed us to obtain the first quantitative characterization of the modulation of the thickness of a native-oxide film on the cleaved surface of alternating GaAs and $Ga_{0.7}Al_{0.3}As$ layers. The thicknesses of the films arising on a (110) cleaved surface of GaAs and $Ga_{0.7}Al_{0.3}As$ layers under room conditions were estimated to be 1 and 2 nm, respectively. The desired stable nanorelief, which can also be inverted by removing the oxide, can be obtained on the cleaved surface of the heterostructure after oxidation by varying the alternation of the layers in the structure.

This work was supported by the Russian Fund for Fundamental Research (Grants 96-02-17952 and 97-02-18291) and the State program ''Physics of Solid-State Nanostructures'' (Grant 97-1035).

[1] W. Mönch, *Semiconductor Surfaces and Interfaces* (Springer-Verlag, 1993) [Springer Series on Surface Science, Vol. 26, 1993, Chap. 17, p. 276].

[2] P. Moriarty and G. Hughes, Ultramicroscopy **42–44**, 956 (1992).

[3] Hirokato Ohno, Larry Akio Nagahara, Shangir Gwo, Wataru Mizutani, and Hiroshi Tokumoto, Jpn. J. Appl. Phys. **35**, Pt. 2, L512 (1996).

[4] V. P. Ulin, V. L. Berkovits, V. M. Lantratov, and T. V. L'vova, in *Proceedings SOTAPOCS-XXVII* (1997) [Electrochem. Soc. Proc. **97–27**, 343 (1997)].

Translated by M. E. Alferieff

SEMICONDUCTORS VOLUME 33, NUMBER 5 MAY 1999

LOW-DIMENSIONAL SYSTEMS

Spectrum and electron-phonon interaction in a medium with a cylindrical quantum wire

N. V. Tkach and V. P. Zharkoĭ

Yu. Fed'kovich Chernovtsy State University, 274012 Chernovtsy, Ukraine

(Submitted April 7, 1998; accepted for publication October 4, 1998)
Fiz. Tekh. Poluprovodn. **33**, 598–602 (May 1999)

The effect of multiphonon processes on the electronic (hole) spectrum in a β-HgS/CdS nanoheterostructure (cylindrical quantum wire in a bulk medium) is studied in the dielectric-continuum model. The electron–phonon interaction Hamiltonian is obtained for a potential well of finite depth. The shift of the electron (hole) energy level as a result of the interaction with optical longitudinal (confined) and interface phonons is determined. The dependence of the band gap of the nanosystem β-HgS/CdS on the radius of the quantum wire is found. It is established that interface phonons play the dominant role in the renormalization of the electronic (hole) spectrum in a quantum wire with small transverse dimensions. © *1999 American Institute of Physics.* [S1063-7826(99)01605-1]

The theory of the phonon spectrum of spatially confined heterosystems [flat quantum wells (QWs), quasi-one-dimensional quantum wires (QWs), and quantum dots] has been under development now for a long time. There exist microscopic,[1] semimicroscopic,[2] and macroscopic hydrodynamic-continuum models[3] and a dielectric-continuum (DC) model,[4] which to a greater or lesser extent determine the spectrum of confined volume (L) and interface (I) phonons in ionic semiconductor nanoheterostructures.

The theory of the electronic (hole) spectrum is well developed for such systems in the effective-mass approximation, which works fairly well even when the linear dimensions of the nanosystems are only several lattice constants.[5] The theory of the electron–phonon interaction is now under intensive development, since there are various unsolved questions that require an adequate understanding and description of physical processes in nanoheterosystems.

One problem is that if any of the microscopic or semimicroscopic models are used to investigate the electron–phonon interaction, then the interaction Hamiltonian becomes so complicated that without additional simplifications, which are difficult to control, the problem of renormalizing the electronic spectrum, for all practical purposes, cannot be solved. For this reason, the basic model for investigating problems of this kind is the DC model, which, despite its comparative simplicity, gives a phonon spectrum that is essentially identical to that of the semimicroscopic Huang–Zhu model.[2] The DC model has the advantage that it contains no free parameters, only the known values of the phonon energies and dielectric constants of the corresponding bulk crystals.

The theory of the renormalization of the electronic spectrum by phonons in a cylindrical QW was developed in Refs. 1 and 5. However, it was based on an extremely idealized model, which presumed that the QW is an infinitely deep potential well. This strongly decreases a priori the real role of the interaction of an electron with I phonons, since the I-phonon field has a maximum potential at precisely the location (at the interface) where the electronic wave function strictly vanishes because of the assumed infinite well depth.

Therefore the goal of the present work is to calculate the renormalization of the ground state of an electron (hole) in a β-HgS/CdS cylindrical nanoheterosystem as a result of the interaction of the electron (hole) with L and I phonons in the presence of a finite jump of the potential at the interface. Since the interaction of the electron with I phonons in such a nanosystem was found to be quite strong, it was necessary to take into account effectively virtual multiphonon processes by the Green's function method.

1. SPECTRUM AND EFFECTIVE MASS OF AN ELECTRON IN A β-HgS/CdS CYLINDRICAL QUANTUM WELL DISREGARDING THE INTERACTION WITH PHONONS

Let us consider a β-HgS/CdS cylindrical QW (Fig. 1a). An electron with charge e and radius vector $\mathbf{r}$ is characterized by an effective mass m, which is different in different media:

$$m(\rho)=\begin{cases} m_0, & 0\leqslant\rho<R \quad (\text{medium ``0'', HgS}),\\ m_1, & R<\rho<\infty \quad (\text{medium ``1'', CdS}).\end{cases} \tag{1}$$

The electron moves in the field of a potential which as a function of ρ has the form (see Fig. 1b)

$$U(\rho)=\begin{cases} -U_0, & 0\leqslant\rho\leqslant R,\\ -U_1, & R<\rho<\infty,\end{cases} \tag{2}$$

where R is the radius of the wire, and U_0 and U_1 are the potential energies of the electron in the corresponding media relative to the vacuum. To determine the bound states it is most convenient to choose the energy reference point relative to the potential in medium 1 (CdS). Then

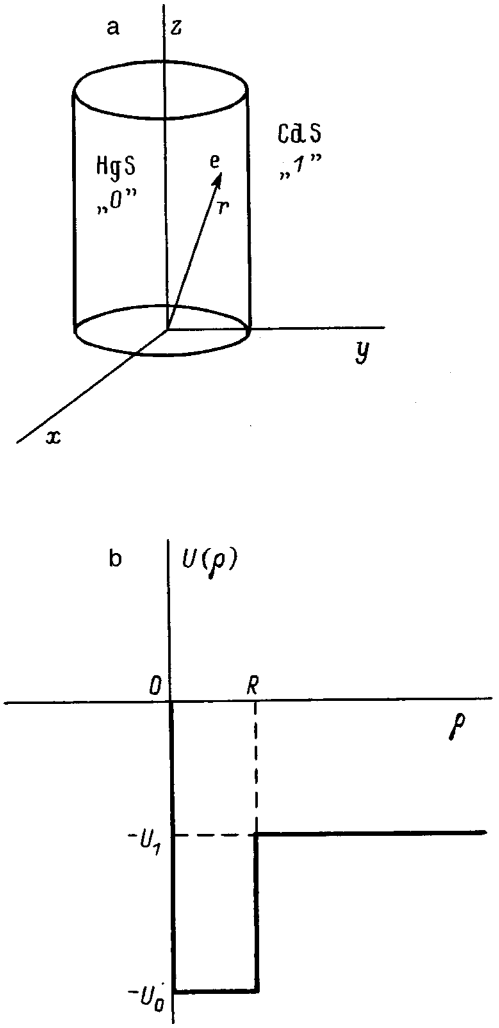

FIG. 1. Model of a cylindrical quantum wire β-HgS/CdS. The numbers 0 and 1 denote the media HgS and CdS with the potentials U_0 and U_1, respectively.

$$V(\rho)=\begin{cases} -V_0, & 0\leqslant\rho<R, \quad V_0=U_0-U_1, \\ 0, & R<\rho<\infty. \end{cases} \tag{3}$$

The electron Hamiltonian in the nanoheterosystem (ignoring the interaction with phonons) in a cylindrical coordinate system is

$$H(\rho,\varphi,z)=-\frac{\hbar^2}{2\rho}\left[\frac{\partial}{\partial\rho}\left(\frac{\rho}{m(\rho)}\frac{\partial}{\partial\rho}\right)+\frac{1}{\rho}\frac{\partial^2}{\partial\varphi^2}\right] -\frac{\hbar^2}{2m(\rho)}\frac{\partial^2}{\partial z^2}+V(\rho). \tag{4}$$

The solution of the steady-state Schrödinger equation

$$[H(\rho,\varphi,z)-E_{nmk}]\psi_{nmk}(\rho,\varphi,z)=0 \tag{5}$$

is

$$E_{nmk}=E_{nm}+\hbar^2k^2/(2\mu_{nm}), \tag{6}$$

where the energy levels E_{nm} of the quantized motion of an electron are determined by the roots of the equation

$$\frac{\chi_0}{m_0}\frac{J_{|m|+1}(\chi_0R)-J_{|m|-1}(\chi_0R)}{J_{|m|}(\chi_0R)} =\frac{\chi_1}{m_1}\frac{K_{|m|+1}(\chi_1R)-K_{|m|-1}(\chi_1R)}{K_{|m|}(\chi_1R)}, \tag{7}$$

and the correlated electron effective mass

$$\mu_{nm}=\overline{m}/(1+I_{nm}\overline{m}), \quad \overline{m}=(m_0+m_1)/2, \tag{8}$$

as a characteristic of this quasiparticle in the nanoheterosystem, depends on the quantum states $|nm\rangle$ in terms of the quantity

$$I_{nm}=R^{-2}\left\{|A_{|m|}|^2\int_0^R[m^{-1}(\rho)-\overline{m}^{-1}]|J_{|m|}(\chi_0\rho)|^2\rho d\rho +|B_{|m|}|^2\int_R^\infty[m^{-1}(\rho)-\overline{m}^{-1}]|K_{|m|}(\chi_1\rho)|^2\rho d\rho\right\}. \tag{9}$$

The electron wave functions are

$$\psi_{nmk}=\frac{\exp[i(m\varphi+kz)]}{R\sqrt{2\pi L}}A_{|m|}\begin{cases} J_{|m|}(\chi_0\rho), & \rho\leqslant R, \\ B_{|m|}K_{|m|}(\chi_1\rho), & \rho\geqslant R, \end{cases} \tag{10}$$

where

$$A^2_{|m|}=2/\{J^2_{|m|}(\chi_0R)-J_{|m|-1}(\chi_0R)J_{|m|+1}(\chi_0R) +B^2_{|m|}[K_{|m|-1}(\chi_1R)K_{|m|+1}(\chi_1R)-K^2_{|m|}(\chi_1R)]\}, \tag{11}$$

$$B_{|m|}=J_{|m|}(\chi_0R)/K_{|m|}(\chi_1R), \quad \chi_0=\sqrt{2m_0(V_0-|E|)/\hbar}, \quad \chi_1=\sqrt{2m_1|E|/\hbar}, \tag{12}$$

E is the electron energy, $n=1,2,3,\ldots$ is the radial quantum number, $m=\ldots, -2,-1,0,1,2,\ldots$ is the magnetic quantum number, k is the axial component of the wave vector, $J_{|m|}$ are Bessel functions, and $K_{|m|}$ are modified Bessel functions.

Thus the electron motion is quantized in a direction perpendicular to the axis of the QW, and in the longitudinal direction the electron undergoes an infinite motion with effective mass μ_{nm}.

2. RENORMALIZATION OF THE GROUND STATE ENERGY OF AN ELECTRON BY *L* AND *I* PHONONS IN A β-HgS/CdS NANOHETEROSYSTEM

The electron–phonon system in a quantum wire (QW) with a finite potential jump at the interface in the dielectric-continuum (DC) model is described by the Hamiltonian

$$H=H_e+H_{\text{ph}}+H_{\text{int}}, \tag{13}$$

where

$$H_e=\sum_{nmk}E_{nmk}\hat{a}^+_{nmk}\hat{a}_{nmk} \tag{14}$$

is the Hamiltonian of the electronic subsystem, obtained by rewritting the Hamiltonian (4) in the second-quantized representation following the general theory,[6] and

$$H_{\mathrm{ph}}=\sum_{\lambda mq}\Omega_{\lambda mq}(\hat{b}^{+}_{\lambda mq}\hat{b}_{\lambda mq}+1/2) \tag{15}$$

is the Hamiltonian of polarized phonons in the dielectric-continuum model.[1,5] The index $\lambda=\pm$ for I phonons and $\Lambda=L$ for L phonons. The Hamiltonian of the electron–phonon interaction in the second-quantized representation with respect to the variables of both subsystems

$$H_{\mathrm{int}}=\sum_{\substack{n_1m_1\\ n_2m_2}}\sum_{\substack{nm\\ k\lambda q}}\Phi^{n_2m_2}_{n_1m_1}(\lambda,n,m,q)\hat{a}^{+}_{n_2m_2,k+q}\hat{a}_{n_1m_1k}\times(\hat{b}_{\lambda mq}+\hat{b}^{+}_{\lambda,-m,-q}) \tag{16}$$

was found by transforming the corresponding Hamiltonian from Ref. 5 to the basis consisting of the wave functions (10). Since the coupling functions $\Phi^{n_2m_2}_{n_1m_1}(\lambda,n,m,q)$ are very complicated analytic expressions, we shall not present them here in general form. In what follows we shall be interested in the renormalization of the ground state of an electron in a heterosystem with a small QW. In such a system the bottom energy band is located far from the other bands, so that we shall ignore the interband interaction via phonons and take into account only the coupling function of the ground-state band with phonons. Then

$$\Phi_{L_0}(n,q)=-\frac{e}{R^2}\sqrt{\frac{2\Omega_L(\varepsilon_{0\infty}^{-1}-\varepsilon_{0s}^{-1})}{LR^2(q^2+x_{n0}^2/R^2)}}\,A_0^2\mathrm{J}_1^{-1}(x_{n0})\times\int_0^R\rho\mathrm{J}_0^2(\chi_0\rho)\mathrm{J}_0(x_{n0}\rho/R)\,d\rho \tag{17}$$

is the coupling function of an electron with confined L_0 phonons of the QW. The electron does not interact with the confined L_1 medium–barrier phonons ($\Phi_{L_1}\equiv 0$), and the interaction of the electron with the two branches of the I phonons corresponds to the functions

$$\Phi_{\pm}(q)=-\frac{e}{R^2}\sqrt{\frac{2\pi\Omega_{\pm}(q)}{y_qR}}\,A_0^2\times\begin{cases}\alpha_{1\pm}(q)\displaystyle\int_0^R\rho\mathrm{J}_0^2(\chi_0\rho)\mathrm{J}_0(q\rho)\,d\rho, & \rho<R,\\[2ex] \alpha_{2\pm}(q)\dfrac{I_0(qR)}{\mathrm{K}_0(qR)}B_0^2\displaystyle\int_0^R\rho\mathrm{K}_0^2(\chi_1\rho)\mathrm{K}_0(q\rho)\,d\rho, & \rho>R,\end{cases} \tag{18}$$

where

$$y_q=2\pi Lq\,\mathrm{I}_0(x)\{[\mathrm{I}_0(x)]'-\mathrm{I}_0(x)\mathrm{K}_0^{-1}(x)[\mathrm{K}_0(x)]'\}\ \ (x=qR), \tag{19}$$

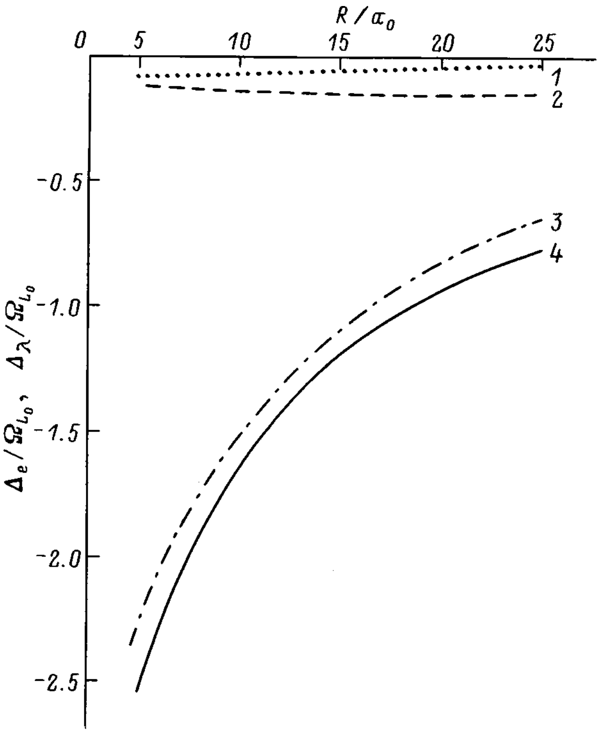

FIG. 2. Total Δ_e and partial Δ_λ shifts of the ground state energy of an electron versus the radius of the quantum wire. The lines *1*, *2*, *3*, and *4* correspond to Δ_-, Δ_L, Δ_+, and Δ_e.

$$\alpha_{j\pm}(q)=\frac{\Omega_{L_j}}{\Omega_{\pm}(q)}\times\frac{\sqrt{\varepsilon_{j\infty}^{-1}-\varepsilon_{js}^{-1}}[\varepsilon_{js}\Omega_{\pm}^2(q)-\varepsilon_{j\infty}\Omega_{L_j}^2]}{\Omega_{L_j}^2(\varepsilon_{js}-\varepsilon_{j\infty})}\quad (j=0,1). \tag{20}$$

Here, according to Ref. 5, $\Omega_{L_{0,1}}$ are the energies of the confined L phonons of media 0 and 1, respectively; and $\Omega_{\pm}(q)$ are the energies of the interfacial I phonons. These energies are determined by the dispersion relation

$$\mathrm{K}_0(x)[\mathrm{I}_0(x)]'\varepsilon_{0\infty}\frac{\Omega^2-\Omega_{L_0}^2}{\Omega^2-\Omega_{T_0}^2}=\mathrm{I}_0(x)[\mathrm{K}_0(x)]'\varepsilon_{1\infty}\frac{\Omega^2-\Omega_{L_1}^2}{\Omega^2-\Omega_{T_1}^2}\quad (x=qR), \tag{21}$$

where I_0 and K_0 are zeroth-order modified Bessel functions.

We shall now investigate the renormalization of the ground state of an electron (hole) by the interaction with phonons. In the one-band approximation at $T=0$ K the rernormalized electron energy is determined by the pole of the Fourier transform of the Green's function ($\hbar=1$)[7]

$$G(k,\omega)=1/[\omega-E(k)-M(k,\omega)], \tag{22}$$

where M is the total mass operator (MO). Since in our problem the electron–I phonon coupling is strong, and since the

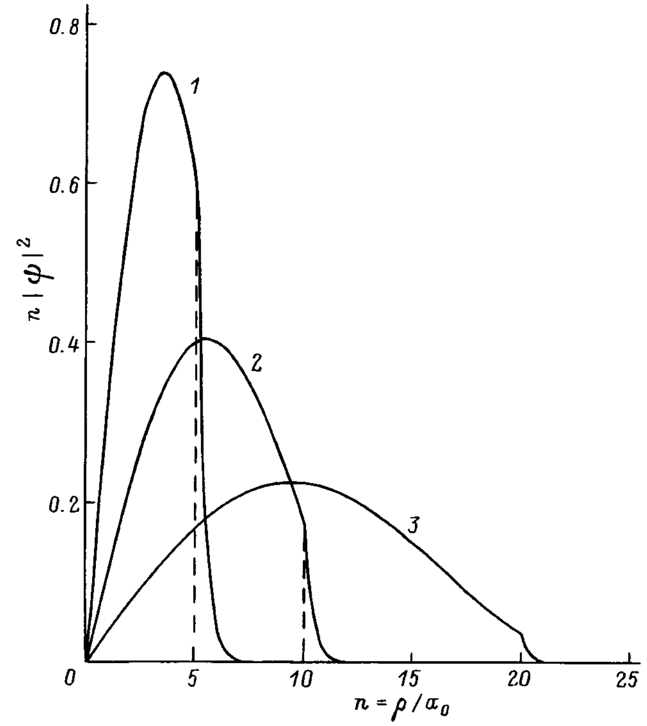

FIG. 3. Probability density distribution for an electron to be located in a quantum wire. Sizes of the quantum wires, R/a_0: *1* — 5; *2* — 10; *3* — 20.

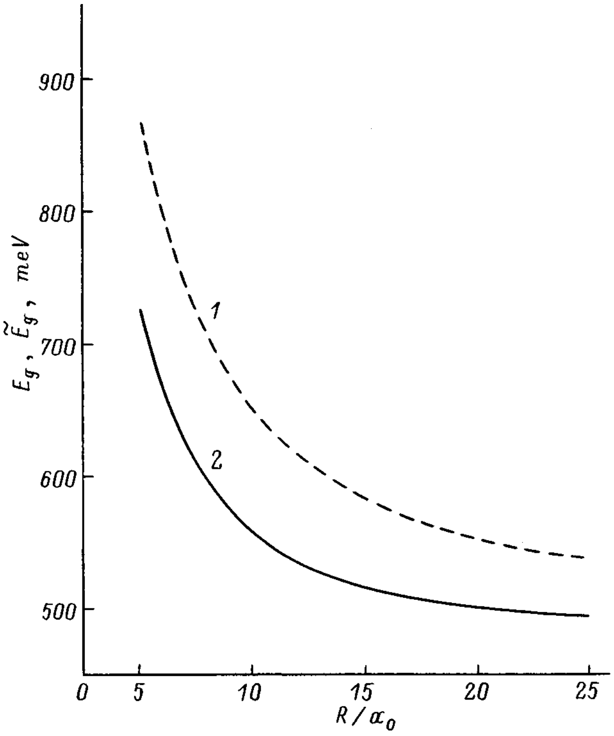

FIG. 4. Band gap in the system β-HgS/CdS versus the radius of the quantum wire. The calculation was performed *1* — disregarding (E_g) and *2* — taking into account ($\tilde{E}_g$) the interaction with phonons.

coupling functions with phonons of all branches have sharp maxima, the MO can be represented in the form of an infinite integral continued fraction[8]

$$M(\omega)=\sum_{\lambda_1}\int_0^1\frac{|\Phi_{\lambda_1}(Q_1)|^2 dQ_1}{\omega-E(Q_1)-\Omega_{\lambda_1}(Q_1)-\dots}$$

$$-2\sum_{\lambda_2}\int_0^1\frac{|\Phi_{\lambda_2}(Q_2)|^2 dQ_2}{\omega-E(Q_1+Q_2)-\Omega_{\lambda_1}(Q_1)-\Omega_{\lambda_2}(Q_2)-\dots}$$

$$-n\sum_{\lambda_n}\int_0^1\frac{|\Phi_{\lambda_n}(Q_n)|^2 dQ_n}{\omega-E\left(\Sigma_{j=1}^{n}Q_j\right)-\Sigma_{j=1}^{n}\Omega_{\lambda_j}(Q_j)-\dots}. \quad (23)$$

Here

$$Q_j=\frac{a_0}{\pi}q_j.$$

The phonon-renormalized position $\tilde{E}$ of the electron-band bottom ($k=0$) is found as the root of the dispersion relation

$$\omega-E-M_n(\omega)=0, \quad (24)$$

where $M_n(\omega)$ is the n-phonon approximation of the MO (23).

We calculated the position of the conduction (valence) band bottom (top) for an electron (hole) without interaction with phonons $E_e(E_h)$ and with interaction with all phonons $\tilde{E}_e(\tilde{E}_h)$ for the heterosystem β-HgS/CdS. The following published parameters characterizing the bulk analogs of nanocrystals of the heterostructure were used:

$\Omega_{L_0}=27.8$ meV, $\varepsilon_{0\infty}=11.4$, $\varepsilon_{0s}=18.2$,
$\Omega_{L_1}=57.2$ meV, $\varepsilon_{1\infty}=5.5$, $\varepsilon_{1s}=9.1$,
$U_0=5.0$ eV, $E_{g0}=0.5$ eV, $a_0=0.585$ nm,
$U_1=3.8$ eV, $E_{g1}=2.5$ eV, $a_1=0.582$ nm.

Here a_0, E_{g0} and a_1, E_{g1} are the lattice constants and band gaps in HgS and CdS, respectively.

Figure 2 shows as an example the computational result for the shift $\Delta_e=\tilde{E}_e-E_e$ of the ground state of an electron and its partial components Δ_+, Δ_-, and Δ_L as a function of the radius of the QW. It is evident from the figure that the shift Δ_e is formed mainly by I_+ phonons, while the contributions of the confined (L) and I_- phonons are very small. As the radius of the QW decreases, the partial contribution of the L_0 phonons changes very little and that of the I_+ phonons increases sharply. The role of I_+ multiphonon processes increases substantially. The latter circumstance can be understood from physical considerations. Indeed, as the radius of the QW decreases, an electron penetrates increasingly more from β-HgS into β-CdS because of the finite height of the potential barrier, so that the probability of the electron being located at the interface of the media increases (Fig. 3). This increases the coupling between the electron and the field of the I_+ phonons, and hence the role of multiphonon processes in the shift of the electron level increases.

In a similar manner we calculated the shift of the hole ground state,

$$\Delta_h=\tilde{E}_h-E_h.$$

As a result, we found the dependence of the band gap of the nanoheterosystem β-HgS/CdS on the radius of the QW without allowance for the interaction of the electron and hole with phonons:

$$E_g = E_{g0} + V_{0e} + V_{0h} + E_{0e} + E_{0h}$$

and allowing for this interaction:

$$\widetilde{E}_g = E_g + \Delta_e + \Delta_h \,.$$

The computed curves are presented in Fig. 4. We thus see that the interaction with phonons does not qualitatively change the fact that the band gap increases with decreasing radius of the QW. However, because of the strong interaction of the electron and hole with I_+ phonons, $\widetilde{E}_g$ is substantially different from E_g (from tens of meV for $R \simeq 25a_0$ to hundreds of meV for $R \simeq 5a_0$). This should have a strong effect in comparing this calculation with experimental data.

In summary, the main result of this study is that the finite potential jump at the boundary of a quantum wire results in a strong interaction of an electron and hole with I_+ phonons. The effect is to decrease substantially the band gap in a β-HgS quantum wire in the medium β-CdS.

[1] X. F. Wang and X. L. Lei, Phys. Status Solidi B **175**, 433 (1993).
[2] K. Huang and B. Zhu, Phys. Rev. B **38**, 13377 (1988).
[3] B. F. Zhu, Phys. Rev. B **46**, 13619 (1992).
[4] R. Fachs and K. L. Kliwer, Phys. Rev. A **140**, 2076 (1965).
[5] X. F. Wang and X. L. Lei, Phys. Rev. B **49**, 4780 (1994).
[6] A. S. Davydov, *The Theory of Solids* (Nauka, Moscow, 1976).
[7] A. A. Abrikosov, L. P. Gor'kov, and I. E. Dzyaloshinskiĭ, *Methods of Quantum Field Theory in Statistical Physics* [Prentice-Hall, Englewood Cliffs, New Jersey, 1963; Fizmatgiz, Moscow, 1962].
[8] N. V. Tkach, Teor. Mat. Fiz. **61**, 400 (1984).

Translated by M. E. Alferieff

SEMICONDUCTORS VOLUME 33, NUMBER 5 MAY 1999

Electron and hole spectra in a superlattice of cylindrical quantum wires

V. M. Golovach and G. G. Zegrya

A. F. Ioffe Physicotechnical Institute, Russian Academy of Sciences, 194021 St. Petersburg, Russia

A. M. Makhanets, I. V. Pronishin, and N. V. Tkach

Chernovtsy State University, 274012 Chernovtsy, Ukraine

(Submitted July 15, 1998; accepted for publication November 3, 1998)
Fiz. Tekh. Poluprovodn. **33**, 603–607 (May 1999)

The electron and hole spectra in a superlattice of cylindrical quantum wires are calculated by the augmented-plane-wave method. The energy component due to the motion of quasiparticles in a direction perpendicular to the long axis of a wire consists of an alternation of bands with positive and negative effective mass. The potential of the quantum-wire superlattice lifts the degeneracy with respect to the magnetic quantum number away from the Γ point of the Brillouin zone. The energies of the main bands are investigated as functions of the radius of the quantum wires and the distance between wires for planar motion of quasiparticles. © *1999 American Institute of Physics.* [S1063-7826(99)01705-6]

Semiconductor heterostructures have been applied successfully in the last few years in opto- and microelectronics. Modern technology makes it possible to produce semiconductor heterostructures with quantum wells, quantum wires, and quantum dots. To predict device characteristics and to create new devices it is necessary to develop a microscopic approach to the analysis of the energy spectra of charge carriers in these heterostructures.

An interesting object of investigation is a heterostructure which consists of quantum wires (QWs) of one material inside a different material which form a superlattice in a plane perpendicular to the long axis of a QW. If the length L of a QW is much greater than the quasiparticle mean-free path, it can be assumed that the QW is infinitely long. The radius of the QW and the distance between the nearest neighbors can then be assumed to be much smaller than L. The spatial variation of the dimensions and arrangement of the QWs is understood to change the electronic, hole, and excitonic spectra in such a superlattice.

Our objective in the present paper is to investigate theoretically the electron and hole spectra and wave functions for a superlattice of cylindrical quantum wires (SCQW).

1. ELECTRON (HOLE) SPECTRUM IN A SUPERLATTICE OF CYLINDRICAL QUANTUM WIRES

We shall investigate a system consisting of cylindrical QWs (material 1) arranged periodically in a medium (material 2). The planar cross section of the system is shown in Fig. 1. We assume for definiteness that the potential energy and effective mass of an electron in the cylindrical coordinate system with z axis oriented along the long axis of one of the QWs are different in the different media.

To find the electronic spectrum and the wave functions it is necessary to solve the Schrödinger equation with the Hamiltonian, written in the cylindrical coordinate system,

$$\hat{H}=-\frac{\hbar^2}{2}\left(\nabla_{\rho\varphi}\frac{1}{\mu(\rho,\varphi)}\nabla_{\rho\varphi}+\frac{1}{\mu(\rho,\varphi)}\frac{\partial^2}{\partial z^2}\right)+U(\rho), \quad (1)$$

$$\hat{H}\Psi(\rho,\varphi,z)=E\Psi(\rho,\varphi,z). \quad (2)$$

We represent $\Psi(\rho,\varphi,z)$ in the form

$$\Psi(\rho,\varphi,z)=\frac{1}{\sqrt{L}}\psi(\boldsymbol{\rho})e^{ik_{\parallel}z}, \quad (3)$$

where L is the length of the main region along the axis of the QW. Substituting the expression (3) into Eq. (2), we obtain for $\psi(\boldsymbol{\rho})$ the equation

$$\left[-\frac{\hbar^2}{2}\left(\frac{1}{\rho}\frac{\partial}{\partial\rho}\rho\frac{1}{\mu(\rho,\varphi)}\frac{\partial}{\partial\rho}+\frac{1}{\rho^2\mu(\rho,\varphi)}\frac{\partial^2}{\partial\varphi^2}\right)+U(\rho,\varphi)\right]\psi(\boldsymbol{\rho})=\left(E-\frac{\hbar^2k_{\parallel}^2}{2\mu(\rho,\varphi)}\right)\psi(\boldsymbol{\rho}). \quad (4)$$

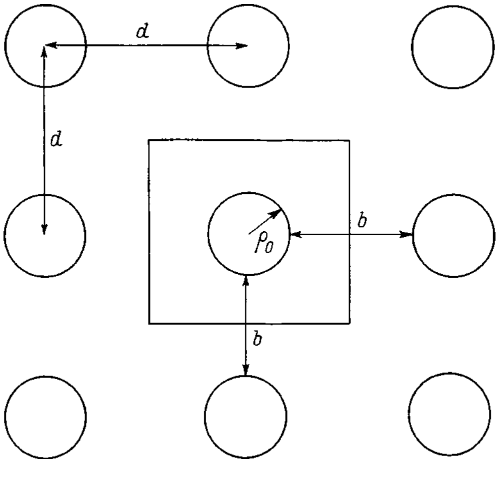

FIG. 1. Geometry of a superlattice of cylindrical quantum wires.

1063-7826/99/33(5)/5/$15.00

The equation (4) can be solved by the method of augmented plane waves (APWs), which is well known for three-dimensional systems.[1] The APW method is modified for our case of a planar system as follows.

We assume that in the xy plane the quantum wires form a square lattice with period $d=2\rho_0+b$, where ρ_0 is the radius of the cross section of a wire, and b is the thickness of the barrier region between neighboring QWs (Fig. 1). We place the coordinate origin at the center of a circle, whose radius is ρ_0, which is centered at a lattice site. Inside a Wigner–Seitz cell, the so-called $m-t$ potential, and the effective mass have the simple form

$$U(\rho)=\begin{cases} -U_0 & \text{for } \rho\leqslant\rho_0, \\ 0 & \text{for } \rho>\rho_0. \end{cases} \tag{5}$$

$$\mu(\rho)=\begin{cases} \mu_1 & \text{for } \rho\leqslant\rho_0, \\ \mu_2 & \text{for } \rho>\rho_0 \end{cases}. \tag{6}$$

Using the APW method,[1] we shall solve exactly the Schrödinger equation for the region of two-dimensional space inside the quantum wells, where the wave function can be represented as a superposition of cylindrical harmonics. In the region outside the wells the trial wave function can be chosen in the form of a plane wave, which can be expanded in cylindrical harmonics. The expansion coefficients are found from the continuity of the functions at the boundary of the circle of radius ρ_0. Thus a trial wave function in the form of an augmented plane wave (APW) can be represented in the form

$$\Phi_{\mathbf{k}_\perp-\mathbf{g}}(\boldsymbol{\rho})=\begin{cases} \dfrac{1}{\sqrt{\Omega_0}}\displaystyle\sum_{-\infty}^{\infty} i^m \frac{\mathrm{J}_m(|\mathbf{k}_\perp-\mathbf{g}|\rho_0)}{\mathrm{J}_m(\chi\rho_0)}\mathrm{J}_m(\chi\rho) \\ \quad\times\exp[im(\varphi-\varphi_{\mathbf{k}_\perp-\mathbf{g}})], & \rho\leqslant\rho_0, \\ \dfrac{1}{\sqrt{\Omega_0}}\exp[i(\mathbf{k}_\perp-\mathbf{g})\cdot\boldsymbol{\rho})=\dfrac{1}{\sqrt{\Omega_0}}\displaystyle\sum_{-\infty}^{\infty} i^m\mathrm{J}_m|\mathbf{k}_\perp-\mathbf{g}|(\rho) \\ \quad\times\exp[im(\varphi-\varphi_{\mathbf{k}_\perp-\mathbf{g}})], & \rho>\rho_0, \end{cases} \tag{7}$$

where $\Omega_0=(2\rho_0+b)^2$ is the unit-cell volume, J_m are Bessel functions, m is the magnetic quantum number, $\mathbf{k}_\perp$ is the wave vector of a quasiparticle (corresponding to motion in the xy plane), $\mathbf{g}$ is a two-dimensional reciprocal-lattice vector, $|\mathbf{k}_\perp-\mathbf{g}|$ and $\varphi_{\mathbf{k}_\perp-\mathbf{g}}$ are polar coordinates of the vector $\mathbf{k}_\perp-\mathbf{g}$, and

$$\chi=\hbar^{-1}\sqrt{2\mu_1\left(U_0-E+\frac{\hbar^2k_\parallel^2}{2\mu_1}\right)}.$$

The augmented plane wave (7) satisfies Bloch's periodicity condition but does not yet satisfy the Schrödinger equation with the superlattice potential, since until now no relation between the energy and the wave vector was assumed to exist. To find this relation, according to Bloch's theorem, we shall seek the quasiparticle wave function as a linear combination of augmented plane waves

$$\psi_{\mathbf{k}_\perp}(\boldsymbol{\rho})=\sum_{\mathbf{g}} c_{\mathbf{k}_\perp-\mathbf{g}}\Phi_{\mathbf{k}_\perp-\mathbf{g}}(\boldsymbol{\rho}), \tag{8}$$

where the summation extends over reciprocal-lattice vectors, and the coefficients $c_{\mathbf{k}_\perp-\mathbf{g}}$ are to be determined.

Since the derivative of any APW is discontinuous at the boundary between quantum wells and the interwell regions, the problem can best be solved not by using the Schrödinger equation but an equivalent variational principle. We define an energy functional in terms of the wave functions (8) as

$$\Lambda=\int_{\Omega_0}\left\{\frac{\hbar^2}{2}\nabla_{\rho,\varphi}\psi^*_{\mathbf{k}_\perp}\frac{1}{\mu(\rho,\varphi)}\nabla_{\rho,\varphi}\psi_{\mathbf{k}_\perp} + \left(U(\rho)-E+\frac{\hbar^2k_\parallel^2}{2\mu(\rho,\varphi)}\right)\psi^*_{\mathbf{k}_\perp}\psi_{\mathbf{k}_\perp}\right\}d\boldsymbol{\rho}. \tag{9}$$

Minimizing the functional Λ with respect to $c_{\mathbf{k}_\perp-\mathbf{g}}$, we obtain the system of equations

$$\left\{\frac{\hbar^2}{2\mu_2}(\mathbf{k}_\perp-\mathbf{g})^2-E+\frac{\hbar^2k_\parallel^2}{2\mu_2}\right\}c_{\mathbf{k}_\perp-\mathbf{g}}+\sum_{\mathbf{g}'}\Gamma_{\mathbf{g}\mathbf{g}'}c_{\mathbf{k}_\perp-\mathbf{g}'}=0, \tag{10}$$

where $\Gamma_{\mathbf{g}\mathbf{g}'}$ is an integral containing the functions $\Phi_{\mathbf{k}_\perp-\mathbf{g}}$, the functions $\Phi_{\mathbf{k}_\perp-\mathbf{g}'}$, and the Hamiltonian with the periodic potential of the system. Performing the integration in $\Gamma_{\mathbf{g}\mathbf{g}'}$ over the unit cell volume Ω_0, we obtain

$$\Gamma_{\mathbf{g}\mathbf{g}'}=\frac{2\pi\rho_0}{\Omega_0}\left\{-\left[\frac{\hbar^2}{2\mu_2}(\mathbf{k}_\perp-\mathbf{g})\cdot(\mathbf{k}_\perp-\mathbf{g}')-E+\frac{\hbar^2k_\parallel^2}{2\mu_2}\right]\times\frac{\mathrm{J}_1(|\mathbf{g}-\mathbf{g}'|\rho_0)}{|\mathbf{g}-\mathbf{g}'|}+\frac{\hbar^2}{2\mu_1}\sum_{m=-\infty}^{\infty}\exp[im\varphi_{\mathbf{g}\mathbf{g}'}]\mathrm{J}_m(|\mathbf{k}_\perp-\mathbf{g}|\rho_0)\mathrm{J}_m(|\mathbf{k}_\perp-\mathbf{g}'|\rho_0)\left[\frac{d}{d\rho}\ln\mathrm{J}_m(\chi\rho)\right]_{\rho=\rho_0}\right\}, \tag{11}$$

where $\varphi_{\mathbf{g}\mathbf{g}'}$ is the angle between the vectors $(\mathbf{k}_\perp-\mathbf{g})$ and $(\mathbf{k}_\perp-\mathbf{g}')$. The first term on the right-hand side of Eq. (11) originates from the regions outside the quantum wells, and all other terms arise as a result of the action of a gradient operator on the augmented plane waves. The quantities $\Gamma_{\mathbf{gg}'}$ are the Fourier components of the effective potential of the superlattice of quantum wells.

The requirement that the system (10) have a nontrivial solution gives the secular equation

$$\det\left|\left[\frac{\hbar^2}{2\mu_2}(\mathbf{k}_\perp-\mathbf{g})^2-E+\frac{\hbar^2k_\parallel^2}{2\mu_2}\right]\delta_{\mathbf{gg}'}+\Gamma_{\mathbf{gg}'}\right|=0. \tag{12}$$

This equation is used to determine the quasiparticle energy spectrum $E_n(\mathbf{k}_\perp, k_\parallel)$, $n=1,2,\dots,\tau$. The normalization condition

$$\sum_{\mathbf{gg}'} c^*_{\mathbf{k}_\perp-\mathbf{g}}c_{\mathbf{k}_\perp-\mathbf{g}'}(\mathrm{P}_{\mathbf{gg}'}+\mathrm{S}_{\mathbf{gg}'})=1, \tag{13}$$

where

$$\mathrm{P}_{\mathbf{gg}'}=\delta_{\mathbf{gg}'}-\frac{2\pi\rho_0}{\Omega_0}\,\frac{\mathrm{J}_1(|\mathbf{g}-\mathbf{g}'|\rho_0)}{|\mathbf{g}-\mathbf{g}'|}, \tag{14}$$

$$\mathrm{S}_{\mathbf{gg}'}=\frac{\pi\rho_0^2}{\Omega_0}\sum_{m=-\infty}^{\infty}\mathrm{J}_m(|\mathbf{k}_\perp-\mathbf{g}|\rho_0)\mathrm{J}_m(|\mathbf{k}_\perp-\mathbf{g}'|\rho_0)\times\frac{\mathrm{J}_m^2(\chi\rho_0)-\mathrm{J}_{m-1}(\chi\rho_0)\mathrm{J}_{m+1}(\chi\rho_0)}{\mathrm{J}_m^2(\chi\rho_0)}, \tag{15}$$

and the system of equations (10) determines uniquely the coefficients $c_{n,\mathbf{k}_\perp-\mathbf{g}}$ and therefore the wave functions

$$\psi_n(\boldsymbol{\rho},z)=\frac{1}{\sqrt{L}}e^{ik_\parallel z}\sum_{\mathbf{g}}c_{n,\mathbf{k}_\perp-\mathbf{g}}\Phi_{n,\mathbf{k}_\perp-\mathbf{g}}(\boldsymbol{\rho}). \tag{16}$$

TABLE I.

	U_0^e, eV	U_0^h, eV	E_g, eV	μ^e/μ_0	μ^h/μ_0	a, Å
β-HgS	1.2	−0.8	0.5	0.036	0.044	5.851
β-CdS	0	0	2.5	0.2	0.7	5.818

2. ELECTRON AND HOLE SPECTRA IN A SUPERLATTICE OF β-HgS QUANTUM WIRES IN A β-CdS MATRIX

The theory developed in the preceding section was used to calculate the electron and hole spectra in a square superlattice formed by β-HgS quantum wires embedded in a β-CdS crystal. This system is chosen because the two crystals have very similar lattice constants (see Table I) and because the boundary between them is very sharp (no transitional region), just as for complex quantum wells obtained experimentally in Ref. 2.

We shall focus our attention mainly on the numerical calculation of the dependences of the electron and hole energy spectra $E_n^{e,h}(\mathbf{k}_\perp, \mathbf{k}_\parallel)$, which correspond to the electron and hole motion in a plane perpendicular to the axis of a QW. We can thus assume that $k_\parallel=0$.

The spectrum $E_n(\mathbf{k}_\perp)$ was calculated for a system with the parameters given in Table I. Figures 2a and 2b show the spectrum of an electron and hole as an example. For the

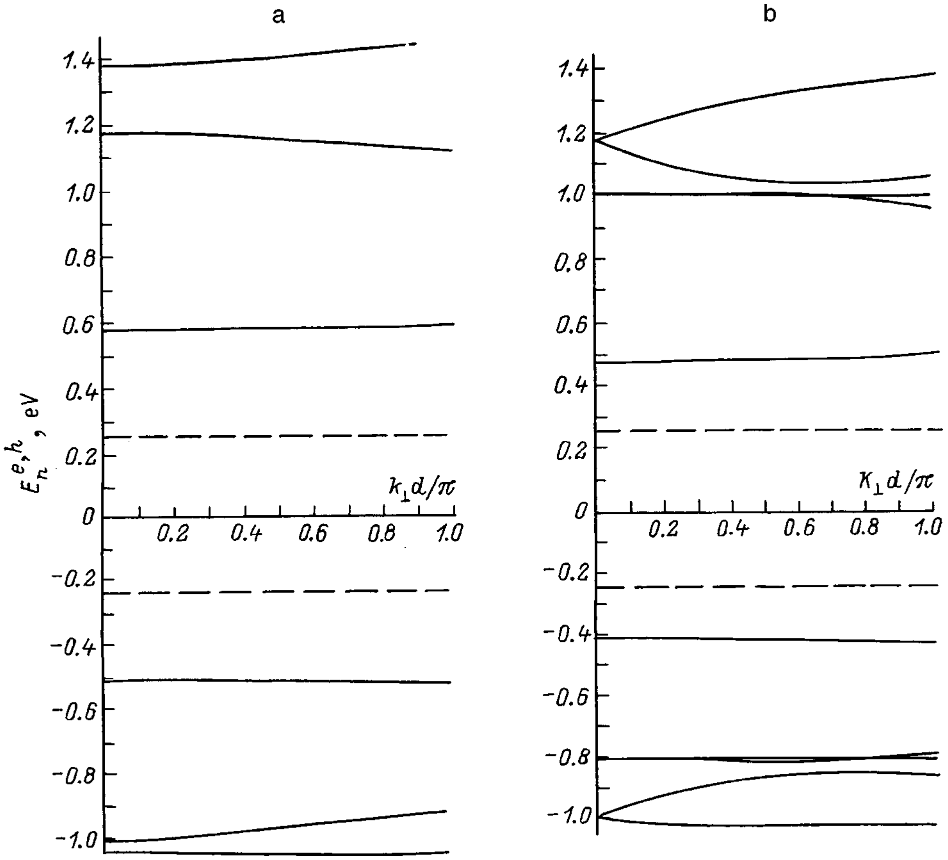

FIG. 2. Dispersion relation for an electron and a hole in a superlattice of cylindrical quantum wires with $\rho_0=7a_{\mathrm{HgS}}$ and $b=14a_{\mathrm{CdS}}$. The dashed curves show the conduction-band bottom and the valence-band top in HgS. The calculations were performed with a — one site of the reciprocal lattice ($\mathbf{g}=0$) and b — the first coordination circle.

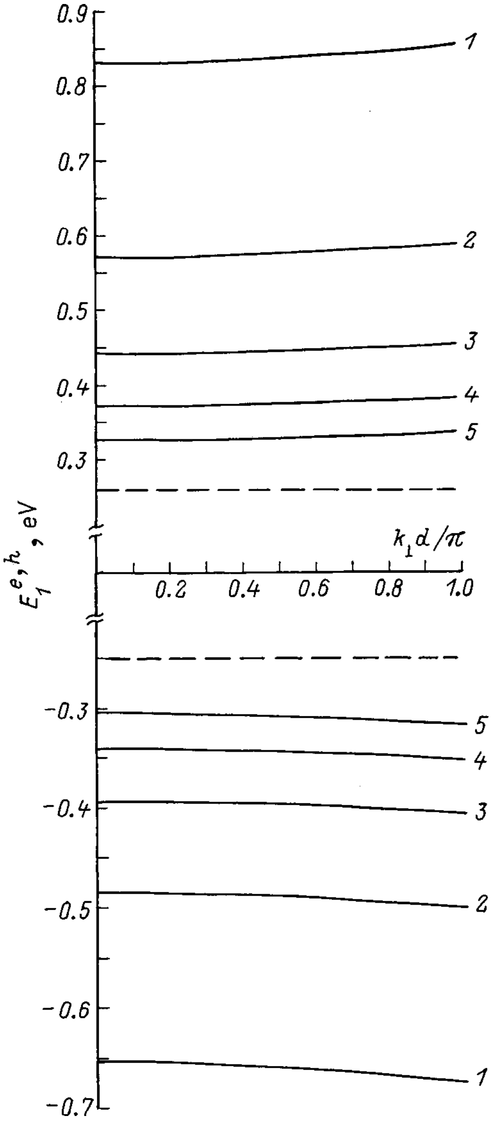

FIG. 3. Dispersion relation for the main band of quasiparticles in a superlattice of cylindrical quantum wires with $b = 16a_{\mathrm{CdS}}$ for the ratios ρ_0/a_{HgS} of the well radius ρ_0 to the lattice constant in HgS: *1* — 4; *2* — 6; *3* — 8; *4* — 10; *5* — 12. Dashed straight lines — same as in Fig. 2.

spectrum in Fig. 2a, only one site of the reciprocal lattice $(\mathbf{g}=0)$ is taken into account, while the spectrum in Fig. 2b was calculated taking into account the first coordination circle. We note that the difference between the spectra calculated taking into account the first and second coordination circles is so small that it is unnoticeable on the scale in Fig. 2b; i.e., the convergence of the APW method is very good in this case. For convenience, the energy $E_n^{e,h}(\mathbf{k}_\perp)$ is measured from the center of the band gap in β-HgS. The dashed lines represent the conduction-band bottom and the valence-band top of the β-HgS crystal–well.

It is evident from Fig. 2 that when $\mathbf{g}\neq 0$ a large (on the order of hundreds of meV) shift of all energy bands toward the energy origin and splitting in half of all bands (except the ground-state band) occur. The higher the electron band (the lower the hole band), the wider it is. The behavior of the bands agrees completely with physical considerations, since allowance for the nonzero components of the vector $\mathbf{g}$ is equivalent to taking into account the crystal potential, which, on the one hand, lowers the absolute value of the quasiparticle energies and, on the other, lifts the degeneracy with respect to the quantum number m (when $k_\perp \neq 0$). The increase in the widths of the bands corresponding to the excited states of quasiparticles stems from the fact that a quasiparticle with a higher energy tunnels more easily through the potential barriers of the medium (CdS) between the quantum wells (HgS).

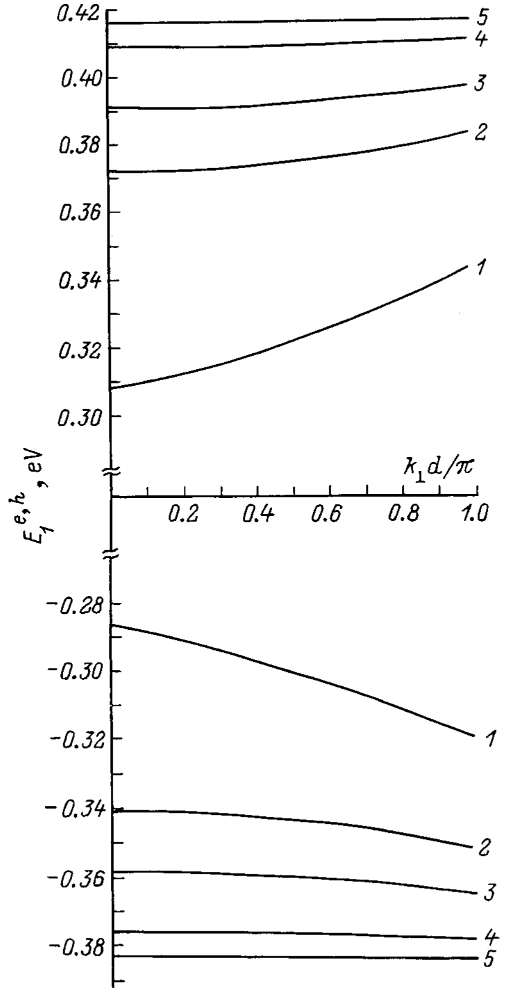

FIG. 4. Dispersion relation for the main band of quasiparticles in a superlattice of cylindrical quantum wires with $\rho_0 = 10a_{\mathrm{HgS}}$ for distances b between the wells corresponding to the ratio b/a_{CdS}: *1* — 12; *2* — 16; *3* — 20; *4* — 30; and *5* — 40.

Figure 3 shows the main bands of the electron and hole energy spectrum. These bands were calculated with different values of the QW radius but with a fixed barrier thickness. It is evident from the figure that the band widths are virtually insensitive to a change in radius, but as the radius of the QW increases, the bands shift very strongly (by hundreds of meV) to smaller absolute values of the energies.

Figure 4 shows the computational results for $E_1^e(k_\perp)$ and $E_1^h(k_\perp)$ with a fixed QW radius but different barrier thicknesses. It is evident from the figure that as the barrier thickness decreases, both bands shift appreciably (as much as a hundred meV) in the direction of smaller absolute energies. The band widths increase by a factor of 10, which is equivalent to a decrease of the corresponding component of the effective mass ($\mu_\perp$).

In summary, our theory of the spectrum of electrons and holes in a superlattice of quantum wires shows that the fundamental characteristics of quasiparticles can be deliberately controlled over very wide limits by varying the spatial dimensions of the superlattice of quantum wires.

This work was supported in part by the Russian Fund for Fundamental Research (Grants 97-02-18151, 98-07-90336, and 99-02-16796) and the State program ''Physics of Solid-State Nanostructures'' (Grants 97-1035 and 97-0003).

[1] I. M. Tsidil'kovskiĭ, *Electrons and Holes in Semiconductors* (Nauka, Moscow, 1972).
[2] D. Schoos, A. Mews, A. Eychmuller, and H. Weller, Phys. Rev. B **49** (24) 17072 (1994).

Translated by M. E. Alferieff

AMORPHOUS, GLASSY AND POROUS SEMICONDUCTORS

Vibrational spectra of erbium- and copper-modified hydrogenated amorphous carbon

V. I. Ivanov-Omskiĭ, A. A. Andreev, and G. S. Frolova

A. F. Ioffe Physicotechnical Institute, Russian Academy of Sciences, 194021 St. Petersburg, Russia

(Submitted September 22, 1998; accepted for publication September 23, 1998)
Fiz. Tekh. Poluprovodn. **33**, 608–613 (May 1999)

[S1063-7826(99)01805-0]

1. INTRODUCTION

The structure of hydrogenated amorphous carbon (*a*-C:H) is naturally related to the rich allotropic forms of this element, some of which, for example, the fullerenes, have been discovered only recently. The diversity of allotropic forms reflects the greater diversity, than for other elements, of atomic structures based on the three possible electronic configurations of carbon in linear structures (sp hybrid) and in trigonal (sp^2 hybrid) and tetrahedral (sp^3 hybrid) environments, respectively. Tetrahedral carbon present in a structure is responsible for the similarity of some properties of *a*-C:H and diamond. In due time, this served as a reason for calling tetrahedral carbon diamond-like (in the English abbreviation — DLC). The coexistence of carbon in the sp^2 and sp^3 states in the structure (*a*-C:H) makes this medium ideal for investigating the equilibrium between the two forms of carbon, which is the basis for the synthesis of diamond and graphite. It is known from such synthesis that different metals act as catalysts for the nucleation of diamonds, which can be interpreted as a metal-induced shift of the equilibrium of sp^2/sp^3 configurations in the direction of the latter. Therefore it is of interest to trace the nucleation of the diamond phase at the stage of nanocrystallite formation in metal-modified *a*-C:H. However, the use for this purpose of *x*-ray and electron diffraction methods, as well as Raman scattering, which are used conventionally for the detection of diamonds, runs into serious difficulties. In the diffraction methods this stems from the fact that the crystal lattice parameters of diamond and the metals employed as the catalyst are similar; in the Raman scattering methods it is attribuable to the resonance intensification of Raman scattering by the graphite component,[1] which masks the weaker scattering by the diamond component if it has nucleated. For these reasons, since one-phonon absorption does not occur in diamond, we chose to measure the optical absorption near two-phonon frequencies of diamond to detect diamonds. The difficulties arising because absorption of this kind is weak were found to be unexpectedly surmountable because of the discovery of anomalous intensification of two-phonon absorption in the experimental layers *a*-C:H:Me (Me = Er, Cu) on silicon.

We investigated the effect of metals on the vibrational spectrum of *a*-C:H. Copper and erbium, which differ in their atomic radii and in the configuration of the outer electron shell, were selected as the metals.

2. PARTICULAR FEATURES OF THE EXPERIMENT

The *a*-C:H:Me films were grown by cosputtering of graphite and metal targets using a planar magnetron in an argon-hydrogen plasma $(80\%\mathrm{Ar} + 20\%\mathrm{H}_2)$. The *a*-C:H:Me layers with metal concentration of the order of 10 at.% were prepared. The layers were grown on [100] silicon substrates at a substrate temperature of about 200 °C. Sputtering was conducted in a flow of working gas at pressures 8–9 mTorr and voltages 360–380 V on the magnetron. It was found that 0.5 to 1.0-μm-thick *a*-C:H:Me layers could be grown under such conditions. The grown layers were subjected to 1-h vacuum thermal annealing at temperatures in the range 200 −450 °C.

Infrared absorption spectroscopy near the vibrational frequencies of carbon–carbon and carbon–hydrogen bonds was used to characterize the grown layers. Optical absorption in the *a*-C:H:Cu films was measured using a Specord 75IR dual-beam infrared (IR) spectrometer. To increase contrast, the double-passage absorption, which was accomplished in the reflection geometry with 45° angle of incidence, was measured together with absorption under normal incidence (single-passage absorption). To prevent radiation losses the sample was mounted on a mirror.

3. EXPERIMENTAL RESULTS

Figure 1 shows typical double-passage transmission spectra of the grown layers. These spectra demonstrate the modification of the layers when the metals are introduced. One can see that the intensity of the characteristic vibrational bands of bound hydrogen in the frequency range $\omega = 3000 - 2800\ \mathrm{cm}^{-1}$ decreases appreciably when the metal is introduced. However, a greater result of introducing metals is the initiation of new bands near the two-phonon absorption frequencies of diamond [2000–2200 cm^{-1} (Ref. 2)] and near the Raman frequencies of graphite (the *G* band $\omega = 1575$ cm^{-1} and the *D* band with a somewhat less well determined frequency near 1400 cm^{-1}).[3] Table I gives for comparison the published data on the features of the two-phonon absorption bands in bulk diamonds and the parameters of the absorption bands which we observed and were initiated by met-

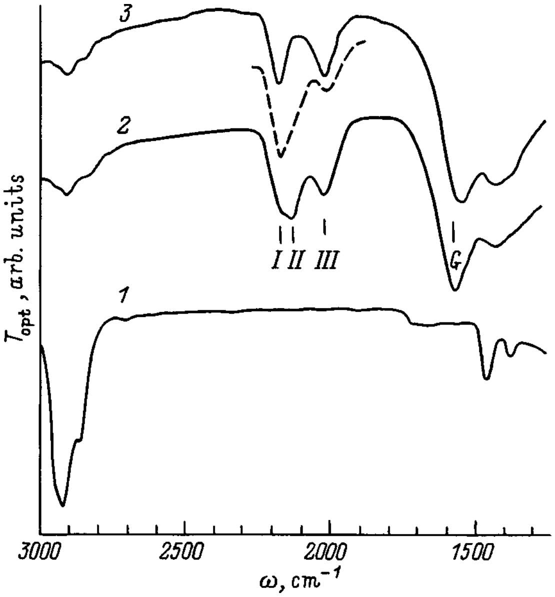

FIG. 1. Double-passage transmission spectra T_{opt}. Films: *1* — *a*-C:H; *2* — *a*-C:H:Cu (dashed line — after annealing at 220 °C); *3* — *a*-C:H:Er. I, II, III — absorption bands presented in Table I.

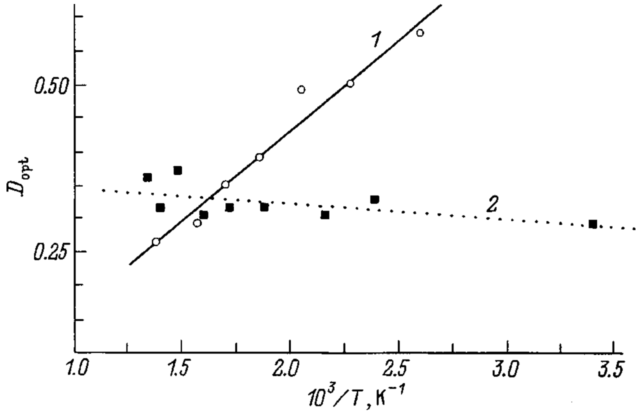

FIG. 2. Temperature dependences of the optical density at the maximum of the pseudo-Raman *G* band of *a*-C:H:Cu (*1*) and *a*-C:H:Er (*2*).

als in the same spectral region. In both cases fewer features are observed in the spectrum than for bulk diamonds, but the very close match between the frequencies of the bands in *a*-C:H:Cu and *a*-C:H:Er layers and the frequencies of the two-phonon bands in bulk diamond permits us to refer to them, for brevity, as quasidiamond bands. The numbers of the bands in Table I are equal to the numbers of the bands indicated in Fig. 1. The differences in the structures of the erbium- and copper-induced bands, as follows from the data presented in Fig. 1 and Table I, are manifested in the number of observed structural elements and in the frequency of the band dominating the spectrum before annealing. One can see that as a result of annealing at a temperature only negligibly higher than the growth temperature of the layer, the band I, whose frequency matches well that of the band observed in bulk diamond and not completely identified, which corresponds to a two-phonon combination at the asymmetric point of the Brillouin zone, dominates in both cases.[4,5] The position of band III also agrees well with the published data for bulk diamond. Band II, which is clearly observed only in *a*-C:H:Cu before annealing, is shifted by ~ 16 cm^{-1} to lower frequencies. Activation of the Raman frequencies of graphite in the optical absorption spectra has been observed previously with introduction of copper into *a*-C:H and has been attributed to intercallation of graphite fragments by the copper.[3] For brevity, we shall refer to them as pseudo-Raman. The same phenomenon also occurs when *a*-C:H is doped with other elements.[6] One can therefore assume that erbium interacts similarly with graphite fragments, intercalating them essentially without changing the structure of the six-member rings, which can be judged only from the very weak softening of the corresponding vibrational mode ($\omega = 1575$ cm^{-1} for Cu and $\omega = 1540$ cm^{-1} for Er). This frequency shift can be attributed to the difference in the binding energies of copper and erbium with graphite fragments. The difference in the thermal stability of the bands activated by them also attests to a higher binding energy of erbium with graphite fragments. Figure 2 shows the temperature dependence of the optical density D_{opt} in the *G* band for *a*-C:H:Cu and *a*-C:H:Er layers in the temperature range 200–475 °C. It is easy to see that while the copper-activated band decays exponentially with temperature, the analogous band in the case of erbium even tends to flare up with temperature. This behavior of the pseudo-Raman band *G* in the *a*-C:H:Cu and *a*-C:H:Er layers correlates in some way with the character of the thermal stability of the quasidiamond two-phonon bands, as will be discussed in greater detail in Sec. 4.2.

TABLE I. Characteristic features of the quasidiamond two-phonon absorption bands.

Band No.	*I*	*II*	*III*
Frequency ω, cm^{-1}	2177	2137	2024
a-C : H	⋯	⋯	⋯
a-C : H : Cu before annealing	Shoulder	Peak	Peak
a-C : H : Cu after annealing	Peak	Shoulder	Peak
a-C : H : Er	Peak	⋯	Peak
Published data			
Frequency ω, cm^{-1}	2177	2153	2024
Refs. 2, 4, 5	Kink	Peak	Peak
Nature of band	?	LO + LA (*L*)	TO + TA (*W*)

4. DISCUSSION

A. Anomalously high two-phonon absorption

The fact that the two-phonon absorption frequencies in bulk diamonds match the frequencies of bands observed in *a*-C:H:Cu and *a*-C:H:Er layers suggests that a diamond phase or at least a phase in which the carbon atoms are bound with one another by diamond-like σ bonds, i.e., tetragonal carbon phases, are present in them. On the other hand, the fact that two-phonon absorption is observed in such thin films means that in the diamond phase built into the copper- or erbium-containing matrix of amorphous carbon two-phonon absorption is apparently unusually large compared with bulk diamond crystals. An estimate of the absorption at the maximum of the 2177-cm^{-1} band gives a value on the order of several hundred cm^{-1}, while the absorption coefficient in the strongest two-phonon band in bulk diamond does not exceed 14 cm^{-1} (Ref. 2). The correctness of this estimate can be verified by comparing in Fig. 1 the depths of the quasidiamond bands and the bound-hydrogen bands, which correspond to an absorption on the order of 800 cm^{-1} (Ref. 7). It should be noted that only the lower limit was presented above, since the ratio of the sizes of diamond inclusions and amorphous-carbon phases is unknown. The observed intensification of two-phonon absorption can be attributed to spatial confinement of phonons in small crystalline diamond formations, which have nucleated in the amorphous-carbon host. We shall estimate the sizes of the diamond nanocrystals from the width of the observed bands, whose half-width is on the order of $\delta\omega \approx 30\ \text{cm}^{-1}$. We shall employ below the dispersion relation, which is available in analytical form, of *LO* phonons that propagate in the diamond lattice in the direction Δ toward the point X at the boundary of the Brillouin zone.[8] Ignoring the true nature of the phonons forming the combination which determines the nature of the quasidiamond bands, we assume for an order of magnitude estimate that the dispersion of the phonons of all branches near the boundary of the Brillouin zone is the same. Using Eq. (5) of Ref. 8, we obtain

$$\frac{d\omega}{dq} = \frac{4\mu \sin \pi q - \pi\alpha \sin(\pi q/2)}{M\omega_{\text{LO}}}, \tag{1}$$

where q is the dimensionless phonon momentum in fractions of the maximum momentum $q_{\max}$ at the boundary of the Brillouin zone, ω is the phonon frequency, μ and α are, respectively, the principal Born force constants of the interaction for the first and second nearest neighbors, and M is the mass of a carbon atom. In addition, the additional relation

$$\mu = \frac{M}{32}(2\omega_{\text{LO}}^2 - \omega_{\text{Ra}}^2) \tag{2}$$

can be derived from dispersion relation (5) in Ref. 8 for the boundary of the Brillouin zone ($q=1$). Here ω_{Ra} is the Raman frequency for diamond (1332 cm^{-1}), and ω_{LO} is the frequency of the band. Together with the relation $\alpha = 7.28\mu$ (Ref. 8), this makes it possible to estimate the dispersion relation $\delta\omega/\delta q \approx 2\times 10^{-3}$ for longitudinal optical phonons at the boundary of the Brillouin zone in diamond. The scale size δx of diamond nanocrystals can then be estimated from the relation $\delta x \cdot \delta q = 1$, where $\delta q = 5 \times 10^2 \delta\omega(\pi/a)$ (a is the lattice constant of diamond), which for the experimental value $\delta\omega \approx 30\ \text{cm}^{-1}$ presented above gives $\delta x \approx 20$ Å . This is small enough to make the contribution of surface phonon modes substantial and to give rise to local electromagnetic field effects. Moreover, molecular-dynamics calculations[9] show that as the contribution of the quasifree surface increases with decreasing particle size, the anharmonicity of the phonons increases on account of the relaxation of the surface atoms, thereby increasing the two-phonon absorption. It is possible to that one of these factors or all of them together could be responsible for the anomalously high two-phonon absorption that we observed.

B. Intercallation of graphite fragments and intensification of absorption

The activation of pseudo-Raman *G* and *D* bands in the optical spectra makes it possible to determine a number of features of the interaction of metals with graphite fragments of the *a*-C:H structure. According to optical and electron-microscopic data, these fragments are on the order of several nanometers in size.[10] It can be expected that the number of graphite planes in such fragments does not exceed the number of six-member carbon rings in these planes, which on average is on the order of 4–6. The small size of the fragments facilitates, on the one hand, their intercalation by the metal, just as the reverse process;[11] on the other hand, it makes it possible to use a comparatively simple model to calculate an elementary intercalation event.[12] For copper this calculation gives for the binding energy with a graphite cluster consisting of four six-member rings a value on the order of 0.4 eV. This value is smaller for a large fragment.

Assuming that the optical density at the maximum of the *G* band is proportional to the concentration of intercalated (adsorbed) atoms, it is possible to estimate using IR spectroscopy the binding energy of the metal with a graphite fragment from the temperature dependence of the band intensity. It follows from the data shown in Fig. 2 that there exists a temperature range in which the number of intercalating copper atoms decreases exponentially with increasing temperature. The activation energy for rupture of the bond of an intercalant with a graphite fragment (the disintercalation energy), determined from the slope of the exponential section, is on the order of 65 meV for copper. We have identified the optical ‘‘activity’’ of atoms adsorbed on the outer faces of the graphite fragment and of the atoms occupying interplanar positions (true intercalants). It is evident that the experimental estimate of the activation energy of disintercalation is several times smaller than the theoretical value presented above for the binding energy of a copper atom with a graphite fragment.[12] There can be a number of reasons for this result: the use of a simplified model for an elementary intercalation event, a larger number of six-member rings in actual graphite fragments, and a subbarrier mechanism of disintercalation (thermally stimulated tunneling). However, for what follows it is important to underscore that the theory of Ref. 12 predicts that an electron is transferred from a copper atom to a graphite fragment; i.e., in this case copper acts as an electron donor to a band of the graphite fragment. Thus the interaction of copper with a graphite fragment together with the activation of pseudo Raman bands in the optical spectra, is also seen as an increase in the density of π electrons in the graphite fragments. Comparing the temperature dependences, shown in Fig. 2, of the optical density of the *G* band shows that the erbium-activated band has a higher thermal stability, which attests to a higher binding energy of erbium atoms with graphite fragments. In the approach developed in Ref. 12, the increase in the binding energy of erbium with a graphite fragment can be attributed to a larger than in copper number of *s* electrons in the outer shell. This difference probably also is responsible for the appreciable softening of the graphite phonon mode corresponding to the *G* band in the

TABLE II. Frequencies of the *G* band.

	Band frequency ω, cm^{-1}		
Composition of layer	Before annealing	After annealing at 200 °C	After annealing at 400 °C
a-C : H : Cu	1577	1540	–
a-C : H : Er	1540	1540	1500

case of *a*-C:H:Er (1540 cm^{-1}) as compared with the typically graphite value for *a*-C:H:Cu (1590 cm^{-1}), as is evident from Table II.

As one can see from Fig. 1 and Tables I and II, thermal annealing affects the characteristic features of the transmission spectra of *a*-C:H:Cu films. Is is noteworthy that the results of additional thermal annealing are equivalent for copper and erbium. In both cases the 2177-cm^{-1} band is dominant. The nature of this band remains unclear even for bulk diamonds, as already mentioned above. The excessive intensification of this mode in nanocrystals suggests that it is due to phonon modes activated by the destruction of long-range order or local modes due to defects. In the first case, we have in mind a limited destruction of long-range order with preservation of pseudosymmetry of the polytope closest to diamond with respect to the symmetry group, for example, the polytope[13] 240. In this case it can be assumed that the dominance of the 2177-cm^{-1} band reflects the slightly higher symmetry of the nanocrystal nucleated in the amorphous matrix as compared with bulk diamond. For band II, which predominates in *a*-C:H:Cu before annealing, we call attention to its frequency shift compared with bulk diamond for the combination of longitudinal phonon modes that propagate in the (111) plane. The observed softening of the phonon modes in this plane could be due to screening of the electric fields associated with them by the charges in the matrix. Following the model of the nucleation of diamonds via the graphite component,[14] it can be inferred that epitaxial growth of diamond nanocrystals occurs on the (0001) face of graphite fragments. The existence of graphite fragments, on which diamond nanocrystals can nucleate, in the experimental films can be judged from the pseudo-Raman *G* and *D* bands activated in the IR spectra (Fig. 1). As a result of such epitaxial growth, a diamond nanocrystal grows in a direction perpendicular to its (111) face, and the combinations of the longitudinal phonon modes propagating in the plane of this face next to the diamond–graphite interface effectively relax as a result of the interaction with the electrons in the graphite substrate. It should be kept in mind that the interaction of copper atoms with graphite fragments increases the free-electron density in the fragments,[12] intensifying this interaction. It is possible that the local changes in the conductivity of the host induced by this interaction are responsible for the anomalous intensification of the electromagnetic field generated by radiation as a result of two-phonon absorption in nanodiamonds. It can therefore be assumed that the intensification of the two-phonon absorption is closely related with the metal-induced intercalation of the graphite fragments at which the diamond nanocrystals nucleate. This is indicated, in particular, by the correlation between the flareup and decay of quasidiamond bands and the behavior of the pseudo-Raman graphite bands, as can be verified by comparing the data shown in Figs. 2 and 3. The temperature interval in which the quasidiamond lines flareup in the case of *a*-C:H:Cu corresponds to the increase in the intercalation efficiency with temperature. A further increase of temperature activates the disintercalation, as one can see from the temperature variation of the optical density of the *G* line (Fig. 2). The low value of the binding energy of a copper atom with a graphite fragment determines the narrow temperature interval in which the intercalation of graphite fragments by copper occurs and, correspondingly, the quasidiamond bands are observed. The temperature dependence of the optical density of the quasidiamond band in *a*-C:H:Er shows a complicate behavior at the center of the temperature interval (Fig. 3), probably because of the restructuring of the hydrogen part of the framework.[15] However, its temperature stability correlates completely with the stability of the *G* band, due to the higher binding energy of erbium with the graphite fragment, as noted above.

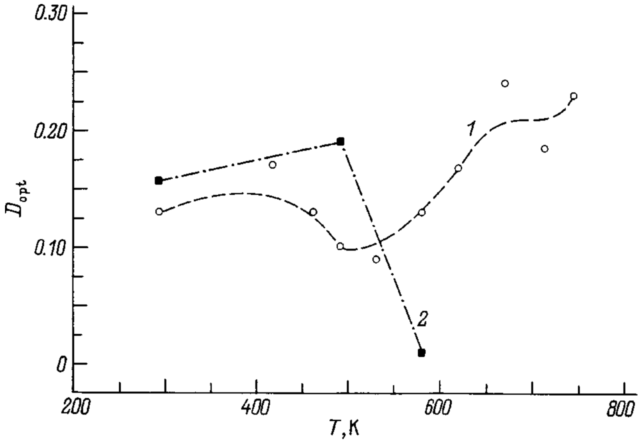

FIG. 3. Temperature dependences of the optical density at the maximum of the quasidiamond band of *a*-C:H:Er (*1*) and *a*-C:H:Cu (*2*).

5. CONCLUSIONS

The introduction of the metals Cu and Er, which do not form carbides, into the structure of hydrogenated amorphous carbon during cold magnetron sputtering of metals with graphite leads to metal-induced intercalation of nanosize graphite fragments of the structure. In both cases a gigantic intensification of absorption is observed in the region of the two-phonon frequencies of diamond. The role of the intercalants in the nucleation of diamonds in *a*-C:H:Me remains unclear. It is possible that nanodiamonds nucleate in hydrogenated amorphous carbon in the process of magnetron sputtering of graphite without the participation of metals,[16] but their catalytic activity in this process cannot be ruled out. In any case, the intercalation of graphite fragments of *a*-C:H by a metal is important for observing nanodiamonds in thin layers by detecting such weak two-phonon absorption in the bulk diamond. The nanodiamonds detected in this manner are of the order of 20 Å in size. It is amazing that the parameters of the phonon spectrum of a bulk diamond crystal are essentially preserved in crystals on the order of five lattice constants in size. The reason for this occurrence is probably the high stiffness of the crystal lattice of diamond resulting from the high binding energy of carbon atoms in this structure.

This work was supported by the Russian Fund for Fundamental Research (Grant 97-02-18110) and partially by Arizona University.

We wish to thank T. K. Zvonareva for providing the *a*-C:H:Cu layers and S. G. Yastrebov for discussing a possible mechanism leading to intensification of two-phonon absorption in nanodiamonds in *a*-C:H:Me. We also thank A. L. Talis for calling to our attention the modular structure of diamonds.

[1] S. Matsumuma, Thin Solid Films **306**, 17 (1997).
[2] F. A. Johnson, Prog. Semicond. **9**, 181 (1965).
[3] V. I. Ivanov-Omskiĭ and G. S. Frolova, Zh. Tekh. Fiz. **65**, 186 (1995) [Sov. Phys. Tech. Phys. **40**, 94 (1995)].
[4] J. L. Warren, J. L. Varnell, G. Dolling, and R. A. Cowley, Phys. Rev. **153**, 805 (1967).
[5] G. Dolling and R. A. Cowley, Proc. Phys. Soc. London **88**, 463 (1966).
[6] J. H. Kaufman, S. Metin, and D. Saperstein, Phys. Rev. B **39**, 13053 (1989).
[7] P. Couderc and Y. Catherine, Thin Solid Films **146**, 93 (1987).
[8] R. Tubino and J. L. Birman, Phys. Rev. B **15**, 5843 (1977).
[9] J. M. Dickey and A. Paskin, Phys. Rev. B **1**, 851 (1970).
[10] V. I. Ivanov-Omskii, A. B. Lodygin, A. A. Sitnikova, A. A. Suvorova, S. G. Yastrebov, A. V. Tolmatchev, J. Chem. Vapor Deposition **5**, 198 (1997).
[11] V. I. Ivanov-Omskii, in *Diamond Based Composites and Related Materials*, edited by M. Prelas (NATO ASI Ser. 3, Kluwer, Dordrecht, 1997, Vol. 38, p. 171).
[12] V. I. Ivanov-Omskiĭ and É. A. Smorgonskaya, Fiz. Tekh. Poluprovodn. **32**, 931 (1998) [Semiconductors **32**, 831 (1998)].
[13] R. Mosseri, D. P. DiVincenzo, J. F. Sadoc, and M. H. Brodsky, Phys. Rev. B **32**, 3974 (1985).
[14] J. C. Angus, A. Argoitia, R. Gat, Z. Li, M. Sunkara, L. Wang, and Y. Wang, Philos. Trans. R. Soc. London, Ser. A **342**, 195 (1993).
[15] V. I. Ivanov-Omskiĭ, G. S. Frolova, and S. G. Yastrebov, Pis'ma Zh. Tekh. Fiz. **23**(7), 1 (1997) [Tech. Phys. Lett. **23**, 251 (1997)].
[16] V. I. Ivanov-Omskii, V. I. Siklitsky, A. A. Sitnikova, A. A. Suvorova, A. V. Tolmachev, T. K. Zvonariova, and S. G. Yastrebov, Philos. Mag. B **76**, 973 (1997).

Translated by M. E. Alferieff

THE PHYSICS OF SEMICONDUCTOR DEVICES

Current-voltage characteristics of Si:As-based photodetectors with blocked hopping conductivity

D. G. Esaev,*) S. P. Sinitsa,**) and E. V. Chernyavskiĭ

Institute of Semiconductor Physics, Siberian Branch of the Russian Academy of Sciences, 630090 Novosibirsk, Russia

(Submitted July 6, 1998; accepted for publication July 7, 1998)
Fiz. Tekh. Poluprovodn. **33**, 614–618 (May 1999)

The results of an experimental investigation of the current–voltage characteristics of Si:As-based structures with blocked hopping conductivity are reported. The behavior of the dark current in the temperature range $T=7-25$ K with bias voltages from -4 to $+4$ V is analyzed and views about the mechanisms of dark-current flow are presented. Recommendations are developed for choosing the bias voltage on the structures for optimal operation as an IR photodetector. © *1999 American Institute of Physics.* [S1063-7826(99)01905-5]

1. INTRODUCTION

A blocked-impurity-band (BIB) structure has been proposed by Petroff and Stapelbrock[1] as a far-IR impurity photodetector that operates at liquid-helium temperatures. Its main advantage over the classical impurity photodetector — high quantum efficiency combined with a high doping level of the photosensitive layer and a low noise level due to the presence of a blocking layer — has made it possible to produce matrix photodetectors (PDs) that operate in the spectral range 0.4–40 μm (Refs. 2 and 3). In isolated BIB structures a quantum-counter regime appears to have been realized[4] and photosensitivity at IR wavelength 190 μm has been attained.[5]

Nonetheless, until now no systematic experimental data on the behavior of the dark current–voltage characteristics (IVCs) of BIB structures that could be used to establish the basic processes that control the flow of dark current and to optimize the parameters of photodetectors have been published. In Ref. 1 the temperature at which the dark IVCs were measured and the areas of the BIB structures were not given. The dark-current IVC presented in Ref. 6 was measured over two orders of magnitude in current and at one temperature and therefore cannot serve as a basis for analysis. In Ref. 7 the dark IVCs were measured over an order of magnitude in current and at two temperatures.

The data presented in Refs. 8 and 9 clearly do not correspond to a BIB structure and its operating regime in a matrix photodetector. The main features predicted in Ref. 10 for the IVC of a BIB structure is asymmetry attributable to the asymmetry of the BIB structure, and a strong nonlinearity due to carrier injection from the contacts. The forward and backward currents in the structures,[8,9] measured with a bias voltage of 1 V, differ by no more than an order of magnitude, indicating that the blocking effect is weak. It will be shown below that the current difference can reach more than six orders of magnitude (Fig. 1). The structures in Refs. 8 and 9 cannot be directly used in matrix PDs, since in the case of backside illumination from the side of the common contact for all elements, which is characteristic of a hybrid matrix PD, the photosensitive region is protected from IR radiation by a thick (400 μm), strongly absorbing layer of silicon.

The maximum detection power of a BIB-PD operating in a low-background situation is limited either by the noise of the matrix silicon switch or the noise due to the flow of the

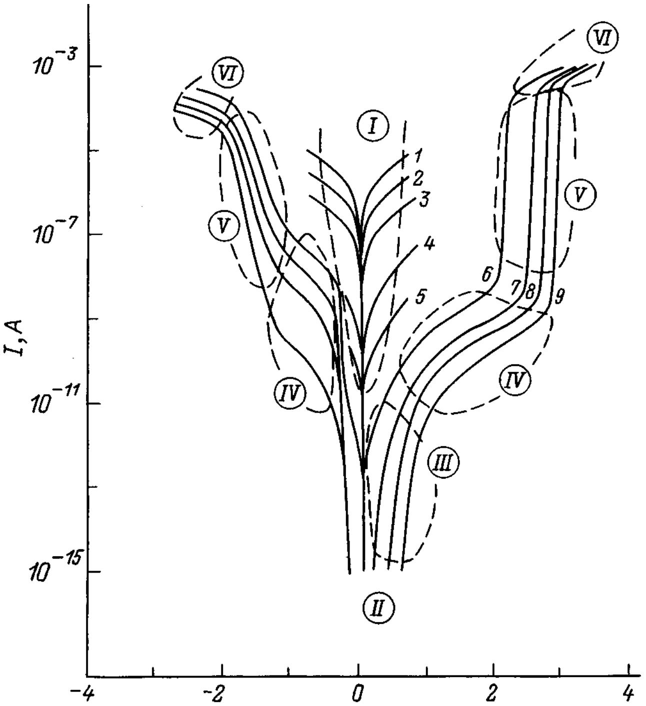

FIG. 1. Family of current–voltage characteristics of a BIB structure at temperature T, K: *1* — 24, *2* — 22, *3* — 20.5, *4* — 19, *5* — 17.5, *6* — 15, *7* — 11.6, *8* — 9.7, *9* — 7.4.

dark current of the BIB photocells of the matrix. The maximum signal integration time that can be obtained in a PD with given storage capacitance of the switch also determines the dark current of the BIB photocells. On this basis we performed an experimental investigation of the dark current–voltage characteristics of BIB structures. The results are reported below.

2. SAMPLES AND EXPERIMENTAL APPARATUS

The BIB structures were fabricated using 76-mm-diam *n*-silicon wafers with (100) surface orientation and resistivity $10\,\Omega\cdot$ cm. The BIB structure was fabricated by gas-transport epitaxy at 1180 °C from $SiCl_4$ with total impurity content less than $10^{-6}\%$ on the UNÉS-2PV setup. Figure 2 shows the typical density distribution of arsenic atoms, measured with an ARS-100 setup by the method of resistance to spreading on a spherical section, in the epitaxial layer using a mixture of arsine with hydrogen for doping.

The impurity concentration in the photosensitive N^+ layer was chosen from the data in Ref. 11 according to the optimal doping to obtain the maximum quantum efficiency. The donor density N_d in the ''built-in'' N^{++} layer should reach a value at which the low-temperature freezing of conductivity is no longer observed and the layer becomes suitable for use as an ohmic contact at low temperatures ($N_d > 5\times10^{18}$ cm^{-3}; Ref. 1). The impurity density in the blocking *I* layer is determined from the condition that the hopping conductivity decreases to low values, and that its value in the experimental structures ($\simeq 10^{15}$ cm^{-3}), which is determined by the residual impurity in the technological setup in this process, satisfies this condition. The thicknesses of the photosensitive and blocking layers are determined by a compromise in the requirements for the BIB structure from the standpoint of maximum photosensitivity and connection with the switch. The density of the compensating impurity in the photosensitive layer, whose value is of fundamental importance for operation of BIB structures as photodetectors, was measured by the low-temperature photoluminescence method on samples obtained in the perfected regimes but without the introduction of arsine into the gas phase. Analysis of the impurity composition showed that the boron density fluctuates in the range $N_B = (2-4)\times10^{13}$ cm^{-3} and the group-V impurity densities are $N_P \simeq 2\times10^{13}$ and $N_{Sb} \simeq 10^{13}$ cm^{-3}.

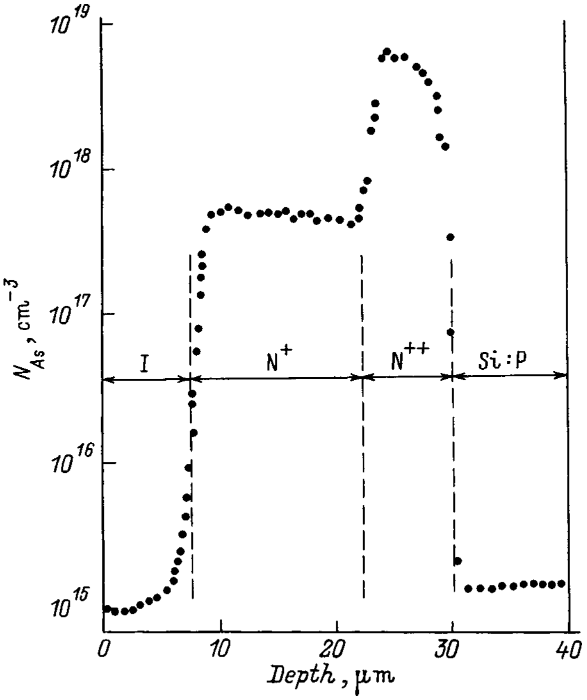

FIG. 2. Arsenic density N_{As} distribution over the depth of the layer in an epitaxial BIB structure.

After the BIB structures were fabricated, the density of the compensating acceptors in the photosensitive layer was measured at temperature $T = 10$ K by the method of capacitance–voltage characteristics ($C-V$). The value $N_a = (2\pm1)\times10^{13}$ cm^{-3} which we obtained matches the data obtained by the low-temperature photoluminescence method. The ''built-in'' layer plays the role of a common ohmic contact for all BIB elements where the charge carriers are not frozen out down to 4.2 K. The second ohmic contact to the blocking layer, which is a separate contact for each element of the matrix, is located on the planar side of the silicon wafer and is obtained by ion implantation of phosphorus with density $N_P = 2\times10^{19}$ cm^{-3}, followed by annealing.

Samples of the BIB structures were secured on a copper holder and cooled in a transport helium Dewar. The construction of the holder reduces to a minimum the thermal background incident on the BIB structure and the leakage currents. The current was measured with a V7É-42 electrometer; the current noise threshold was 10^{-15} A. The absolute value and stability of the temperature were monitored with a semiconductor detector. The temperature was varied by regulating the distance to which the holder was lifted above the helium surface.

3. RESULTS OF MEASUREMENTS OF THE CURRENT–VOLTAGE CHARACTERISTICS AND DISCUSSION

The current–voltage characteristics of the BIB structure are quite complicated and cover many orders of magnitude in current. Their typical form is shown on a logarithmic scale in Fig. 1. The area of the experimental structural elements is 70×80 μm^2. A positive potential on the planar electrode corresponds to the working polarity of the photodetector, and a negative potential corresponds to the reverse polarity. Analysis shows that in region I at relatively high temperatures $T > 17$ K and low voltages the IVC is linear and the current is an exponential function of temperature (Fig. 3) with activation energy ε close to the activation energy of an As donor level in Si. Hence it follows that in this region the current is determined by the equilibrium electrons that move along the conduction band. As the temperature is lowered, the current in section I becomes immeasurably small. The main feature of the IVCs of BIB structures, as predicted in Ref. 10, is their asymmetry, specifically, the zone II ranging in width from tenths of a volt to several volts where the current becomes immeasurably small, i.e., current blocking

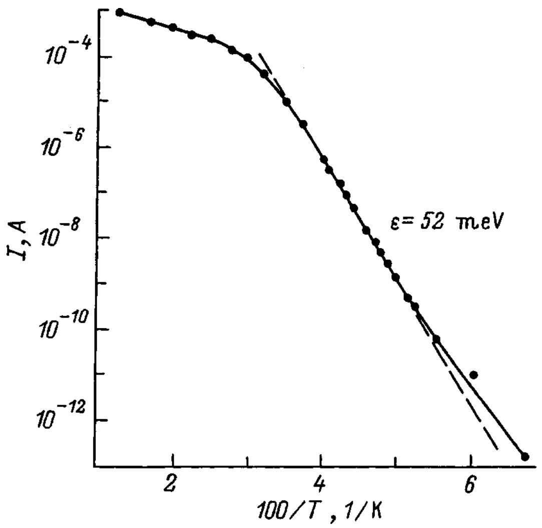

FIG. 3. Temperature dependence of the current in a BIB structure at temperatures $T>17$ K and bias voltage $V=0.3$ V. The ionization energy of a single arsenic atom in silicon is $E_{\mathrm{As}}=54$ meV.

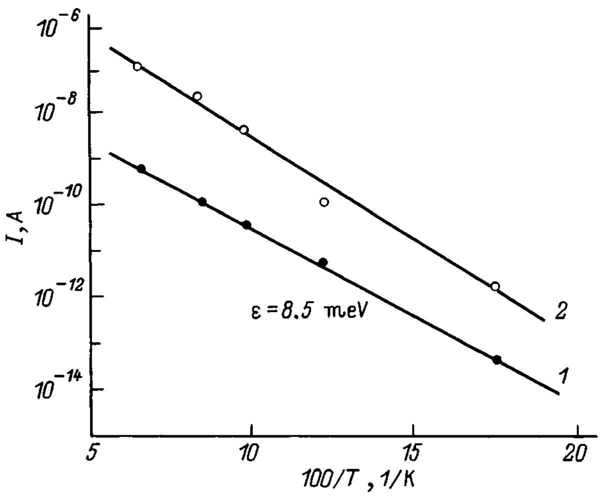

FIG. 5. Temperature dependence of the current in a BIB structure with: *1* — the working polarity ($+1$ V), *2* — the reverse polarity (-1 V).

due to the asymmetry of the BIB structure appears. This blocking stems from the fact that for the working polarity of the BIB structure (Fig. 4a) the applied external bias voltage decreases in the blocking layer and in the space-charge region of the photosensitive layer arising as a result of the finite density of compensating acceptors. For the reverse polarity, the external bias voltage is applied entirely across the blocking layer (Fig. 4b), which is several times thinner than the photosensitive layer. As a result, there is a larger electric field on the injecting planar ohmic contact and exponential current growth, starting with small biases. For the working polarity of the external voltage, similar current growth is observed when a certain bias voltage is reached. Unfortunately, the other features of the IVCs of BIB structures are not contained in Ref. 10 because the computational model used there is extremely simple — the punch-through structure model.

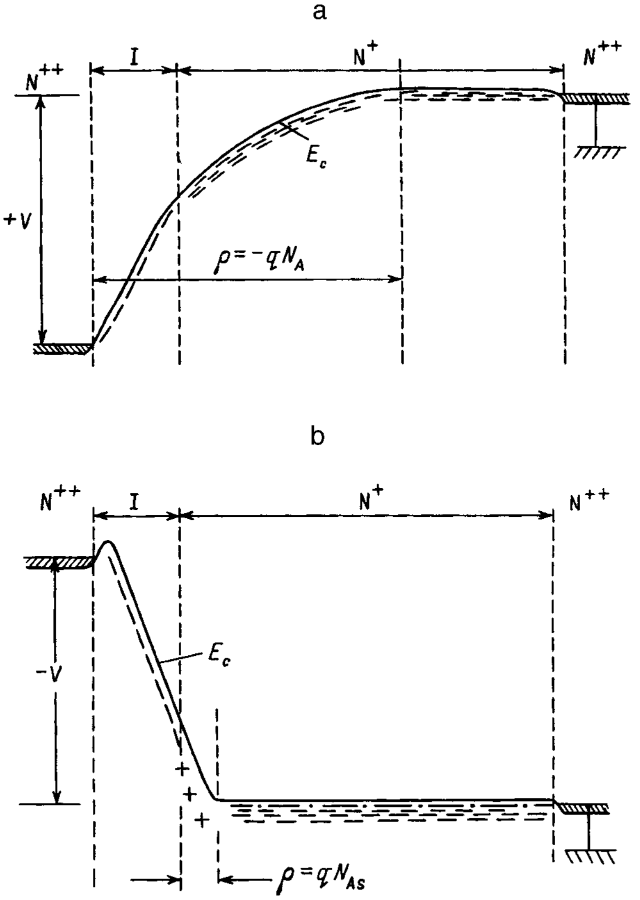

FIG. 4. Distribution of the potential in a BIB structure: a — with the working polarity of the external bias, b — with the reverse polarity.

Exponential current growth in section III can apparently be treated as electron tunneling from the impurity band into the conduction band of silicon at the photolayer–⟨blocking layer⟩ interface with a positive bias and as electron tunneling from the N^{++} region of the planar ohmic contact into the conduction band of the blocking layer for negative polarity. A tunneling current in the simpler $N^{++}-N-N^{++}$ structures has been observed in Ref. 12 at liquid-helium temperatures. For both polarities this exponential current growth (section III) passes into a more even section IV. An exponential temperature dependence of the current is observed in this section (Fig. 5). At $V=+1$ V the activation energy is $\varepsilon=8.5$ meV, which corresponds to the current bounded by the hopping conductivity along the impurity band in silicon at the given donor density, $N_d=5\times10^{17}$ cm^{-3}, and acceptor density, $N_a=2\times10^{13}$ cm^{-3}. To check this explanation of the current behavior in section IV, $N^{++}-N^{+}-N^{++}$ structures were fabricated from the BIB structures by etching off the blocking layer. Their IVC in this temperature range correspond completely to the section IV of the IVC of BIB structures. In accordance with the model for weak compensation,[13] the position of the Fermi level in the impurity band with respect to the level of an isolated donor is given by the relation $E_F=0.99q^2N_D^{1/3}/4\pi\chi$. Here q is the electron charge, and χ is the permittivity of the semiconductor. In our case we obtain $E_F=9$ meV, which is close to the experimental value of the activation energy and indicates that the conductivity along the impurity band is due to holes transferred from the Fermi level into the peak in the density of states of the impurity band. The mobility in the impurity band, estimated in section IV from the current density in the structure and the acceptor density, is $\mu \simeq 1\ \mathrm{cm}^2/(\mathrm{V}\cdot\mathrm{s})$, consistent with the data of Ref. 4.

Switching from the bias region IV to region V, the power–current sensitivity of the BIB elements increases, reaching several hundreds of A/W. In Refs. 14 and 15 this growth is attributed to avalanche multiplication of charge carriers due to impact ionization of impurity centers. However, in this case the hopping conductivity along the impurity band, which is connected in series with the avalanche conductivity, must be able to provide carrier outflow from the multiplication region and the observed value of the current. It has not been ruled out that the intensification of the photocurrent is due to the positive charge of impurity centers on the growth of a tunneling contact current; this explains the behavior of the IVC in section V. Exponential current growth is observed with a further increase of voltage with both positive and negative biases. The final answer concerning the nature of the exponential current growth in section V can be obtained by comparing experiment with calculations, the results of which will be reported in the near future.

The current and behavior of the IVC in section VI are determined by the substrate resistance.

4. CONCLUSIONS

The results of an experimental study of the current–voltage characteristics of BIB structures in a wide temperature range were reported.

The investigation of the dark IVCs of BIB structures showed that only two sections, specifically, the sections II and VI (see Fig. 1), can be used for efficient operation of the structure as a photodetector in a two-dimensional matrix. In section II there is no noise due to the dark current, since the latter is immeasurably small. In section IV this noise component is present, but its variance along the matrix is small because of the small variance of the current in this section from one element to another. In addition, if the noise caused by the hopping conductivity does not dominate the oveall noise of the PD, then it could be desirable to increase the voltage on the photocells becasue of the greater thickness of the space-charge layer and therefore higher power–current sensitivity.

The section V, in which the noise intensity and the photoresponse were found to increase simultaneously, is interesting for operation of an isolated BIB photocell. In this section the power–current sensitivity reaches several hundreds of A/W, and the detection power passes through a maximum, but the large variance of the dark currents from one element to another makes it impossible to use them in the matrix. Section III can therefore be used for detection of the IR radiation in matrix PDs.

We wish to thank D. O. Leonov for assisting in the fabrication of the samples.

*⁾E-mail: esaev@thermo.isp.nsc.ru
**⁾Fax: (3832) 35-52-92

---

[1] M. D. Petroff and M. G. Stapelbroek, *Blocked Impurity Band Detectors*, U. S. Patent No. 4, 568, 960; filed Oct. 1980; granted 4 Feb. 1986.
[2] D. B. Reynolds, D. H. Seib, S. B. Stetson, T. Herter, N. Rowlands, and J. Schoenwald, Trans. Nucl. Sci. **36**, 857 (1989).
[3] R. A. Noel, (*Infrared Detectors and Focal Plane Arrays*), Proceedings SPIE **1685**, 250 (1992).
[4] M. D. Petroff, M. G. Stapelbroek, and W. A. Kleinhans, Appl. Phys. Lett. **51**, 406 (1987).
[5] D. M. Watson and J. E. Huffman, Appl. Phys. Lett. **52**, 1602 (1988).
[6] J. E. Huffman, A. G. Grouse, B. L. Halleck, T. V. Downes, and T. L. Herter, J. Appl. Phys. **72**, 237 (1992).
[7] B. A. Aronzon, D. Yu. Kovalev, A. M. Kozlov, Zh. Leotin, and V. V. Ryl'kov, Fiz. Tekh. Poluprovodn. **32**, 192 (1998) [Semiconductors **32**, 174 (1998)].
[8] V. V. Bolotov, G. N. Kamaev, G. N. Geofanov, and V. M. Émeksuzyan, Fiz. Tekh. Poluprovodn. **24**, 1697 (1990) [Sov. Phys. Semicond. **24**, 1061 (1990)].
[9] V. M. Émeksyzyan, G. N. Kamaev, G. N. Feofanov, and V. V. Bolotov, Fiz. Tekh. Poluprovodn. **31**, 311 (1997) [Semiconductors **31**, 255 (1997)].
[10] B. G. Martin, Solid-State Electron. **33**, 427 (1990).
[11] N. Sclar, Prog. Quantum Electron. **9**, 149 (1984).
[12] E. Simoen, B. Dierickx, L. Deferm, C. Claeys, and G. Declerck, J. Appl. Phys. **68**, 4091 (1990).
[13] N. F. Mott and E. A. Davis, *Electronic Properties of Non-Crystalline Materials* [Clarendon Press, Oxford, 1971; Mir, Moscow, 1982].
[14] F. Szmulowicz and F. L. Madarsz, J. Appl. Phys. **62**, 2533 (1987).
[15] F. Szmulowicz, F. L. Madarsz, and J. Diller, J. Appl. Phys. **63**, 5583 (1988).

Translated by M. E. Alferieff

D'yakonov–Shur instability in a ballistic field-effect transistor with a spatially nonuniform channel

M. V. Cheremisin

A. F. Ioffe Physicotechnical Institute, Russian Academy of Sciences, 194021 St. Petersburg, Russia;
GES, 074, Universite Montpellier-II, France

G. G. Samsonidze

A. F. Ioffe Physicotechnical Institute, Russian Academy of Sciences, 194021 St. Petersburg, Russia;
Department of Electrical Engineering, University of Maryland, Baltimore, MD 20742-3284, USA

(Submitted August 5, 1998; accepted for publication September 29, 1998)
Fiz. Tekh. Poluprovodn. **33**, 619–628 (May 1999)

The instability of a two-dimensional electronic liquid in the channel of a ballistic field-effect transistor is analyzed by investigating the energy balance. A criterion of instability is found for arbitrary boundary conditions. Using energy-balance analysis we propose a device with a high instability growth rate. The transistor possesses a spatially nonuniform channel and is analogous to a divergent channel in classical hydrodynamics. Our computed growth rate and threshold of the instability for this device agree with the computational data. © *1999 American Institute of Physics.* [S1063-7826(99)02005-0]

1. INTRODUCTION

D'yakonov and Shur[1] have described a new mechanism of plasma-wave generation in the channel of a ballistic field-effect transistor (BFT). It was shown that the behavior of electrons in the channel can be described by the hydrodynamic equations for shallow water, where the water level plays the role of the gate–channel potential and the plasma waves correspond to waves on the water surface. When the source voltage is fixed and the current is maintained constant at the drain end, the stationary state is unstable, which results in the generation of plasma waves. As shown in Ref. 1, the instability is a consequence of the amplification of a plasma wave reflected by the drain of the transistor.

In Ref. 2 the effect of the friction of the electronic liquid, due to the scattering of carriers as result of collisions with phonons and (or) impurities, on the instability growth rate was examined. In the presence of friction the growth rate decreases and the instability acquires a threshold character. As shown in Ref. 2, the high plasma oscillation modes are always less stable than the low modes. Accordingly, in Ref. 2 the increment and threshold of instability were calculated in the high-mode approximation. The results of the analytic calculation are in agreement with the results of a numerical simulation.

In the present paper we analyze the D'yakonov and Shur instability by investigating the energy balance and we find an instability criterion for arbitrary boundary conditions.

2. THEORY OF INSTABILITY IN A BALLISTIC FIELD-EFFECT TRANSISTOR. EFFECT OF THE BOUNDARY CONDITIONS

We shall analyze the D'yakonov–Shur instability with arbitrary boundary conditions. For simplicity we disregard scattering of the carriers. First, using the standard-perturbation method we shall find the growth rate of the instability of the stationary state. Next, following the hydrodynamic analogy we shall analyze the energy balance for a two-dimensional (2D) electronic liquid. Both approaches lead to the same result: Instability depends on the boundary conditions and arises if the energy flows from an external circuit into the transistor channel.

In Ref. 1 it was shown that the behavior of the electronic liquid in the channel of a ballistic field-effect transistor can be described by the following expressions, which are similar to the hydrodynamic equations for shallow water:[3,4]

$$\frac{\partial V}{\partial t}+\frac{\partial}{\partial x}\left(\frac{V^2}{2}+\frac{eU}{m}\right)=0, \tag{1}$$

$$\frac{\partial U}{\partial t}+\frac{\partial}{\partial x}(VU)=0, \tag{2}$$

where $V(x,t)$ is the local electronic flow velocity, and $U=U_{gs}(x)-U_t$; here $U_{gs}(x)$ is the local voltage between the gate and the channel, U_t is the threshold voltage, and m is the electron effective mass. The equation (1) is identical to the Euler equation for shallow water, where the voltage U corresponds to the level of the shallow water. In the continuity equation (2) we already took into account the relation[5] for the approximation of a smooth Shockley channel

$$n=CU/e, \tag{3}$$

where n is the local surface density of carriers induced in the channel, $C=\varepsilon_0\varepsilon/d$ is the capacitance of the insulating layer beneath a gate of unit area, and ε_0 and ε are the permittivity and relative permittivity of the subgate layer.

In the absence of carrier scattering the stationary state of a two-dimensional electronic liquid is characterized by a potential U_0, which is constant along the channel, and the flow velocity V_0. Following the standard procedure, the small perturbations $V=V_0+\delta V(x,t)$ and $U=U_0+\delta U(x,t)$ of the stationary state can be written as

$$\delta V=V_1(x)\exp(-i\omega t),$$
$$\delta U=U_1(x)\exp(-i\omega t). \tag{4}$$

Using Eqs. (4), we can easily find a solution of the system of linearized equations (1) and (2) in the form

$$\begin{cases} u_1=A\exp(ik_1\eta)+B\exp(ik_2\eta), \\ v_1=A\exp(ik_1\eta)-B\exp(ik_2\eta), \end{cases}$$

and

$$j_1=A(1+M)\exp(ik_1\eta)-B(1-M)\exp(ik_2\eta), \tag{5}$$

where A and B are arbitrary constants, $v_1=V_1/S_s$, $u_1=U_1/U_s$, and $j_1=u_1M+v_1$ are the dimensionless values of the perturbations of the voltage, velocity, and current, respectively; U_s and V_s are the potential and flow velocity at the transistor source, and M_s and $S_s=(eU_sm)^{1/2}$ are, respectively, the Mach number and the velocity of the plasma wave at the source. The dimensionless wave vectors $k_{1,2}=\pm\omega l[S_s(1\pm M)]$ correspond to plasma waves that propagate parallel and antiparallel to the current, respectively. The complex frequency $\omega=\omega'+i\omega''$ can be determined from the solution (5) with prescribed boundary conditions. A positive imaginary part $\omega''>0$ of the complex frequency corresponds to instability.

We shall now discuss in greater detail the instability mechanism of Ref. 1 with a fixed source voltage, $u_1(1)=0$, and a fixed drain current, $j_1(1)=0$, of the transistor. As shown in Ref. 1, instability occurs because of the amplification of the plasma wave as a result of reflection at the source. In Ref 1, for example, the case of a voltage perturbation u_1, for which the amplitude gain at the drain $R_d^U=(1+M)/(1-M)$ is much greater than 1 for $0<M<1$, was analyzed. Here the superscript corresponds to the type of perturbation wave and the subscript corresponds to the device boundary. Amplification does not occur at the source, since $R_s^U=-1$. At the same time, the wave of current perturbation, j_1, intensifies at the drain. It follows from Eq. (5) that in this case the amplitude gains at the source and drain are, respectively, $R_s^I=(1+M)/(1-M)>1$ and $R_d^I=-1$. It is easy to see that in both cases the product of the amplitude coefficients remains constant: $R_{sd}=R_s^UR_d^U=R_s^IR_d^I$. This rule also extends to the case of the perturbation wave v_1. Thus the quantity R_{sd} is an invariant and does not depend on the type of perturbation wave. This quantity is the gain of a plasma wave over the total time that the wave propagates in both directions. The instability growth rate ω'' is positive when $|R_{sd}|>1$.

We shall consider arbitrary boundary conditions at the source and sink of the transistor:

$$u_1(0,t)=\hat{Z}_sj_1(0,t),$$
$$u_1(l,t)=\hat{Z}_dj_1(l,t). \tag{6}$$

In the expressions (6) the gate–source and the gate–drain impedances are indicated by operators. In what follows, the imaginary impedances $Z_s(\omega)$ and $Z_d(\omega)$, respectively, are correlated with these operators. It is easy to rewrite in this notation the boundary conditions considered in Ref. 1: $Z_s=0$ for a fixed source voltage and $Z_d=\infty$ for a fixed drain current.

Solving Eq. (5) with the boundary conditions (6), the instability growth rate can be written in the form

$$\omega''=\frac{S_s}{2l}(1-M^2)\ln|r_{sd}|, \tag{7}$$

where

$$r_{sd}=\frac{1-M+Z_s^{-1}}{1-M+Z_d^{-1}}\,\frac{1+M-Z_d^{-1}}{1+M-Z_s^{-1}}$$

is the complex reflection coefficient at the source and drain with the boundary conditions (6). We note that in the absence of current (i.e. for $M=0$) there is no instability. Using the expression (4), we can easily find the necessary condition for instability (i.e., when $|r_{sd}|>1$) in the form

$$|Z_s|<|Z_d|. \tag{8}$$

The expression (8) determines the necessary condition for instability. This condition is satisfied identically for the boundary conditions $Z_s=0$ and $Z_d=\infty$ considered in Ref. 1.

In reality, there is an additional condition for instability. In the limit $M\rightarrow 1$, the gain $|r_{sd}|$ is infinite. At the same time, the instability growth rate vanishes as $M\rightarrow 1$ because of the additional cofactor in the expression (7). This occurs for the following reason.[1] The wave propagates in the forward direction for time $l/[S_s(1+M)]$, while it propagates in the backward direction for the longer time $l/[S_s(1-M)]$. In the limit $M\rightarrow 1$, the propagation time of the wave in the backward direction becomes infinite. We note that under the conditions of superfluid flow[3] ($M>1$) the plasma wave can propagate only in the direction of flow. For this reason, even if the gain $|r_{sd}|$ is infinite, the instability growth rate is vanishingly small in the limit $M\rightarrow 1$, and for $M>1$ it becomes negative. Thus, we have clearly shown that there exists an additional condition for instability $M<1$, suggesting that the flow in the channel must be subsonic.

We shall now analyze stability starting from the equation of energy balance. Using the hydrodynamic equations for shallow water,[3] we obtain

$$\frac{\partial}{\partial t}\left(\int_0^l E\,dx\right)=\Delta\Phi, \tag{9}$$

$$E=\frac{eU}{2m}\left(\frac{eU}{m}+V^2\right),\quad \Phi=\frac{eUV}{m}\left(\frac{V^2}{2}+\frac{eU}{m}\right),$$

where $E(x,t)$ is the energy density, and $\Phi(x,t)$ is the energy flux density of the electronic liquid. Energy flows in the same direction as the current in the channel, $\Delta\Phi=\Phi(0,t)-\Phi(l,t)$. The integral on the left-hand side of the expression (9) is the total energy of the electron flow. The sign of the time variation of the total energy depends on the sign of the right-hand side of the expression (9). The total energy of the electronic liquid increases if energy flows from an external source into the channel, i.e., $\Delta\Phi>0$.

Linearizing the expression (9) and using the expressions (1) and (2), we easily find the energy flux density $\Phi(x,t)$ in the form

$$\Phi=\delta j(\delta u+M\,\delta v)S^5, \tag{10}$$

where $\delta u=\delta U(x,t)/U_s$, $\delta v=\delta V(x,t)/S_s$, and $\delta j=M\,\delta u+\delta v$. Let us consider the source contact. In general, when the impedance Z_s at the source contact is given, we obtain the following expression for the energy flux density $\Phi(0,t)$:

$$\Phi(0,t)=\delta u_1^2 S^5 |Z_s|^{-2} M. \tag{11}$$

Since $\Phi(0,t)>0$, the energy flux at the source is directed from the external circuit into the device channel. It is important that for a fixed current M the energy flux density increases with decreasing value of Z_s.

Let us consider a channel at whose source and drain contacts the impedances Z_s and Z_d, respectively, are given. The energy flux at the drain is directed away from the transistor channel into the external circuit and is given by an expression similar to the expression (11). The modulus of the difference $\Delta\Phi$ of the energy flux entering at the source, $\Phi(0,t)$, and the energy flux leaving at the drain, $\Phi(l,t)$, are positive if $|Z_s|<|Z_d|$. This condition is identical to the condition (8) obtained above.

Thus, both approaches — the perturbation method and the energy-balance analysis — lead to the conclusion that, in general, the instability occurs when $|Z_s|<|Z_d|$. An additional instability condition $M<1$ is that the motion of the two-dimensional liquid must be subsonic.

3. DIVERGENT- AND CONVERGENT-CHANNEL TRANSISTORS— NEW BALLISTIC MOS TRANSISTORS WITH A LONGITUDINALLY NONUNIFORM CHANNEL

We shall now investigate the D'yakonov–Shur instability in a ballistic transistor with a longitudinally nonuniform channel. For simplicity, we shall consider boundary conditions such that the source voltage is fixed ($Z_s=\infty$) and the drain current is fixed ($Z_d=0$).[1] For these boundary conditions energy is pumped at the source, while the energy flux at the drain is zero. Therefore, for a fixed pumping level (i.e., fixed M_s) the Mach number M_d at the drain is arbitrary. At the same time, the total transit time of the plasma wave in the forward and backward directions and, as a result, the instability growth rate depend on the distribution of the Mach number along the channel. Let the Mach number ($M_s<1$) be given at the source. Let us also assume that it increases along the channel to the Mach number M_d at the drain. In this case forward passage of the wave requires less time and the reverse passage more time than in a device with a uniform channel. For some critical Mach number at the source, $M_s^{\mathrm{cr}}<1$, we have $M_d=1$. The instability vanishes, since the propagation time of the plasma wave in both directions is infinite. We therefore have an instability when $M_s<M_s^{\mathrm{cr}}<1$.

Let us now consider the opposite case in which the Mach number decreases along the channel, $M_s>M_d$. Now the passage of the wave requires more time in the forward direction and less time in the reverse direction than in the preceding case and in the case of a uniform channel. Instability exists when $M_s<1$. It can be shown that the growth rate of the instability is always greater in this case than in the other two cases. Both cases ($M_s>M_d$ and $M_s<M_d$) can be realized[6] in a device whose channel is spatially nonuniform, i.e., $C=C(x)$. A nonuniform transistor channel can be obtained by varying the permittivity ε or the thickness d of the subgate insulating layer. In what follows we shall distinguish convergent-channel ($C'<0$) and divergent-channel ($C'>0$) transistors, respectively. These devices have corresponding analogs in classical hydrodynamics.[3] As will be shown below, the instability growth rate is much higher in a divergent-channel transistor than in a transistor with a uniform channel.[1]

The behavior of the 2D electronic liquid in a channel which is longitudinally nonuniform is described by the Euler equation (1) and by the continuity equation

$$\frac{\partial U}{\partial t}+\frac{1}{C}\frac{\partial}{\partial x}(CVU)=0. \tag{12}$$

We note that this equation differs from the hydrodynamic continuity equation[3] which describes ''shallow-water'' flow in a pipe with a varying cross section.

Let us consider the boundary conditions

$$U(0,t)=U_s \qquad \text{and} \qquad j=C_d U(l,t)V(l,t), \tag{13}$$

where U_s is the constant voltage maintained at the source ($x=0$), j is the constant current at the drain ($x=l$), and C_d is the subgate capacitance at the drain.

The steady state in a ballistic transistor with a nonuniform channel is characterized by the voltage U_0, the velocity V_0, and the Mach number M, which all vary along the channel of the transistor. For the steady state Eqs. (1) and (12) can be written in the form

$$j=CV_0U_0, \tag{14}$$

$$\frac{dM}{d\eta}\frac{1}{M}=-\frac{1}{2}\frac{2+M^2}{1-M^2}\frac{dC}{d\eta}\frac{1}{C}. \tag{15}$$

The equation (14) plays the role of the law of conservation of mass in hydrodynamics. The equation (15) can be used to determine the spatial distribution of the Mach number along the channel and has an analog in classical hydrodynamics in the form of an equation that describes the motion of a liquid (gas) in hydrodynamic (aerodynamic) nozzles. The solution of Eq. (15) can be easily found in the form

$$\frac{C(M)}{C_s}=\frac{M_s}{|M|}\left(\frac{2+M^2}{2+M_s^2}\right)^{3/2}, \tag{16}$$

where $i=M_s=j/C_sU_sS_s$ is the dimensionless current, equal to the Mach number M_s at the source, and C_s is the capacitance at the transistor source.

Figure 1a shows the function $c(M)=C(M)/C_s$, normalized to the value of the capacitance at the source and calculated for the case $M>0$ using the expression (16). The function $c(M)$ has a minimum at Mach number $M=1$. Figure 1b shows the reduced subgate capacitance $c^{\min}=c(1)$,

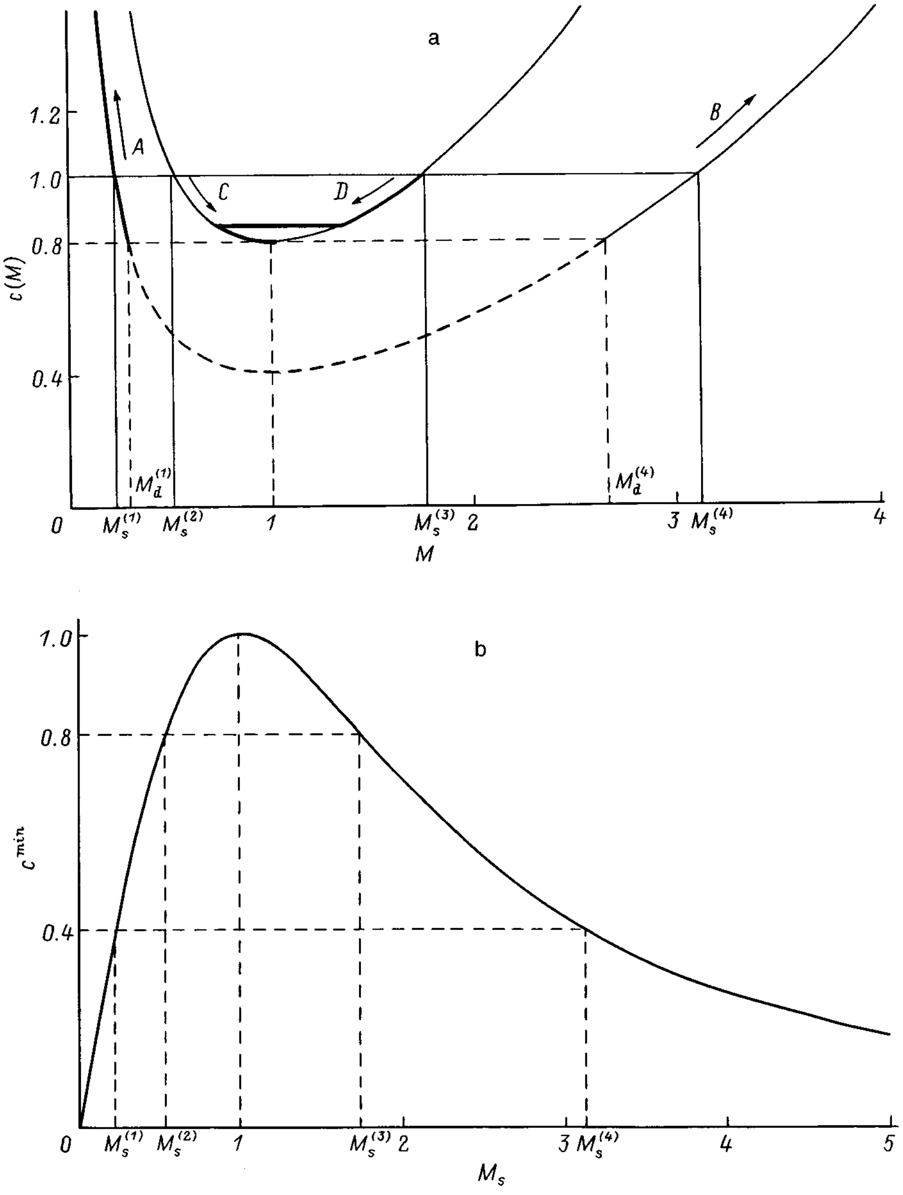

FIG. 1. a — $c(M)$ calculated using the expression (15) for $c^{\min}=0.4$ and $c^{\min}=0.8$. The thick line shows the possible distribution of the Mach number in the shock wave. b — Dimensionless quantity $c^{\min}$ versus the Mach number M_s at the source.

calculated at the minimum of the function $c(M)$, versus the Mach number M_s at the source. The condition $c(M_s)=1$ always holds at the source. For the upper curve in Fig. 1a this condition holds for $M_s=M_s^{(2)}$ or $M_s=M_s^{(3)}$, while $c^{\min}=0.8$. The lower curve in Fig. 1a corresponds to $c^{\min}=0.4$, and the Mach numbers at the source satisfy $M_s^{(1)}<M_s^{(2)}$ and $M_s^{(4)}>M_s^{(3)}$. Following the hydrodynamic analogy, subsonic $(M<1)$ and supersonic $(M>1)$ branches can be distinguished in the function $c(M)$.

Let the capacitance $C(x)$ vary along the channel from a certain value C_s at the source to the value C_d at the drain. We consider first a convergent–channel transistor, where $C_s>C_d$. For subsonic motion the Mach number increases along the channel (the left-hand branch on the lower curve in Fig. 1a), starting at some value at the source $M_s^{(1)}<M_s^{(2)}$ up to the value $M_d^{(1)}$ at the drain. When the Mach number at the source equals $M_s^{(2)}$, the current in the transistor channel saturates (the arrow C in Figs. 1a and 2c), since the flow velocity at the drain is equal to the plasma velocity, i.e., $M_d=1$. This effect, called the choking effect, has an analog in classical

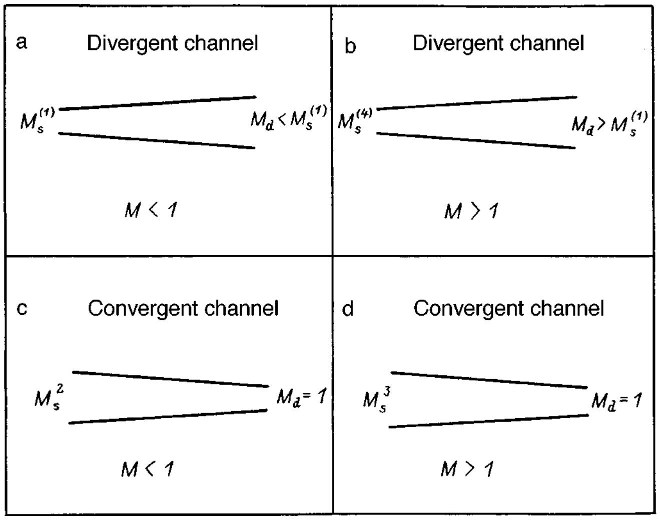

FIG. 2. Schematic diagrams of a divergent-channel transistor $(C_d/C_s>1)$ and a convergent-channel transistor $(C_d/C_s<1)$ for subsonic $(M<1)$ and supersonic $(M>1)$ flows. c, d — Choking regime.

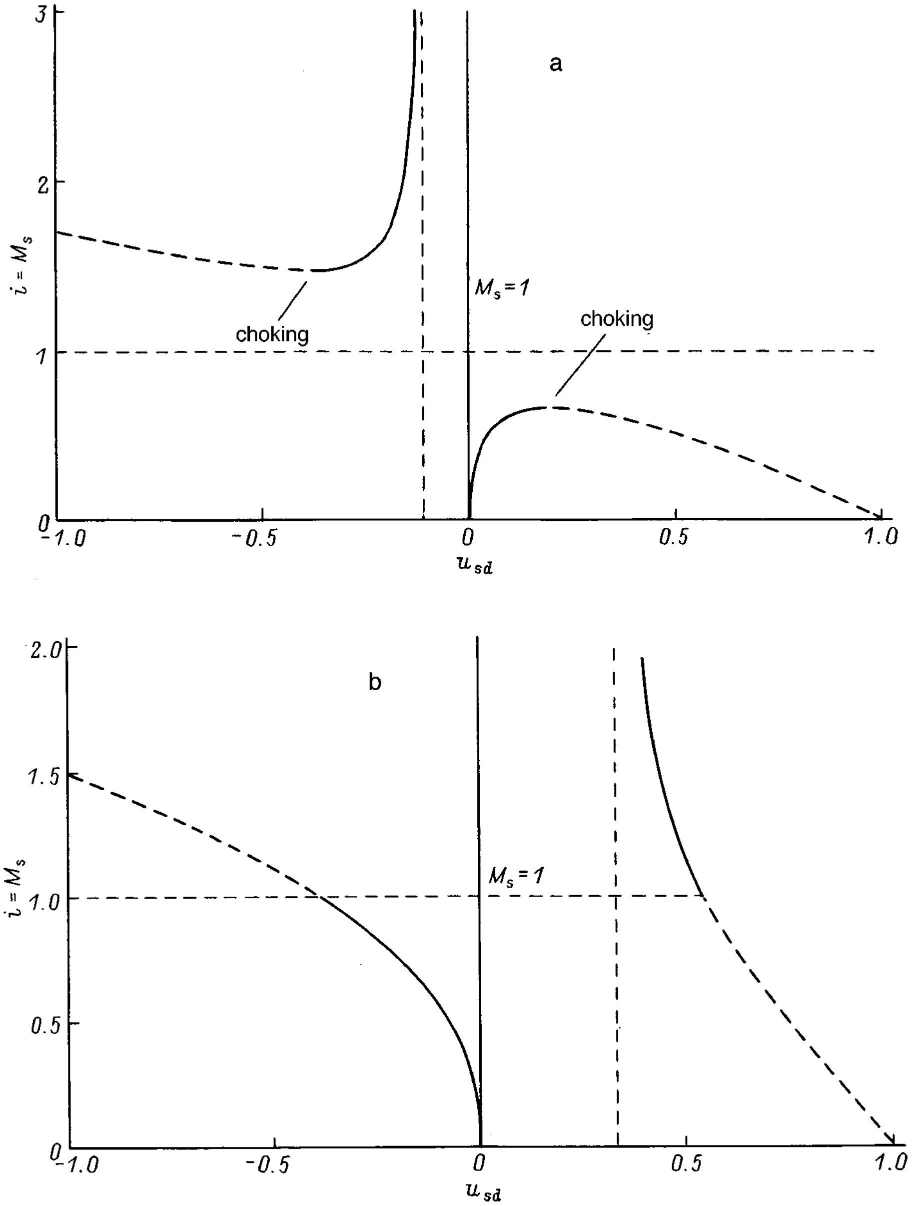

FIG. 3. Current-voltage characteristic of a ballistic transistor with a nonuniform channel. a — convergent-channel transistor, $C_d/C_s = 0.9$; b — divergent-channel transistor, $C_d/C_s = 1.5$. Thick lines — solution of Eq. (15) for regular shock waves. Thin dashed lines — physically meaningless discontinuous solutions of Eq. (15).

hydrodynamics.[3,4] Thus the current cannot exceed $M_s^{(2)}$.

For supersonic flow the Mach number decreases along the channel (right-hand branch on the lower curve in Fig. 1a), starting at some value of the Mach number at the source $M_s^{(4)}$ down to the Mach number at the drain $M_d^{(4)}$. The choking effect appears when $M_s = M_s^{(3)}$ (the arrow *D* in Figs. 1a and 2d). Using Fig. 1b, we easily find the values of the saturation currents for subsonic and supersonic flows in an arbitrary convergent-channel transistor.

We now examine a divergent-channel transistor ($C_s < C_d$). The Mach number increases for supersonic flow (Figs. 3b and the arrow *B* in Fig. 1a) and decreases for subsonic flow (Fig. 2a and the arrow *A* in Fig. 1a). There is no choking effect in a divergent-channel transistor for subsonic and supersonic flows.

We note that Eq. (15) admits solutions which have discontinuities. These solutions correspond to shock waves in classical hydrodynamics.[3,8] Shock waves can exist (Fig. 1a) in divergent- and convergent-channel transistors. It is important to underscore that in reality there exist only shock waves for which the Mach number varies abruptly, switching from the supersonic to the subsonic branch. Otherwise, the second law of thermodynamics is violated.[3] In a shock wave the flow velocity and the potential vary abruptly, while the current remains constant. The spatial position of the shock wave in the channel is arbitrary.

Let us now consider the behavior of the current–voltage characteristics of a ballistic transistor with a longitudinally nonuniform channel. Introducing the dimensionless voltage in the form $u_0 = U_0/U_s$ and using the relation

$$u_0 = \left(\frac{M_s C_s}{MC} \right)^{2/3}, \tag{17}$$

which follows from Eq. (14), the current-voltage characteristic of the transistor can be written in the form

$$i=\pm\left(\frac{2u_{sd}}{(C_s/C_d)^2-(1-u_{sd})^2}\right)^{1/2}(1-u_{sd}),\tag{18}$$

where $u_{sd}=1-u_0(1)$ is the dimensionless source–drain bias. The ± signs correspond to positive (Fig. 3) and negative directions of the current. We note that the current–voltage characteristic of a convergent-channel transistor is similar to that found in Ref. 7 for a uniform-channel transistor, where carrier scattering occurs. In both cases current saturation is determined by the choking effect.

It is interesting to note that the current–voltage characteristic for a divergent-channel transistor (Fig. 3b) contains a subsonic branch where the current falls in a direction opposite to the applied voltage. This contradiction can be easily explained on the basis of the similarity between the electronic and aerodynamic[3,4] divergent channels. In both cases the flow velocity decreases along the channel, while the potential (the pressure in the case of the aerodynamic divergent channel) increases. Correspondingly, the source–drain voltage drop (the pressure drop in aerodynamics) is negative.

4. INSTABILITY GROWTH RATE IN A DIVERGENT-CHANNEL TRANSISTOR

Let us now consider the instability of the steady state in a ballistic transistor with a longitudinally nonuniform channel. Again the expression (13) gives the boundary conditions at the source and drain of the transistor. We can write expressions (1), (11), and (12), which are linearized with respect to small fluctuations of the velocity $V_1(x)$ and voltage $U_1(x)$, in the form

$$\begin{aligned}
&-i\omega V_1+\frac{d}{dx}\left(V_0V_1+\frac{e}{m}U_1\right)=0,\\
&-i\omega U_1+\frac{d}{dx}[C(U_0V_1+U_1V_0)]=0,\\
&U(0)=0,\\
&U_1(l)V_0(l)+U_0(l)V_1(l)=0.
\end{aligned}\tag{19}$$

We now transform the expressions (19) using the dimensionless correction to the current $w=(C/C_s)(U_0V_1+U_1V_0)/S_s^3$ and the variable η introduced earlier:

$$\begin{aligned}
&(1-M^2)w''+\left(2i\frac{\Omega}{s}M+\frac{4M^2-1}{1-M^2}\alpha\right)w'\\
&+\left(\frac{\Omega^2}{s^2}-\frac{2i\Omega M\alpha}{s(1-M^2)}\right)w=0,\\
&w'(0)=0,\quad w(1)=0,
\end{aligned}\tag{20}$$

where $\alpha=C^{-1}dC/d\eta$ is a parameter that characterizes the nonuniformity of the channel, $\Omega=\omega l/S_s$ is the dimensionless frequency, and $s=S/S_s$ is the dimensionless plasma velocity. A solution of Eq. (20) with prescribed boundary conditions exists only for strictly determined values of the complex frequency Ω (eigenvalues in our problem). We note that finding an analytic solution of Eqs. (20) is a quite difficult problem, since this second-order equation contains variable coefficients in front of the main derivatives. Despite this circumstance, Eq. (20) can be easily solved by the high-mode method proposed in Ref. 2. It was shown there that the high modes of plasma oscillations are always less stable than the low modes. The instability growth rate is determined by the most highly unstable high modes. For this reason, it is expedient to use the high-mode approximation[2] to find the instability growth rate for convergent- and divergent-channel transistors. Correspondingly, we shall seek a solution of Eq. (20) with the condition $|\Omega|>1$, i.e., $\Omega\approx\Omega'\gg\Omega''$, $|\alpha|$.

We note that Eq. (20) is similar to the one-dimensional Schrödinger equation in quantum mechanics, and the high-mode approximation corresponds to the semiclassical approximation. The complex frequency plays the role of energy in quantum mechanics. Substituting into expression (20) a trial function of the form

$$w=F(\eta)\exp\left[i\int_0^\eta k(\eta)d\eta\right],\tag{21}$$

where $F(\eta)$ is a function of the coordinate, and $k(\eta)$ is a dimensionless wave vector, we can easily find the dispersion relations

$$\begin{aligned}
&\begin{cases}
k_1=\dfrac{1}{1+M}\left[\dfrac{\Omega}{s}+\dfrac{i\alpha}{2}\left(\dfrac{2M^2-M-1}{1-M^2}\right)\right],\\[2ex]
k_2=-\dfrac{1}{1+M}\left[\dfrac{\Omega}{s}-\dfrac{i\alpha}{2}\left(\dfrac{2M^2+M-1}{1-M^2}\right)\right],
\end{cases}\\
&F_{1,2}(\eta)=\exp\left(-\frac{1}{2}\int_0^\eta\frac{\partial k_{1,2}/\partial\eta}{k_{1,2}+b}d\eta\right),
\end{aligned}\tag{22}$$

where $b=\Omega M/s(1-M^2)$. All leading terms in Ω are retained in the expression (22). The wave vectors k_1 and k_2 correspond to two plasma waves that propagate in the forward and backward directions, respectively. The terms containing the parameter α characterize a longitudinally nonuniform channel.

Finally, we seek the solution of Eq. (20) in the form

$$\begin{aligned}
w=&A_1F_1(\eta)\exp\left(i\int_0^\eta k_1(\eta)d\eta\right)\\
&+A_2F_2(\eta)\exp\left(i\int_0^\eta k_2(\eta)d\eta\right),
\end{aligned}\tag{23}$$

where $A_{1,2}$ are arbitrary constants. Using the prescribed boundary conditions, we obtain the relation

$$\frac{F_2(1)}{F_1(1)}\exp\left(i\int_0^1(k_2-k_1)d\eta\right)=-R,\tag{24}$$

where $R=(1+M_s)/(1-M_s)$ is the amplitude gain for a transistor with a nonuniform channel. We note that for a uniform channel $(\alpha=0)$ $R=R_{sd}$, since $M=M_s=M_d$.

Using the expression (24), it is easy to find both the real and imaginary components of the complex frequency Ω:

$$\Omega'=\pi n/2\int_0^1\frac{d\eta}{s(1-M^2)},$$

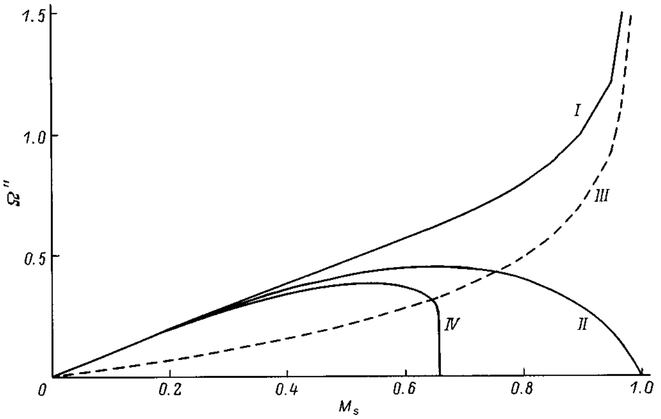

FIG. 4. Instability growth rate Ω'' versus the Mach number at the source for a divergent-channel transistor, $c(\eta)=1+0.5\eta$, with constant source voltage and drain current (*I*), with constant source and drain voltages (*III*), transistor with a uniform channel[1] (*II*), and a convergent-channel transistor, $c(\eta)=1-0.1\eta$ (*IV*).

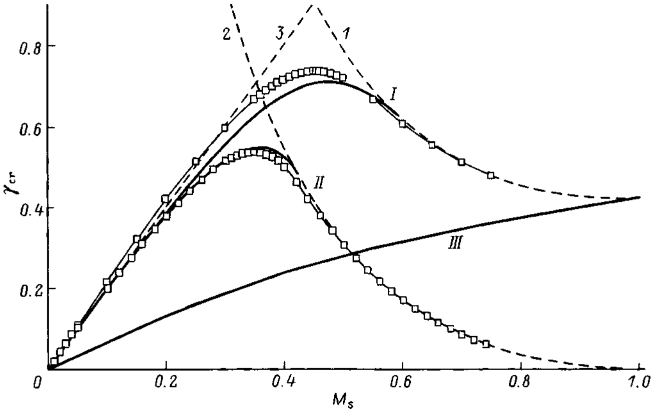

FIG. 5. Diagram of the instability threshold. The function $\gamma_{\rm cr}(M_s)$ with the boundary conditions (19) for a divergent-channel transistor, $c(\eta)=1+0.5\eta$, and a uniform-channel transistor[2] (*II*). *III* — Instability threshold for a divergent-channel transistor with fixed source and drain voltages. Dots — numerical calculation, thick solid line — theory. Asympotes: threshold $\gamma_{\rm ch}(M_s)$ of the choking regime for divergent-channel (*1*) and uniform-channel[2] (*2*) transistors; (*3*) weak-friction limit, $\gamma \ll 1$.

$$\Omega''=\left\{\ln(R)+f(M_d)-f(M_s)+\int_0^1\frac{\alpha M}{3}\left(\frac{2+M^2}{1-M^2}\right)^2 d\eta\right\}\Big/\,2\int_0^1\frac{d\eta}{s(1-M^2)}, \tag{25}$$

where $f(y)=\ln[(1+y)/(1-y)]-2y/3$. We underscore that the expressions (25) are written in the high-mode approximation, i.e., for $n \gg 1$. Given the function $C(\eta)$, using Eq. (14), we easily find the spatial distribution $M(\eta)$ of the Mach number, which in turn can be used to calculate the instability growth rate Ω'' from Eq. (25). Finally, the instability growth rate depends only on the Mach number M_s at the source. Figure 4 shows the function $\Omega''(M_s)$ for convergent- and divergent-channel transistors. The instability growth rate is much larger for divergent-channel transistor than for a convergent-channel and uniform-channel transistors. Moreover, as $M_s\to 1$, the instability growth rate becomes infinite, since $R\to\infty$. In reality, carrier scattering is always present in a real transistor and, as will be shown below, it decreases the growth rate substantially.

5. INSTABILITY THRESHOLD IN A DIVERGENT-CHANNEL TRANSISTOR IN THE PRESENCE OF CARRIER SCATTERING

As shown in Ref. 2, in the case of a transistor with a uniform channel the presence of carrier scattering (the analog of friction between a liquid and the walls in hydrodynamics) leads to lower instability growth rates. The instability acquires a threshold character. For sufficiently large friction the instability vanishes. A similar threshold behavior of instability in the presence of friction is also observed for divergent-channel transistor.

It is easy to rewrite Eqs. (1) and (12) with allowance for friction in the electronic liquid. Accordingly, we must add a term V/τ, which corresponds to scattering,[1,2,7] to the right-hand side of Eq. (1). We can then rewrite Eq. (15), which describes the steady state, in the form

$$\frac{M'}{M}=-\frac{\alpha}{2}\frac{2+M^2}{1-M^2}+\frac{3\gamma}{2s}\frac{M}{1-M^2}, \tag{26}$$

where $\gamma=l/S_s\tau$ is the friction parameter.[2]

We recall that for divergent-channel transistor in the absence of friction the inequality $M_s>M_d$ is satisfied. The effect of friction reduces to the following: For a fixed Mach number M_s at the source the value of the Mach number at the drain increases with the friction γ. At some value of the friction parameter the opposite inequality $M_s<M_d$ is satisfied. Then there is a strictly determined value of the friction parameter $\gamma_{\rm ch}$ such that the choking effect appears at the drain, i.e. $M_d=1$. Instability vanishes in the choking regime. Figure 5 shows the threshold curve $\gamma_{\rm ch}(M_s)$ for a divergent-channel transistor in this regime.

It is easy to show that for weak friction $(\gamma\ll 1)$ the expression (25) for the instability increment Ω'' contains the additional term $-\gamma/2$. It is also obvious that the instability should vanish completely in the limit of strong scattering $(\gamma\gg 1)$. Therefore, for a given value of M_s there should exist a critical value of the friction parameter, $\gamma_{\rm cr}$, such that flow is always stable for $\gamma>\gamma_{\rm cr}$. The instability threshold can be easily found by substituting $\Omega''=0$ into Eq. (25) and by substituting the parameter α (which takes into account the presence of friction):

$$\alpha\to\alpha-\frac{1+M^2+M^4}{(2+M^2)^2}\frac{3\gamma}{Ms}. \tag{27}$$

Figure 5 shows a diagram of the instability threshold, $\gamma_{\rm cr}(M_s)$, for divergent-channel transistor. The threshold diagram lies between the two asymptotes. The first asymptote (dashed line 1) corresponds to the threshold $\gamma_{\rm ch}(M_s)$ of the choking regime in a divergent-channel transistor. The other asymptote $\gamma_{\rm cr}=2M_s$ (dashed line 3) corresponds to weak friction $\gamma \ll 1$, where the Mach number is essentially constant along the channel. Moreover, Fig. 5 shows the result of a numerical calculation of the instability threshold obtained by solving the system of equations (1), (12), and (13) directly by the method described previously in Ref. 8. The results of the analytic and numerical methods are in excellent agreement within the limits of the numerical error. This agreement confirms the correctness of the high-mode approximation which we used to investigate the instability in a divergent-channel transistor.

Let us now compare the diagram of the instability threshold of a divergent-channel transistor with the analogous diagram calculated for a transistor with a uniform channel. The two curves are identical in the limit of weak currents and weak carrier scattering, since in both cases the Mach number distribution along the channel is essentially uniform. In contrast, for high currents the instability threshold for a divergent-channel transistor is much higher than for a device with a uniform channel. For the divergent-channel transistor considered in Fig. 5 there is no instability for $\gamma_{\mathrm{cr}} \geqslant 0.75$, while this criterion is much smaller for a device with a uniform channel. For this reason, to achieve the same instability level as in a transistor with a uniform channel a material with a lower mobility can be used for the divergent-channel transistor. We propose using a divergent-channel transistor as a more efficient generator (detector) than existing generators.[9,10]

In conclusion, we shall examine the instability in a divergent-channel transistor (no friction) when both the gate–source and gate–drain voltages are held constant. We underscore that for a device with a uniform channel there is no instability under these boundary conditions (Sec. 1). The energy flux into the transistor channel at the source equals exactly the energy efflux at the drain. In contrast, under these boundary conditions the instability growth rate is strongly positive in a divergent-channel transistor. For fixed voltage at the boundary the energy flux density is proportional to the Mach number M. Since $M_s > M_d$ for a divergent-channel transistor, the difference $\Delta\Phi$ of the energy fluxes at the source and drain will be strongly positive under the given boundary conditions. Energy flows from the external circuit into the transistor channel, leading to instability. It can be shown that the gain in a divergent-channel transistor is $R = [(1+M_s)/(1-M_s)][(1-M_d)/(1+M_d)]$. Substituting this expression into Eq. (26), we can then find the instability growth rate (Fig. 4) for the given boundary conditions. Using the expressions (25)–(27), it is also easy to find the instability threshold (Fig. 5) in the presence of carrier scattering in a divergent-channel transistor. It is evident that the instability growth rate is comparable to its value for a transistor with a uniform channel. The advantage of a divergent-channel transistor is that boundary conditions such that the source and drain voltages are fixed can be easily realized in practice. Thus a generator (detector) constructed on the basis of a divergent-channel transistor can be viewed as an alternative for existing devices.[9,10]

Let us now make some quantitative estimates of the characteristic parameters of a field-effect MOS transistor based on AlGaAs which are required to obtain the conditions for the instability and generation of plasma oscillations. At temperatures $T = 4-20, 77$, and 300 K the carrier mobility in the channel of a field-effect transistor can reach 300, 30, and 1 $\mathrm{m}^2/(\mathrm{V}\cdot\mathrm{s})$, respectively. For channel length $l = 1\ \mu$m and typical gate–source voltage $U_{sd} = 0.1$ V we obtain the following values of the friction parameter for the three chosen values of the mobility: $\gamma = 0.02, 0.2$, and 6, respectively. For the boundary conditions (13) and the divergent-channel transistor considered above (Fig. 4) instability will occur only at cryogenic temperatures, since $\gamma < \gamma_{\mathrm{cr}} = 0.75$. We note that the value of the parameter γ_{cr} depends only on the geometry of divergent-channel transistor and can differ substantially from the value obtained above, including being larger. Therefore instability can be obtained in a divergent-channel transistor by using less pure materials. This greatly simplifies the problem of observing instability in practice.

6. CONCLUSIONS

The instability of a two-dimensional electronic liquid in the channel of a ballistic field-effect transistor was analyzed on the basis of the energy balance. An instability criterion was found for arbitrary boundary conditions. On the basis of the energy-balance analysis we propose a specially constructed transistor with a high instability growth rate. This device, which we call a divergent-channel transistor, has a corresponding analog in classical electrodynamics. Simple analytic expressions were found for the growth rate and threshold of the instability for a divergent-channel transistor of arbitrary shape. We propose this device as a more efficient generator (detector) than existing devices.[9,10]

We thank M. D'yakonov, M. Shur, and M. Levinshteĭn for support and fruitful discussions.

This work was supported by the French government and the Russian Fund for Fundamental Research (Grant No. 96-02-17895).

[1] M. I. Dyakonov and M. S. Shur, Phys. Rev. Lett. **71**, 2465 (1993).
[2] M. V. Cheremisin, M. I. Dyakonov, M. S. Shur, and G. G. Samsonidze, *Proceedings ISDRS'97* (Solid-State Electron. , 1998), p. 485.
[3] L. D. Landau and E. E. Lifshitz, *Fluid Mechanics* (Pergamon, N. Y., 1966).
[4] V. L. Streeter and E. B. Whylie, *Fluid Mechanics* (McGraw Hill, N. Y., 1985).
[5] M. Shur, *Physics of Semiconductor Devices* (Engelwood Cliffs, N. J., Prentice-Hall, 1990).
[6] M. V. Cheremisin and G. G. Samsonidze, *Proceedings ISPC24* (Jerusalem, 1998); *Proc. CMD17–JMC6* (Grenoble, 1998).
[7] M. I. Dyakonov and M. S. Shur, Phys. Rev. B **51**, 14341 (1995).
[8] A. P. Dmitriev, V. Yu. Kachorovskii, and A. S. Furman, Phys. Rev. B **54**, 14020 (1996).
[9] M. I. Dyakonov and M. S. Shur, IEEE Trans. Electron Devices **43**, 380 (1996).
[10] R. Weikle II, J.-Q. Lu, M. S. Shur, and M. I. Dyakonov, Electron. Lett. **32**, 2148 (1996).

Translated by M. E. Alferieff

InGaAs/GaAs structures with quantum dots in vertical optical cavities for wavelengths near 1.3 μm

N. A. Maleev, A. E. Zhukov, A. R. Kovsh, A. Yu. Egorov, V. M. Ustinov, I. L. Krestnikov, A. V. Lunev, A. V. Sakharov, B. V. Volovik, N. N. Ledentsov, P. S. Kop'ev, and Zh. I. Alfërov

A. F. Ioffe Physicotechnical Institute, Russian Academy of Sciences, 194021 St. Petersburg, Russia

D. Bimberg

Institut für Festkörperphysik, Technische Universität Berlin, Hardenbergstr. 36, D-10623 Berlin, Germany

(Submitted October 29, 1998; accepted for publication November 5, 1998)
Fiz. Tekh. Poluprovodn. **33**, 629–633 (May 1999)

Semiconductor heterostructures with vertical optical cavities with active regions, based on arrays of InAs quantum dots inserted in an external InGaAs quantum well, have been obtained by molecular-beam epitaxy on GaAs substrates. The dependences of the reflection and photoluminescence spectra on the structural characteristics of the active region and optical cavities have been investigated. The proposed heterostructures are potentially suitable for optoelectronic devices at wavelengths near 1.3 μm. © *1999 American Institute of Physics.* [S1063-7826(99)02105-5]

In the last few years semiconductor heterostructures with arrays of quantum dots (QDs) have aroused interest not only because of their unique physical properties but also as promising materials for various optoelectronic devices.[1] One advantage of InGaAs/GaAs structures with QDs is the fundamental possibility of utilizing the wavelength range near 1.3 μm (Ref. 2), which is not accessible in the indicated system of materials with strained quantum wells (QWs) because of the limitations that the conditions of pseudomorphous growth impose on the QW width.[3] This opens up new possibilities in the search for optoelectronic materials for wavelengths near $\lambda = 1.3$ μm that could be alternatives to the conventional InGaAsP/InP heterostructures. Although the heterostructures mentioned above make it possible to match the lattice parameters and give the required band gap, they nonetheless have two fundamental drawbacks: poor temperature characteristics of laser diodes, because of the weak confinement of electrons in the active region, and low parameters of InGaAsP/InP Bragg mirrors because of the small difference of the refractive coefficients of the layers and the poor thermal conductivity of InGaAsP.[4,5] The poor quality of the InGaAsP/InP mirrors makes it necessary to use for surface-emitting lasers and photodetectors with vertical optical cavities (OCs) a complicated technology based either on separate growth of AlGaAs/GaAs Bragg mirrors, followed by sintering with the active layer,[6] or the use of dielectric mirrors.[7]

The production of heterostructures in the system of materials InGaAs/AlGaAs/GaAs, which give the required spectral characteristics near $\lambda = 1.3$ μm, would make it possible to produce in a single epitaxial process structures for surface-emitting lasers and resonance photodetectors with AlGaAs/GaAs Bragg mirrors. Two main directions for utilizing the long-wavelength range have emerged in the last three or four years for InGaAs/AlGaAs/GaAs heterostructures: the addition of small quantities of nitrogen into InGaAs layers and the use of QD arrays obtained by depositing a strongly strained $In_xGa_{1-x}As$ ($x \geqslant 0.5$) layer. For devices with an active region in the form of a QW based on the quaternary compound InGaAsN, laser generation has been achieved at a wavelength of 1.3 μm at room temperature,[8] and the use of InGaAs-QD arrays with 50% InAs content made it possible to obtain a photodetector with a vertical optical cavity for 1.3 μm (Ref. 9). The results of the latest investigations show that it is possible to obtain photoluminescence (PL) in the range 1.3–1.75 μm and electroluminescence (EL) at 1.3 μm at room temperature for structures with InGaAs-QD grown by molecular-beam epitaxy (MBE) on GaAs substrates.[10,11]

In this article we report the results of an experimental study of the possibility of obtaining by MBE on GaAs substrates heterostructures with a vertical optical cavity and an active region based on InAs-QD, placed in an external InGaAs-QW, which are potentially suitable for producing optoelectronic devices for wavelengths near 1.3 μm.

Inserting an array of InAs quantum dots into an external strained InGaAs quantum well makes it possible to increase substantially the wavelength limit of radiation in structures grown by MBE on gallium arsenide substrates. The position of the maxima in the photo- and electroluminescence spectra can be varied in a controlled manner over a wide range by varying the In content in the outer quantum well.[12] To produce the active regions for structures with vertical optical cavities (OCs) we used InAs-QD arrays inserted into an external 4-nm-wide $In_{0.3}Ga_{0.7}As$ QW. The experimental structures were grown by MBE with the solid state source of As_4 in a Riber 32P setup on semiinsulating GaAs (100) substrates. The substrate temperature was 485 °C for deposition of the active region and 600 °C for the rest of the structure.

Photoluminescence was excited with an Ar^+ laser (514.5 nm) and detected with a Ge photodiode. The excitation power density was 100 W/cm^2. The reflection spectra were measured in normal geometry at room temperature using a Ge photodiode.

The experimental structures were fabricated in three steps. First, the bottom mirror, based on an undoped AlAs/GaAs structure with nominal layer thicknesses equal to one-fourth the working wavelength $(\lambda/4)$, were grown by MBE. Mirrors of this type are used for structures with buried p^+ and n^+ contact layers, formed inside the active layer of the OC. After the mirrors were grown, the structure was removed from the chamber and the reflection spectra were measured. The structure was then divided into individual parts on which the different variants of the active layers were grown. This approach makes it possible to investigate different types of active layers with the same bottom mirror. To avoid problems due to the possibility of oxidation of AlAs, all structures of the mirrors were completed with a $(\lambda/4)$ GaAs layer. To ensure that the active-layer material is of high crystallographic quality, the surface of the bottom mirror had to be properly prepared or it had to be protected after the completion of the epitaxial process. We used a $\sim 0.1-\mu$m-thick layer of amorphous arsenic, deposited on the surface of the structure at $\sim$20 °C immediately after the epitaxial process was completed, in order to shield the surface of the bottom mirror. Before starting growth of the active layer, the protective coating was removed in the MBE chamber by annealing the substrate at 610 °C for 10 min with an excess As_4 flow. A sharp diffraction pattern was observed even at temperatures $<$400 °C, which attests to the absence of oxide films beneath the arsenic layer. After the reflection and PL spectra of structures with a grown active region were measured, the upper dielectric mirrors of various types were formed and their influence on the spectral characteristics was investigated. The final variant of the experimental structure with bottom and top mirrors is shown schematically in Fig. 1.

When a $\lambda/4$ reflector is designed for a definite wavelength, it is assumed that this wavelength is the central wavelength λ_c for the reflection spectrum of a structure with periodically repeating layers, whose parameters are related as[13]

$$\lambda_c = 2n_L(\lambda_c)h_L + 2n_H(\lambda_c)h_H. \tag{1}$$

Here $n_L(\lambda_c)$ and h_L are the refractive index and thickness of the layer with the low refractive index (AlAs), and $n_H(\lambda_c)$ and h_H are the analogous parameters of the layer with the high refractive index (GaAs). In addition, it is assumed that the ratio of the optical thicknesses of the layers

$$\rho = n_H(\lambda_c)h_H / n_L(\lambda_c)h_L \tag{2}$$

is exactly 1. For a AlAs/GaAs reflector with $\lambda_c = 1.3$ μm and refractive indices $n_H = 3.44$ and $n_L = 2.90$ the corresponding nominal layer thicknesses are $h_H = 94.4$ nm and $h_L = 111.9$ nm.

However, the condition (2) holds only approximately for real mirrors. The mismatch between the actual and the design layer thicknesses can have a large effect on the deviation of the experimental reflection spectra from the computed spectra. This is due to the inaccuracy in calibrating the growth rate and possible instability of the parameters of the epitaxial process (for example, slow variation of the growth rate for GaAs or AlAs layers or disruption during growth of one of the layers). Moreover, there are discrepancies in the data on the composition and wavelength dependences of the refractive indices of $Al_xGa_{1-x}As$.[14,15] For this reason, it is important to analyze the experimental reflection spectra and to compare them with the computed spectra. The following relations were used to calculate the reflection spectra of the multilayer structures:[16]

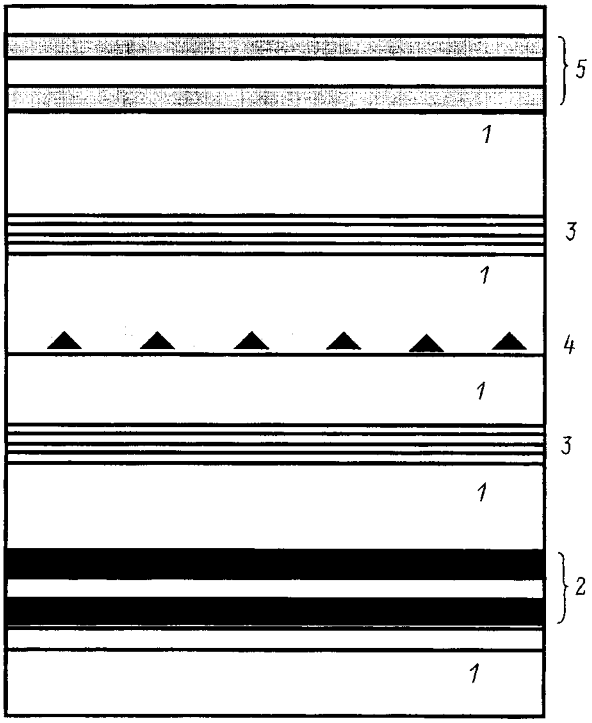

FIG. 1. Schematic representation of the transverse section of the experimental structure with a bottom semiconductor (*2*) and top dielectric (*5*) Bragg reflectors. *1* — GaAs, *3* — short-period AlAs/GaAs superlattice, *4* — active region with InAs-QD in an InGaAs quantum well.

$$R_{i+1}(\lambda) = \{r_{i+1}(\lambda) + R_i(\lambda)\exp[-2j\beta_i(\lambda)l_i]\}/$$
$$\times\{1 + r_{i+1}(\lambda)R_i(\lambda)\exp[-2j\beta_i(\lambda)l_i]\}, \tag{3}$$
$$R_1(\lambda) = r_1(\lambda),$$
$$r_1(\lambda) = (n_i - n_{i-1})/(n_i + n_{i-1}),$$
$$\beta_i(\lambda) = 2\pi n_i(\lambda)/\lambda,$$

where λ is the wavelength of the optical radiation, $R_i(\lambda)$ is the reflection coefficient for the part of the structure containing *i* layers, $r_i(\lambda)$ is the local reflection coefficient between the *ith* and the $(i-1)$ layers, $\beta_i(\lambda)$ is the propagation constant for the *ith* layer, $l_i = h_i\cos\theta_i$ is the effective thickness of the *ith* layer, and h_i, n_i, and θ_i are, respectively, the thickness, the refractive index, and the propagation angle for the *ith* layer. Figure 2 shows the computed and measured reflection spectra at normal incidence of optical radiation for the fabricated Bragg mirror, which consists of 12 pairs of AlAs/GaAs $\lambda/4$-layers and which is used to make devices for the

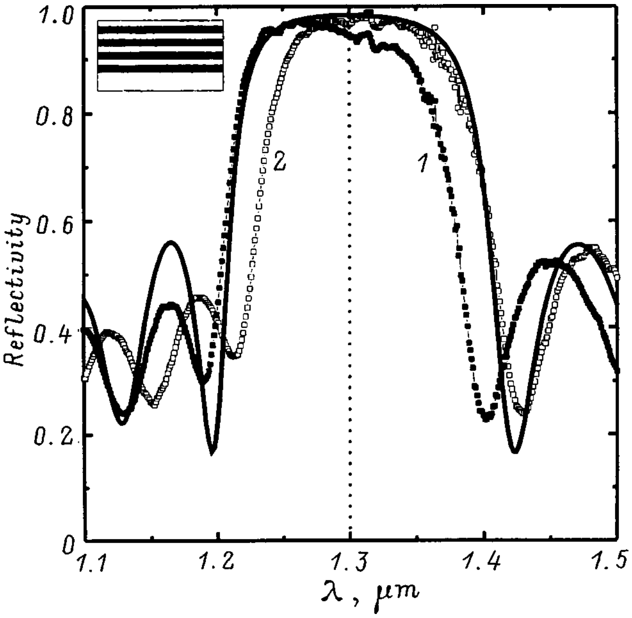

FIG. 2. Computed reflection spectrum for an AlAs/GaAs Bragg reflector with 12 pairs of $\lambda/4$ layers (solid line) and measured spectra at the center (*1*) and edge (*2*) of the structure.

range near 1.3 μm. The chosen number of pairs of layers is inadequate to obtain vertically emitting lasers, since the maximum value of the reflection coefficient does not exceed 0.98, but it is completely sufficient for investigating the fundamental features of structures with vertical OCs. Careful calibration, performed with use of pregrown test structures in the form of several AlAs/GaAs layers, allowed us to obtain reflection spectra close to the computed spectra. However, as follows from Fig. 2, in the real structures there is a gradient of the parameters over the area of the substrates. In our case, where the substrate was grown during the epitaxy process, the parameters exhibited a sharp radial nonuniformity. This feature was taken into account in the design of the active region of the structures, since any deviations from the nominal parameters of the mirrors lead to the appearance of an additional phase shift at the working wavelength.[13]

Figure 3 shows the PL spectra for a structure with an undoped OC with a total nominal thickness $L=377.6$ nm, corresponding to one wavelength $\lambda=1.3$ μm (taking into account the refractive index of GaAs). The parameters of the active layer correspond to a test sample with the PL spectrum maximum at $\lambda=1.3$ μm. To eliminate the influence of surfaces, short-period AlGaAs/GaAs superlattices were inserted 20 nm from the active layer at the top and bottom. The GaAs–air boundary played the role of the top mirror. At room temperature the PL spectrum maximum corresponds to 1.33 μm. The width of the PL line, determined at half-maximum amplitude, is 40 nm for a structure with a vertical OC, and 70 nm for the test structure. This shows that in our case the form of the PL spectrum is largely determined by the parameters of the OC. The small drop in the PL intensity upon raising the temperature from 77 to 300 K suggests that the epitaxial structure is of high quality.

The measured reflection spectrum for the experimental structure is shown in Fig. 4a, and the computed spectra with

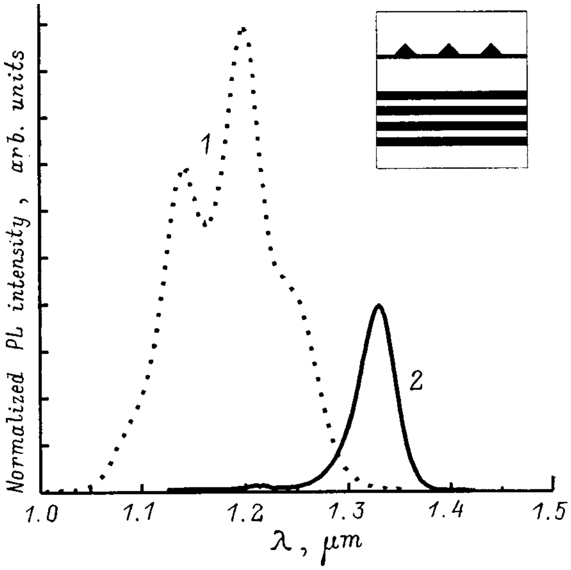

FIG. 3. PL spectra of a sample with an active layer, grown on a Bragg reflector, at 77 (*1*) and 300 K (*2*).

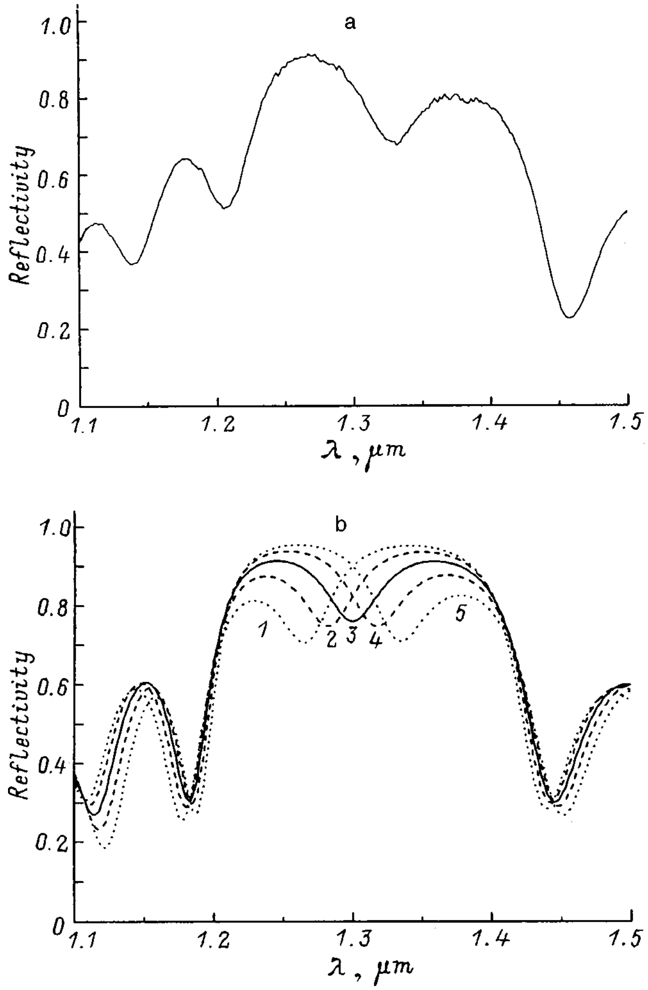

FIG. 4. Reflection spectra for a sample with an active layer, measured (a) and computed (b) with different GaAs active layer thicknesses: *1* — $15\lambda/16n$, *2* — $31\lambda/32n$, *3* — λ/n, *4* — $33\lambda/32n$, *5* — $17\lambda/16n$. $\lambda=1300$ nm, $n=3.44$.

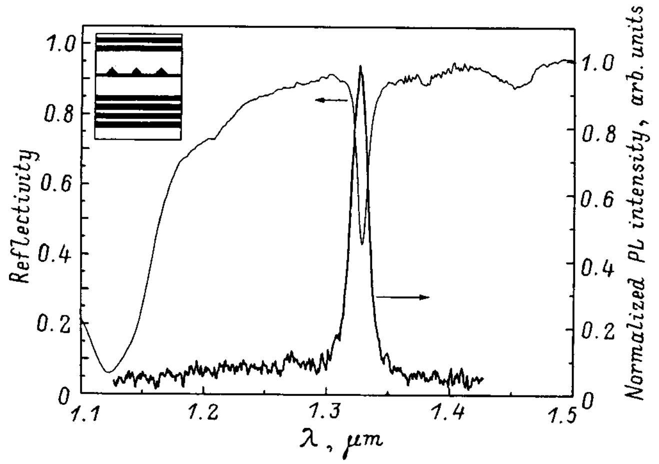

FIG. 5. Reflection and PL spectra for a sample with an active layer after the formation of the top λ/4 dielectric mirror.

various OC thicknesses are shown in Fig. 4b. Analysis shows that the real thickness of the OC layer is somewhat greater than the design thickness; this is what leads to the long-wavelength shift of the position of the minimum in the reflection coefficient spectrum. A calculation using the relations (3) with cavity length $L=401$ nm (which corresponds to $17\lambda/16n$ for GaAs at $\lambda=1.3$ μm) gives for the resonance wavelength in vacuum $\lambda_r=1.335$ μm, in good agreement with the experimental value $\lambda_r=1.331$ μm. At the same time, a simple estimate using the standard relation[13]

$$2\beta L+\phi_1+\phi_2=2m\pi, \quad m=1,2,3\ldots,$$

where $\beta=2n\pi/\lambda_r$, and n is the refractive index of the active layer material, disregarding the phase corrections ($\phi_1,\phi_2=0$), gives $\lambda_r=1.381$ μm. The phase corrections resulting from inaccurate matching of the central wavelength of the quarter-wave reflector to the resonance wavelength therefore play a large role and they must be taken into account when designing the active region.

The top dielectric mirrors were constructed to determine the influence of the OC parameters on the spectral characteristics. Figure 5 shows the measured reflection and PL spectra for a structure with a quarter-wave SiO_2/ZnS reflector at the top. As expected, increasing the figure of merit of the OC substantially narrows the PL spectral line (to 15 nm).

Semiconductor heterostructures with vertical OCs with active regions based on InAs quantum-dot arrays inserted into an external InGaAs quantum well were obtained on GaAs substrates by the MBE method. Bragg reflectors were used to form the OC: the bottom reflector was based on AlAs/GaAs and the top reflector was based on SiO_2/ZnS. The dependences of the reflection and photoluminescence spectra on the characteristic structural features of the active region and the optical cavities were investigated. The technology developed is potentially suitable for producing vertical emitters and resonance photodetectors for wavelengths near 1.3 μm on gallium arsenide substrates.

This work was supported by the Russian Fund for Fundamental Research and INTAS-96-0467. B. V. Volovik is grateful for an INTAS Grant 94-1028-YSF41.

[1] N. N. Ledentsov, V. M. Ustinov, V. A. Shchukin, P. S. Kop'ev, and Zh. I. Alfërov, Fiz. Tekh. Poluprovodn. **32**, 385 (1998) [Semiconductors **32**, 343 (1998)].

[2] R. P. Mirin, J. P. Ibbetson, K. Nishi, A. C. Gossard, and J. E. Bowers, Appl. Phys. Lett. **67**, 3795 (1995).

[3] J. W. Matthews and A. E. Blakeslee, J. Cryst. Growth **27**, 118 (1974).

[4] G. P. Agrawal and N. K. Dutta, *Long Wavelength Semiconductor Lasers* (Van Nostrand Reinhold, New York, 1986).

[5] A. Tsigopoulos, V. Paschos, C. Caroubalos, P. Salet, and J. Jacquet, IEEE J. Quantum Electron. **33**, 2221 (1997).

[6] Y. Qian, Z. H. Zhu, Y. H. Lo, D. F. Huffaker, D. G. Deppe, H. Q. Hou, B. E. Hammons, W. Lin, and Y. K. Tu, Appl. Phys. Lett. **71**, 25 (1997).

[7] T. Baba, Y. Yogo, K. Suzuki, F. Koyama, and K. Iga, *Quantum Optoelectronics Conference* (Palm Springs, 1994) PD2-2.

[8] M. Kondow, T. Kitatani, M. C. Larson, K. Nakamura, K. Uomi, and H. Inoue, *LEOS'97* (San Francisco, 1997) ThE3.

[9] J. C. Campbell, D. L. Huffaker, H. Deng, and D. G. Deppe, Electron. Lett. **33**, 1337 (1997).

[10] D. L. Huffaker and D. G. Deppe, Appl. Phys. Lett. **73**, 520 (1998).

[11] V. Ustinov, A. Egorov, A. E. Zhukov, A. R. Kovsh, N. N. Ledentsov, M. V. Maximov, B. V. Volovik, A. F. Tsatsul'nikov, P. S. Kop'ev, D. Bimberg, and Z. Alferov, in *Tenth International Conference on Molecular Beam Epitaxy* (Cannes, France, 1998) PT4.9.

[12] A. E. Zhukov, A. R. Kovsh, A. Yu. Egorov, N. A. Maleev, V. M. Ustinov, B. V. Volovik, M. V. Maksimov, A. F. Tsatsul'nikov, N. N. Ledentsov, Yu. M. Shernyakov, A. V. Lunev, Yu. G. Musikhin, N. A. Bert, P. S. Kop'ev, and Zh. I. Alfërov, Fiz. Tekh. Poluprovodn. **33**, 180 (1999) [Semiconductors **33**, 153 (1999)].

[13] M. S. Unlu and S. Strite, J. Appl. Phys. **78**, 607 (1995).

[14] M. A. Afromovitz, Solid State Commun. **15**, 59 (1974).

[15] *Properties of Aluminium Gallium Arsenide*, edited by S. Adachi [INSPEC, EMIS Datareviews, N7 (1993)].

[16] P. Yeh, *Optical Waves in Layered Media* (Wiley, New York, 1988).

Translated by M. E. Alferieff

SEMICONDUCTORS VOLUME 33, NUMBER 5 MAY 1999

Correlation between the reliability of laser diodes and the crystal perfection of epitaxial layers estimated by high-resolution x-ray diffractometry

V. P. Evtikhiev, E. Yu. Kotel'nikov, I. V. Kudryashov, V. E. Tokranov, and N. N. Faleev

A. F. Ioffe Physicotechnical Institute, Russian Academy of Sciences, 194021 St. Petersburg, Russia

(Submitted November 10, 1998; accepted for publication November 18, 1998)
Fiz. Tekh. Poluprovodn. **33**, 634–638 (May 1999)

The dependence of the degradation of high-power quantum-well GaAs/AlGaAs laser diodes, grown by molecular-beam epitaxy, on the crystal perfection of the individual layers of the heterostructure is investigated. The crystal perfection of the layers is estimated by high-resolution x-ray spectrometry. A numerical fit of the diffraction-reflection curves is performed using the Debye–Waller static factor. It is shown that considerably higher crystal perfection of laser heterostructures can be obtained by using as the waveguide layers binary AlAs/GaAs superlattices instead of the solid solution AlGaAs. *© 1999 American Institute of Physics.* [S1063-7826(99)02205-X]

The need to increase the service life of powerful injection lasers is stimulating further investigations of the initial epitaxial structures to determine the possible reasons for the degradation of these devices. Investigations of the degradation of injection laser diodes can be divided into two directions. The first one is the study of degradation arising near the mirrors of the laser diodes as a result of surface phenomena and the interaction of the material with atmospheric oxygen.[1,2] In this area of research several methods for improving the reliability of lasers have been suggested: the use of Al_2O_3 thin films for the mirrors[3] and the use of nonabsorbing mirrors.[4] The second one involves the study of volume degradation due to the imperfection of the epitaxial layers.[5–7] We posed the problem of finding methods for predicting degradation this type for epitaxial layers, obtained by molecular-beam epitaxy (MBE), on the basis of structure-sensitive diagnostics methods. High-resolution x-ray diffractometry, widely used for investigating various heterostructures,[8,9] was chosen as the main method of investigation.

High-resolution x-ray diffractometry is based on the inference of x-rays in multilayer heterostructures.[10,11] This method possesses, on the one hand, high spatial resolution which is comparable for certain types of heterostructures to the resolution of transmission electron microscopy,[12,13] and, on the other, high sensitivity to crystal structural perfection, which can be used to study the characteristic features of the mechanisms of epitaxial growth and defect formation in heterostructures.[14,15]

Using structure-sensitive diagnostics methods, we resolved the problem involving the investigation of the possibilities of predicting the development of degradation processes (during the operation of laser diodes) which are attributable to the imperfection of the crystal structure of epitaxial layers.

Two types of MBE diode structures (Fig. 1) were chosen as the objects of investigation. The main method of investigation was the nondestructive method of two-crystal x-ray diffractometry. The laser structures for the investigations were grown using the TsNA-4 molecular-beam epitaxy system on oriented n^+-type GaAs (001) substrates. The structures contained 0.5-μm-thick n^+-type GaAs buffer layers, n- and p-type $Al_{0.6}Ga_{0.4}As$ emitter layers, waveguide layers, 100-Å-thick GaAs quantum wells (QWs), and 0.5-μm-thick p^+-type GaAs contact layers. The quantum well in type-I structures (Fig. 1a) was confined by 0.2-μm-thick $Al_{0.2}Ga_{0.8}As$ waveguide layers and in type-II structures (Fig. 1b) the well was confined by a 0.25-μm-thick layer of a variable-gap superlattice (VSL) with linearly varying band gap, similarly to the equivalent graded layer $Al_{0.33}Ga_{0.67}As$–$Al_{0.2}Ga_{0.8}As$. The n-type dopant was Si and the p-type dopant was Be. The choice of growth regimes for all layers and monitoring of the growth process (growth rates and substrate temperatures) were performed by the HEED method. The growth rates were measured from the oscillations of the intensity of the specularly reflected reflection (off Bragg). The ratio of the fluxes of group-V/III elements was chosen in the range 1.5–2.0. The buffer and contact layers were grown with substrate temperature 600 °C and 2×4 surface reconstruction. The wide-gap $Al_{0.6}Ga_{0.4}As$ emitter layers of all laser heterostructures were grown with a substrate temperature of about 720 °C. The solid solutions $Al_{0.2}Ga_{0.8}As$ — waveguide layers and QW in GaAs — were grown near a substrate temperature of 690 °C. The growth of the VSL and the QW was optimized near a substrate temperature 660 °C. The laser diodes fabricated from the experimental structures for lifetime tests consisted of 100-μm-wide and approximately 700-μm-long strips with SiO_2 insulation and mirrors formed by natural cleavage surfaces. The diodes were soldered onto copper heat dissipators with the p-layer oriented downwards. The devices had good characteristics: the threshold generation densities 180–250 A/cm^2, differential quantum efficiencies 75–80% on two mirrors, and characteristic temperatures T_0 on the order of 200 K.

The x-ray diffraction studies were performed on a TRS-1 high-resolution diffractometer. A dislocation-free Ge single

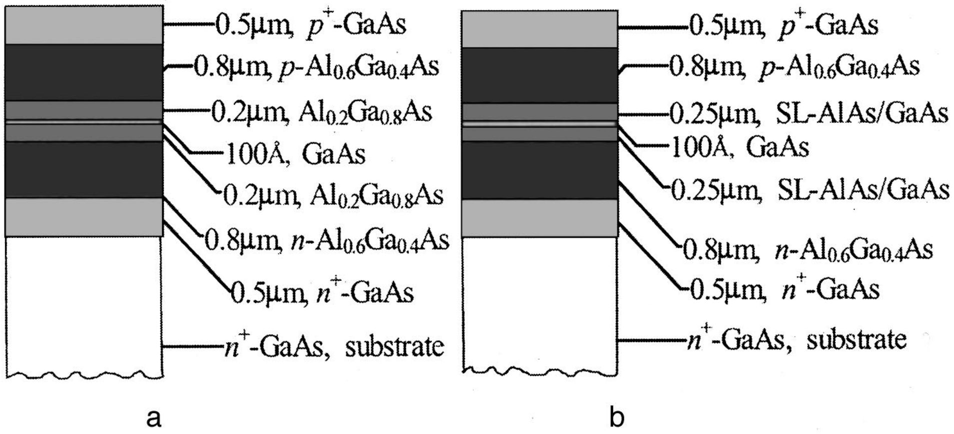

FIG. 1. Schematic diagram of two types of laser heterostructures: a — with an AlGaAs waveguide; b — with a waveguide in the form of an AlAs/GaAs superlattice.

crystal, asymmetric for the (004) reflection ($CuK_{\alpha 1}$ radiation), giving a divergence of 1.0–1.2″ for monochromatized radiation, was used to monochromatize and collimate the x-rays. The beam size after the monochromator was limited by the exit slit to $0.1\times 2.0\ mm^2$ in order to decrease the influence of the bending of the heterostructures. The diffraction reflection curves (DRCs) were measured in a symmetric geometry near the (004) reflection of GaAs.

At the first stage a qualitative preliminary analysis of the shape and parameters of the DRCs showed (Fig. 2) that all laser heterostructures that were grown possess high crystal perfection — there are no extended defects (of the mismatch dislocation type). The epitaxial layers are planar and the interfaces are sharp. The density and size of the structural defects (primarily of the point type or clusters of such defects) are not so large that under our conditions of measurement of the diffraction curves the off-planarity of the layers, the volume stresses, and diffuse scattering would wash out the thickness oscillations and broaden the diffraction peaks. At the second stage of the investigations, to simplify the subsequent numerical fit the parameters obtained from the DRCs (layer thicknesses and percentage composition) for each structure grown were compared with the technological parameters measured using the HEED oscillations and incorporated in the growth program. Typical data obtained by the two methods are presented in Table I for structures from different series *A*-224 and *A*-327. Comparing these data shows that they are at least consistent with one another.

When analyzing the RDCs, it is necessary to take into account the fact that the laser diode structures are ‘‘interference’’-type multilayer heterostructures. In crystallographically perfect layers of this type, each layer and a collection of some layers influence in a definite way the shape and parameters of the resulting diffraction curve. For example, the parameters of the quantum well (thickness and composition) influence primarily the shape of the envelope of the curve near the peaks that correspond to the waveguide layers. The thickness and composition of the QW and the waveguide layers determine the shape of the emitter peaks, whose position and shape, with good matching of the compositions in the bottom and top emitter layers (within 2–4% with respect to the quantity of Al), is uniquely determined by the interference of the radiation diffracted by them. The resulting pattern near a substrate peak is a superposition of

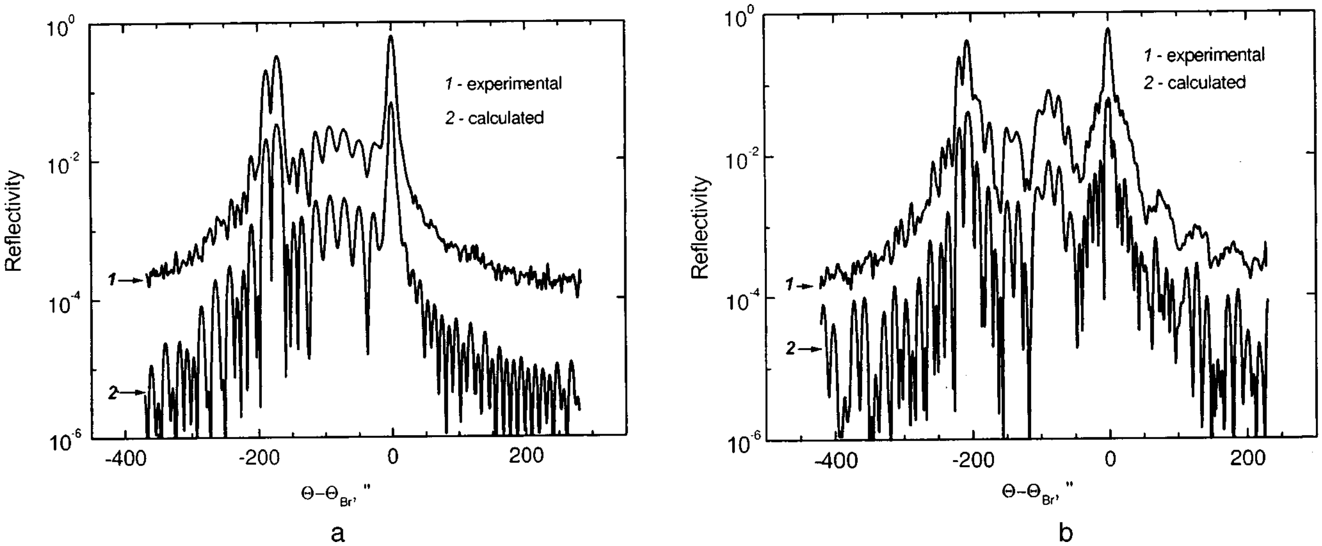

FIG. 2. Experimental (*1*) and computed (*2*) diffraction curves of the (004) reflection ($CuK_{\alpha 1}$ radiation) for samples: a — with an AlGaAs waveguide (*A*-224) and b — with a waveguide in the form of an AlAs/GaAs superlattice (*A*-327).

TABLE I. Comparison of parameters obtained by the RDC method for two structures whose technological parameters were measured using HEED oscillations.

Structure No.	Structural parameters	Measurment method HEED	Measurment method DRC
A-224	t_e, μm	0.8	0.75
	N_e(Al), %	48	50
	t_w, μm	0.4	0.36
	N_w(Al), %	20	22
A-327	t_e, μm	0.75	0.77
	N_e(Al), %	55	57
	t_w, μm	0.45	0.46
	N_w(Al), %	26	25

Note: HEED — high-energy electron diffraction, RDC — diffraction reflection curve, t_e and t_w — thicknesses of the emitter and waveguide layers, N_e(Al) and N_w(Al) — Al content in the emitter and waveguide layers.

thickness oscillations from the epitaxial layers as a whole (except for the buffer layer)[11] and from the top contact layer. The existence and sharpness of these oscillations, together with the other indicated characteristics, are consequences of the high crystalline perfection of the structures investigated. As a rule, large changes in the parameters and shape of the RDCs, due to large disruptions of the crystalline perfection of the heterostructures can be easily interpreted. The absence of a particular group of thickness oscillations in the RDCs or a change in the shape of the curves, for example, near the emitter or substrate peaks, indicates that the growth process has been disrupted at a definite stage.

At the third stage of the investigations numerical fitting of the RDCs was used to refine the distribution profile of the deformation and composition and to estimate the density of structural defects. The dynamic Takagi–Topen model for an ideal deformed crystal was used.[16] The corrections taking account of the scattering of x-rays by structural defects (decrease in the intensity of the main peaks in the RDCs) were introduced using the static Debye–Waller (D–B) factor, which characterizes the degree of structural perfection of the epitaxial layers. The technological distribution profile of the composition, refined according to the composition and thicknesses of the layers with respect to the parameters of the experimental curves, was used as a starting approximation to calculate the deformation profile. As a rule, this makes it possible to decrease the number of adjustable parameters and to improve the computational reliability. When fitting the computed RDC by varying the parameters of the heterostructure (the composition and thickness of the layers), it is first necessary to match the positions and shape of the main peaks and thickness oscillations, taking into account the interference nature of the formation of the diffraction curves. When the shapes of the computed and experimental curves match well, a difference of their parameters (the comparison should be made according to the reflection coefficients of the main diffraction peaks — from the substrate, from the waveguide and emitter layers) indicates that small cluster-type crystalline defects are present in the structure under study.[17] The static D–B factor was used for the final fit of the parameters of the computed curves. The experimental and computed values of the reflection coefficients for the main peaks must be matched by adjusting this factor.

The investigations of the degradation of laser diodes were performed on several (three or four) samples of each structure in the regime where the initial working current for output optical power $P = 0.4$ W from each mirror with fixed heat-removal temperature $T = 25\,^\circ$C is maintained. The curves of the time-dependence of the output optical power obtained in this manner for samples operating for more than 1000 h usually consisted of a continuous saturating decrease of the output optical power, which occurred most likely because of the degradation of the material near the mirror surfaces. A characteristic feature in the time dependence of the output optical power for samples with a short service life was the terminal section where the power dropped sharply (5–30 min), most likely because of the development of dark-line defects in the interior of the material. The final stage of the process of rapid degration was observed under an optical microscope on specially prepared samples with an optically transparent contact and by examining the degraded samples in a scanning electron microscope. The lifetime of the laser diodes was taken as the time when the initial output optical power decreased by more than 30% from the initial level and then averaged over several characteristic degradation curves for samples with the same structure. Data on device degradation and the computed values of the static D–W factor are presented in Table II.

Table II gives the values of the static D–W factor for the waveguide and emitter layers closest to the QW, in which the optical radiation propagates and a high-density electron-hole plasma arises; the structural perfection of these layers strongly influences the degradation characteristics of the devices. Comparing the values of the static D–W factor for the epitaxial layers of various structures with the lifetime of de-

TABLE II. Comparison of the values of the static Debye–Waller factor for epitaxial layers of structures (with two types of waveguide layers) with the lifetime of devices fabricated from them.

Sample	Type of structure	Threshold current, A/cm^2	Differential quantum efficiency, %	Device lifetime, h	Debye–Waller factor waveguide	Debye–Waller factor emitter
A-254	1	200	35	10		
A-219	1	250	34	80	0.67	0.835
A-224	1	220	35	200	0.92	0.915
A-327	2	175	40	2900	0.99	1.0
A-309	2	180	40	2500	0.97	0.95

Note: Types of structures: 1 — AlGaAs waveguide; 2 — waveguide with variable-gap AlAs/GaAs superlattice.

vices fabricated from them shows that the estimates obtained for the crystalline perfection of the epitaxial layers (static D–W factor) by calculation from the x-ray diffraction spectra correlate well with the degradation characteristics of laser diodes. On this basis we can assert that the crystal perfection of the device heterostructures is decisive for achieving a long service life for this class of devices. Note, in particular, that in laser structures the crystal perfection of heterostructures as a whole, not individual layers, is important. It is impossible to single out the layer whose perfection guarantees high device performance. In epitaxial structures the crystalline perfection of the lower layers determines the structural perfection of the upper-lying layers. In addition, the structural defects formed in the upper layers migrate into the lower-lying layers during growth and during device operation, and they degrade the crystalline perfection of the layers.

Growth of thick layers of the solid solutions AlGaAs in a wide range of compositions is the most difficult task in obtaining crystallographically perfect multilayer AlGaAs/GaAs heterostructures by the MBE method. If this, at first glance, local problem is not solved, it is impossible to obtain by the MBE method diode laser structures with high working parameters. Because of the characteristic features of the molecular-beam epitaxy, surface segregation of Ga occurs when AlGaAs is grown in the substrate temperature range 630–710 °C. This results in substantial degradation of the morphological and optical properties of the heterostructures. Growth of solid solutions outside this temperature range also has its own peculiarities. Growth at substrate temperatures below 630 °C, for example, is characterized by a large number of point defects (*DX* centers, and so on). When this material interacts with powerful optical radiation, it leads to stimulated diffusion of point defects, in which large defects are ultimately formed (dark-line defects, and so on). Growth at substrate temperatures above 710 °C cannot be monitored as well by the method of oscillations of the DRCs and results in a higher probability for the appearance of As vacancies and complexes based on them, which also affects the quality of the layers.

Special emphasis was placed on the choice of growth regimes of the QW and the waveguide layers confining it. It is desirable to grow these layers of the laser structure under identical conditions, without additional stoppages at the waveguide–QW heterojunction to change the growth temperature or the flux ratio. Any additional stoppage can result in the appearance of nonradiative recombination centers at this heterojunction, which is very important for a laser with an active quantum-well region. An alternative to AlGaAs solid solutions for waveguide layers are short-period binary AlAs/GaAs superlattices, since high-quality AlAs and GaAs layers can be obtained in a wide temperature range.[18] In addition, the periodic deformation potential due to the superlattice effectively prevents migration of defects that could have formed in the adjoining layers during the growth process.[19]

It has been shown that high-resolution x-ray diffractometry is a reliable method for estimating the crystal perfection of device laser heterostructures. The results of our investigations show that there is a strong correlation between the density of growth defects in device heterostructures (to estimate them we employed a computational parameter — the static Debye–Waller factor) and the degradation rate of laser diodes fabricated from these structures. Comparing the degradation parameters and the crystallographic perfection according to the D–W factor for devices with various types of waveguides shows that epitaxial layers with much higher crystal perfection can be obtained by using as waveguide layers variable-gap binary AlAs/GaAs superlattices instead of the solid solution $Al_{0.2}Ga_{0.8}As$. Of course, the threshold nature of this method should be noted, since the methods of high-resolution x-ray diffractometry are sensitive not to individual point defects but rather to accumulations and clusters of such defects. Nonetheless it is correct to use the method of double-crystal diffractometry and the static Debye–Waller factor as the main parameter to estimate the crystal perfection of heterostructures.

This work was supported by grants from the Russian Fund for Fundamental Research.

[1] H. Yonezu, K. Endo, T. Kamejima, T. Torikai, T. Yuasa, and T. Furuse, Appl. Phys. Lett. **50**, 5150 (1979).
[2] F. R. Nash, R. L. Hartman, N. M. Denkin, and R. W. Dixon, J. Appl. Phys. **50**, 3122 (1979).
[3] F. R. Gfeller and D. J. Webb, J. Appl. Phys. **68**, 14 (1990).
[4] H. Naito, O. Imafuji, M. Kume, H. Shimizu, and M. Kazumura, Appl. Phys. Lett. **61**, 515 (1992).
[5] R. G. Waters and R. K. Bertaska, Appl. Phys. Lett. **52**, 179 (1988).
[6] S. G. Konnikov, M. I. Sverdlov, F. Ya. Filipchenko, and A. A. Khazanov, Fiz. Tekh. Poluprovodn. **24**, 2010 (1990) [Sov. Phys. Semicond. **24**, 1249 (1990)].
[7] M. M. Sobolev, A. V. Gittsovich, M. I. Papentsev, I. V. Kochnev, and B. S. Yavich, Fiz. Tekh. Poluprovodn. **26**, 1760 (1992) [Sov. Phys. Semicond. **26**, 985 (1992)].
[8] B. Estop, A. Izrael, and M. Sauvage, Acta Crystallogr., Sect. A: Cryst. Phys., Diffr., Theor. Gen. Crystallogr. **32**, 627 (1976).
[9] M. A. G. Halliwell and M. H. Lyons, J. Cryst. Growth **68**, 523 (1984).
[10] L. Tapfer and K. Ploog, Phys. Rev. B **40**, 9802 (1989).
[11] N. N. Faleev, L. I. Flaks, S. V. Batashova, S. G. Konnikov, and I. K. Solimin, Phys. Status Solidi A **120**, 327 (1990).
[12] C. R. Wie, J. C. Chen, H. M. Kim, P. L. Liu, Y.-W. Choi, and D. M. Hwang, Appl. Phys. Lett. **55**, 1774 (1989).
[13] L. Tapfer, M. Ospelt, and H. Kanel, J. Appl. Phys. **67**, 1298 (1990).
[14] N. Faleev, R. Stabenov, M. Sinitsyn, B. Yavich, A. Haase, and A. Grudski, Mater. Sci. Forum **166–169**, 293 (1994).
[15] V. G. Gruzdov, A. O. Kosogov, and N. N. Faleev, Pis'ma Zh. Tekh. Fiz. **20**, 1 (1994) [Tech. Phys. Lett. **20**, 561 (1994)].
[16] R. N. Kyutt, P. V. Petrashen, and L. M. Sorokin, Phys. Status Solidi A **60**, 381 (1980).
[17] K. M. Pavlov, V. I. Punegov, and N. N. Faleev, Zh. Éksp. Teor. Fiz. **107**(6), 1967 (1995) [JETP **80**, 1090 (1995)].
[18] F. Alexandre, L. Goldstein, G. Leroux, M. C. Joncour, H. Thibierge, and E. V. Rao, J. Vac. Sci. Technol. B **3**, 950 (1985).
[19] N. A. Bert, N. N. Faleev, and Yu. G. Musikhin, in *Abstracts of the 9th International Conference on the Microscopy of Semiconductor Materials* (SMM IX) (UK Oxford, 1995), p. 98.

Translated by M. E. Alferieff